DISSERTATION

Titel der Dissertation

″Geochemical and Petrographic Studies of the Volcano-Tectonic Evolution of Northern Afar: Implications for the Structural Setup of the Actively Expanding Erta'Ale Depression″

Verfasser

Mag. Miruts Hagos

angestrebter akademischer Grad

Doktor der Naturwissenschaften (Dr. rer. nat.)

Wien, im November 2010

PREFACE:

This thesis presents the results of three full years of work conducted at the Department of Lithospheric Research, University of Vienna, on the rock samples and structural data collected from the Ethio-Afar volcanic province, Ethiopia. The main objective of this study was to establish the Oligocene–Present volcano-tectonic evolution of the northern Afar Depression and set the appropriate nature of the Afar Depression lithosphere. This work was done at the megascopic scale for the regional geological map and structural setup of the northern Ethiopian plateau and the northern Afar Depression volcanic provinces. The petrogenetic link between the Ethiopian flood and the Danakil Depression basalts was evaluated, using petrographic analyses of the samples together with their major and trace element composition, as well as the Sr and Nd isotopic composition of selected samples. Geochemical and isotopic data were obtained using instrumental neutron activation analysis (INAA), X-ray fluorescence (XRF) spectrometry, electron microprobe (EMP), and thermal ionization mass spectrometry (TIMS) at the Department of Lithospheric Research, University of Vienna.

This thesis consists a total of eight chapters with a much summarized general introduction of the East African Rift System (Chapter 1) and review of the regional tectonics and magmatism throughout East Africa (Chapter 2) followed by short description of the methodologies used (Chapter 3). The other five chapters are dealing with the specific tectonic and volcanics details of the Afar Depression. Chapter 4 (a conference proceedings) presents the structural and kinematic aspects of the young ocean basin (Afar Depression), followed by characterization of the pre- and post-rift volcanism of the rift bounding plateau (Chapters 5 and 6). The compositional differences of basaltic rocks in a highly evolved rift segments is presented in Chapter 7, and plume-head to tail magmatic evolution of the Afar volcanic province is summarized in Chapter 8.

Chapter 4 (a conference paper, presented at the 7th Congress of the Ethiopian Geosciences and Mineral Engineering Association, August 27–28, 2010, Addis Ababa, Ethiopia) presents an overview of the structural and kinematic analysis of the Afar Depression starting from continental breakup to incipient sea-floor spreading. Measured structural data together with the existing data shows that the Afar Depression geometric make-up is under progressive transformation. Incipient breakup of the Afar Depression was mainly due of the slab pull at the

Zagros Orogenic Front leading to an initial oblique extension similar to that of the Red Sea and Gulf of Aden. The increasing influence of the Afar mantle plume and the westwards propagation of the Gulf of Aden enabled the depression to change its geometric and kinematic characteristics and rotate the eastern flank (Danakil Block) in a counter clockwise direction. After 30–25 My of deformation, extension in the Central and Northern Afar Depression is orthogonal to its axial zone.

Chapter 5, a manuscript currently in press in a book called 'Topics on Petrology' at Springer publishers, presents and discusses major and trace element data of the northern Ethiopian flood basalts, Axum area. Basically, two distinct lava groups have been discovered in the region: the first one (Axum flood basalt sequence) is part of the Ethiopian flood basalts; whereas the second group (Axum post-trap basalt sequence) is totally distinct from the flood basalts. The chemical difference is observed in both the major (TiO_2, Fe_2O_3, MgO, CaO) and trace (Rb, Ba, Nb, Th, Ta, La) element contents, reflecting variation in degree and depth of melting among the two groups.

Chapter 6, a paper accepted for publication in the Austrian Journal of Earth Sciences, discusses the geochemical characteristics of the Axum basaltic series and the phonolite/trachyte plugs. Unlike any other region in the northern Ethiopian volcanics, the Axum–Adwa area is shattered by a series of E–W aligned trachyte and phonolite plugs. This chapter presents the first detailed study of the Axum volcanics (Alkali basalts and phonolites/trachytes). Two major episodes of volcanic activities occurred in the region. The Axum flood basalt sequence erupted contemporaneously with the major Ethiopian flood basalt and the second (the Axum post-trap volcanics) erupted late, most probably at the end of Miocene and beginning of Pliocene.

Chapter 7 presents various geochemical studies of the Erta'Ale axial range (northern Afar Depression). Using the XRF, INAA EMP and TIMS data, together with the petrographic study, different series of basalts were identified. The TIMS analysis also assisted in deciphering the possible source of the basaltic rocks of the region.

Chapter 8 deals mainly on the comparison of the Ethiopian Plateau basalts (plume-head) the Danakil Depression basalts (Plume-tail). A comparison was made based on the chemical analyses used in this thesis and other analyses from the Ethiopian flood basalts.

ACKNOWLEDGEMENTS:

ABSTRACT:

The Ethio-Afar mantle plume is one of the youngest plume structures on earth that continually pours significant amounts of magmatic products to the surface of the earth for the last 30 Ma or more and reshaping the sublithospheric crust of east Africa. As a result of the complex geodynamic nature of the region, the petrologic diversity is very significant, the lavas ranging from basanites to tholeiitic basalts and phonolites to trachytes. This thesis presents geochemical and petrographic investigations of 90 volcanic rocks, mainly basaltic, from both the northern Ethiopian flood basalts and northern Afar Depression, the Erta'Ale Range. It also incorporates the kinematic analysis of the northern and central Afar Depression from incipient breakup to seafloor spreading.

Rock sampling was performed in two field seasons: the first was in 2007 from the Ethiopian highland volcanic rocks and the second in 2008/09 from the northern Afar Depression axial basalts. Many petrologically distinct volcanic sequences in the northern Ethiopian plateau as well as Afar Depression have been identified. The oldest volcanic rocks of the Afar mantle plume are represented by the high-Ti (HT) and low-Ti (LT) groups of the Oligocene flood basalts. However, compositionally distinct magmatic series have been sporadically erupted in the Ethiopian highlands. One of these volcanic sequences is comprised of the Axum post-trap volcanics, a geochemically complex and lithologically varied part of the northwestern Ethiopian flood basalt province that erupted during a narrow time span.

After the peak activity of the Ethiopian flood basalts, magmatic activities were mainly concentrated in the form of shield volcanoes in the plateau area and/or rift triggered fissure basalts in the floor of the Afar Depression. At present, volcanic activities are entirely confined along the axial zones of the Afar Depression representing the last phase of the Afar mantle plume (plume tail). All available trace element data and isotopic investigations show that both the high-Ti plateau basalts (HT2) from the plume head and the axial zone basalts from the plume tail have indistinguishable source regions (OIB-type), which are different from the depleted mantle source. However, the concentrations of the highly incompatible elements vary from one basaltic suite to another, showing a variation in degree and depth of melting of the source region.

Structural and geophysical investigations (in the literature), on the other hand, show that the nature of the Afar Depression is purely an oceanic crust-type. Crustal thickness of the

northern Afar Depression does not exceed 15 km and spreading rate along the actively expanding Erta'Ale Depression is ~12 mm/yr/100 km. This, obviously, implies that the floor of the northern Afar Depression is oceanic crust, as its spreading rate being analogous to the rates of the Red Sea and Gulf of Aden rifts; on the other hand, geochemical results confirm that magmatism resulted from the tail of the Afar mantle plume.

ZUSAMMENFASSUNG:

Der äthiopische Afar-Manteldiapir ist einer der jüngsten Diapirstrukturen der Welt. Seit ca. 30 Mio Jahren fördert er große Mengen an Magmen an die Erdoberfläche und trägt damit zur Umgestaltung der sublithosphärischen ostafrikanischen Kruste bei. Aufgrund der komplexen geodynamischen Natur dieser Region existiert eine eindruckvolle petrologische Vielfalt. Die Laven umfassen ein Spektrum von Basaniten zu tholeiitischen Basalten und von Phonoliten zu Trachyten. Diese Arbeit präsentiert geochemische und petrographische Untersuchungen an 93 vulkanischen, hauptsächlich basaltischen, Gesteinen, die aus den nördlichen äthiopischen Flutbasalten und der nördlichen Afar-Störung, der Erta`Ale Vulkankette, stammen. Sie beinhaltet ebenso eine kinematische Analyse der nördlichen und zentralen Afar-Störung, von deren ursprünglichen Beginn bis zur heutigen Ozeanbodenspreizung. Das Gesteinsmaterial stammt aus zwei Feldkampagnen: die erste fand 2007 in Vulkaniten des äthiopischen Hochlands statt, die zweite, 2008/09, hatte die axialen Basalte der nördlichen Afar-Senke zum Ziel. Es konnten viele petrologisch unterscheidbare vulkanischen Sequenzen im nördlichen äthiopischen Plateau und in der Afar-Senke identifiziert werden. Die ältesten vulkanischen Gesteine des Afar-Manteldiapirs werden durch die titanreichen (HT) und die titanarmen (LT) Gruppen der oligozänen Flutbasalte repräsentiert. Es kam jedoch auf der äthiopischen Hochebene sporadisch zur Eruption von in der Zusammensetzung variierenden Magmaserien. Eine dieser vulkanischen Serien setzt sich aus den, in einer kurzen Zeitspanne ausgetretenen, Axum post-Trappvulkaniten zusammen, eines geochemisch komplexen und lithologisch differierenden Teils der nordwestlichen äthiopischen Flutbasalt-Provinz. Nach dem Höhepunkt der äthiopischen Flutbasalteruption konzentrierte sich die magmatische Aktivität hauptsächlich auf Schildvulkane der Hochebene und auf riftgesteuerte Spaltbasalte am Grund der Afar-Senke. Zur Zeit beschränken sich die vulkanischen Aktivitäten komplett auf die axialen Bereiche der Afar-Senke, welche die letzte Phase des Afar-Manteldiapirs darstellen. Alle vorhandenen Spurenelementdaten und Isotopenuntersuchungen zeigen, dass sowohl die Plateaubasalte (Ti-reich) des Diapirkopfes, wie auch die axialen Basalte des Diapirendes eine nicht unterscheidbare Quellregion (OIB-Typ) besitzen, welche von der abgereicherten Mantelquelle abweicht. Die Konzentration der sehr inkompatiblen Elemente kann jedoch zwischen den einzelnen basaltischen Abfolgen variieren, was auf einen Wechsel im Aufschmelzungsgrad und -tiefe der Quellregion hinweist. Andererseits zeigen tektonische und

geophysikalische Untersuchungen, dass die Afar-Senke zu den reinen Ozeankrusten-Typen gehört. Die Krustendicke der nördlichen Afar-Senke geht nicht über 15 km hinaus, die Spreizungs-Geschwindigkeit entlang der aktiven Erta´Ale Senke beträgt ca. 12 mm/Jahr/100 km. Es liegt auf der Hand, daß der Boden der nördlichen Afar-Senke ein ozeanischer ist, da seine Ausdehnungsraten denen des Roten Meeres und des Golfs von Aden enstpricht. Allerdings bestätigen die geochemischen Ergebnisse, dass der Magmatismus immer noch aus dem Rest des Afar-Manteldiapirs resultiert.

CONTENTS:

CHAPTER 1

CHAPTER 1: INTRODUCTION TO CONTINENTAL RIFTING

1.1 General Introduction

The East African Rift System (EARS) is one of the largest sub-aerial tectonic wonders of the globe, a place where the earth's internal (active and passive) forces are currently trying to create new plates (e.g., the Somalian and Danakil Microplates) by splitting apart the old African plate. It is about 6000-km-long rift system that extends from Syria in the north and passes through eastern Sinai, Red Sea, Afar Depression, and Kenyan Rift and terminates in central Mozambique (Fig.1.1; Beyene and Abdelsalam, 2005, and references therein). However, Hayward and Ebinger (1996) argued that the EARS starts at the southern end of the Red Sea (Afar Depression) and terminates in southern Africa (Mozambique). According to these authors, the ~2000-km-long EARS includes a wide range of rift evolution from partly magmatic rift segments in Tanzania (less evolved rift segment) to highly magmatic rift segments in Afar Depression (incipient seafloor spreading).

The EARS is composed of topographically contradicting landmasses, uplifted plateaus surrounding the nearly N– to NNE–trending axial rift zones, extending from the southern Red Sea in the north to Lake Malawi in the south (Pik et al., 2008). Along this rift system, two major long-wavelength plateaus have been identified in Ethiopia and Kenya (Fig. 1.1), which are related to the upwelling of one or two hotspots, active since Eocene–Oligocene times (Pik et al., 2008, and references therein). The EARS, therefore, provides opportunities to examine plume-driven continental flood volcanism (Furman et al., 2004) and the birth and growth of the Afar triple junction as continental rifting advances to incipient seafloor spreading (Hayward and Ebinger, 1996).

The EARS crosses the Ethiopian and Kenyan topographic uplifts, both considered as the surface manifestations of the Ethio-Afar and Kenyan hotspots/ mantle plumes (Thiessen et al., 1979). The highly extended Turkana Depression and the older Anza graben lie between the Ethiopian and Kenyan domes, a wide zone of NW-SE extension that developed in the early Cretaceous (Furman et al., 2004). The absence of old, cold and strong lithosphere underlying the Ethiopian dome allows extension to spread in a narrow zone and more uniform manner across the plateau (Rogers, 2006). It is, therefore, only in Ethiopia that the EARS shows a well-defined NE-SW–trending narrow zone of extension and axially oriented volcanic edifices. This single and narrow zone of crustal extension is termed as the Main Ethiopian Rift (MER). South of Turkana (southern end of the Ethiopian rift), the rift system splits in two branches that enclose the old and mechanically strong Tanzania carton, referred

to as the Eastern (the Kenya or Gregory) rift and Western (Lake Albert) rift (Furman, 2007). The eastern branch of the EARS is directly linked with the Ethiopian rift and extends further south for over 1000 km to Tanzania (Fig. 1.1). The western branch, which contains the East African Great Lakes and bordered by some of the highest mountains in Africa (e.g., Ruwenzori Range, Mitumba Mountains, and Virunga Mountains; Furman et al., 2004), is an arcuate-shaped rift valley extending for more than 2000 km from west Uganda in the north and terminating in north Mozambique in the south.
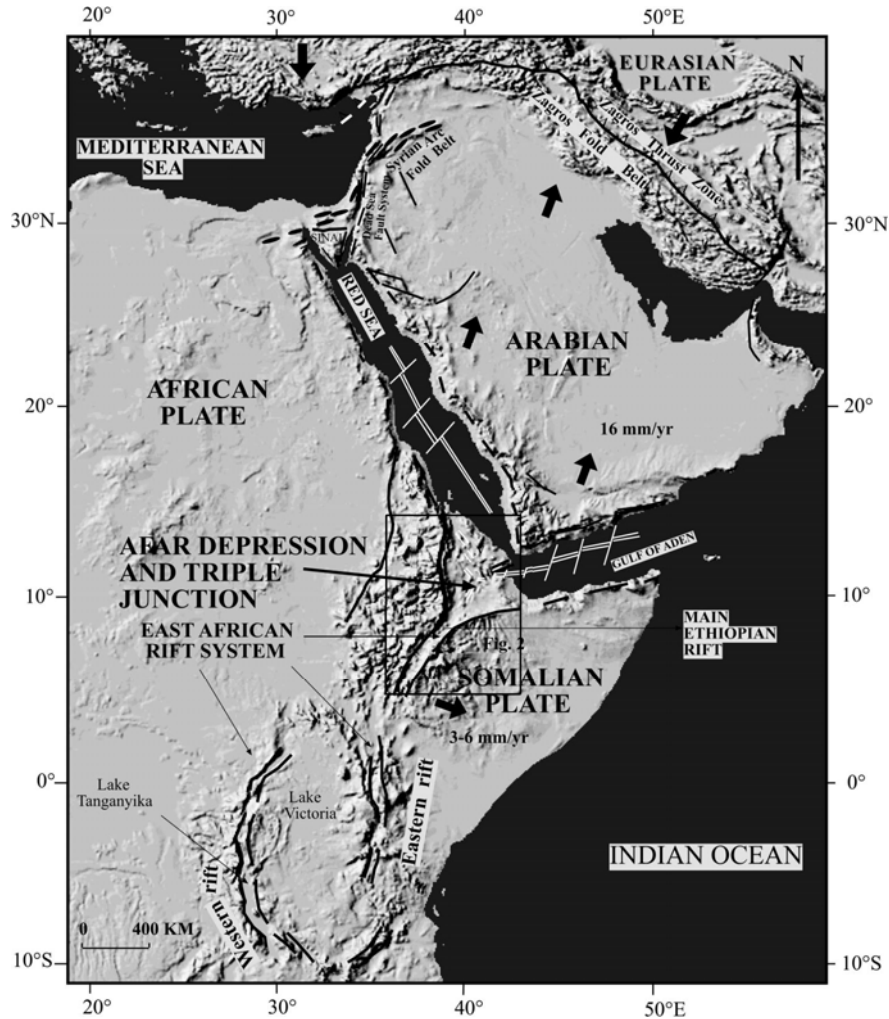
Figure 1.1   Digital elevation model (DEM) of northeastern Africa and Arabian plates showing the location of the East African Rift System, Afar Depression, Red Sea Rift, Gulf of Aden Rift, and the Zagros Orogenic Belt (after Tesfaye et al., 2003).

The magmatic characteristics of the Eastern and Western rifts are distinct. The Eastern rift accommodates large volumes ($>10^5$ km^3) of mafic lava and evolved felsic products that have erupted throughout the Neogene (e.g., Williams, 1982; Baker, 1987; Rogers, 2006). By contrast, magmatism along the entire Western rift, prominent for its carbonatite lavas and abundance of potassic alkaline rocks, is limited in volume and extent,

and appears to be erupted long overlapping zones of contiguous rift basins (Rosendahl, 1987; Rogers, 2006). The Eastern and Western rifts converge to the north at Turkana Depression and merge with the Ethiopian rift to form the EARS (Rogers, 2006).

It is now understood that uprising of the deep-rooted mantle plume under the present Afar Depression lithosphere triggered the eruption of huge volume of continental flood basalts at ~30 Ma (Hofmann et al., 1997), and was associated with the Afro-Arabian continental breakup and domal uplift, Ethiopian dome (Pik et al., 2008). However, magmatic activities in the EARS commenced in southern Ethiopia near 45 Ma (George et al., 1998), and this is most probably linked with the uplift of the Kenyan dome.

1.2 Physiography of the Ethiopian Rift

The Ethiopian Rift, running for about 1000 km in a nearly NE-SW direction, constitutes the northernmost segment of the EARS (Abebe et al., 2007), connecting the rift system with the young ocean basins (i.e., the Red Sea and Gulf of Aden rifts). This volcano-tectonically active rift zone can be divided into two major physiographic segments, namely the Afar Depression and the MER (Fig. 1.1); the rift architecture is classically developed in the MER, where a N-S– to NE-SW–trending narrow zone (~80 km-wide rift valley) separates the uplifted Nubian and Somalian plates (Corti, 2009). The transition zone between the Afar Depression and MER does not correspond to any structural and physiographic characteristics. As the rift valley steadily funnels out into the Afar Depression, the MER broadens from a width of ~100 km to ~200 km north of the Dofan magmatic segment at ~9°30' (Corti, 2009; Tesfaye et al., 2003). Tesfaye et al. (2003) considered this region as an arcuate accommodation zone, which Wolfenden et al. (2004) also inferred as the southern limit of the NNE-SSW–running Red Sea propagator.

1.2.1 Afar Depression

The Afar Depression, a diffuse triple junction where the Gulf of Aden, the Red Sea and the MER radiate, covers an area of ~250,000 km^2 and is encircled by steeply inclined fault escarps, which close at the Alid graben north of Dallol Depression (Abbate et al., 1995; Beyene and Abdelsalam, 2005) (Fig. 1.2). The depression is bordered on the west by the Ethiopian escarpment, on the east and northeast by the Danakil Microplate, and on the south by the Somalian Plateau (Figs. 1.2 and 1.3). The elevation drops radically from the rift bounding Ethiopian plateau that stands well above 3500 meters above sea level to the lowest point in northern Afar Depression (Dallol Depression) at ~146 meters below sea level

(Tesfaye et al., 2003). On the basis of its physiography and tectonic domains, the Afar Depression is divided into northern, central, and southern sectors (Fig. 1.2).

The northern Afar Depression, alternatively known as the 'Danakil Depression', is a low-lying region bounded by the Ethiopian escarpment on the west and the Danakil Microplate on the east (Beyene and Abdelsalam, 2005). The depression, with a mean elevation of ~200 m, is characterized by NNW-SSE–trending elevated axial volcanic range (Erta'Ale Range). Elevation at the peak of the range rises to ~1150 meters above sea level making a remarkable topographic contrast with the nearby deepest sub-aerial depression on earth (i.e., the Dallol Depression). The northern Afar Depression gets progressively deeper and narrower towards a northern zone within the depression known as Dallol (Fig. 1.3; Beyene and Abdelsalam, 2005). At Dallol the elevation drops to ~146 meters below sea level (CNR-CNRS, Afar Team, 1973). The Quaternary volcanic edifices of the depression are usually produced by basaltic fissure lavas and some felsic derivatives aligned in a NNW-SSE–trending axial zone, which is parallel to the regional tectonic trend of the Red Sea rift (Tesfaye et al., 2003). The deepest parts of the depression are commonly filled with recent lacustrine sediments, evaporite beds and floored by fissure-fed basaltic lava flows. The earliest sedimentation started in the Oligocene–Miocene along the newly developed marginal grabens with the clastic 'Red Series', and continued in the Pliocene–Recent by Piedmont sediments and shallow water carbonates (Barrat et al., 1998). According to these authors, the northern Afar Depression became arid after its isolation from the Red Sea by the Alid volcanic center at lat 15°N.

The central Afar Depression, corrugated by grabens and horsts and few local high relief peaks representing volcanic shields, is a typical physiographic feature in the region hosting the only active sub-aerial triple junction in the globe. The Tendaho rift is one of the largest axial structures in the central sector of the Afar Depression marking the southwestern limit of the region. The NE and SW graben margins of the Tendaho rift, marked by prominent fault scarps with a maximum throw of ~100 m, show the highest topographic gradients (Acocella, 2010). Northwest–striking parallel sets of grabens and horst are characteristic features of the region accumulating a mean elevation of ~450 m (Tesfaye et al., 2003).

The southern Afar Depression (northern extension of the MER), like central Afar, is characterized by horst and graben morphologic features (Tesfaye et al., 2003). Unlike central Afar, however, it is dominated by a series of NNE–trending right-stepping horsts and grabens (Beyene and Abdelsalam, 2005). The ~700 m mean elevation of the southern Afar

Depression gets progressively lower towards the Tendaho graben. The well-known NNE–trending discontinuous but en-echelon arranged grabens at the center of southern Afar are the northward propagation of the Wonji Fault Belt (WFB), active extensional rift zone of the MER (Tesfaye et al., 2003)
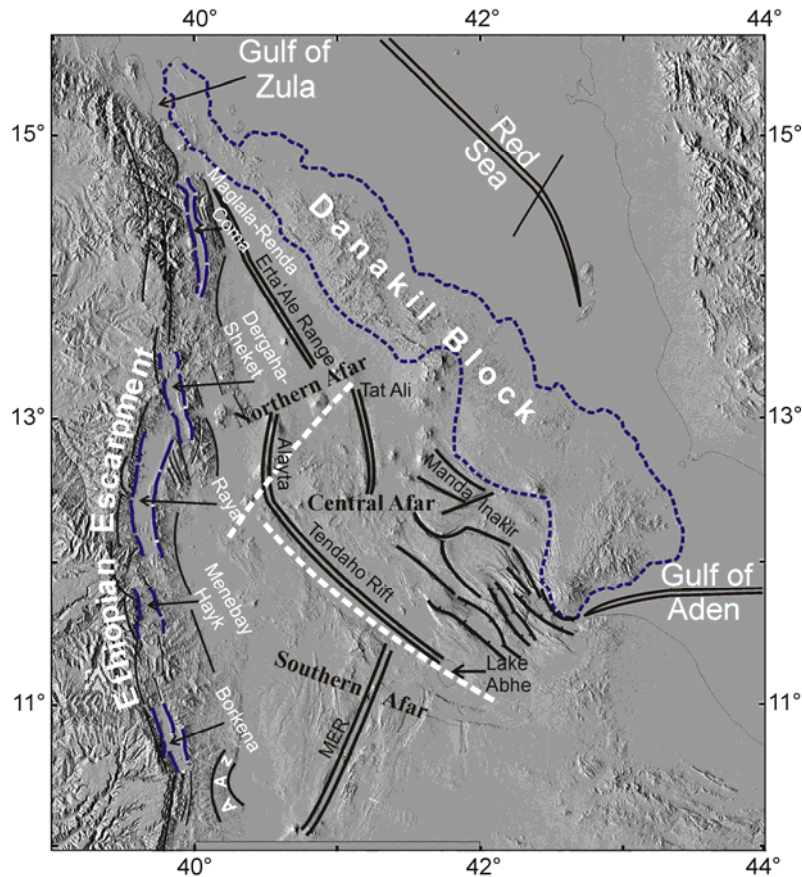
Figure 1.2 Shaded relief image of Afar Depression and the surrounding marginal area and plateaus produced from Digital Terrain Elevation Data (DTED; modified after Tesfaye et al., 2003). Tectonic zones and marginal basins of the depression are separated by white and blue dashed lines, respectively. The white dashed lines separate the northern, central and southern Afar Depression. Double black lines represent the active spreading ridge segments of Afar Depression, the Red Sea, and Gulf of Aden. AAZ-arcuate accommodation zone.

Figure 1.3 3D view of the Afar Depression and the west and east flanking plateaus (source: http://en.wikipedia.org/wiki/Image:AfarDrape.jpg).

1.2.2 Marginal areas of the Afar Depression

The low-lying Afar Depression is separated from the Ethiopian highland by the N-S–running Ethiopian escarpment, N-S trending marginal grabens and half-grabens of tilted fault blocks constituting the western margin of the Afar Depression (Beyene and Abdelsalam, 2005) (Figs. 1.2, 1.3). This margin is bordered by a seismically active, right-laterally offset, en-echelon arrangement of grabens that extend from 14°30'N to 10°30'N (Tesfaye et al., 2003). These grabens, typical physiographic features of the western margin, are Maglala–Renda Coma, Dergaha–Sheket, Guf–Guf, Menebay–Hayk, and Borkena (Fig. 1.2; Mohr, 1967, 1974; Tesfaye et al., 2003; Beyene and Abdelsalam, 2005).

The marginal grabens, developed at the foot of the Ethiopian escarpment, average 30-km-long and 5-km-wide and are associated with transtensional faulting initiated during the middle Oligo–Miocene (Chorowicz et al., 1999; Beyene and Abdelsalam, 2005). Systems of en-echelon strike-slip faults are also aligned parallel to the marginal grabens (Chorowicz et al., 1999). Reactivated deformational features associated with magma injection constitute the western Afar margin (Collet et al., 2000; Beyene and Abdelsalam, 2005, and references therein). The western Afar margin was formed by down-warping of the Afar Depression and consequent antithetic and synthetic faulting and eastward tilting of faulted blocks (Fig. 1.4a; Zanettin and Justin-Visentin, 1975).

The Afar Depression is separated from the eastern plateau by the E-W–trending Somalian escarpment. It is characterized by a mosaic of closely spaced synthetic and

antithetic normal faults. Unlike the Ethiopian escarpment, the southern Afar margin has no dilatational grabens developed adjacent to the Somalian highland (Fig. 1.4b). Instead series of half-grabens and some felsic volcanic centers are aligned along the lower and upper parts of the southern margin, respectively, where they are more concentrated towards the eastern accommodation zone (Tesfaye et al., 2003) of southwestern Afar Depression (Beyene and Abdelsalam, 2005).
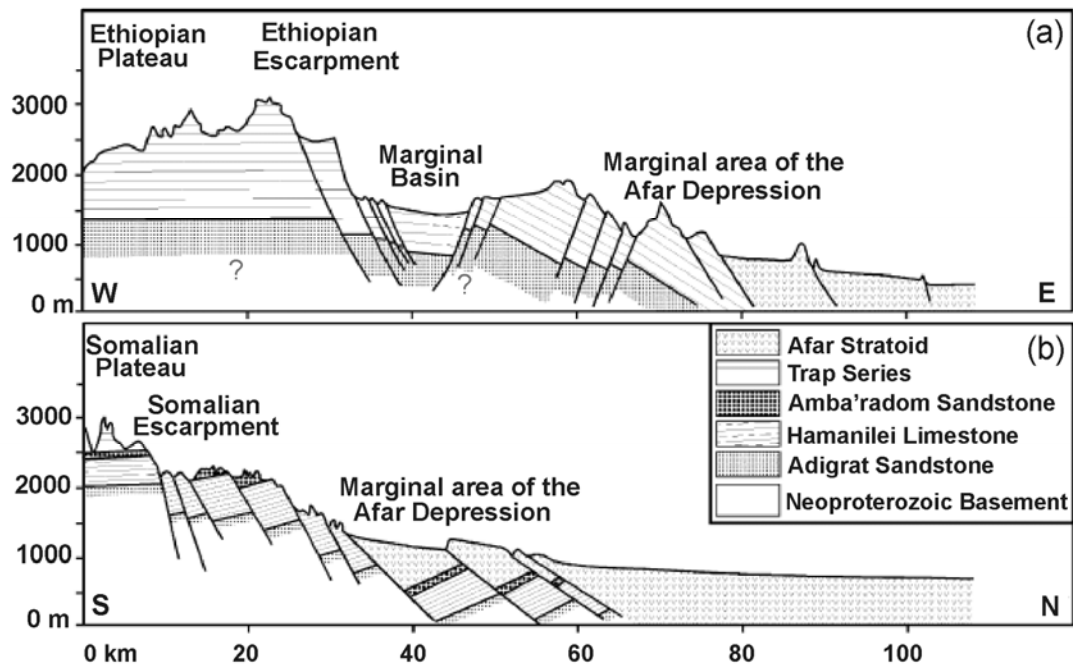
Figure 1.4 Schematic geological cross-sections showing the nature of crustal deformation across the Ethiopian and Somalian margins of Afar. (a) Antithetic and synthetic faults bounding the marginal basins of the western margin. (b) book-shelf type faulting and associated half-grabens dominate the southern/Somalian margin (after Beyene and Abdelsalam, 2005).

1.2.3 The Main Ethiopian Rift

The MER represents the northernmost active segment of the EARS, connecting the rift system with the Afar Depression (Abebe et al., 2007). The MER, a narrow and well-defined N-S− to NE-SW−trending rift segment, extends from the southern Afar Depression (arcuate accommodation zone; Tesfaye et al., 2003) at ~10° N to the northern end of the Turkana Depression at ~5° N, (Fig. 1.5), and was formed through the southward propagation of the SSW−trending Red Sea rift since the late Miocene and the northward migration of the EARS starting at ~20 Ma (Tommasini et al., 2005). The initial phase of the MER extension started to develop during the middle Miocene time (WoldeGabriel et al., 1990; Chernet et al., 1998), following a broad doming and widespread flood basalt volcanism centered on the present Afar Depression (Ebinger et al., 1989). During the late Miocene–Quaternary, the MER gradually deepened and widened, developing through a series of overlapping half-graben

segments tracing the incipient boundary between the Nubian and Somalian plates (Acocella and Korme, 2002). The MER is divided into three sectors/segments based on surface geology and geomorphology: the northern (NMER), central (CMER), and southern (SMER) sectors (Fig. 1.5; Keranen and Klemper, 2008).
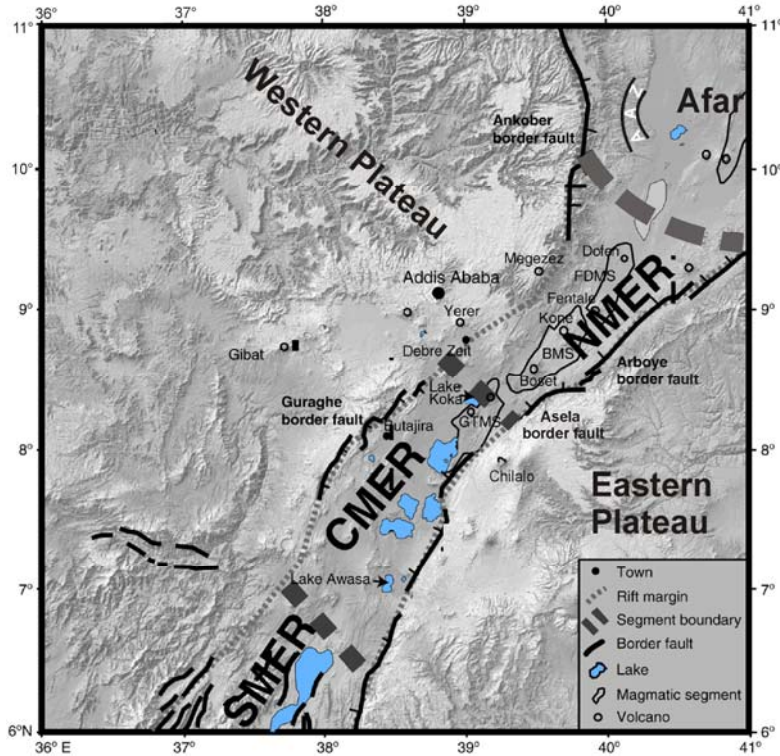
Figure 1.5 General outline of the Main Ethiopian Rift. NMER : northern MER, CMER : central MER, SMER : southern MER. Segments are separated by thick dashed gray lines. Approximate rift boundaries are traced by thin dashed gray lines. FDMS: Fentale–Dofen Magmatic Segment, BMS: Boset Magmatic Segment, GTMS: Gademsa–Tullu Moye Magmatic Segment, AAZ: arcuate accommodation zone (modified after Keranen and Klemper, 2008).

The NMER extends for ~200 km from the AAZ, southern terminus of the Red Sea Rift, to near Lake Koka with steep boundary faults that trend on average at N50°E (Keranen and Klemper, 2008). This sector is the merger of the southern Afar marginal faults and the MER border faults, which have formed since 10–11 Ma (Wolfenden et al., 2004). The NMER has the lowest elevation and consequently thin crust compared to the CMER. The crust progressively thins towards the southern Afar from 33–35 km adjacent to the CMER to ~26 km near the AAZ (Fig. 1.6; Keranen and Klemper, 2008). Apparent and abrupt change in physiography and crustal properties is observed at the junction between the NMER and CMER. The CMER is bounded by the Lake Koka to the north and Lake Awasa to the south with boundary faults trending on average N30°E–N35°E. Major crustal extension accompanied by rift deepening and widening are apparent for the CMER during the late

Miocene–early Pliocene, with intensive volcano-tectonic activity after 5 Ma (Abebe et al., 2010). Elevation rises by several hundreds of meters as it inters to the CMER. Based on gravity and seismic data, crustal thickness of the CMER increases rapidly from the boundary with the NMER (33–35 km) to the middle of the CMER (38–40 km) (Fig. 1.6; Keranen and Klemper, 2008, and references therein). The SMER extends south from Lake Awasa into the broadly rifted zone of southern Ethiopia (Ebinger et al., 2000) with faults trending N-S to N20°E. Faulting in the SMER was well-established by ~18 Ma (Ebinger et al., 1993; WoldeGabriel et al., 1991).
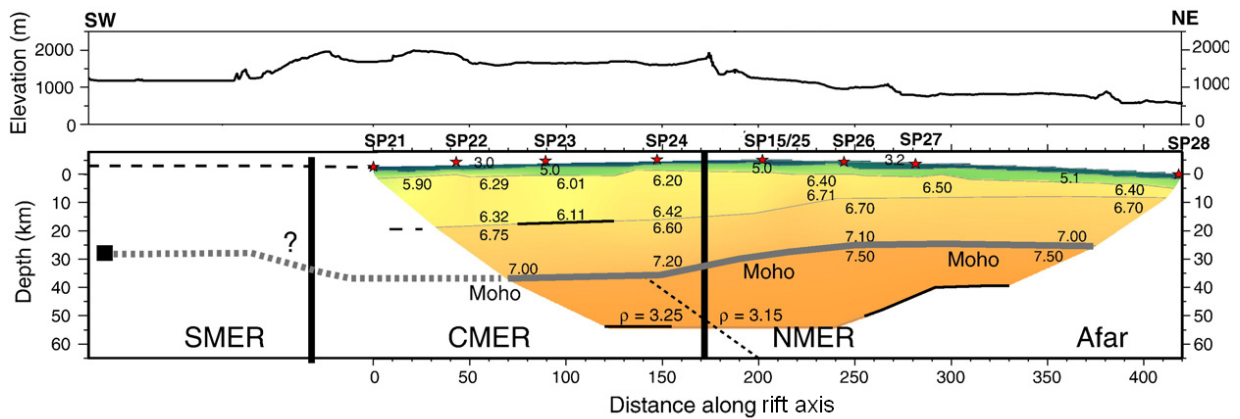
Figure 1.6 Simplified **c**ross-section along the rift axis of MER from the Ethiopia-Afar Geoscientific Lithospheric Experiment (EAGLE) controlled-source experiment. The crust–mantle boundary (Moho) is traced by solid gray line (actual boundary) and dashed gray line (approximate boundary) (after Keranen and Klemper, 2008).

1.3 Geology of the Afar Depression

The geology of the Afar Depression and its margins is of great interest because it may represent the complete sequence of rocks spanning from the Late Proterozoic to the present. The Afar Depression is not only a site of volcanism; it is also an excellent site of depositional environment. In addition to the Miocene to Holocene basalts and their felsic derivatives, late Miocene– to late Pliocene syn-rift Red Series sandstones, evaporites, and shales were deposited in newly developed basins in the northern Afar Depression (Redfield et al., 2003). However, these formations are not precisely mapped, because they are completely covered by the vast exposure of Pliocene–Pleistocene Afar Stratoid series and Quaternary sediments of the region. The geological formations of the Afar Depression and its marginal areas and surrounding plateaus can be divided into four broad divisions (Fig. 1.7): (1) Pre-rift complexes; (2) Syn-rift igneous rocks; (3) Pliocene–Pleistocene volcanic rocks; and (4) Quaternary volcanic and sedimentary rocks (Beyene and Abdelsalam, 2005; Bosworth et al., 2005).

Pre-rift complexes: These complexes consist of the Neoproterozoic crystalline basement rocks (Arabian-Nubian Shield), the Paleozoic–Mesozoic sedimentary sequences, and the Eocene–Oligocene volcanic rocks, which are exposed along the peripheries and plateaus surrounding the Afar Depression and within the Danakil and Ali-Sabieh micro-blocks (Kazmin et al., 1978; Vail, 1985) (Fig. 1.7). The Arabian–Nubian Shield (ANS) also called the 'low-grade basement complex' covers a wide region to the west and northwest of the Afar Depression (Vail, 1985; Berhe, 1990). These weakly metamorphosed crystalline rocks of the shield also constitute lower parts of the Ali-Sabieh and Danakil Microplates (Beyene and Abdelsalam, 2005). The ANS are overlain by thick successions of Mesozoic and in some places by Paleozoic sedimentary rocks and Tertiary volcanic rocks.

The oldest clastic sediments (Lower Sandstone) are generally early Triassic or possibly Permian overlying the basement complexes, with younger formations (Upper Sandstone) extending into the early Cretaceous (Bosworth et al., 2005). These Paleozoic–Mesozoic sedimentary successions correspond to a major transgressive–regressive cycle, which has been assigned to the Adigrat–Amba-Aradom formations. The Mesozoic sedimentary rocks of the western (Ethiopian) Plateau comprise early Jurassic Adigrat Sandstone, middle–late Jurassic Antalo Supersequence and Agulae shale, and early–middle Cretaceous Amba-Aradom Formation (Fig. 1.4a; Varet and Gasse, 1978; Tefera et al., 1996; Bosellini et al., 1997). The Mesozoic sedimentary successions of the eastern (Somalian) Plateau comprise early Jurassic Adigrat Sandstone, early–middle Jurassic Hamanilei fossiliferous Limestone, late Jurassic Urandab gypsiferous Limestone, and early Cretaceous Amba-Aradom formation (Fig. 1.4b; Beyene and Abdelsalam, 2005, and references therein).

On the Ethiopian Plateau, the upper surface of the Mesozoic successions is marked by a great unconformity, over which the Oligocene Ethiopian volcanic rocks or 'trap series' were extruded (Bosworth et al., 2005). The Ethiopian volcanic rocks cover an area of ~600,000 km^2, with a layer of basaltic lavas and interbedded felsic and pyroclastic products constituting ~2000 m thick (Kieffer et al., 2004). The flood basalt was commonly extruded onto the lateritized sandstone surface and sometimes found inter-fingered with the Oligocene lacustrine, fluviatile origin sedimentary rocks near or above sea level (Beyene and Abdelsalam, 2005, and references therein).

Syn-rift igneous rocks: Flood and shield basalts of ~25–15 Ma are found both on the Ethiopian plateau and within the Afar Depression. In the Afar Depression, the oldest volcanic rocks are assigned to the Adolei, Mabla, and Dahla series (Fig. 1.7; Varet and Gasse, 1978; Vellutini, 1990; Bosworth et al., 2005). However, these intensely faulted and deeply

weathered Miocene basalts occur in limited areas around the eastern peripheries of the Afar Depression (Gulf of Tadjoura and Ali-Sabieh Microplate). Alkaline to peralkaline granites were also intruded into the Neoproterozoic basement, Jurassic limestone and the pre-rift flood basalts along the western and eastern margins of Afar Depression (Varet and Gasse, 1978; Beyene and Abdelsalam, 2005).

Pliocene–Pleistocene volcanic rocks: More than two-thirds of the Afar Depression are covered by Pliocene–Pleistocene volcanic rocks. These widely distributed fissure-fed units are commonly assigned to the Afar Stratoid series (Fig. 1.7; Barberi et al., 1975; Varet and Gasse, 1978). They are the most important volcanic formation in the depression in terms of aerial coverage, volume, and preservation of volcanic structures and tectonic features (Beyene and Abdelsalam, 2005). The Stratoid lavas may be a manifestation of the commencement of ridge spreading in central Afar Depression at 4 Ma (Wolde, 1996), also roughly contemporaneous with the initiation of oceanic spreading in the southcentral Red Sea (Eagles et al., 2002). The massive outpouring of lava, mode of eruption and structuring of the Afar Stratoid series represent the transition of the central Afar Depression from continental rifting to incipient seafloor spreading (Barberi et al., 1975). Pliocene–Present fluviatile and lacustrine sedimentary rocks interbedded with basaltic lava flows and felsic–pyroclastic products fill extensional grabens in central and southern Afar Depression (Tesfaye et al., 2003).

Quaternary volcanic and sedimentary rocks: Wide-spread fissure-fed basaltic flows and basaltic shields, scoria cones, and alkaline to peralkaline silicic rocks were erupted along the actively expanding axial ranges in the Afar Depression over the past 1 Ma (Varet and Gasse, 1978; Tefera et al., 1996). The transitional–tholeiitic axial range basalts are injected along the NNW–trending fissures displaying symmetric magnetic character that are underlain by very young and thin oceanic-type lithosphere, and get increasingly older and colder towards the marginal areas (Barberi and Varet, 1977; Beyene and Abdelsalam, 2005). Because of these unique characteristics, Barberi and Varet (1977) considered the axial basaltic ranges to be sub-aerial equivalents of mid-oceanic spreading ridges, linked by transform faults. South of the Tat'Ali and Alyata, NE aligned volcanic centers, which are thought to be similar with the transform faults, transverse the NNW-SSE–trending basins found along the eastern and western Afar margins (Fig. 1.2; Beyene and Abdelsalam, 2005).

Because of the unique physiographic feature, the Afar Depression also hosts lacustrine deposit dominated Quaternary sedimentary rocks. Significant shallow water sedimentary rocks were deposited along the newly developed grabens (i.e., Manda Hararo–

Goba'ad, Manda Inakir and Dobe rift basins) in the central Afar between ~12 and 1 ka (Beyene and Abdelsalam, 2005, and references therein). Evaporites and lacustrine sedimentary rocks of several hundred m thick cover the Dallol Depression in the north and Awsa plain in the eastcentral Afar, respectively (Varet and Gasse, 1978).
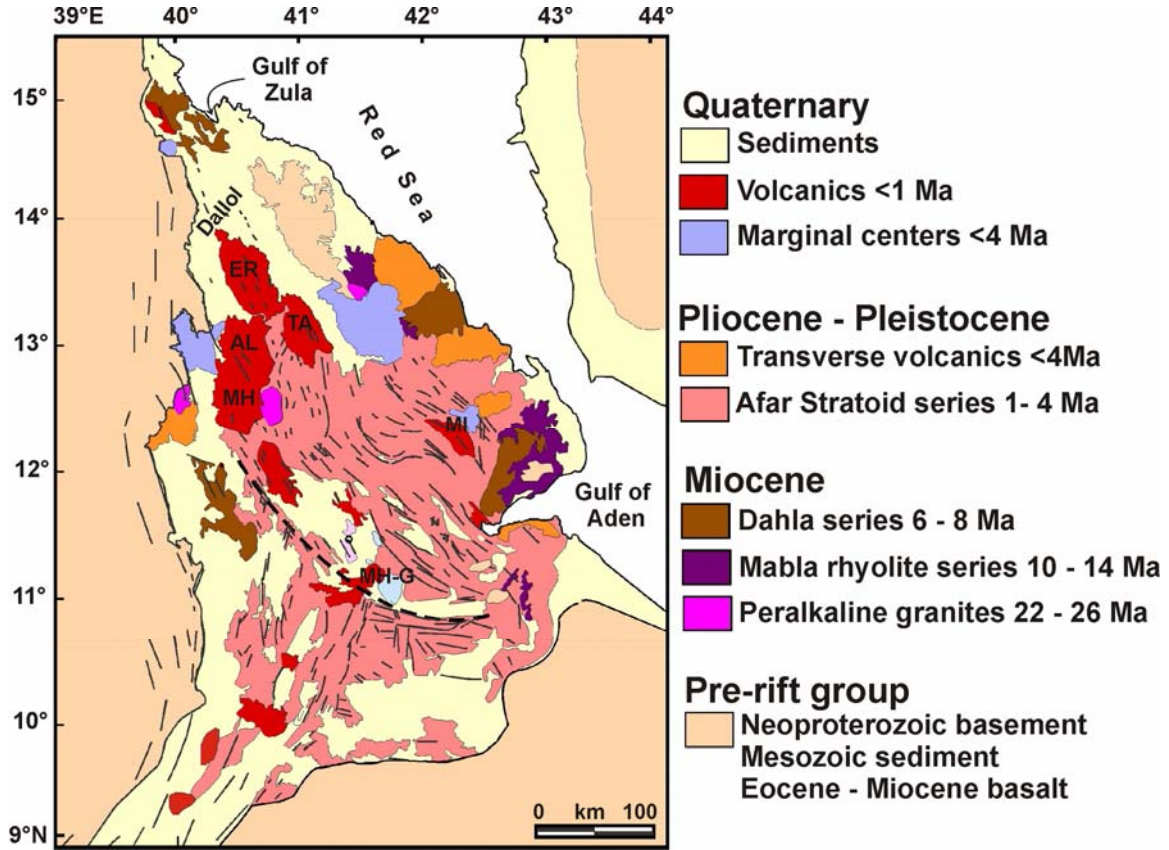
Figure 1.7 Geological map of the Afar Depression and the surrounding plateaus. Active axial ranges are represented by: ER – Erta'Ale Range; TA – Tat'Ale; AL – Alyata; MH – Manda Hararo; MI – Manda Inakir; MH-G – Manda Hararo-Goba'ad (after Beyene and Abdelsalam, 2005, and references therein).

References:

Abbate E., Passerini P., and Zan L. 1995. Strike-slip faults in a rift area: A transect in the Afar Triangle, east Africa. Tectonophysics 241, 67–97.

Abebe B., Acocella V., Korme T., and Ayalew D. 2007. Quaternary faulting and volcanism in the Main Ethiopian Rift. Journal of African Earth Sciences 48, 115–124.

Abebe T., Balestrieri M. L., and Bigazzi G. 2010. The Central Main Ethiopian Rift is younger than 8 Ma: confirmation through apatite fission-track thermochronology. Terra Nova 6, 470–476.

Acocella V. 2010. Coupling volcanism and tectonics along divergent plate boundaries: Collapsed rifts from Central Afar, Ethiopia. Geological Society of America Bulletin 122, 1717–1728.

Acocella V. and Korme T. 2002. Holocene extension direction along the Main Ethiopian Rift, East Africa. Terra Nova 14, 191–197.

Baker B.H. 1987. Outline of the petrology of the Kenya rift alkaline province. In: Fitton J.G. and Upton B.G.J. (Eds), Alkaline Igneous Rocks. Geological Society, London, Special Publication 30, 293–311.

Barberi F. and Varet J. 1977. Volcanism of Afar: Small-scale plate tectonics implications. Geological Society of America Bulletin 88, 1251–1266.

Barberi F., Ferrara G., Santacroce R., and Varet J. 1975. Structural evolution of the Afar triple junction. In: Pilger A. and Rösler A. (Eds.), Afar Depression of Ethiopia. Schweizerbart, (Inter-Union Commission on Geodynamics Scientific Report 14), Stuttgart, Germany, 38–54.

Barrat J.A., Fourcade S., Jahn B.M., Cheminee J.L., and Capdevila R. 1998. Isotope (Sr, Nd, Pb, O) and trace-element geochemistry of volcanics from the Erta'Ale Range (Ethiopia). Journal of Volcanology and Geothermal Research 80, 85–100.

Berhe S.M. 1990. Ophiolites in northeast and east Africa: implication for Proterozoic crustal growth. Journal of Geological Society, London, 147, 41–57.

Beyene A. and Abdelsalam M.G. 2005. Tectonics of the Afar Depression: A review and synthesis. Journal of African Earth Sciences 41, 41–59.

Bosellini A., Russo A., Fantozzi P., Assefa G., and Solomon T. 1997. The Mesozoic succession of the Mekelle outlier, Tigray province, Ethiopia. Memorie Di Scienze Geologiche 49, 95–116.

Bosworth W., Huchon P., and McClay K. 2005. The Red Sea and Gulf of Aden Basins. Journal of African Earth Sciences 43, 334–378.

Chernet T., Hart W.K., Aronson J.L., and Walter R.C. 1998. New age constraints on the timing of volcanism and tectonism in the Northern Main Ethiopian Rift-southern Afar transition zone (Ethiopia). Journal of Volcanology and Geothermal Research 80, 267–280.

Chorowicz J., Collet B., Bonavia F., and Korme T. 1999. Left-lateral strike-slip tectonics and gravity induced individualisation of wide continental blocks in the western Afar margin. Eclogae Geologicae Helvetiae 92, 149–158.

CNR-CNRS (Afar team) 1973. Geology of northern Afar (Ethiopia): Revue de Géographie Physique et de Géologie Dynamique 15, 443–490.

Collet B., Taud H., Parrot J.F., Bonavia F., and Chorowicz J. 2000. A new kinematic approach for the Danakil Block using a digital elevation model representation. Tectonophysics 316, 343–357.

Corti G. 2009. Continental rift evolution: From rift initiation to incipient breakup in the Main Ethiopian Rift, East Africa. Earth Science Review 96, 1–53.

Eagles G., Gloaguen R., and Ebinger C. 2002. Kinematics of the Danakil Microplate. Earth and Planetary Science Letters 203, 607–620.

Ebinger C.J., Bechtel T., Forsyth D., and Bowin C. 1989. Effective elastic plate thickness beneath the East African and Afar plateaus and dynamic compensation of the uplifts. Journal of Geophysical Research 94, 2883–2901.

Ebinger C.J., Yemane T., WoldeGabriel G., Aronson J.L., and Walter R.C. 1993. Late Eocene–Recent volcanism and faulting in the southern main Ethiopian rift. Journal of Geological Socinces, London, 150, 99–108.

Ebinger C., Yemane T., Harding D., Tesfaye S., Rex D., and Kelley S. 2000. Rift deflection, migration, and propagation: linkage of the Ethiopian and Eastern rifts, Africa. Geological Society of America Bulletin 102, 163–176.

Furman T. 2007. Geochemistry of East African Rift basalts: An overview. Journal of African Earth Sciences 48, 147–160.

Furman T., Bryce J.G., Karson J., and Iotti A. 2004. East African Rift System (EARS) Plume Structure: Insights from Quaternary Mafic Lavas of Turkana, Kenya. Journal of Petrology 45, 1069–1088.

George R., Rogers N., and Kelley S. 1998. Earliest magmatism in Ethiopia: evidence for two mantle plumes in one flood basalt province. Geology 26, 923–926.

Hayward N.J. and Ebinger C.J. 1996. Variations in the along-axis segmentation of the Afar rift system. Tectonics 15, 244–257.

Hofmann C., Courtillot V., Féraud G., Rochette P., Yirgu G., Ketefo E., and Pik R. 1997. Timing of the Ethiopian flood basalt event and implications for plume birth and global change. Nature 389, 838–841.

Kazmin V., Alemu S., and Tilahun B. 1978. The Ethiopian basement: stratigraphy and possible manner of evolution. Geologische Rundschau 67, 531–546.

Keranen K. and Klemperer S.L. 2008. Discontinuous and diachronous evolution of the Main Ethiopian Rift: Implications for development of continental rifts. Earth and Planetary Science Letters 265, 96–111.

Kieffer B., Arndt N., Lapierre H., Bastien F., Bosch D., Pecher A., Yirgu G., Ayalew D., Weis D., Jerram A.D., Keller F., and Meugniot C. 2004. Flood and Shield basalts from Ethiopia: magmas from the African superswell. Journal of Petrology 45, 793–834.

Mohr P. 1967. The Ethiopian Rift System: Bulletin of the Geophysical Observatory, Haile Selassie I University 11, 1–65.

Mohr P. 1974. Mapping of the major structures of the African Rift System. Smithsonian Institution Astrophysical Observatory Special Report 361, 70 pp.

Pik R., Marty B., Carignan J., Yirgu G., and Ayalew T. 2008. Timing of East African Rift development in southern Ethiopia: Implication for mantle plume activity and evolution of topography. Geology 36, 167–170.

Redfield T.F., Wheeler W.H., and Often M. 2003. Kinematic model for the development of the Afar Depression and its paleogeographic implications. Earth and Planetary Science Letters 216, 383–398.

Rogers N.W. 2006. Basaltic magmatism and the geodynamics of the East African Rift System. In Yirgu G., Ebinger C.J. and Magure P.K.H. (Eds), The Afar Volcanic Province within the East African Rift System. Geological Society, London, Special Publication 259, 77–93.

Rosendahl B. 1987. Architecture of continental rifts with special reference to east Africa. Annual Reviews, Earth and Planetary Sciences 15, 445–503.

Tefera M., Chernet T., and Haro W. 1996. Explanation of the Geological Map of Ethiopia. Ethiopian Institute of Geological Survey Addis Ababa 3, 79 pp.

Tesfaye S., Harding D.J., and Kusky T. 2003. Early continental breakup boundary and migration of the Afar Triple Junction, Ethiopia. Geological Society of America Bulletin 115, 1053–1067.

Thiessen R., Burke K., and Kidd W. S. F. 1979. African hotspots and their relation to the underlying mantle. Geology 7, 263–266.

Tommasini S., Manetti P., Innocenti F., Abebe T., Sintoni M. F., and Conticelli S. 2005. The Ethiopian subcontinental mantle domains: geochemical evidence from Cenozoic mafic lavas. Mineralogy and Petrology 84, 259–281.

Vail J.R. 1985. Pan-African (late Precambrian) tectonic terranes and reconstruction of the Arabian–Nubian Shield. Geology 13, 839–842.

Varet, J. and Gasse F. 1978. Geology of Central and Southern Afar (Ethiopia and Djibouti Republic). Editions de Centre National de la Recherche Scientifique Report, Paris, 124 pp.

Vellutini P. 1990. The Manda-Inakir Rift, Republic of Djibouti: a comparison with the Asal Rift and its geodynamic interpretation. Tectonophysics 172, 141–153.

Williams L.A.J. 1982. The volcanological development of the Kenya rift. In: Neumann E.R. and Ramberg I.B. (Eds), Petrology and Geochemistry of Continental Rifts. Reidel, Dordrecht, 101–121.

Wolde B. 1996. Spatial and temporal variations in the compositions of late Miocene to Recent basic lavas in the Northern Main Ethiopian Rift: implications for the causes of Cenozoic magmatism in Ethiopia. Geologische Rundschau 85, 380–389.

WoldeGabriel G., Aronson J.L., and Walter R.C. 1990. Geology geochronology and rift basin development in the central sector of the Main Ethiopian Rift. Geological Society of America Bulletin 102, 439–458.

WoldeGabriel G., Yemane T., White T., Asfaw B., and Suwa G. 1991. Age of volcanism and fossils in the Burji–Soyoma area, Amaro Horst, southern Main Ethiopian Rift. Journal of African Earth Sciences 13, 437–447.

Wolfenden E., Ebinger C., Yirgu G., Deino A., and Ayale D. 2004. Evolution of the Northern Main Ethiopian rift: birth of a triple junction. Earth and Planetary Science Letters 224, 213–228.

Zanettin B. and Justin-Visentin E. 1975. Tectonical and volcanological evolution of the Western Afar margin (Ethiopia). In: Pilger A. and Rösler A. (Eds.), Afar Depression of Ethiopia. Schweizerbart, (Inter-Union Commission on Geodynamics Scientific Report 14), Stuttgart, Germany, 300–309.

CHAPTER 2

CHAPTER 2: VOLCANISM AND RIFT EVOLUTION IN THE AFAR DEPRESSION AND MAIN ETHIOPIAN RIFT

2.1 Introduction

The evolution of the East African Rift System (EARS) as a narrow and deep rifts in regions characterized by weak lithosphere (e.g., Main Ethiopian Rift) and as a wide and diffused rifts in areas characterized by cold cratons (e.g., Kenyan Rifts) signifies that inherent pre-rift deformation features, not rheological layering, may be the prime control on the architecture of extension in these continental rifts (Corti, 2009, and references therein) (Fig. 1.1). The occurrence of old, cold and mechanically strong lithosphere underneath the central EARS (i.e., Tanzanian craton) deflects the rift propagators to the surrounding suture zones, 'the middle Proterozoic Kibaran belt to the west' and 'the late Proterozoic Mozambique belt to the east' (Rogers, 2006). By contrast, the absence of cold cratonic lithosphere underlying the Ethiopian dome allows extension to spread in a more uniform manner superimposed on the NE-SW–oriented pre-Tertiary structures of the plateau (Korme et al., 2004; Rogers, 2006).

The extended pre-Tertiary history of crustal deformation across the Ethiopian and Kenyan plateaus created pre-existing weaknesses of different orientation that have represented a mould for the evolution of the continental rift in East Africa (Corti, 2009). Pre-rift NNE-SSW, NE-SW and E-W to NNW-SSE–oriented tectonic lineaments mainly controlled the direction and location of the Tertiary rift-faulting of the EARS (e.g., Mohr, 1962; Black et al., 1974; Kazmin et al., 1980; Corti, 2009). Most of the Tertiary extensional structures in the East African landmass have been interpreted as rejuvenated features of the late Proterozoic Mozambique belt (e.g., Dunbar and Sawyer, 1989; Chorowicz, 1992; Ring, 1994) and the Arabian-Nubian shield (Bosworth, 1992; Kazmin et al., 1979). Recent seismic and gravity studies confirm that the pre-rift mega-scale deformational structures controlled the initial rift evolution of the EARS, with pre-existing weaknesses controlling rift architecture and location (Corti, 2009).

At the northern end of the EARS, Afar triple junction, the overall NNE-SSW–trending Ethiopian rift is abruptly shifted to the NNW-SSE and WSW-ENS–trending rift segments. The Eocene–Miocene rifting history of the whole region (EARS, Red Sea, and Gulf of Aden) cannot, therefore, be easily explained by a single rifting model (passive or active rifting models). Hempton (1987) and Bohannon et al. (1989) proposed that forces external to the Afro-Arabian Plates (far-field stresses) generated the incipient Oligocene stretching and rupturing of the Red Sea and the Gulf of Aden rifts. According to Corti (2009),

the extensional deformation of the Afro-Arabian lithosphere is followed by volcanism (and local uplift), since the asthenospheric uplift is a passive response to extensional-related lithospheric stretching. The evolution of the Afar Depression within a broadly elevated region (Ethiopian dome) and its development after massive outpouring of the Ethiopian flood basalts are instead consistent with the dynamic and/or thermal effects of the Afar hotspot operating at the base of the lithosphere (Ebinger et al., 1989; Corti, 2009).

The EARS and the associated embryonic ocean basins of the Gulf of Aden, the Red Sea, and Afar Depression, provide example of the complete evolution of continental rifting from incipient breakup to seafloor spreading that are in close proximity to the underlying asthenospheric material (Rogers, 2006). The northern part of the EARS (i.e., Afar Depression and MER), Red Sea, and Gulf of Aden rifts are the highly evolved rift segments, and rift evolution gradually weakens to the south. Many structural elements are found to suggest the influence of pre-existing lineaments in the evolution of Afar Depression and MER. Black et al. (1974) and Korme et al. (2004) traced a nearly due north–trending ~900 km long Marda Fault Zone, which extends from the Indian Ocean through the Somalian plateau into Afar Depression, to be in perfect arrangement with the Erta'Ale axial zones and/or the western margin of the Red Sea rift (Fig. 2.1). Further analyses from geophysical and imagery data showed that the Marda Fault Zone is a major Mesozoic–Cenozoic volcano-tectonic structure traced along a pre-existing Precambrian lithospheric weakness zone that could be projected along the NNW-SSE–trending Erta'Ale axial Range (Purcell, 1976; Korme et al., 2004; Beyene and Abdelsalam, 2005). Korme et al. (2004) recognized another three more N-S– to NNE-SSW, NE-SW, and E-W–oriented crustal weaknesses that gave birth for the Oligocene–Miocene rifting in the Afar Depression and the MER. According to these authors, the axial part of the MER (Wonji Fault Belt) is inherited from the Pan-African N-S– to NNE-SSW aligned shear and suture zones which were rejuvenated as right-lateral transpressional faults due to the NW-SE Cenozoic extension.

Mega-scale structures like the EARS are well analyzed and interpreted with instruments that have very wide synoptic-view. Analyses of SPOT (Satellite Pour L'Observation De La Terre) images reveal the existence of large inactive NE-SW–trending strike-slip faults cutting through the Danakil and Ali Sabieh Blocks (Audin et al., 2004). This trend overlaps with the Red Sea and Gulf of Aden transform fault trend (Tamsett and Searle, 1990; Audin et al., 2004). These days, it is believed that the EARS, the Gulf of Aden and Red Sea rifts have been rejuvenated from the pre-rift structures existed in the region. But it is still debatable if the reactivation of the rift system is as a result of upwelling mantle plume or far-field stresses.

2.2 Stresses acting on the Afar Depression

The poor understanding of the sequential order of the Afar hotspot, continental flood volcanism, and rifting complicated the evolutionary history of the Afar Depression. The development of the Afar Depression and the surrounding nascent ocean basins has, therefore, been characterized as active and/or passive rifting. The fundamental difference between the active and passive rifting models is whether the upwelling mantle plume forces the lithosphere or whether the asthenosphere (induced by mantle convection) is passively moving upwards as the lithosphere drifts away due to a far-field stress to open along the pre-existing weak zones (Beyene and Abdelsalam, 2005). The order of volcano-tectonic events in active rifting would be uplift–volcanism–rifting. On the other hand, for passive rifting the progression becomes rifting–uplift–volcanism (Bohannon et al., 1989).

Passive rifting (Far-field stress): Bohannon et al. (1989) suggested that the slab pull along the Zagros Orogenic Front triggered the Eocene–Miocene crustal thinning and stretching of the Red Sea and the Gulf of Aden rifts. Courtillot et al. (1987) and Schilling et al. (1992) elucidated that the Arabian Plate has progressively drifted away from the African Plate to the northeast due to passive rifting exerted as a result of the collision of Eurasian and Arabian Plates along the Zagros Orogenic Front (Fig. 2.1). The Arabian and the Eurasian Plates collision is partly concentrated in the central collision zone (shortening of ~8 mm/yr) and the subduction of the Oman oceanic lithosphere beneath the Zogros Orogenic Front further east at rate of ~18 mm/yr (Beyene and Abdelsalam, 2005, and references therein). Initial rupture in the Gulf of Aden commenced before the uprising of the Afar mantle plume; and hence, the slab pull stress might have played a role in splitting the Arabian from the African plate at the early stages of rifting. The impact of the passive rifting might have continued until the middle Miocene (~14 Ma) when terminal convergence along the Orogenic Belt occur (Beyene and Abdelsalam, 2005).

Active rifting (Upwelling mantle plume): Active rifting involves uplifting of the continental lithosphere through an orthogonal stress fields resulting from an upwelling hot, low-density mantle material (Schilling et al., 1992). It would be a working model for the evolution of the Afar Depression, but this model alone is not still adequate enough to fully explain its evolution. The two active arm of the depression (the Red Sea and Gulf of Aden rifts) have not much connection with the upwelling Afar mantle plume; it is only the third arm (the Main Ethiopian rift) that entirely related with it. Until the Oligocene time, the African Plate (Nubia and Somalia) was under the influence of the ridge push generated at the

divergent plate margins except in the north where slab pull might have been exerted up to 14 Ma (Beyene and Abdelsalam, 2005). Gass (1975) proposed that the African Plate was motionless for long period in the Eocene–Miocene and high heat flux released from the mantle plume focused on the same lithospheric target that raised its base (incipient of the Ethio-Afar dome). This implies that the NE-SW–oriented far-field stress exerted on the African Plate due to slab pull along the Zagros Orogenic Front is not dynamically feasible to disintegrate the African lithosphere and derive the Somalian Plate away from the Nubian Plate (Beyene and Abdelsalam, 2005). Instead, it is the upwelling mantle plume that derived the Somalian Plate to move away from the Nubian Plate in a direction nearly orthogonal to the far-field stress. The spreading rate along the Nubian–Somalian plates is minimal. This is mainly because; the southeast motion of Somalian Plate is counterbalanced by the ridge push across the East Sheba ridge, the Gulf of Aden ridge and the central Indian ridge (Bilham et al., 1999). The slow rate of evolution of the MER or East African rift in general (~4 mm/yr; Bilham et al., 1999) as compared with the Red Sea and Gulf of Aden rifts (~16–20 mm/yr; Chu and Gordon, 1998), is most probably because of the result of ridge push encompassing the Somalian Plate resulting in a counterbalance of the extensional force exerted by the outpouring hot low-density mantle material (Beyene and Abdelsalam, 2005).

2.3   Tectonic evolution of the Gulf of Aden and Red Sea Rifts

The incipient lithospheric stretching and the emergence of embryonic oceanic crust in the Red Sea and Gulf of Aden tectonic domains is still a debatable event. Recent works by different authors (e.g., Hofmann et al., 1997; Watchorn et al.,1998; D'Acremont et al., 2005) estimated that continental breakup in the Gulf of Aden commenced at ~35 Ma, just prior to the massive outpouring of the Ethiopian flood basalts and associated felsic pyroclastics at ~30 Ma. In the southern Gulf of Aden coast, syn-rift sedimentary facies indicate that initial crustal extension was occurring during Oligo–Miocene time (Fantozzi, 1996; Redfield et al., 2003).

On the other hand, continental rifting in the Red Sea region commenced at ~28 Ma, shortly after the peak trap volcanism (Wolfenden et al., 2005). It is generally accepted that the main extensional deformation events in the Red Sea region began about 7 My after the onset of Aden Gulf extension during the late Oligocene–early Miocene (Redfield et al., 2003). Other workers have assigned somewhat different ages for the initiation of Red Sea rifting. Dixon et al. (1989) estimated an age of 29–23 Ma for the incipient breakup of the Afro-Arabian plate, whereas Menzies et al. (1992) proposed a slightly younger age, 25–22 Ma, for

the initial phase of crustal extension. From the study of conjugate rifted volcanic margins of Ethiopia and Yemen, Ukstins et al. (2002) computed the initiation of crustal extension at ~26–25 Ma.

Oceanic spreading in the Gulf of Aden commenced at ~16.5 Ma (D'Acremont et al., 2005) with westward propagation through the Tadjoura Gulf into the central Afar Depression at ~0.7 Ma (Wolfenden et al., 2005). Northeast oriented oceanic spreading in the southcentral Red Sea rift initiated at ~4 Ma (Wolfenden et al., 2005). Crustal stretching and oceanic spreading in the Gulf of Aden is, therefore, more advanced than in the Red Sea, and directly connects to the matured mid oceanic plate boundaries through the Sheba Ridge in the east to the Indian ocean (Fig. 2.1; Bosworth et al., 2005). The Gulf of Aden spreading center is highly dissected by NE-SW–trending transform faults.

The lithosphere underneath the southern Red Sea and the Gulf of Aden regions might have undergone momentous stretching under normal asthenospheric temperature mainly due to the passive rifting associated with the convergence of the Eurasian and Arabian Plates along the Zagros Orogenic Belt (Fig. 2.1; Beyene and Abdelsalam, 2005). Thus, the upwelling hot Afar plume has, therefore, minor contribution to the evolution of both the Red Sea and Gulf of Aden rifts. The extension direction of the Gulf of Aden rift and Red Sea rift is orthogonal to the Zagros Orogenic Front; and the slab-pull generated at this Front is supposed to be the initial cause for the separation of the Arabian from the African plate. Later, the rising mantle plume beneath the current Afar Depression may enhance the development of both rift segments.

The Gulf of Aden Rift and southern Red Sea Rift are spreading towards the Afar Depression but have not yet met; leaving a zone of highly attenuated continental crust in the Bab El Mendab Strait (Manighetti et al., 1997; Tesfaye et al., 2003). The Gulf of Aden rift has propagated into the eastcentral Afar Depression through the Tadjoura Gulf (Fig. 2.2). The rift had been spreading in a WSW direction for millions of years till it reached the Gulf of Tadjoura (e.g., Courtillot et al., 1980; Manighetti et al., 1997) and then turned to the NW, parallel to the Red Sea trend, as it joins the eastcentral Afar Depression. The western branch of the Red Sea Rift, on the other hand, runs along the Gulf of Zula, steps onto land within the Danakil Depression forming the NNW–striking axial range and leaving the elevated Danakil Microplate between the Depression and the southern Red Sea (Figs. 2.2 and 2.4; Tesfaye et al., 2003).
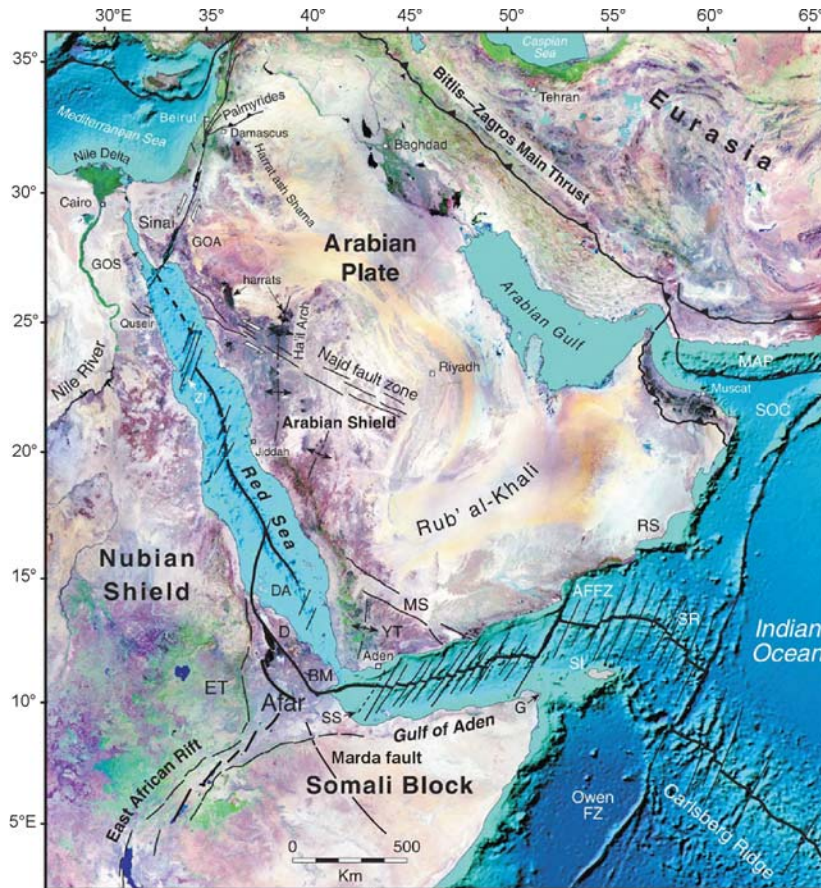
Figure 2.1 Structural outline of the Afro-Arabian landmass. Subduction at the Zagros Orogenic Belt induces tensile stress at the Gulf of Aden and Red Sea regions (after Bosworth et al., 2005).

The magnetic anomalies of the Gulf of Aden ridge propagating from the Sheba ridge at a velocity of ~30 mm/yr and spreading rate of ~12 mm/yr blocks and terminates against the magnetically quite continental zone in the central Afar Depression (Courtillot et al., 1984; Manighetti et al., 2001). Even though, they are weak, magnetic anomalies are still recognized as far as the central Afar Depression, implying either an enormously asymmetric spreading (Courtillot et al., 1984) or complex history of ridge evolution (Beyene and Abdelsalam, 2005, and references therein). The inland rift spreading and propagation along the NW–trending Asal–Manda Inakir grabens are sporadic and occur in intervals of 10^6 and 10^5 years, showing irregular effusive and tectonic processes (Courtillot et al., 1984). These authors proposed that close to 4 Ma the Gulf of Aden propagators arrived at the east-coast of Djibouti (Gulf of Tadjoura), at ~2 Ma propagation progressed farther west up to Arta-Tadjoura, and at ~1 Ma propagation reached the current Asal–Sakalol–Manda Inakir grabens.

2.4 Tectonic evolution of the Afar Depression and Main Ethiopian Rift

The Afar Depression and MER, also called the 'Ethiopian rift', are part of the continental EARS (Figs.1.1, 1.2, and 1.5). These two kinematically and geometrically distinct intracontinental rifts are at different phases of rift evolution (Tesfaye et al., 2003, and references therein). Structural and geophysical data show that the Afar Depression is in a state of oceanic-type crust meeting the young oceanic rifts (i.e., the Gulf of Aden and Red Sea) to the east and north, respectively. Gravity measurements and seismic refraction show that the thickness of the crust beneath Afar Depression varies from 23–26 km in the south to ~14 km in the north, Dallol area (Makris et al., 1975; Makris and Ginzburg, 1987). In the MER, the crustal thickness ranges from 26–38 km (Mickus et al., 2007; Keranen and Klemper, 2008). The crustal thickness of the rift bounding plateaus escalated abruptly to 35–44 km (Searle and Gouin, 1972; Hebert and Langston, 1985). The spreading rates obtained from geodetic and plate-kinematic studies indicate about 16 mm/yr across the Afar Depression between the Nubian and Arabian plates (Chu and Gordon, 1998). The spreading rate between Nubian and Somalian plates across the northern sector of the MER is much slower, 3–6 mm/yr (e.g., Mohr, 1972; Mohr et al., 1978; Chu and Gordon, 1998; Bilham et al., 1999).

The earliest rejuvenated extensional deformation documented in the EARS occurred in inactive basins at the southern end of the present-day southern MER at ~25 Ma, within lithosphere formerly stretched during the entire Mesozoic rifting episodes (Hendrie et al., 1994; Yirgu et al., 2006). However, the timing of initial breakup of Afar Depression and MER is not well recognized. Different authors put different time-frame for the initiation of rifting in Afar and MER. Barberi et al. (1975) and CNR-CNRS (Afar team) (1973) indicated that extensional deformation in southern Afar Depression and the northern part of MER commenced at ~25 Ma. From the Ethiopia and Yemen conjugate rifted volcanic margin study, Ukstins et al. (2002) computed ~26–25 Ma for the initiation of separation between Nubia and Arabia. Kazmin et al. (1980) argued that rifting at the southern end of the Red Sea, the boundary zone between the southern Afar and MER started at ~14 Ma. Wolfenden et al. (2005) come close to the age estimates of Kazmin et al. (1980) and mentioned that south of 10°N, boundary faults evolved during or after the deposition of felsic shields (Mezezo, Megezez) at 12–11 Ma. These boundary faults efficiently connected the southern Red Sea and MER system. Despite the disagreement related to the age of initial rifting in the southern Afar margin and the northern MER, it appears that they developed roughly progressively

from Oligocene–Miocene at the northern Afar to the middle–late Miocene in the northern MER (Tesfaye et al., 2003, and references therein).

2.4.1 **The Afar Depression**

The Afar Depression is an area of active extensional deformation and basaltic volcanism from which the Red Sea, the Gulf of Aden and the MER radiate (Abbate et al., 1995). The depression is characterized by three geometrically distinct structural trends (Fig. 2.2): (1) a NNW trend that parallels the Red Sea rift; (2) a nearly E-W trend that runs through the Aden Gulf and continues onto land at the Tadjoura Gulf in the east-coast of Djibouti; and (3) a NNE trend of the MER (Thurmond et al., 2006). The Red Sea and Gulf of Aden are highly evolved and active rift segments currently propagating into the Afar Depression through a series of en-echelon arranged emerging spreading centers (Courtillot et al., 1984).

The Afar Depression, core of the Oligocene-Recent Afro-Arabian continental breakup, is one of the few active tectonic zones in the globe where one can easily study the activites of mantle plume, rift-rift-rift triple junction and Microplate formation on land (Eagles et al., 2002). Moreover, it is probably the only active intracontinental rift in the globe where both the incipient continental breakup history and the current seafloor spreading can be observed on the surface (Almond, 1986; Tesfaye et al., 2003). The early Oligocene–Present volcano-tectonic development of the Afar Depression has been deduced to have been causally influenced by the influx of the Ethio-Afar hot mantle plume, resulting in extensive dome-shaped elevated plateaus between ~40 Ma and ~30 Ma (Redfield et al., 2003, and references therein). The Ethio-Afar mantle plume interpretation is largely coincident with outpouring of the ~30 Ma massive Ethiopian flood basalt and the 31–25 Ma Yemen continental flood volcanism (Baker et al., 1996; Hofmann et al., 1997; Redfield et al., 2003).

The progressive NE movement of the Arabian plate for the last 30 My produced the 300–400-km-wide Afar triangle, which comprises the triple junction (Wright et al., 2006).
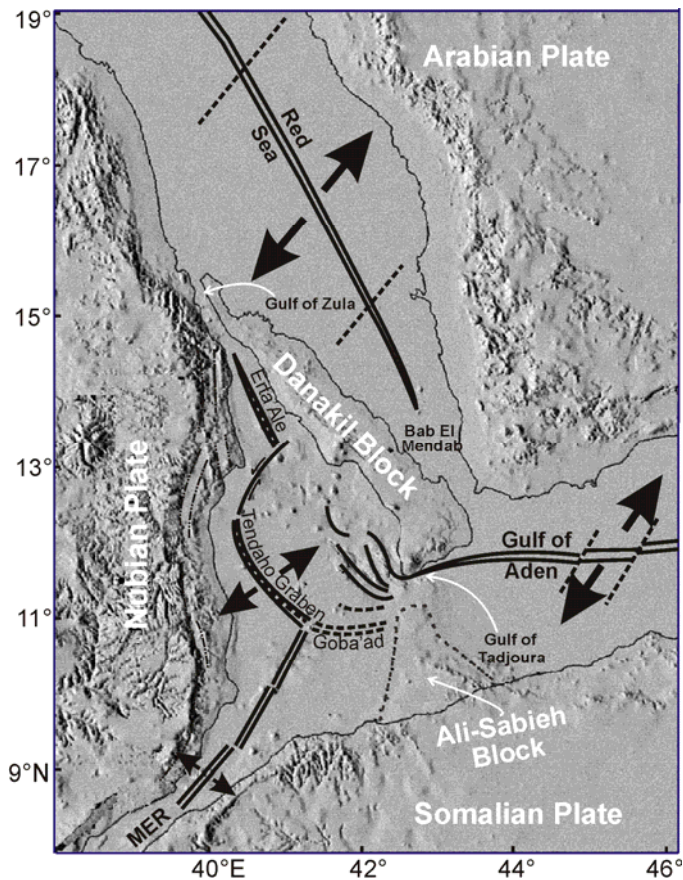
Since the late Oligocene, the Ethio-Afar mantle plume head has influenced an extensive area centered on the present day Afar triple junction (Hofmann et al., 1997; Audin et al., 2004). When both the Red Sea and Gulf of Aden spreading centers approached the triple junction area at ~20 Ma (Courtillot et al., 1987), the Afar Depression began to open and detached two continental microplates, the Danakil and Ali Sabieh Microplates (Fig. 2.2), from the Nubian and Somalian plates, respectively (Audin et al., 2004).

Figure 2.2 Outline of the Red Sea, Gulf of Aden and MER tectonic trends and the position of Danakil and Ali Sabieh blocks with respect to the Nubian, Somalian and Arabian plates (modified after Collet et al., 2000).

Nature of the Afar Depression crust: The nature of the crust or lithosphere in the Afar Depression is controversial (Makris and Ginsburg, 1987). The Afar Depression lithosphere has been described differently by various authors as oceanic, continental, and transitional (Beyene and Abdelsalam, 2005). Most of the axial zones of the depression (e.g., Erta'Ale Range, Asal–Manda Inakir, Manda Hararo–Goba'ad, and the Sabure-Hertale–Adado rifts) are characterized by transitional to tholeiitic basalt flows accreted along open fractures similar to a young oceanic-type lithosphere (Fig. 2.3; Barberi and Varet, 1977). According to these authors, the entire Afar Depression lithosphere could be an oceanic-type that was formed during the onland propagation of the Aden Gulf and the Red Sea (i.e., Pliocene–Pleistocene) or a thin continental lithosphere injected by basaltic dykes and covered by the Stratoid flood basalts.

Geophysical and structural studies regarding the center of the depression pointed out that the Afar is progressing to an oceanic type of lithosphere, similar to the lithosphere observed in Iceland or Mid-Atlantic Ridge, with anomalously low asthenospheric velocities found at fairly shallow depth (Barberi et al., 1980, and references therein). The combined effect of extension and volcanism and/or diffused faulting could have resulted in the evolution of the Afar lithosphere that is transitional between continental and oceanic where crustal thinning is compensated by accumulation of new magmatic material (Beyene and Abdelsalam, 2005). The nature of the Afar Depression lithosphere has been described as oceanic along its axial zones and becomes progressively continental towards the marginal areas. From this perspective, Morton and Black (1975) believed the western Afar margin to be a zone of highly stretched continental crust induced by series of normal faulting, block rotation, and magma injections along weak zones (Fig. 1.4a).

The lithospheric thickness in Afar is not uniform throughout the Depression. Makris and Ginzburg (1987), Maguire et al. (2006), and Stuart et al. (2006) estimated the thickness of the lithosphere to be ~26 km in the southern and central Afar and gradually decreases towards the north reaching a minimum of 14 km in the Dallol area, northern Afar Depression. Bonatti and Emiliani (1971) supposed that separation of the Danakil Microplate from the Nubian plate by concentrated tensional and rotational movements created the depression. As a consequence of these concentrated extensional deformation, continental lithosphere is very thin below the axial zone of the northern Afar Depression.

The extended and intruded crust beneath the central Afar Depression is 18–22 km thick with strong similarities to crust beneath Iceland (Hirn et al., 1993; Dugda and Nyblade, 2006). The existence of abnormally thinned crust in this active tectonic zone is the main reason for the assumption that the Afar Depression is in a state of oceanic-type crust. From volumetric considerations, Redfield et al. (2003) pointed out that either the base of the lithosphere underlying the Afar Depression is not well constrained or there has been massive removal of the lithospheric material by the upwelling hot mantle plume since the onset of the extension. From the elastic strength measurements, the crustal thickness of the Afar Depression decreases from 17 to 5 km in the highly stretched portions of the region (Ebinger and Hayward, 1996). The NW-SE–trending Asal–Manda Inakir rift (Figs. 2.3 and 2.4) on the eastcentral tectonic zone of the Afar Depression is widely cited as a location where incipient seafloor spreading can be observed on land (Gupta and Scholz, 2000).
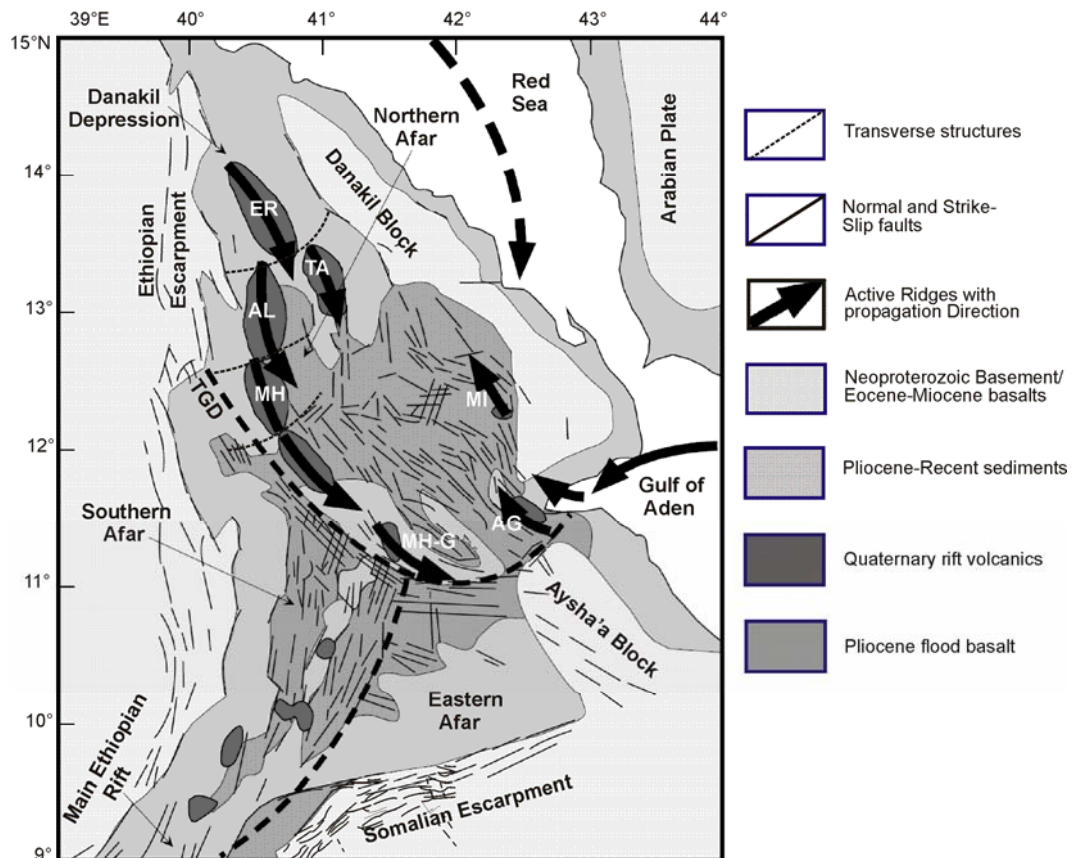
Figure 2.3 Simplified geological map and major tectonic structures (segments) of the Afar Depression. ER, Erta'Ale; TA, Tat'Ali; AL, Alyata; MH, Manda Hararo; MI, Manda Inakir; MH-G, Manda Hararo–Goba'ad; AG, Asal Ghoubett (after Hofstetter and Beyth, 2003).

2.4.2 The Afar Triple Junction

The Gulf of Aden–Red Sea–MER triple junction lies in a tectonically complex zone at ~11.5°N along the Manda-Hararo–Goba'ad rifts within the central Afar Depression (Fig. 2.4; Corti, 2009). The evolution of the triple junction is not well constrained as the development of the three rifted arms of the junction is different. Continental rifting in the Gulf of Aden and Red Sea initiated at ~35 Ma, and ~28 Ma (e.g., D'Acremont et al., 2005; Watchorn et al., 1998; Wolfenden et al., 2005), respectively. Early phase of crustal extension in the southern and central MER initiated between 18 and 15 Ma, but little was known of early crustal stretching in the northern MER (Wolfenden et al., 2004, and references therein). The extension direction of both the Red Sea and Gulf of Aden is identical. NE–oriented oceanic spreading in the Red Sea started at ~4 Ma (Wolfenden et al., 2005); NE–oriented seafloor spreading in the Gulf of Aden has propagated westward through the Gulf of Tadjoura into the central Afar since 16 Ma (D'Acremont et al., 2005). The stage of seafloor spreading is not yet achieved in the MER (Wolfenden et al., 2004).

Models for the development of the Afar ridge–ridge–ridge type triple junction have assumed the concurrent evolution of the three rift arms soon after the peak of Ethiopian flood basalt magmatism at ~30 Ma (Hofmann et al., 1997; Corti, 2009). But still there is a controversy on when exactly the triple junction formed. Tesfaye et al. (2003) postulated that the Oligocene triple junction (paleo-triple junction) of Afar was located at about lat 10°N in an arcuate accommodation zone and then drifted parallel to the extension direction of the Gulf of Aden and Red Sea to the Tendaho-Goba'ad Discontinuity (TGD), ~11.5°N latitude (Fig. 2.4). The sequential order of rifting in the three rift segments described above proposed,
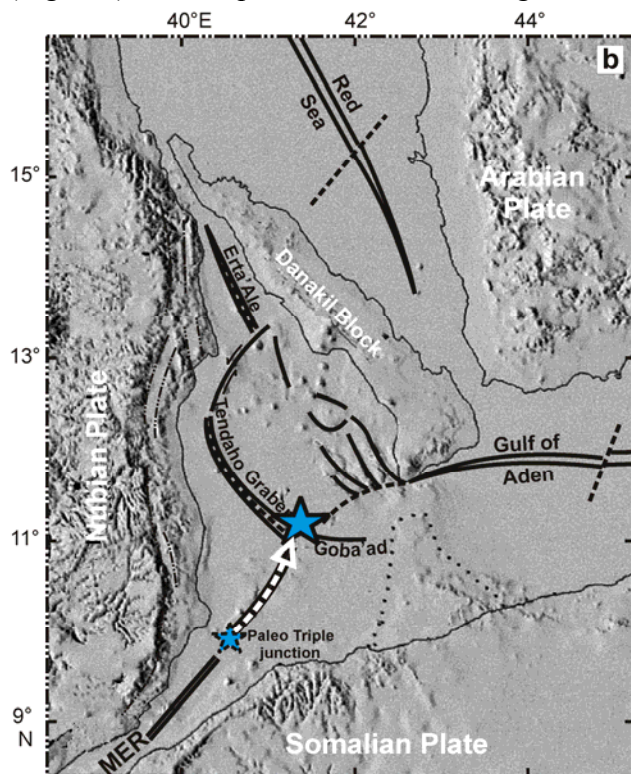
however, a more complex setup with a diachronous expansion of the junction zone between the tectonically distinct rift systems (Corti, 2009). Although Tesfaye et al. (2003) supposed the late Oligocene triple junction at the accommodation zone, Wolfenden et al. (2004) argued against the evolution of a triple junction in the Afar Depression during the Oligocene. The birth of the triple junctions is, rather, linked with the development of marginal faults along the northern MER at 11 Ma; and then wandered northeastwards to the present-day TGD (Wolfenden et al., 2004).

Figure 2.4 The present location of the triple junction and geometric setup of the Afar Depression. The paleo-triple junction is situated 1.5° southwest at the current tectonic boundary of the Southern Afar and MER (modified after Collet et al., 2000).

The current triple junction is not at the same location as it was before; i.e., during its formation. Different spreading rates across the actively propagating ridges, the Red Sea–Gulf of Aden–MER, started at different times, which enable the Afar triple junction to drift with time. On the basis of marginal volcanic rocks distribution, Kazmin et al. (1980) argued that tectonic displacement in the southern Afar escarpments commenced at ~14 Ma. This middle Miocene tectonic movement contradicts with the Oligocene timing proposed for the initiation of fault block drift (Tesfaye et al., 2003).

After an extended period of propagation and extension, the southern Red Sea rift (northwest–trending) and the MER (north-northeast–trending) merge together in central Afar

Depression (Fig. 2.4). The westward propagating active rift of the third arm (the ENE-WSW–trending Gulf of Aden rift) fails to directly merge with the other two rift segments; it bends to the northwest and dies out in the eastern part of central Afar forming a horse-tail structure (Tesfaye et al., 2003). As a result of these spattered and coupled-effect structures, a wide zone of highly stretched depression is present in central Afar (Manighetti et al., 1998, 2001). The broad Manda Hararo–Goba'ad graben region of central Afar, bounded by lat 11°–11°48'N and long 40°45'–41°42'E is regarded as the focus of the junction of the three rifts (Tesfaye et al., 2003). The current triple junction is positioned ~1.5° far from the paleo-triple junction. According to the estimate of Tesfaye et al. (2003), the Africa–Somalia–Arabia rift–rift–rift triple junction hosted at the center of Afar Depression has migrated ~160 km to the northeast since its formation with an average rate of spreading of ~14 mm/yr.

2.4.3 *The Danakil Microplate*

The Danakil Microplate or block is an elongated landmass of ~500-km-long and ~100-km-wide topographic high (Tesfaye et al., 2003; Beyene and Abdelsalam, 2005). Its elevation varies from sea level in the north to ~1700 m in the south, with a mean elevation of 400 m (Courtillot et al., 1984; Boccaletti et al., 1999; Manighetti et al., 2001; Tesfaye et al., 2003). The Danakil Microplate is still under progressive deformation affected by extensional and strike-slip faulting to a much greater degree than the nearby plates (Nubian and Arabian). It is at the focus of the EARS connecting the Red Sea, Gulf of Aden and the Afar Depression. The Danakil Microplate separates the Southern Red Sea Rift basin from the Afar Depression. The northern part of the Microplate is composed of basement complexes overlain by clastic and carbonate sedimentary rocks similar to those on the Ethiopian highlands (Tesfaye et al., 2003). Syn-rift sedimentary rocks are found on the peripheries of the Danakil Microplate, and Pliocene– to Recent volcanic rocks in the southern portion of the Microplate (Varet and Gasse, 1978).

Even though, the timing of the initial breakup and magnitude of block-rotation is till debatable; Le Pichon and Francheteau (1978) computed ~30° counterclockwise rotation for the Danakil Microplate with respect to Nubia since the breakup. This idea is strengthen by the suggestion that the Danakil Microplate initiated to break away from the relatively stable Nubian plate ~20 Ma to attain a 30° angle of counterclockwise rotation to the Ethiopian escarpment (Manighetti et al., 2001; Beyene and Abdelsalam, 2005). However, the rotation of the Danakil Microplate has been provoked by the westward spreading of the Gulf of Aden ridge that created a new plate margin between the Somalian Plate and the Danakil Microplate

along the Asal–Manda Inakir graben (Fig. 2.5; Vellutini, 1990; Eagles et al., 2002). Much of the Danakil Microplate rotation is, therefore, accommodated after the onland propagation (i.e., into the Afar Depression) of the Gulf of Aden in the Pliocene period. From this perspective, Souriot and Brun (1992) pointed out that the Danakil Microplate has rotated 10° in the past ~4 Ma. This angular rate of block rotation is much faster than the rates of rotation computed by Le Pichon and Francheteau (1978) and Manighetti et al. (2001). The possible reason for the recent (Pliocene-Present) increment in angular rate of rotation of the Danakil Microplate is the onset of mid oceanic-like accretion in central Afar Depression (Eagles et al., 2002). Based on the crank-arm model of Sichler (1980), the counterclockwise rotation of the Danakil Microplate created intense faulting in the Danakil Depression, diffused faulting in the central Afar, oblique faulting in the Tadjoura region, and right-lateral strike-slip faulting in the southern Afar Depression (Fig. 2.5; Beyene and Abdelsalam, 2005).
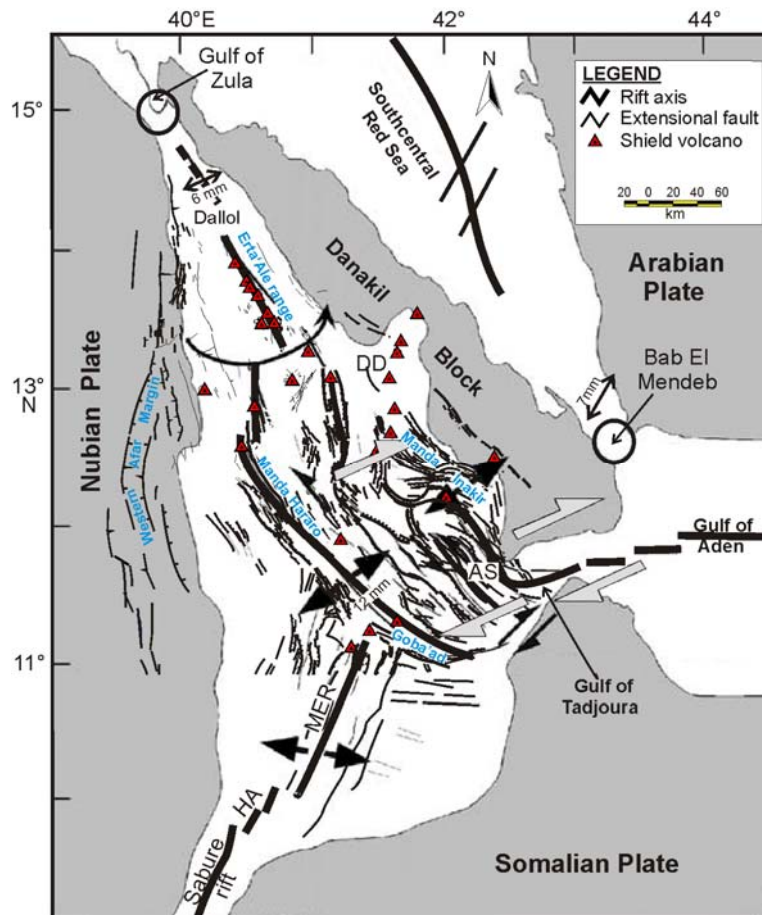
Figure 2.5 The possible structural interactions of the Afar Depression. Ridges and Rifts are in thick black line. The rate of extension and direction are from Chu and Gordon, 1998, and Amelung et al., 2000). The grey arrows show the strike-slip motion of the various Afar Depression blocks (modified after Maneghitti et al., 2001).

2.4.4 The Main Ethiopian Rift

The Main Ethiopian Rift (MER) is the least evolved of the three arms of the triple junction, but new data confirm that it is also ~18 My younger than the Gulf of Aden and Red Sea rifts (Wolfenden et al., 2004). It is a narrow (60–100-km-wide) and deep depression with an overall NE-SW orientation (Tesfaye et al., 2003). The MER can be subdivided into three sectors that have been inferred to reflect different stages of rift evolution processes, being characterized by different fault styles, timing of magmatism, and deformation of lithospheric structures (Figs. 1.5 and 2.5; Corti, 2009, and references therein). The northern MER extends for ~200 km from the southern Afar–MER limit (near Ayelu volcano) southwards to near Lake Koka area (Bonini et al., 2005). This sector represents the volcano-tectonically active zone within the MER constituting closely-spaced volcanic centers along the axial zone. The geometric and physiographic characteristics of the northern MER and southern Afar Depression are not readily identifiable within the rift floor. On a broader view, however, the funneling out of the MER from a width of ~100 km to ~300 km in the vicinity of lat 10° N, south of the Ayelu-Amoisa volcanic centers, is inferred to delineate a physiographic boundary between the two identical tectonic domains (Tesfaye et al., 2003). The boundary between the central and southern MER rift is not physiographic; instead, it is purely tectonic, from which the border and marginal faults rotate from the NE–SW to nearly N–S orientation at ~7° N latitude (Corti, 2009).

Structural and stratigraphic observations supported by new ^{40}Ar/^{39}Ar dates from the Northern MER reveal that initial extensional deformation in the region commenced at ~11 Ma contemporaneous with the development of NNE–trending Arboye boundary fault system (Wolfenden et al., 2004). According to these authors, the Gulf of Aden–Red Sea–MER triple junction is a relatively young tectonic structure developed ~20 My after initial crustal breakup in the Gulf of Aden and southern Red Sea rifts.

The direction of expansion in both the Red Sea and Gulf of Aden is simple, which is characterized by the southwards and westwards inland propagations, respectively; however, the propagation of the MER is till debatable. The MER connects the two old rift segments of the EARS: the Red Sea rift, which initiated in the Oligocene–Miocene, in the north, and the early Miocene period Turkan rift in the south. In one side, Wolfenden et al. (2004) suggested that the MER, the northernmost sector of the EARS, propagated northwards from the Turkana Depression (at ~25 Ma) through the central MER into the northern MER after ~11 Ma. On the other side, Bonini et al. (2005) proposed southwards rift migration from the southern Afar through the northern and central MER in the late Miocene (11–8 Ma) into the

southern MER during the late Pliocene–Pleistocene. As an alternative hypothesis, Rooney et al. (2007) came with the suggestion that the MER allows the merger of two relatively old rift systems, the Red Sea rift and the EARS. The East African rift-related crustal extension influences the southern and central MER and spreads to the north, whereas the Red Sea-related extension affects the southern Afar and northern MER and propagates southwards into the central MER (Corti, 2009). The central MER is the result of the linkage between the two structurally and tectonically distinct domains defined by the southward propagating Red Sea Rift and northward propagating East African Rift (Rooney et al., 2007).

After complete rupture of the MER, crustal deformation continued (during Pliocene times) along large border faults, with big throws on the faults giving rise to a widening and deepening of the rift floor (Corti, 2009). At ~1.6 Ma, the geometry and kinematics of the MER changed considerably: deformation shifted from the marginal areas to the right-stepping en-echelon arrangement of closely spaced fault swarms of the Wonji segments obliquely cutting the rift floor (Fig. 2.6; Mohr, 1962, 1967; Meyer et al., 1975; Boccaletti et al., 1998). The major change in the geometry of the rift was accompanied by bimodal Quaternary magmatic activity within the central part of the depression along the intensely faulted zone. Such recent volcano-tectonic activities are well expressed in the northern MER, where geophysical and structural data suggest that large-offset border faults are no longer active and most crustal extension is concentrated within the deeply faulted axial zones (Corti, 2009). In the southern and central MER, magmatic activities are not as extensive as the northern MER and the rift geometry is asymmetrical with the Wonji fault segments that starts to propagate from the eastern rift margin towards the rift center (Fig. 2.6).

The MER is characterized by two chronologically and kinematically distinct fault systems. The older comprises Oligocene–Miocene, NNE– to NE–trending, widely spaced, rift bounding fault systems (Kazmin et al., 1980; Tesfaye et al., 2003). The younger includes Quaternary–Present, NNE–trending en-echelon fault segments and chains of volcanic centers affecting the rift floor (Fig. 2.6; Tesfaye et al., 2003, and references therein). These closely spaced fault swarm are referred to as the Wonji fault belt (WFB), mainly affecting the center of the MER (e.g., Mohr, 1967; Kazmin et al., 1980; Mohr, 1983; Acocella et al., 2003; Corti, 2009). These normal faults are mostly arranged in a right stepping en-echelon configuration oblique to the main direction of the rift bounding faults, where arrangement of these fault zones with the large-offset boundary faults gives rise to a typical S-shaped curvature resulting in an overall sigmoidal geometry (e.g., Mohr, 1968; Boccaletti et al., 1998; Corti, 2009). The faults within the WFB are commonly short, closely spaced and extension is marked by

normal faulting, open fissures, and fissure-fed basalt flows (e.g., Mohr, 1967; Kazmin et al., 1980; Tesfaye et al., 2003; Corti, 2009). At the northern end of the MER, the WFB includes a set of well-developed parallel grabens and a broad zone, ~60-km-wide, of north-northeast–trending normal faulting (Tesfaye et al., 2003).

Almost all the recent volcano-tectonic activities, which occurred in the MER, are now concentrated in the 5–12-km-wide zone of the WFB (Mohr and Woods, 1976). However, in the southern Afar Depression, between Ayelu-Abida (Amoissa) volcanic centers and the Tendaho-Goba'ad graben, the width of the axial fault zone reaches ~80 km (Fig. 2.6; Mohr, 1967; Tesfaye et al., 2003). The WFB is segmented (Mohr and Woods, 1976; Kazmin et al., 1980) with segment length ranges from a few kilometers up to 80 km and segment offset up to 40 km (Mohr, 1967; Mohr and Woods, 1976; Kazmin et al., 1980). Various structural analyses reveal no evidence for transfer faults linking the segments of WFB; rather, the tips of segments overlap, thereby accommodating strain transfer (Casey et al., 2006; Corti, 2009). Global Positioning System (GPS) measurement and field observation prove that almost all recent extensional deformation across the MER is accommodated in a ~20-km-wide zone of magmatism and faulting within Wonji segments (Corti, 2009, and references therein).

Figure 2.6 Simplified structural map of the entire Main Ethiopian Rift. Important structures are: the axial Wonji Fault Belt (thick grey shaded zone), the rift bounding faults, regional transverse lineaments, and linearly aligned major volcanic centers (modified after Chernet et al.,1998).

2.5 Magmatism throughout East Africa

Continental flood volcanism (CFV) is often associated with rapturing of the earth's lithosphere. As continental breakup advances towards matured rifting, the geochemical characteristic of the lavas commonly evolves toward that of oceanic lavas (ocean island basalts, OIBs; and mid oceanic ridge basalts, MORBs), suggesting the progressive involvement of the upper mantle materials (Pik et al., 1999). Although continental flood basalt (CFB) provinces are usually linked to deep origin hot mantle plumes (Richards et al.,

1989), the involvement of the upper mantle and crustal sources contribute a lot to their genesis.

Different models dealing with volcanism assume that the convecting hot mantle plume beneath an anomalous asthenosphere causes the uplift of the Ethiopian dome followed by widespread volcanism and rifting (Beyene and Abdelsalam, 2005). However, the details of the relations between CFB provinces, plate kinematics, and extensional deformation have to be well constrained, so as to understand the melt generation and eruption rates (George et al., 1998). Some volcanic provinces (e.g., Deccan in India) had been erupted very rapidly and required adiabatic decompression melting for such voluminous lavas within a hot mantle material (White and McKenzie, 1995). On the other hand, the Paraná flood basalts of southern Brazil erupted slowly over 10–12 My period, have a distinctive chemical composition, and may have been generated by melting of the lithospheric mantle above a hotspot (George et al., 1998, and references therein).

The highly irregular rates of eruption and duration must reflect either the very distinct character of the hotspots, or the different nature of the lithospheric structures and the stress fields that drive the mantle plumes. In this case, Baker et al. (1996) suggested that the slow northeastward drift of the Arabian pate (<20 km/My) from the African plate compared with, for example, separation of India and the Deccan flood basalts (>50 km/My), may have been responsible for the rather bimodal nature and continuing record of CFV at the Ethio-Afar triple junction.

Earliest magmatic activities in the EARS occurred in southwestern Ethiopia at ~45 Ma (Ebinger and Sleep, 1998; George et al., 1998), followed by widespread flood basalt activities in northwestern Ethiopia, Eritrea, and Yemen at ~30 Ma (Baker et al., 1996; Hofmann et al., 1997). Gass (1975) proposed that the African Plate was motionless for long period in Eocene–Miocene and high heat flux released by the hot mantle plume targeted on the same lithosphere that raised its base (the start of the Ethiopian Dome). The high heat flow beneath the same lithosphere has provoked the production of isolated chambers of magma within the extended anomalous mantle and the major magmatism of the ~30 Ma flood basalt series (Gass, 1975; Beyene and Abdelsalam, 2005). The spatial and temporal gap between the earliest phase of magmatism and plume-driven volcanic activity represents basic geodynamic controversy surrounding the development of the EARS (Furman et al., 2004).

The contribution of hotspots in the development of the present physiography and dynamics of East African landmass has led to contending models as to the number of distinct plumes that may lie beneath (Rogers, 2006). Ebinger and Sleep (1998) suggested that

volcanism across the entire East Africa (i.e., Ethiopia and Kenya) can be elucidated as a result of the outpouring of a single hot mantle plume beneath southwestern Ethiopia ~45 Ma. After the first impact at southwestern Ethiopia, the mantle plume propagated beneath the lithosphere, controlled by the inverse topography at its base, produced during pre-rift extensional structures (Rogers, 2006). In the single plume model, the plume head intrudes the base of the lithosphere beneath southwestern Ethiopia and then spreads southwards to the current Lake Victoria following the topography of the lithosphere/ asthenosphere boundary (Fig. 2.7; Corti, 2009).

On the other hand, George et al. (1998) and George and Rogers (2002) suggested that two spatially and temporally distinct mantle plumes are required to explain the East African magmatism: one beneath the Ethio-Afar and the other beneath Kenya (Fig. 2.7). In the two-plume model, the southward propagation of basaltic magmatism from southwestern Ethiopia through Kenya into Tanzania reflects the northward motion of the African plate with respect to the stable Kenya plume for the last ~50 My, whereas volcanism in central and northern Ethiopia reflects 30 My of sustained activity of the Afar plume (Furman et al., 2004). The oldest volcanism in southwestern Ethiopia reflects the thermal and mechanical influence of the Kenyan asthenosphere, rather than the Ethio-Afar mantle plume (George et al., 1998). The two-plume model requires that Eocene–Oligocene magmatism in southwestern Ethiopia, a region now within the influence of the Afar hotspot, was originally under the influence of the Kenyan plume (George et al., 1998).

The basic compositional difference among the two proposed plumes has continued until the present. The geochemical differences between the recent mafic lavas of the Ethio-Afar volcanic province (i.e., Erta'Ale, and MER) and those from Turkana, the Gulf of Aden, and Red Sea have led previous workers (e.g., George et al., 1998; Rogers et al., 2000) to suggest the presence of two spatially and temporally distinct mantle plumes beneath the Ethio-Afar and Kenya lithosphere (Furman et al., 2004).
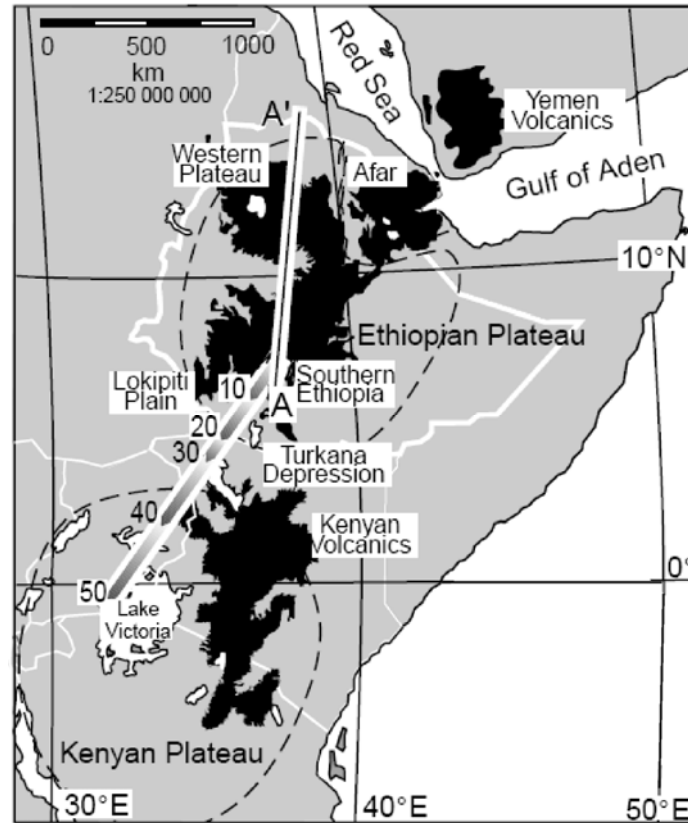
Figure 2.7 Spatial distribution of the Eocene-Recent East African volcanism (black). Dashed circles show extent of Ethiopian and Kenyan domes. Thick shaded line shows the extent and direction of African plate motion since 50 Ma, in 10 My intervals. These imply southwestern Ethiopia was positioned close to the present geographic location of Lake Victoria during the middle Miocene, directly over the current Kenyan plume (after George et al., 1998).

2.5.1 Southern Ethiopian and Kenyan Volcanism

The earliest magmatism in the EARS occurred hundreds of kilometers south of the present Afar Depression (e.g., southern Ethiopia, southeastern Sudan, northern Kenya) at ~45–40 Ma (Ebinger et al., 1993; George et al., 1998) followed by an extensive volcanism all over central and northwestern Ethiopia, Eritrea, and Yemen where flood–shield basalts and interbedded felsic and pyroclastic deposits were erupted between ~31 and 22 Ma, (e.g., Baker et al., 1996; Hofmann et al., 1997; Kieffer et al., 2004; Yirgu et al., 2006). The earliest phase of volcanism in southwestern Ethiopia, therefore, predates the start of crustal deformation in the Gulf of Aden–Red Sea region at ~35–28 Ma (Omar and Steckler, 1995; D'Acremont et al., 2005; Wolfenden et al., 2005) by as much as ~10–5 My. Instead, it is broadly contemporaneous with the rift basin expansion farther west in the Melut-Pibor rift systems (southern Sudan), and such a view is supported by westward increases in late Eocene basalt thicknesses from the southern Ethiopia, toward the southern Sudan (Lokipiti plain), the location of the now-subsurface Melut-Pibor rift (George et al., 1998).

The earliest phase of volcanic activities in southwestern Ethiopia lasted for longer period but with low rates of eruption. Ebinger et al. (1993) have estimated the volume of the Amaro basalts from southern Ethiopia, which erupted in a duration of 10 My, to be at least 30,000 km^3, implying an average eruption rate of 0.003 km^3/yr. The eruption rates of the Kenyan basalts are also very low, ~0.006 km^3/yr (Baker, 1987). These led to a conclusion that eruption rates in Southern Ethiopia in the Eocene period were more comparable with the eruption rate calculated for the Kenyan rift integrated over the past 30 Ma, implying a similar geodynamic condition beneath the lithospheric mantle (George et al., 1998).

The southern Ethiopian (Amaro) basalts, which are spatially and temporally comparable with the Kenyan basalts, are also geochemically analogous. The Amaro basalts were originally recognized as an early phase of Afar-related magmatism (Stewart and Rogers, 1996). Their early eruption has provided a key component for estimating the timing of initial volcanism in East Africa using the single plume model (Ebinger and Sleep, 1998). However, the more detailed geochemical studies of basalts from the southern Ethiopia (George and Rogers, 2002) have shown that they have distinct characteristic signature that enable to differentiate easily from both the Oligocene high-Ti magmas from the northwestern Ethiopian flood basalts and Quaternary Afar basalts but more similar to basalts from Kenya (Rogers, 2006). According to Rogers (2006), the major and the trace element contents as well as the Sr and Nd isotopes of the Amaro basalts imply marked petrological differences compared with the high-Ti magmas from the northern Ethiopian CFB.

The style and composition of volcanism in the Kenyan region is more or less similar with the volcanism of the southern Ethiopian magmatism. However, the Kenyan basalts show a wide range in composition as the rift architecture and evolution of the two branches (Eastern and Western) of the Kenyan rifts are variable. The Eastern and Western Kenyan rifts have distinct magmatic characteristics. The former rift is covered by large volumes (>10^5 km^3) of mafic lavas and felsic differentiates that have erupted throughout the Miocene–Pliocene (Baker, 1987; Rogers, 2006). On the other hand, magmatism along the entire Western rift is erratic and limited in volume and coverage, and appears to be associated with overlapping zones between adjacent rift segments (Rosendahl, 1987; Rogers, 2006).

In addition to the differences in eruption rate of basaltic magmatism in the two rift branches, there are apparent differences in composition between the volcanic products of the Eastern and Western rifts (Rogers, 2006). The Eastern rift basalts at given silica wt% have a lower potassium content than those from the Western rift and are apparently analogous with

ocean island basalts (OIB) (Latin et al., 1993; Macdonald et al., 2001). In contrast, basalts from the Western rift have higher potassium content than its counter Eastern rift.

2.5.2 Ethiopian and Yemen Volcanism

The Ethiopian continental flood basalt (CFB) province has been related to the uprising of a deep hot mantle plume beneath the present day Afar (Marty et al., 1996), which provoked a widespread basaltic magmatism around 30 Ma (Hofmann et al., 1997; Coulie et al., 2003). This province is located at the intersection of three active rifts: two oceanic rifts, Gulf of Aden and Red Sea, and the Main Ethiopian Rift (Fig. 2.8; Pik et al., 1998). The interaction between the vigorously convecting hot mantle material and the pre-rift deformed Ethiopian lithosphere (Korme et al., 2004) strongly influenced the regional tectonic setup of the Ethio-Arabian landmass (Coulie et al., 2003). Before 35–25 Ma, rifting of the Gulf of Aden and Red Sea might have been controlled by the far-field stress originated at the Zagros Orogenic Front, but the rising of hot mantle plume underneath the Afar Depression forced the propagation of the Gulf of Aden towards Afar Depression (Courtillot et al., 1999; Coulie et al., 2003).

In central– to northern Ethiopia and Yemen, volcanism initiated during the Oligocene with the eruption of voluminous lavas (Pik et al., 1999) encompassing the present Afar Depression. The Ethiopian CFB is the youngest flood basalt activity associated with continental breakup and embryonic seafloor spreading (i.e., Gulf of Aden and Red Sea). From tectonic point of view, major volcanism in the Afro-Arabian plate is believed to have taken place immediately after the onset of rifting in the Gulf of Aden, and before or contemporaneous with the initiation of rifting in the Red Sea (Bott et al., 1992; Menzies et al., 1997). However, dating of syn-tectonic sedimentary facies from the Red Sea coast confirmed that volcanic activity is slightly older than crustal extension in the region while it is synchronous with major extension in the Gulf of Aden (Beyene and Abdalsalam, 2005, and references therein). Most of the Ethio-Yemen flood basalts were extruded over a short time period, not <2 My, at ~30 Ma (Baker et al., 1996; Hofmann et al., 1997) and significantly predate the early–late Miocene Red Sea and MER extensional phases (Menzies et al., 1992). Succeeding volcanism, from 24 Ma to Present, occurs as large shield volcanoes on the Ethiopian plateau (Kieffer et al., 2004) or is associated with extensional deformation in the rift floor as fissure-fed basalts (Fig. 2.7; Pik et al., 1999).

The Ethiopian and Yemenite flood basalts are now separated by the 300–400-km-wide rift that hinders the genetic link between the two volcanic centers. Coulie et al. (2003)

have conducted, for the first time in a single study, dating of samples from both the Ethiopian and Yemenite sequences in order to eliminate interlaboratory discrepancy. The results (Coulie et al., 2003) support that the initiation of basaltic volcanism in both regions were coeval, with indistinguishable ages of ~31 and ~30 Ma obtained from Ethiopia and Yemen, respectively.

The flood basalt sequence found in Yemen shows features very analogous to its Ethiopian counterpart, such as a mafic rock dominated bimodal distribution of volcanic products, and a maximum sequence of ~2000 m overlying a lateritized Mesozoic sedimentary rock (Coulie et al., 2003). The conventional K/Ar ages constrained the CFV between 30 and 26 Ma (Civetta et al., 1978). Felsic volcanism commenced 1 My after the peak flood basalt activities throughout Yemen, while the flood basalts ended between 26.9 and 26.5 Ma (Coulie et al., 2003, and references therein). The CFV in Yemen apparently closed down during the crustal stretching in the region, which instinctively should have provoked further outpouring of magma through decompression melting (Baker et al., 1996). Where as crustal stretching in Afar appears to have caused a further eruption of volcanic products at ~20 Ma (Baker et al., 1996).

The Ethiopian and Yemenite flood basalts are supposed to be the oldest volcanic markers of Afar breakup and are found on the western, northern, and northeastern topographic margins of the Afar Depression (Audin et al., 2004) (Fig. 2.8). Before rifting along the Red Sea, these two volcanic regions were continuous and extensive magmatic province with an initial volume of ~1 million km^3 (Courtillot et al., 1999). Today, after intense erosion for the last 30 My, the quantity of the preserved flood basalts and associated volcanic rocks is estimated to account about only a thirds of its pre-erosion volume with a surface area of 600,000 km^2 (Baker et al., 1972; Mohr, 1983). About 90% of the current volume forms the Ethiopian plateau basalts, and the remaining 10% the Yemen part (Baker et al., 1996). The much greater volume (>350 000 km^3; Mohr, 1983), and shorter duration (2–5 My) of the central– to northern Ethiopian and Yemenite traps result in higher eruption rates of between 0.15 and 0.06 km^3 yr^{-1}, considerably greater than those in Kenya and southern Ethiopia (George et al., 1998). Instead, these values are similar to eruption rates in Afar (0.08 km^3 yr^{-1}), the current focus of volcanism related to the Afar plume (George et al., 1998).

The traditional system of classification of the Ethiopian CFB province, which encompasses the Ashangi, Aiba, and Alaji formations (stages 1–3) was explained by (Mohr, 1983; Berhe et al., 1987). The Ashangi and Aiba formations are characterized by transitional– tholeiitic basalts commonly found with interbedded felsics and pyroclastic products towards

its top (Coulie et al., 2003). However, this classification was more local and not supported by any geochemical analysis. Then, Pik et al. (1998, 1999) introduced a geochemical classification for the northwestern Ethiopian flood basalts. These flood basalts have been subdivided into three magma groups, the low-Ti (LT) and two high-Ti groups (HT1 and HT2) (Fig. 2.8; Pik et al., 1998). The flood basalts are defined on the basis of incompatible trace element and TiO_2 concentrations (Rogers, 2006). The LT rocks are confined to the northwestern part of the volcanic province (Fig. 2.8). The HT (HT1 and HT2) basalts with elevated incompatible trace element contents and more fractionated REE patterns are found to the south, southeast and east of the volcanic province (Pik et al., 1998).
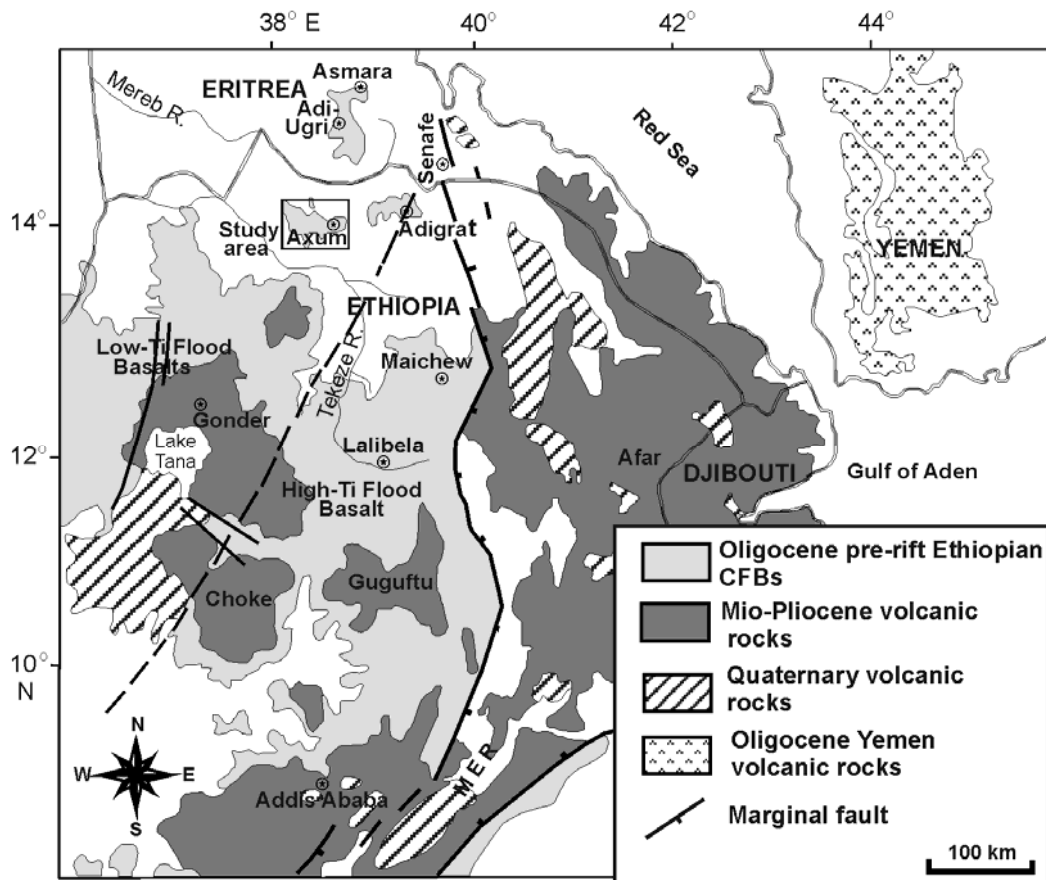
Figure 2.8 Sketch map of the central, northwestern, and northern parts of the Ethiopian and Yemen flood basalt province and the Afar triple junction. The dashed line divides the high-Ti and low-Ti basalt province (modified after Pik et al., 1998; and Küster et al., 2005).

Soon after the northwestern Ethiopian flood basalt deposition, a number of large central/shield volcanoes developed sporadically from 23 Ma to about 10 Ma on the surface of the flood basalts (Fig. 2.8; Kieffer et al., 2004; Corti, 2009). The basal diameter of these less voluminous shields range from 50 to 100 km and forms the highest mountains in northern Ethiopia, the 4533 m high peak of Ras Dashan (Kieffer et al., 2004). The deposition of these prominent central volcanoes above the fissure-fed flood basalts, together with a distinct

magmatic composition within the province and an incorporation of high amount of felsic lavas and pyroclastic products, distinguishes the Ethiopian volcanic province from other typical flood basalt provinces (e.g., Parana, Deccan), which are characterized by thick homogeneous series, continuous, sub-horizontal flows of oceanic-type basalts without overlying shield volcanoes (Corti, 2009).

2.5.3 *The Afar Depression Volcanism*

Magmatic activities in the Afar Depression commenced ~4 My after the peak volcanism in the Ethiopian plateau. The Adolei basaltic series, oldest volcanic formation recorded within the Afar Depression, erupted during the late Oligocene–early Miocene, from 27–20 Ma (Audin et al., 2004). They are commonly deposited in the form of dykes with variable orientations that intrude the sedimentary basement rocks of the eastern tectonic domain of the depression (Black et al., 1975). Silicic volcanics in the depression are mainly associated with the shield and composite volcanoes of the area. The origin of these silicic extrusive rocks (i.e., trachytes and rhyolites) in the Afar is attributed to fractional crystallization (FC) of basaltic magmas with no or little crustal contamination (Gibson, 1972; Barberi et al., 1975; Ayalew et al., 2002).

The Mabla series, still minor in the depression, deposited from 25–12 Ma around the eastern tectonic zone of the depression (Ali Sabieh block) and consists of basaltic lava flows, rhyolitic dykes, and some trachytic layers (Zumbo et al., 1995; Audin et al., 2004). Recent volcanism (Pleistocene–Quaternary) is mainly confined to the active tectonic and magmatic segments within the embryonic spreading centers in Afar, and axial zones of MER (e.g, Vidal et al., 1991; Boccaletti et al., 1998; Yirgu et al., 2006). Thus, the Afar Depression has experienced a 30 My history of mafic, felsic and pyroclastic volcanism since Oligocene, with the voluminous eruptions (i.e., Stratoid series) tied with the initiation of seafloor spreading in the Gulf of Aden and Red Sea (Yirgu et al., 2006).

Magmatic activities have been bimodal in Afar Depression at least for the last 4 My, but with basaltic rocks predominating over silicic products (Lahitte et al., 2003b). The silicic shield volcanoes (ignimbrites to pantellerites) emerge locally from the upper part of the Stratoid series and some younger volcanic formations (Lahitte et al., 2003a, and references therein). In the northern Afar Depression, zone of active extensional deformation, magmatim is marked by bunches of volcanic edifices and extensive fissure-fed transitional–tholeiitic basalt (Corti, 2009). These axial range basalts, which are the replica of the mid oceanic ridge basalts (Barberi et al., 1972), are also called the 'Aden Series' basalts.

The Afar Stratoid series with an aerial exposure of ~55,000 km^2 covers approximately two-thirds of the low-lying Afar Depression and has been dated at 3.5–0.6 Ma (Thurmond et al., 2006). This series consists largely of fissure-fed trap-like basaltic flows and significant proportion of interbedded felsic lavas (Thurmond et al., 2006). This important volcanic deposit in the central and northern Afar Depression, both in volume and surface area, is not found within the eastern part of the depression (Audin et al., 2004). Towards the axial zone, the Stratoid series is gradually substituted by the youngest transitional–tholeiitic basalt called the 'Erta'Ale axial range basalts'.

The Erta'Ale Range, in the Danakil Depression, is one of the volcano-tectonically active segments of the EARS. The range is composed of seven shield volcanoes that are aligned parallel to NNW-SSE–trending Red Sea rift. These are from south to north Hayli Gub, AleBagu, Erta'Ale, Borale'Ale, Dalaffilla, Alu, and Gada'Ale (Barrat et al., 1998). Erta'Ale, the only active shield volcano in the region, is ~60-km-long and 30-km-wide and rises nearly 700 m above the low-lands of the Danakil Depression (Barberi et al., 1972; Oppenheimer and Francis, 1997). At the summit of the shield volcano, there are two active craters that have been erupting lavas continuously for the last 100 years (Thurmond et al., 2006).

The Erta'Ale Range basalts, derived from the modern Afar plume, have slightly lower Sr isotopic composition than the Oligocene Ethiopian HT flood basalts, although the Nd isotopic compositions of these two magma series overlap (Furman et al., 2004). It could be deduced that the plume tail undergoing melting is now compositionally different from the plume head that gave-rise to the production of HT basalts (Furman et al., 2004). Compositionally, the Afar Depression basalts are dominated by transitional-tholeiites, falling within the subalkaline field/olivine tholeiites (Rogers, 2006). This characteristic extends to the Ethiopian HT flood basalts, making them unusual amongst other flood basalt provinces generally which are most frequently quartz-normative tholeiites (Rogers, 2006).

Now, an important question remains: Are both Oligocene Ethiopian HT flood basalts and Quaternary Afar Depression basalts related to a single long-lived plume? (Furman et al., 2004).

References:

Abbate E., Passerini P., and Zan L. 1995. Strike-slip faults in a rift area: A transect in the Afar Triangle, east Africa. Tectonophysics 241, 67–97.

Acocella V., Korme T., and Salvini F. 2003. Formation of normal faults along the axial zone of the Ethiopian rift. Journal of Structural Geology 25, 503–513.

Almond D.C. 1986. Geologic evolution of the Afro- Arabian dome. Tectonophysics 131, 301–332.

Amelung F., Oppenheimer C., Segall P., and Zebker H. 2000. Ground deformation near Gada'Ale volcano, Afar, observed by radar interferometry. Geophysical Research Letters 27, 3093–3096.

Audin L., Quidelleur X., Coulie E., Courtillot V., Gilder S., Manighetti I., Gillot P. Y., Tapponnier P., and Kidane T. 2004. Palaeomagnetism and K-Ar and ^{40}Ar/^{39}Ar ages in the Ali Sabieh area (Republic of Djibouti and Ethiopia): constraints on the mechanism of Aden ridge propagation into southeastern Afar during the last 10 Myr. Geophysical Journal International 158, 327–345.

Ayalew D., Barbey P., Marty B., Reisberg L., Yirgu G., and Pik R. 2002. Source, genesis and timing of giant ignimbrite deposits associated with Ethiopian continental flood basalts. Geochimica et Cosmochimica Acta 66, 1429–1448.

Baker B. H. 1987. Outline of the petrology of the Kenya rift alkaline province. In: Fitton J. G. and Upton B. G. J. (Eds.), Alkaline igneous rocks. Geological Society, London. Special Publication 30, 293–311.

Baker B.H., Mohr P.A., and Williams L.A.J. 1972. Geology of the eastern rift system of Africa. Geological Society America, Special Paper 136, 1–67.

Baker J., Snee L., and Menzies M. 1996. A brief Oligocene period of flood volcanism in Yemen: implications for the duration and rate of continental flood volcanism at the Afro-Arabian triple junction. Earth and Planetary Science Letters 138, 39–55.

Barberi F. and Varet J. 1977. Volcanism of Afar: small-scale plate tectonics implication. Geological Society of America Bulletin 88, 1251–1266.

Barberi F., Tazieff H., and Varet J. 1972. Volcanism in the Afar Depression: its tectonic and magmatic significance. Tectonophysics 15, 19–29.

Barberi F., Ferrara G., Santacroce R., and Varet J. 1975. Structural evolution of the Afar triple junction. In: Pilger A. and Rösler A. (Eds.), Afar Depression of Ethiopia. Schweizerbart, (Inter-Union Commission on Geodynamics Scientific Report 14), Stuttgart, Germany, 38–54.

Barberi F., Civetta L., and Varet J. 1980. Sr Isotopic composition of Afar volcanics and its implication for mantle evolution. Earth and Planetary Science Letters 50, 247–259.

Barrat J.A., Fourcade S., Jahn B.M., Cheminee J.L., and Capdevila R. 1998. Isotope (Sr, Nd, Pb, O) and trace-element geochemistry of volcanics from the Erta'Ale Range (Ethiopia). Journal of Volcanology and Geothermal Research 80, 85–100.

Berhe S.M., Desta B., Nicoletti M., and Teferra M. 1987. Geology, geochronology and geodynamic implications of the Cenozoic magmatic province in W and SE Ethiopia, Journal of Geological Society, London, 144, 213–226.

Beyene A. and Abdelsalam M.G. 2005. Tectonics of the Afar Depression: A review and synthesis. Journal of African Earth Sciences 41, 41–59.

Bilham R., Bendick R., Larson K., Mohr P., Braun J., Tesfaye S., and Asfaw L. 1999. Secular and tidal strain across the Main Ethiopian Rift. Geophysical Research Letters 26, 2789–2792.

Black R., Morton W.H., and Hailu T. 1974. Early structure around the Afar triple junction. Nature 248, 496–497.

Black R., Morton W.H., and Rex D.C. 1975. Block tilting and volcanism within the Afar in the light of recent K/Ar age data. In: Pilger A. and Rösler A. (Eds.), Afar Depression of Ethiopia. Schweizerbart, (Inter-Union Commission on Geodynamics Scientific Report 14), Stuttgart, Germany, 296–300.

Boccaletti M., Bonini M., Mazzuoli R., Abebe B., Piccardi L., and Tortorici L. 1998. Quaternary oblique extensional tectonics in the Ethiopian Rift (Horn of Africa). Tectonophysics 287, 97–116.

Boccaletti M., Mazzuoli R., Bonini M., Trua T., and Abebe B. 1999. Plio-Quaternary volcanotectonic activity in the northern sector of the Main Ethiopian Rift; relationships with oblique rifting. Journal of African Earth Sciences 29, 679–698.

Bohannon R.G., Naeser C.W., Schmidt D.L., and Zimmermann R.A. 1989. The timing of uplift, volcanism, and rifting peripheral to the Red Sea; a case for passive rifting. Journal of Geophysical Research 94, 1683–1701.

Bonatti E. and Emiliani C. 1971. Final Desiccation of the Afar Rift, Ethiopia. Science 172, 468–469.

Bonini M., Corti G., Innocenti F., Manetti P., Mazzarini F., Abebe T., and Pecskay Z. 2005. Evolution of the Main Ethiopian Rift in the frame of Afar and Kenya rifts propagation. Tectonics 24, 1–21.

Bosworth, W. 1992. Mesozoic and early Tertiary rift tectonics in east Africa. Tectonophysics 209, 115–137.

Bosworth W., Huchon P., and McClay K. 2005. The Red Sea and Gulf of Aden Basins. Journal of African Earth Sciences 43, 334–378.

Bott W., Smith B., Oakes G., Sikander A., and Ibrahim A. 1992. The tectonic framework and regional hydrocarbon prospectivity of the Gulf of Aden. Journal of Petroleum Geology 15, 211–243.

Casey M., Ebinger C.J., Keir D., Gloaguen R., and Mohamad F. 2006. Strain accommodation in transitional rifts: extension by magma intrusion and faulting in Ethiopian rift magmatic segments. In: Yirgu G., Ebinger C.J., and Maguire P.K.H. (Eds.), The Afar Volcanic Province within the East African Rift System. Geological Society, London, Special Publication 259, 143–163.

Chernet T., Hart W.K., Aronson J.L., and Walter R.C. 1998. New age constraints on the timing of volcanism and tectonism in the Northern Main Ethiopian Rift–southern Afar transition zone (Ethiopia). Journal of Volcanology and Geothermal Research 80, 267–280.

Chorowicz J. 1992. The role of ancient structures in the genesis and evolution of the East African Rift. Société Géologique de France Bulletin 163, 217–227.

Chu D. and Gordon R.G. 1998. Current plate motions across the Red Sea: Geophysical Journal International 135, 313–328.

Civetta L., La Volpe L., and Lirer L. 1978. K-Ar age of the Yemen Plateau, Journal of Volcanology and Geothermal Research 4, 307–314.

CNR-CNRS (Afar team) 1973. Geology of Northern Afar (Ethiopia): Revue de Geographie Physique et de Geologie Dynamique, 15(2), 443–490.

Collet B., Taud H., Parrot J.F., Bonavia F., and Chorowicz J. 2000. A new kinematic approach for the Danakil Block using a digital elevation model representation. Tectonophysics 316, 343–357.

Corti G. 2009. Continental rift evolution: From rift initiation to incipient breakup in the Main Ethiopian Rift, East Africa. Earth Science Reviews 96, 1–53.

Coulié E., Quidelleur X., Gillot P.Y., Courtillot V., Lefèvre J.C., and Chiesa S. 2003. Comparative K-Ar and Ar/Ar dating of Ethiopian and Yemenite Oligocene volcanism: Implications for timing and duration of the Ethiopian Traps. Earth and planetary Science Letters 206, 477–492.

Courtillot V., Galdeano A., and Moeul J.L. 1980. Propagation of an accreting plate boundary: A discussion of new aeromagnetic data in the Gulf of Tadjuora and Southern Afar. Earth and Planetary Science Letters 47, 144–160.

Courtillot V., Achache J., Landre F., Bonhommet N., Montigny R., and Feraud G. 1984. Episodic spreading and rift propagation; new paleomagnetic and geochronologic data from the Afar nascent passive margin. Journal of Geophysical Research 89, 3315–3333.

Courtillot V., Armijo R., and Tapponnier P. 1987. Kinematics of the Sinai triple junction and a two-phase model of Arabia–Africa rifting continental extensional tectonics. Geological Society, London, Special Publications 28, 559–573.

Courtillot V., Jaupart C., Manighetti I., Tapponnier P., and Besse J. 1999. On causal links between flood basalts and continental breakup. Earth and Planetary Science Letters 166, 177–199.

Dixon T.H., Ivins E.R., and Franklin B.J. 1989. Topographic and volcanic asymmetry around the Red Sea: Constraints on rift models. Tectonics 8, 1193–1493.

Dugda M. and Nyblade A. 2006. New constraints on crustal structure in eastern Afar from the analysis of receiver functions and surface wave dispersion in Djibouty. In: Yirgu G., Ebinger C. J. and Maguire P. K. H. (Eds.), The Afar Volcanic Province within the East African Rift System. Geological Society, London, Special Publication 259, 239–253.

Dunbar J.A. and Sawyer D.S. 1989. Continental rifting at pre-existing lithospheric weaknesses. Nature 242, 565–571.

D'Acremont E., Leroy S., Beslier M.O., Bellahsen N., Fournier M., Robin C., Maia M., and Gente P. 2005. Structure and evolution of the eastern Gulf of Aden conjugate margins from seismic reflection data. Geophysical Journal International 160, 869–890.

Eagles G., Gloaguen R., and Ebinger C. 2002. Kinematics of the Danakil Microplate. Earth and Planetary Science Letters 203 607–620.

Ebinger C.J. and Hayward N.J. 1996. Soft plates and hotspots: views from Afar. Journal of Geophysical Research 101, 21,859–21,876.

Ebinger C. and Sleep N.H. 1998. Cenozoic magmatism in central and east Africa resulting from impact of one large plume. Nature 395, 788–791.

Ebinger C.J., Bechtel T.D., Forsyth D.W., and Bowin C.O. 1989. Effective elastic plate thicknesses beneath the East African and Afar domes. Journal of Geophysical Research 94, 2883–2990.

Ebinger C.J., Yemane T., WoldeGabriel G., Aronson J.L., and Walter R.C. 1993. Late Eocene–Recent volcanism and rifting in the southern main Ethiopian rift. Journal of the Geological Society, London 150, 99–108.

Fantozzi P.L. 1996. Transition from continental to oceanic rifting in the Gulf of Aden: structural evidence from field mapping in Somalia and Yemen. Tectonophysics 259, 285–311.

Furman T., Bryce J.G., Karson J., and Iotti A. 2004. East African Rift System (EARS) plume structure: insights from Quaternary mafic lavas of Turkana, Kenya. Journal of Petrology 45, 1069–1088.

Gass I.G. 1975. Magmatic and tectonic processes in the development of the Afro-Arabian Dome. In: Pilger A. and Rösler A. (Eds.), Afar Depression of Ethiopia. Schweizerbart, (Inter-Union Commission on Geodynamics Scientific Report 14), Stuttgart, Germany, 10–18.

George R.M. and Rogers N.W. 2002. Plume dynamics beneath the African plate inferred from the geochemistry of the Tertiary basalts of southern Ethiopia. Contributions to Mineralogy and Petrology 144, 286–304.

George R., Rogers N., and Kelly S. 1998. Earliest magmatism in Ethiopia: evidence for two mantle plumes in one flood basalt province. Geology 26, 923–926.

Gibson I. L. 1972. The chemistry and petrogenesis of a suite of pantellerites from the Ethiopian rift. Journal of Petrology 13, 31–44.

Gupta A. and Scholz C.H. 2000. Brittle strain regime transition in the Afar depression: Implications for fault growth and seafloor spreading. Geology 28, 1087–1090.

Hebert L. and Langston C.A. 1985. Crustal thickness estimate at AAE (Addis Ababa, Ethiopia) and NAI (Nairobi, Kenya) using teleseismic P-wave conversions. Tectonophysics 111, 299–327.

Hempton M.R. 1987. Constraints on Arabian Plate motion and extensional history of the Red Sea. Tectonics 6, 687–705.

Hendrie D. B., Kusznir N. J., Morley C. K., and Ebinger C. J., 1994. Cenozoic extension in Northern Kenya: A quantitative model of rift basin development in the Turkana region. Tectonophysics 236, 409–438.

Hirn A., Lépine J.C., and Sapine M. 1993. Triple junction and ridge hotspots: Earthquakes, faults, and volcanism in Afar, the Azores, and Iceland. Journal of Geophysical Research 98, 11995–12001.

Hofmann C., Courtillot V., Feraud G., Rochette P.,Yirgus G.,Ketefo E., and Pik R. 1997. Timing of the Ethiopian flood basalt event and implications for plume birth and global change. Nature 389, 838–841.

Hofstetter R. and Beyth M. 2003. The Afar Depression: interpretation of the 1960-2000 earthquakes. Geophysical Journal International 155, 715–732.

Kazmin V., Shifferaw A., Teffera M., Berhe S.M., and Chowaka S. 1979. Precambrian structures of western Ethiopia. Proceeding 5th Conferencc on African Geology, Annals of the Geological Survey of Egypt, Cairo 9, 1–8.

Kazmin V., Seife M.B., Nicoletti M., and Petrucciani C. 1980. Evolution of the northern part of the Ethiopian Rift. Geodynamic Evolution of the Afro-Arabian Rift System. Accademia Nazionale Dei Lincei, Atti dei Convegni Lincei 47, 275–292.

Keranen K. and Klemperer S.L. 2008. Discontinuous and diachronous evolution of the Main Ethiopian Rift: implications for the development of continental rifts. Earth and Planetary Science Letters 265, 96–111.

Kieffer B., Arndt N., Lapierre H., Bastien F., Bosch D., Pecher A., Yirgu G., Ayalew D., Weis D., Jerram A.D., Keller F., and Meugniot C. 2004. Flood and Shield basalts from Ethiopia: magmas from the African superswell. Journal of Petrology 45, 793–834.

Korme T., Acocella V., and Abebe B. 2004. The role of pre-existing structures in the origin, propagation and architecture of faults in the Main Ethiopian Rift. Gondwana Research 7, 467–479.

Küster D., Dwivedi S.B., Kabeto K., Mehary K., and Matheis G. 2005. Petrogenetic reconnaissance investigation of mafic sills associated with flood basalts, Mekelle basin, Northern Ethiopia: implication for Ni-Cu exploration. Journal of Geochemical Exploration 85, 63–79.

Lahitte P., Gillet P.Y., and Courtillot V. 2003a. Silicic central volcanoes as precursor to rift propagation: the Afar case. Earth and Planetary Science Letters 207, 103–116.

Lahitte P., Gillot P., Kidane T., Courtillot V., and Bekele A. 2003b. New age constraints on the timing of volcanism in central Afar, in the presence of propagating rifts. Journal of Geophysical Research, B 108, ECV 10.1–10.17.

Latin D., Norry M.J., and Tarzey R.J.E. 1993. Magmatism in the Gregory Rift, East Africa: evidence for melt generation by a plume. Journal of Petrology 34, 1007–1027.

Le Pichon X. and Francheteau J. 1978. A plate-tectonic analysis of the Red Sea–Gulf of Aden area. Tectonophysics 46, 369–406.

Macdonald R., Rogers N. W., Fitton J. G., Black S., and Smith M. 2001. Plume-lithosphere interactions in the generation of the basalts of the Kenya Rift, East Africa. Journal of Petrology 42, 877–900.

Maguire P.K.H., Keller G.R., Klemperer S.L., MacKenzie G.D., Keranen K., Harder S., O'Reilly B., Thybo H., Asfaw L., Khan M.A., and Amha M. 2006. Crustal structure of the

Northern Main Ethiopian Rift from the EAGLE controlled-source survey; a snapshot of incipient lithospheric breakup. In: Yirgu G., Ebinger C.J., and Maguire P.K.H. (Eds.), The Afar Volcanic Province within the East African Rift System. Geological Society, London, Special Publication 259, 269–292.

Makris J. and Ginzburg A. 1987. The Afar Depression; transition between continental rifting and sea-floor spreading. Tectonophysics 141, 199–214.

Makris J., Menzel H., Zimmermann J., and Gouin P. 1975. Gravity field and crustal structure of north Ethiopia. In: Pilger A. and Rösler A. (Eds.), Afar Depression of Ethiopia. Schweizerbart, (Inter-Union Commission on Geodynamics Scientific Report 14), Stuttgart, Germany, 135–144.

Manighetti I., Tapponnier P., Courtillot V., Gruszow S., and Gillot P.Y. 1997. Propagation of rifting along the Arabia Somalia plate boundary: The Gulf of Aden and Tadjoura. Journal of Geophysical Research 102, 2681–2710.

Manighetti I., Tapponnier P., Gillot P.Y., Jacques E., Courtillot V., Armijo R., Ruegg J.C., and King G. 1998. Propagation of rifting along the Arabia-Somalia plate boundary: Into Afar. Journal of Geophysical Research 103, 4947–4974.

Manighetti I., Tapponnier P., Courtillot V., Gallet Y., Jacques E., and Gillot P.Y. 2001. Strain transfer between disconnected, propagating rifts in Afar. Journal of geophysical Research 106, 13,613–13,665.

Marty B., Pik R., and Yirgu G. 1996. Helium isotopic variations in Ethiopian plume lavas: Nature of magmatic sources and limit on lower mantle contribution, Earth and Planetary Science Letters 144, 223–237.

Menzies M.A., Baker J., Bosence D., Dart C., Davison I., Hurford A., Al-Kadasi M., McClay K., Nichols G., Al-Subbary A.,Yelland A. 1992. In: Storey B.C., Alabaster T., and Pankhurst R.J. (Eds.), Magmatism and the Causes of Continental Breakup. Geological Society Special Publications 68, 293–304.

Menzies M., Gallagher K., Yelland A., and Hurford A. 1997. Volcanic and non-volcanic rifted margins of the Red Sea and Gulf of Aden. Geochimica et Cosmochimica Acta 61, 2511–2527.

Meyer W., Pilger A., Rosler A., and Stets J. 1975. Tectonic evolution of the northern part of the Main Ethiopian Rift in Southern Ethiopia. In: Pilger A. and Rösler A. (Eds.), Afar Depression of Ethiopia. Schweizerbart, (Inter-Union Commission on Geodynamics Scientific Report 14), Stuttgart, Germany, 352–362.

Mickus K., Tadesse K., Keller G., and Oluma B., 2007. Gravity analysis of the Main Ethiopian Rift. Journal of African Earth Sciences 48, 59–69.

Mohr P. 1962. The Ethiopian Rift System. Bulletin of the Geophysical Observatory of Addis Ababa 5, 33–62.

Mohr P. 1967. The Ethiopian Rift System: Bulletin of the Geophysical Observatory, Haile Selassie I University 11, 1–65.

Mohr, P., 1968, Transcurrent faulting in the Ethiopian Rift System. Nature 218, 938–941.

Mohr P. 1972. Surface structure and plate tectonics of Afar. Tectonophysics 15, 3–18.

Mohr P. 1983. Ethiopian flood basalt province. Nature 303, 577–584.

Mohr P.A. and Wood C.A. 1976. Volcano spacing and lithospheric attenuation in the Eastern Rift of Africa. Earth and Planetary Science Letters 33, 126–144.

Mohr P., Girnius A., and Rolff J. 1978. Present-day strain rates at the northern end of the Ethiopian Rift. Tectonophysics 44, 141–160.

Morton W.H. and Black R. 1975. Crustal attenuation in Afar. In: Pilger A. and Rösler A. (Eds.), Afar Depression of Ethiopia. Schweizerbart, (Inter-Union Commission on Geodynamics Scientific Report 14), Stuttgart, Germany, 55–61.

Omar G. I. and Steckler M. S. 1995. Fission track evidence on the initial rifting of the Red Sea: two pulses, no propagation. Science 270, 1,341–1,344.

Oppenheimer C. and Francis P. 1997. Remote sensing of heat, lava and fumarole emissions from Erta'Ale volcano, Ethiopia. International Journal of Remote Sensing 18, 1661–1692.

Pik R., Deniel C., Coulon C., Yirgu G, Hofmann C., and Ayalew D. 1998. The northwestern Ethiopian Plateau flood basalts: Classification and spatial distribution of magma types. Journal of Volcanology and Geothermal Research 81, 91–111.

Pik R., Deniel C., Coulon C., Yirgu G., and Marty B. 1999. Isotopic and trace element signatures of Ethiopian flood basalts: Evidence for plume-lithosphere interactions. Geochimica Cosmochimica Acta 63, 2263–2279.

Purcell P.G. 1976. The Marda Fault Zone, Ethiopia. Nature 261, 569–571.

Redfield T.F., Wheeler W.H., and Often M. 2003. Kinematic model for the development of the Afar Depression and its paleogeographic implications. Earth and Planetary Science Letters 216, 383–398.

Richards M. A., Duncan R. A., and Courtillot V. E. 1989. Flood basalts and hotspot tracks: Plume heads and tails. Science 246, 103–107.

Ring U. 1994. The influence of preexisting structure on the evolution of the Cenozoic Malawi rift (east African rift system). Tectonics 12, 313–326.

Rogers N.W. 2006. Basaltic magmatism and the geodynamics of the East African Rift System. In: Yirgu G., Ebinger C.J., and Maguire P.K.H. (Eds.), The Afar Volcanic Province within the East African Rift System. Geological Society, London, Special Publication 259, 77–93.

Rogers N., Macdonald R., Fitton J. G., George R., Smith M., and Barreiro B. 2000. Two mantle plumes beneath the East African rift system: Sr, Nd and Pb isotope evidence from Kenya Rift basalts. Earth and Planetary Science Letters 176, 387–400.

Rooney T., Furman T., Bastow I., Ayalew D., and Yirgu G. 2007. Lithospheric modification during crustal extension in the Main Ethiopian Rift. Journal of Geophysical Research 112, 21 pp.

Rosendahl B. 1987. Architecture of continental rifts with special reference to east Africa. Annual Reviews Earth and Planetary Science 15, 445–503.

Searle R.C. and Gouin P. 1972. A gravity survey of the central part of the Ethiopian Rift Valley. Tectonophysics 15, 41–52.

Schilling J.G., Kingsley R.H., Hanan B.B., and McCully B.L. 1992. Nd–Sr–Pb isotopic variations along the Gulf of Aden; evidence for Afar mantle plume-continental lithosphere interaction. Journal of Geophysical Research 97, 10,927–10,966.

Sichler B., 1980. La biellette Danakile; un modéle pour l'évolution géodynamique de l'Afar Colloque rift d'Asal. Reunion extraordinaire de la Societe Geologique de France. Bulletin de la Societe Geologique de France 22, 925–932.

Souriot T. and Brun J.P. 1992. Faulting and block rotation in the Afar triangle, East Africa; the Danakil ''crank-arm'' model. Geology 20, 911–914.

Stewart K. and Rogers N.W. 1996. Mantle plume and lithosphere contributions to basalts from southern Ethiopia. Earth and Planetary Science Letters 139, 195–211.

Stuart G.W., Bastow I.D., and Ebinger C.J. 2006. Crustal Structure of the Northern Main Ethiopian Rift from receiver function studies. In: Yirgu G., Ebinger C.J., and Maguire P.K.H. (Eds.), The Afar Volcanic Province within the East African Rift System. Geological Society, London, Special Publication 259, 253–267.

Tamsett D. and Searle R. 1990. Structure of the Alula Fartak Fracture Zone, Gulf of Aden. Journal of geophysical Research 95, 1239–1254.

Tesfaye S., Harding D.J., and Kusky T. 2003. Early continental breakup boundary and migration of the Afar Triple Junction, Ethiopia: Geological Society of America Bulletin 115, 1053–1067.

Thurmond A. K., Abdelsalam M. G., and Thurmond J. B. 2006. Optical-radar-DEM remote sensing data integration for geological mapping in the Afar Depression, Ethiopia. Journal of African Earth Sciences 44, 119–134.

Ukstins I., Renne P., Wolfenden E., Baker J., Ayalew D., and Menzies M.A. 2002. Matching conjugate volcanic rifted margins: ^{40}Ar/^{39}Ar chronostratigraphy of pre- and syn-rift bimodal flood volcanism in Ethiopia and Yemen. Earth and Planetary Science Letters 198, 289–306.

Varet J. and Gasse F. 1978. Geology of central and southern Afar (Ethiopia and Djibouti Republic). Editions du Centre National de la Recherche Scientifique, Report, Paris, 124 pp., and map, scale 1:500,000.

Vellutini P. 1990. The Manda-Inakir Rift, Republic of Djibouti: a comparison with the Asal Rift and its geodynamic interpretation. Tectonophysics 172, 141–153.

Vidal P., Deniel C., Vellutini P.J., Piguet P., Coulon C., Vincent J., and Audin J. 1991. Changes of mantle sources in the course of rift evolution: the Afar case. Geophysical Research Letters 18, 1913–1916.

Watchorn F., Nichols G., and Bosence D. 1998. Rift-related sedimentation and stratigraphy, southern Yemen (Gulf of Aden). In: Purser B. and Bosence D. (Eds.), Sedimentary and Tectonic Evolution of Rift Basins. Chapman and Hall, London, 165–189.

White R. S. and McKenzie D. P. 1995. Magmatism at rift zones: The generation of continental margins and flood basalts. Journal of Geophysical Research 94, 7685–7729.

Wolfenden E., Ebinger C., Yirgu G., Deino A., and Ayale D. 2004. Evolution of the Northern Main Ethiopian rift: birth of a triple junction. Earth and Planetary Science Letters 224, 213–228.

Wolfenden E., Ebinger C., Yirgu G., Renne P., and Kelley S.P. 2005. Evolution of the southern Red Sea rift: birth of a magmatic margin. Geological Society of America Bulletin 117, 846–864.

Wright T.J., Ebinger C., Biggs J., Ayele A., Yirgu G., Keir D., and Stork A. 2006. Magma-maintained rift segmentation at continental rupture in the 2005 Afar dyking episode. Nature 442, 294–297.

Yirgu G., Ebinger C.J., and Maguire P.K.H. (Eds.), 2006. The Afar Volcanic Province within the East African Rift System. Geological Society, London, Special Publication 259, 1–6.

Zumbo V., Féraud G., Vellutini P., Piguet P., and Vincent J. 1995. First 40Ar/39Ar dating on Early Pliocene to Plio-Pleistocene magamatic events of the Afar-Republic of Djibouti. Journal of Volcanology and Geothermal Research 65, 281–295.

CHAPTER 3

CHAPTER 3: METHODOLOGY

'Hostile environment' is an expression tailor-made for the Afar Depression (Waltham, 2005). The region is an awful, extremely hot and barren desert covered by fresh basaltic lavas and sediments. In winter, daily temperatures are between 33 and 44 °C; summer commonly reaches shade temperatures of >50 °C in the northern part of the depression (Dallol Depression), the deepest continental landmass in the EARS. Extended fieldwork is very difficult in the Afar Depression. Despite all these challenges, the Afar is a naturally made laboratory for volcanologists, structural geologists, sedimentologists, and anthropologists. To alleviate the aforementioned problems, we used both direct and indirect ways of observations.

For the study of this PhD work, quite large numbers of techniques were applied. Before and after the fieldwork, digital image processing techniques were used to prepare basemap, geological and structural maps. For the study of petrography, a variety of analytical methods, from the traditional once (i.e., optical microscopy) to more advanced high precision analytical methods (i.e., electron microprobe, EMP) were used. For the study of whole rock chemistry, instrumental neutron activation analysis (INAA), X-ray fluorescence (XRF) spectrometry, and thermal ionization mass spectrometry (TIMS) were applied. An overview of the different techniques used for this thesis is provided in the following sections:

3.1 Digital Image Processing Technique

Digital image processing is the use of computer applications to perform different processing techniques on raw digital images. The main inputs for this processing technique were partially processed Landsat-TM and ETM images. All Landsat data are obtained from the archive of Mekelle University-Inter University Cooperation (MU-IUC) project. The Thematic Mapper (TM) and Enhanced Thematic Mapper (ETM) sensors are highly advanced, multichannel scanning devices designed to acquire high resolution image, improved geometric fidelity, sharper spectral separation, and greater radiometric resolution than the older Multi Spectral Scanner (MSS) sensors (Muzein, 2006). The TM and ETM sensors with their six compatible multispectral bands and one thermal infrared band (having a spectral resolution of 60 m) are capable of providing more spectral information. They also have higher radiometric resolution (detail visibility of images) as the data are acquired in 8 bits (or 0–255 levels).

3.1.1 Radiometric and Atmospheric Correction

All ground objects are characterized by their specific characteristics of absorption, reflection, and emission properties. These properties are the basic entities of all objects that have to be properly documented and processed during image processing techniques. In experimental works, it is relatively straightforward to compute the amount of reflectance of an object because one can easily measure the intensity of interference free radiation when it reaches the target material (Markam and Barker, 1986). Most laboratory based experiments in remote sensing are well controlled and there is no much energy loss between the energy source and the target or the target and the sensor. In the actual remote sensing applications, however, the light - object interaction is complicated. It is only possible to know the intensity of the light before it penetrates the atmosphere but as it crosses the atmosphere, it interacts with atmospheric constituents (i.e., water vapor, CO_2, dust, fog) and appreciably alters the signal before and after interacting with the target (Muzein, 2006, and references therein). The energy interaction with atmospheric constituents before and after reaching the target area produces disturbance/haze in the digital image. Different methods are now used for atmospheric correction, but the one we applied in this work was the *dark object subtraction method*.

The dark object subtraction method works based on the assumption that in every scene (full image) there should be at least a small area completely made of dark pixels (i.e., with 0% reflectance). These areas correspond to deep and clear water bodies and deep shadows that theoretically have no reflectance from their surfaces, however, because of the atmospheric haze, they record non-zero values. This characteristic is used in empirically computing the haze component. The minimum digital number (DN) value recorded in the pixels of dark objects is taken as a noise and is subtracted from all other pixel values in the entire image. Path radiance has no effect in the Short-Wave InfraRed (SWIR) bands and these bands are not normally corrected.

3.1.2 Image Filtering

The purpose of image filtering is to make the digital images more understandable and interpretable by enhancing information of interest (i.e., area of interest should become better discernible). This technique is carried out by using kernels, also called boxes or filter weight matrices. A kernel consists of an array of odd number square matrix. In order to compute the new DN values of an image, it is expected that the kernel is superimposed over the old image-data array. The original DN values are weighted by the overlying coefficients in the

kernel and the resulting total DN value is ascribed to the central pixel in the new image. The kernel is successively moved over all the old image pixels, in rows and columns, and the array of new DNs calculated.

3.2 Sampling

3.2.1 Selection of samples

A total of 175 samples, each weighing slightly less than a kg, were collected from three volcano-tectonically distinct areas in the northern Afar. One hundred and twelve (112) rock samples were collected from the Axum volcanics, the northern part of the Ethiopian trap basalt, in December 2006 and April 2007. Fifty (50) rock samples were collected from the axial zone of the northern Afar Depression (Danakil Depression) in December 2008 and thirteen (13) rock samples were collected from the marginal areas that connect the plateau basalts from the rift basalts in February 2009. Thirty three (33) representative samples were carefully selected from the 112 samples of the Axum volcanics and set for the petrographic and geochemical sample preparations during the first phase of analysis (see chapters five and six for detail). During the second phase of sample preparation, a total of fifty (50) representative rock samples from the axial and marginal areas of Afar volcanics were selected and put for petrographic and geochemical (XRF and INAA) analyses. Moreover, 15 and 6 representative samples were selected for the Sr-Nd isotope and electron microprobe analyses, respectively (Table 7.2 and appendix 2).

3.2.2 Sample Preparation

Fresh and unaltered rock samples, weighing 100 to 150 g, were first wrapped in a polyethylene and manually crushed by a hammer and then finely crushed and homogenized in a stainless steel jaw crusher (Fig. 3.4a). The first batch of samples (from the Axum volcanics), each sample weighing ~45–60 g, were powdered in a mechanical agate mill, and the second batch of samples (from Erta'Ale Range and marginal volcanics), each sample weighing ~90–120 g, in a vibratory disk mill of zirconium oxide for the bulk chemical (XRF and INAA) analyses (Fig. 3.4b and c). Special care was given to avoid cross contamination during crushing and milling. Moreover, all the samples were finely powdered for the pressed pellets. The full results of INAA and XRF analyses are reported as tables in each of the relevant chapters (chapters 5, 6 and 7).

Petrographic thin-sections were also prepared for 62 samples from each of the basaltic, trachytic, and phonolitic rocks, and detailed mineralogical analyses were made under an

optical (petrographic) microscope. For some of the minerals, the semiquantitative modes were determined by visually estimating the mineral proportions in thin sections.

Figure 3.1 Powdering machines of the Department of Lithospheric Research: (a) Jaw crusher; (b) Mechanical agate mill, and (c) Vibratory disk mill.

3.3 Analytical Methods

3.3.1 X-ray Fluorescence (XRF) spectrometry

X-ray fluorescence (XRF) spectrometry is a non-destructive and widely available analytical technique used to determine the concentrations of elements present in all states. The concentrations of major oxides (SiO_2, TiO_2, Al_2O_3, Fe_2O_3, MnO, MgO, CaO, Na_2O, K_2O, and P_2O_5) and minor elements heavier than F (Sc, V, Cr, Cu, Ni, Zn), as well as some trace and rare earth elements can be determined using this accurate technique. Elements with low atomic number favor Auger electron emission and, therefore, XRF is not a very accurate technique for light elements having less than 10 atomic number. In XRF spectrometry, the atoms of the samples were irradiated with high-energy X-ray photons emitted from an X-ray tube. The primary X-ray photons, when interacting with a sample, can drive out electrons from orbitals (commonly K or L) near the nucleus of an atom. When this process occurs, the resulting vacant positions are refilled by electrons coming from the higher energy levels; a process which is accompanied by the emission of secondary X-rays (characteristic or

fluorescence X-rays). These rays, which have energies equivalent to the difference of the two energy levels, are characteristics of specific elements.

A simple XRF spectrometer can be schematically represented by an X-ray tube, a sample holder, a primary collimator, an analyzing crystal, a secondary collimator, and a detector (Fig. 3.2). The characteristic X-rays emanated from the sample are collimated to a parallel beam and then spectrally splitted, with an analyzing crystal to a spectrum. The diffracted X-rays are collimated again and only a parallel beam of the secondary X-rays reaching the detector are detected (Fig. 3.2). The main aim of both collimators is to parallelize the radiations before and after the analyzing crystal. The secondary collimator and the detector, attached to the analyzing crystal, turn around the rotation axis of the crystal. Such process, which regulates the rotation angle of the system, is called a goniometer. Not all secondary X-rays are directed to the detector; only a portion of these X-rays with wavelength (λ) rewarding the Bragg equation ($n\lambda = 2d \sin\theta$) are redirect from the analyzing crystal and collimated again and detected. In the Bragg equation, n is an integer, θ is the Bragg angle, and d is the lattice spacing of the analyzing crystal (Ferriére, 2008, and references therein).
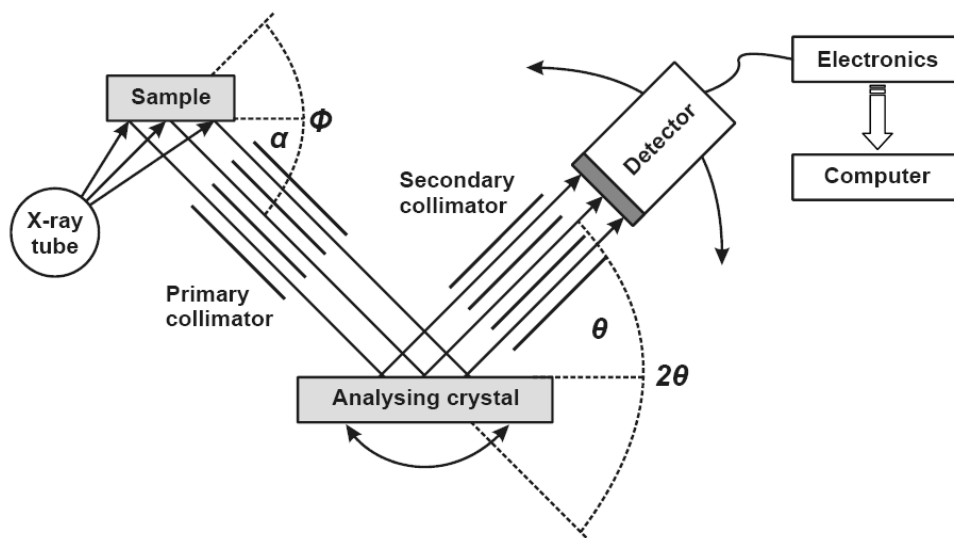
Figure 3.2 Schematic diagram of a simplified XRF spectrometer (after Gill, 1997).

The basis of the XRF analytical techniques for geological materials at the University of Vienna follows well-proven conventional methods with slight modifications resulting from the availability of the spectrometer and the accompanying and specially developed supplementary software. Sample powders were prepared in two different forms: as a glass bead made from sample powder fused with lithium metaborate or tetraborate for major element oxide (SiO_2, TiO_2, Al_2O_3, Fe_2O_3, MnO, MgO, CaO, Na_2O, K_2O, and P_2O_5) analysis,

and as a pressed powder disc for trace element (V, Cr, Co, Ni, Cu, Zn, Ga, Rb, Sr, Y, Zr, Nb, and Ba) analysis. Samples were measured with a Philips PW 2400 XRF spectrometer.

3.3.1.1 Data Processing

The quantitative measurement of the intensity of samples is compared with the intensity of reference standards to quantify the results. Internationally certified rock reference materials of different compositions (i.e., Serpentine UB-N, Granite GSR-1, Andesite GSR-2, Basalt GSR-3, Sandstone GSR-4, Shale GSR-5, Limestone GSR-6) were used as control samples. The precision of the measurements is evaluated with the help of monitoring samples, which confirms instrument stability and pledges reproducibility and repeatability. The intensities of the geostandards help to establish the calibration curve for each element. However, the correlation between the net count rate and the concentration is linear only for a limited concentration range, as there are some variations due to interelement effects (Bartosova, 2010). Accordingly, corrections have to be applied to reduce the matrix effects. For the trace element analysis, accurate background and line overlap corrected net peak intensities are important (Bartosova, 2010).

3.3.1.2 Sample Preparation for XRF Measurement

Approximately 15 g of sample powder was required for the XRF analysis. About 5 g and 10 g of the sample were used for the preparation of fused bead and pressed pellet, respectively. Preparation of both the fused bead and pressed pellet require careful and accurate measurements.

The XRF analysis for major elements started first by determining the loss on ignition (LOI). First a porcelain crucible was heated at 1050°C and cooled to room temperature. The weight of the empty crucible was recorded and approximately 5 g of the rock powder was added to the crucible. The sample was placed in an oven, heated at 110°C for >10 hours and cooled. The sample was placed in a muffle furnace and heated at 950°C for ~3 hours and then cooled. The basic principle of LOI is measuring of weight loss of a sample after heating at ~950°C. The loss on ignition (LOI) can be then calculated using the following formula:

LOI = [(pre heated weight – heated weight)*100]/ pre heated weight

Fused bead preparation (major elements: 1.2 g of the previously calcined/heated sample powder was weighed into a porcelain mould, and then 6.0 g of dilithium tetraborate was added with a ratio of exactly 1:5 (1 sample : 5 lithium tetraborate). Both powders were homogenized before the mixture was poured into a platinum crucible. Additionally 3 drops of

an aqueous LiBr$_2$-solution as a non-wetting agent were added and the production of a fused bead was done using a programmed PHILIPS Perl'x3 automatic bead machine.

Pressed pellet preparation (Trace elements): 0.5 ml of a polyvinyl alcohol solution was added to approximately 10 g of the non-ignited/non-heated rock powder and then well mixed. After the mixture was filled into a press tool with 40 mm diameter; the powder was gently tapped down using a glass rod, before the tight-fitting steel die was inserted. The sample was pressed to circa 16 tons/cm^2 in a hydraulic press and dried in an oven over the night at 70°C. See Nagl P. (Univ. Vienna written com. 2009).

References used for section 3.3.1: Potts (1987), Vandecasteele and Block (1993), Gill (1997), Jenkins (1999), Ferrière (2008), Bartosova (2010), P. Nagl (Univ. Vienna, written com., 2009).

3.3.2 Instrumental Neutron Activation Analysis (INAA)

Instrumental neutron activation analysis (INAA) is a sensitive multi-element analytical technique used to determine the concentration of trace, minor and some major elements. This non-destructive technique can determine the concentrations of more than 40 elements simultaneously with high precision.

The basic principle of INAA is to produce short-lived radioactive isotopes by bombarding the atoms with a high flux of neutrons in a nuclear reactor. In a neutron capture reaction, a naturally occurring stable isotope is transformed into a short-lived radioactive isotope. These isotopes then decay mostly by β-decay combined with the emission of a photon (X-ray or γ–ray) (Fig. 3.3). The energies of the emitted γ-rays are characteristic for a particular isotope. The intensities of the radiation (γ–ray) emitted from the target material quantify the amount of the isotopes present. As all the radio-active isotopes do not have uniform half-lives, counting is done in three cycles: the first cycle for the extremely short-lived once (e.g., Na, K, Br), second cycle for the moderately short-live (e.g., REE), and third cycle for the relatively long-lived isotopes (Co, Cs, Gd). Finally, computational work of the elements is achieved by comparing the different γ-spectra with spectra of at least three reference materials that are irradiated and measured together with the samples. Note that INAA computes the concentrations of isotopes, but because isotopic abundances of most high atomic number elements are constant in natural materials, isotopic abundance is readily translated to elemental abundances.
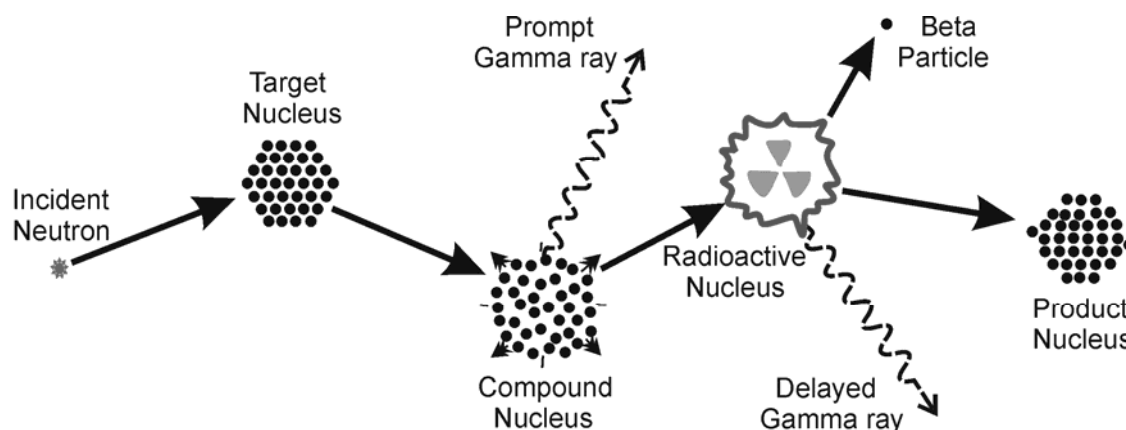
Figure 3.3 Diagram illustrating the process of neutron capture by a target nucleus followed by the emission of gamma rays (http://www.ne.ncsu.edu/nrp/naa.html).

3.3.2.1 Fundamental Principles

Nowadays, different sources can be used for irradiation of samples with neutrons, such as nuclear reactors, radioisotopic emitters, or accelerators, but nuclear reactors (commonly using neutrons from ^{235}U fission) are frequently used in INAA. The Departement of Lithospheric Research, University of Vienna irradiated our samples in the 250 kW TRIGA Mark II reactor (at the Atominstitut der Österreichischen Universitäten, Vienna).

For this analysis, normally thermal neutrons, with low energies (<0.5 eV), are used. One important value during irradiation is the quantification of the neutron capture cross section (σ). It quantifies the probability of the interaction a neutron with a target nuclide. The neutron capture cross section is a function of the neutron energy. It is commonly smaller for epithermal neutrons compared to thermal neutrons. The activity for a particular radionuclide, at any time t during an irradiation, can be calculated from the following equation:

$$A_t = \sigma_{act}\varphi N(1 - e^{-\lambda t})$$

Where At = the activity of radionuclide per unit time, σact = the neutron capture cross-section, φ = the neutron flux (usually given in number of neutrons cm^{-2} s^{-1}), N = the number of target nuclide or parent atoms, λ = the decay constant (number of decays per unit time), and t = the irradiation time. A neutron flux of about 2.10^{12} $n.cm^{-2}s^{-1}$ was used during the irradiation of the samples in the Triga Mark II reactor.

Table 3.1: Precision of INAA analyses (in relative %) at the University of Vienna.

Na (wt%)	2	Ce	3
K (wt%)	5	Nd	5
Fe (wt%)	4	Sm	2
Sc	2	Eu	2
Cr	3	Gd	5
Co	2	Tb	2
Ni	15	Tm	2
Zn	3	Yb	2
As	10	Lu	2
Se	10	Hf	2
Br	10	Ta	2
Rb	2	W	10
Sr	5	Ir (ppb)	<1ppb*
Zr	10	Au (ppb)	15
Sn	2	Th	2
Sb	5	U	10
Cs	2		
Ba	10		
La	2		

Data from Son and Koeberl (2005). Data were obtained by at least 10 replicate analyses of international geological standard reference materials.

All data in ppm, except as listed; * below detection limit of 1 ppb

3.3.2.2 *Measurement of Gamma Rays: An overview*

To measure the delayed γ-rays from the artificially generated radioactive samples generally needs a well integrated instrument, which consist of a semiconductor detector, associated electronics, and a computer-based, multi-channel analyzer (MCA/computer) (Fig. 3.4). The INAA lab at the Department of Lithospheric Research uses High purity Germanium (HpGe) semiconductor detectors working at liquid nitrogen temperatures (77 degrees K) to reduce electronic noise and to avoid damage of the lithium layer in the germanium crystals. These days, the HpGe detectors can be configured in various sizes and designs, however, the widely used type is the coaxial detector, which in NAA is useful for measurement of gamma-rays with a wide range of energies from about 60 keV to 3.0 MeV. The pre-amplifier that collects signal from the detectors dispatches voltage pulses to a digital signal processor (DSP), and then, the signal is stored in a memory channel of the multichannel analyzer (MCA). The two most important performance characteristics requiring consideration when purchasing a new HpGe detector are resolution and efficiency (Fig. 3.4).
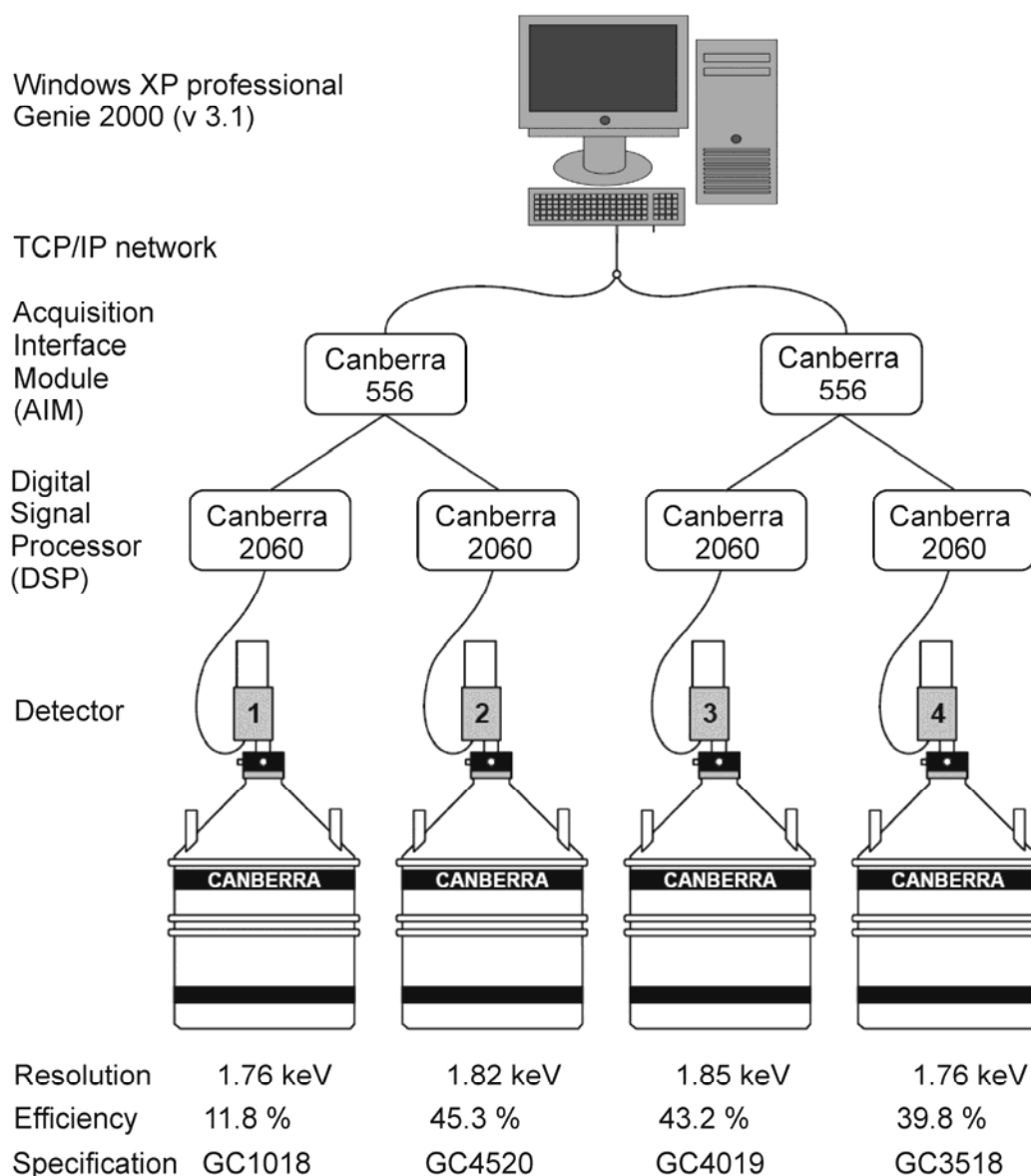
Figure 3.4 Arrangement of the INAA system at the Department of Lithospheric Research, University of Vienna (after Huber, 2003).

3.3.2.3 *Sample Preparation*

Unlike the XRF, the INAA does not require a convoluted sample preparation. For this work, sample powders weighing between 115 and 130 mg as well as 60- to 100 mg of three of the following international rock standards: carbonaceous chondrite Allende (Smithsonian Institute, Washington DC, USA; Jarosewich et al., 1987), the granite AC-E (Centre de Recherche Pétrographique et Géochimique, Nancy, France: Govindaraju, 1994), and the Devonian Ohio shale SDO-1 (United States Geological Survey, Govindaraju, 1989) were weighed into polyethylene vials, heat sealed, and the vials have to be water-tight to avoid material loss and/or radioactive contamination after irradiation. Then, 20 to 22 vials, including the three standards, were packed together into aluminum foil and were placed into a

plastic tube (polyethylene capsule) for irradiation (Fig. 3.5). (For irradiation see section 3.3.2.1). Finally, after irradiation and a cooling period of about four days, the samples vials
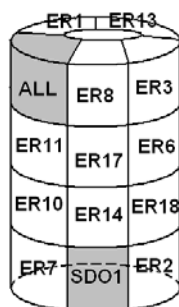
were decontaminated in solutions of diluted HCl, diluted NaOH, and distilled water. After drying, the samples were measured.

Figure 3.5 Schematic representation showing the proper positions of the standards in a four layer packing.

3.3.2.4 INAA Sample Measurement

All measurements regarding INAA were performed at the Department of Lithospheric Research, University of Vienna. At the department, four independent HpGe detectors with relative efficiencies between ~12 and 45 % (Mader and Koeberl, 2009) and energy resolutions between 1.76 and 1.85 keV (see Fig. 3.4) have been installed. Measurements were done during three counting cycles, L1, L2, and L3, respectively, because of the different half-life of the nuclides (Table 3.2). The first cycle of counting (L1) was executed about 5 days after irradiation (depending on the composition and the activity of the sample) for about one hour. Some Na-rich samples were so active even after 5 days from the irradiation, and then it was better to wait one more day. The second cycle (L2) was done about 10 days after irradiation, with counting time of three–eight hours; and the last counting period (L3) started about one month after the irradiation, with counting time between 20 and 26 hours. After the three cycles of measurements were completed, the spectra were calibrated, and a peak search procedure was carried out. Finally, with the help of PC-based Neutron Activation Analysis Software (PNAA v1.1) the concentrations of the elements (Table 3.2) were calculated.

The INAA determines the content of all elements listed in Table 3.2. The contents of other additional elements used in this thesis were determined by X-ray Fluorescence (XRF) Spectrometry (see section 3.3.1 for details); and the contents of, Na, K, Fe, Sc, Cr, Co, Ni, Zn, Rb, Sr, Zr, Ba, La, Nd and Th were determined by both, XRF and INAA methods.

Table 3.2: Elements determined by INAA. Indicator isotopes are reported as well as energy lines, half-lives, and measuring cycles.

Element	Indicator isotope	Energy lines (keV)	Half-life T1/2	Measurement cycle
Na	^{24}Na	1368.6	14.96 h	L1
K	^{42}K	1524.7	12.36 h	L1
Sc	^{46}Sc	889.3; 1120.5	83.79 d	L2, L3
Cr	^{51}Cr	320.1	27.70 d	L2, L3
Fe	^{59}Fe	192.3; 1099.2; 1291.6	44.50 d	L2, L3
Co	^{60}Co	1173.2; 1332.5	5.27 y	L3
Ni	^{58}Co	810.8	70.82 d	L2, L3
Zn	^{65}Zn	1115.5	244.26 d	L3
As	^{76}As	559.1	26.32	L1
Br	^{82}Br	554.3; 776.5	35.30 h	L1
Sr	^{85}Sr	514.0	64.84 d	L2, L3
Rb	^{86}Rb	1076.6	18.63 d	L2, L3
Zr	^{95}Zr	724.2; 756.7	64.02 d	L2, L3
	^{124}Sb	1691.0	60.0 d	L3
Sb	^{122}Sb	564.1	2.70.d	L1
Cs	^{134}Cs	795.8	2.06 y	L3
Ba	^{131}Ba	496.3	11.50 d	L2, L3
La	^{140}La	328.8; 487.0; 1596.2	1.68 d	L1, L2
Ce	^{141}Ce	145.4	32.50 d	L2, L3
Nd	^{147}Nd	91.1; 531.0	10.98 d	L2
Sm	^{153}Sm	103.2	46.27 h	L1, L2
Eu	^{152}Eu	121.8; 1408.0	13.54 y	L2, L3
Gd	^{153}Gd	97.4; 103.2	241.6 d	L3
Tb	^{160}Tb	298.6; 897.4; 966.2, 1178.0	72.3	L2, L3
Tm	^{170}Tm	84.3	128.6 d	L2, L3
	^{175}Yb	282.5; 296.3	4.18 d	L1, L2
Yb	^{169}Yb	177.2; 198.0	32.03 d	L1, L2
Lu	^{177}Lu	208.4	6.73 d	L1, L2
Hf	^{181}Hf	482.2	42.39 d	L2, L3
Ta	^{182}Ta	67.7; 222.1; 1221.4; 1231	114.43 d	L2, L3
W	^{187}W	685.8	23.72 h	L1
Ir	^{192}Ir	299.0; 308.5; 316.5; 468.1	73.83 d	L3
Au	^{198}Au	411.8	2.70 d	L1
Th	^{233}Pa	300.3; 312.2	26.97 d	L2, L3
U	^{239}Np	228.2; 277.6	2.36 d	L1

Energy lines and half-lives are from From Ferriere (2008, and references therein); "h" for hour, "d" for day, and "y" for year.

Additional references for section 3.3.2 from: Potts (1987), Ehmann and Vance (1991), Vandecasteele and Block (1993), Koeberl (1995), Gill (1997), Ferrière (2008), and Bartosova (2010).

3.3.3 *Electron Microprobe (EMP)*

An electron microprobe (EMP), also called an electron probe micro-analyzer (EPMA), is the most widely used technique for in-situ X-ray micro-analysis investigations of very small parts of a solid materials (rocks). This non-destructive analytical technique has a high spatial resolution and sensitivity, and works in a similar way to that of a scanning electron microscope (SEM). As for an SEM, the EMP determines the intensity of emitted X-rays generated by a beam of accelerated electrons, from which the composition is determined. All elements heavier than Lithium can be accurately detected because each element has a specific

characteristic X-rays that the element emits. Individual analysis (e.g., silicates) is reasonably short, requiring only two to three minutes in most cases. The chemical composition of a sample is determined by comparing the intensity of emitted X-rays with intensities of standard composition. More information on EMP can be found in, e.g., Potts (1987), Potts et al. (1995), Gill (1997), Watt (1997), and Bartosova (2010).

3.3.3.1 Sample Preparation

The sample is cut and mounted in epoxy resin in the shape of 4.7 cm x 2.8 cm. The sample mount is lapped first with coarse SiC-powder and then fine polished with diamond paste or corundum (Al_2O_3) grit slurry. The final grit size should be at least 0.25 μm and 0.06 μm (only necessary for probes with high resolution, field emission electron gun). The polished sample is then washed with clean water or ethanol in an ultrasonic cleaner to get rid of the polishing grit and other surface dirt. For water soluble samples, petrol ether can be used. The cleaning fluid is immediately blown off with clean air from the sample surface to avoid residual from dissolved dirt.
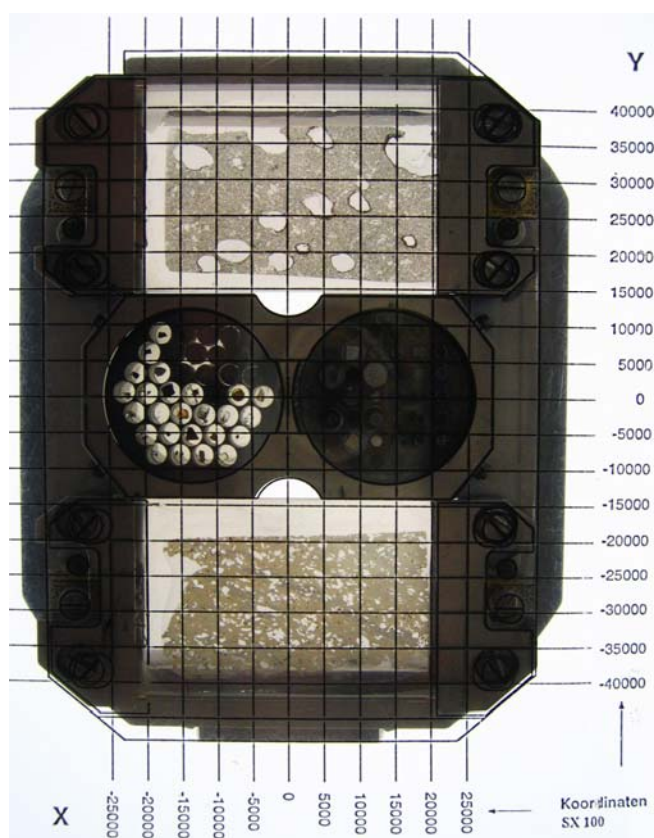
Figure 3.6 Co-ordinated samples in sample holder-2 before loaded to the Cameca SX100.

Electrically insulating samples were carbon-coated to ensure conduction to drain off the beam electrons from the sample. Conductive samples need not be coated. However, if they are mounted in a non-conductive material, carbon-coating is recommended. The carbon-coated samples then put to sample holder-2, 3 or 6 and co-ordinated (Fig. 3.6).

3.3.3.2 Wavelength dispersive spectrometry (WDS)

Electron microprobe analyses were performed using a Cameca SX100, at the Department of Lithospheric Research, University of Vienna. The instrument operates at accelerating voltages (between 1 to 30 kV) over a (wide) range of probe currents (from 1 nA to 200 nA). For the measures, 15 kV accelerated voltage and 20 nA beam current were used. Quantitative

analysis can be made for elements from Be to U with detection limits depending on the beam current and on X-ray counting times. This analytical technique was used for the study of different mineral phases of the Erta'Ale Range basalts.

3.3.4 Mass Spectrometry (MS)

Mass Spectrometry (MS) is a powerful analytical technique used for the measurement of isotope compositions to very high precision. The working principle of MS is based on the fact that charged atoms can be separated according to their different mass-to-charge ratio using a magnetic field separator. Though, there are several types of mass spectrometers; generally, they consist of three major components: a source (or ionization source), a mass analyzer (i.e., a magnet), and an ion collector. A simplified scheme of a mass spectrometer is shown in Figure 3.7.

3.3.4.1 Magnetic Sector Mass Spectrometer

At first, the sample is charged and these ions are accelerated by high voltage field through a potential gradient and collimated by slits. The charged ions are then deflected according to their mass-to-charge ratio in a strong magnetic field and are separated. This technique is sensitive only for positively charged ions. Negatively charged and uncharged ions and isobars (i.e., atoms with the same mass number but with different atomic numbers) are not treated using this technique. Instead, they collide with the wall of the tube and are pumped away. In the magnetic field, the trajectory of the ion is ideally circular. The radius of the trajectory is inversely related to the magnetic field strength of the spectrometer. The radius of the trajectory can be computed based on the equation resulting from the balance of the magnetic centripetal force and the centrifugal force:

$$m/z = r^2 H^2 / 2V$$

where m = mass of the charged ion, z = charge of the ion, r = radius, H = magnetic field strength, V = potential gradient of the trajectory. The mass spectrum can be scanned by varying either the magnetic field strength (more common) or the potential gradient of the spectrum. The resolution and efficiency of a mass spectrometer is determined by the ability how well it separates ions close in mass. Abundance sensitivity tells to which extent the tails of the peak at mass m contribute to neighboring peaks at masses (m-1) and (m+1).
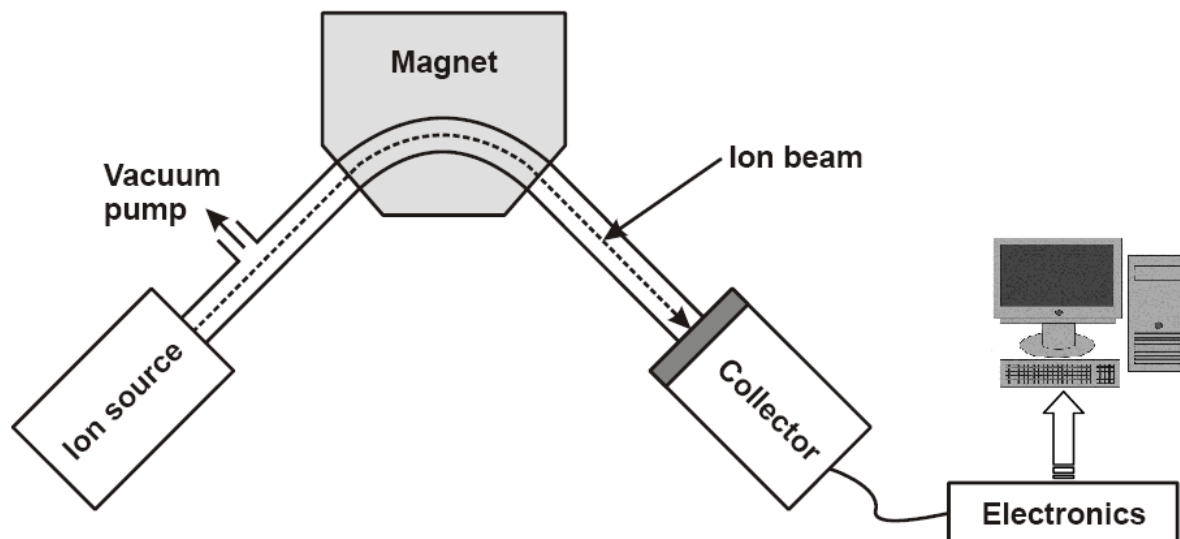
Figure 3.7 Simplified diagram of the main components of a mass spectrometer (after Gill, 1997).

3.3.4.2 Sample Preparation and Analysis

Whole-rock sample digestion for Sm–Nd analysis was executed in Savillex[TM] beakers using an ultrapure 1:5 mixture of HNO_3 and HF for about two weeks at 100–150°C on a hot plate. The acids are evaporated and the residue is further dissolved in a 5.8 $_N$HCl. During cooling, one component of the sample solution constituting ~7–20% was separated from and spiked for Sm and Nd concentration identification by isotope dilution (ID) using a mixed REE tracer (^{147}Sm–^{150}Nd spike). Using AG[TM] 50W-X8 (200–400 mesh; Bio-Rad) resin and 4.0 $_N$HCl, the REE fraction was extracted and then Nd and Sm separation from the fraction was followed using Teflon-coated HdEHP, and 0.24 and 0.8 $_N$HCl, respectively. Both Sm and Nd had a maximum total procedural blanks of <50 pg. Using HF/HNO_3 (4:1) sample dissolution for Rb–Sr analysis carried out, and element separation followed conventional procedures. Both Rb and Sr had a total procedural blanks of <1 ng. Sm, Nd and Sr were treated as metals from a Re double filament, using a ThermoFinnigan[TM] Triton TI TIMS (for IC) and a Finnigan[TM] MAT262 (for ID), whereas Rb was evaporated using a Ta filament. An ^{87}Sr$/$^{86}Sr ratio of 0.710241 ± 0.000002 (n = 18) and an ^{143}Nd$/$^{144}Nd ratio of 0.51185 ± 0.000001 (n = 38) were determined for the NBS987 (Sr) and the La Jolla (Nd) international standards, respectively, during the period of investigation. Within-run mass fractionation for Nd and Sr isotope compositions (IC) was corrected for relative to ^{146}Nd$/$^{144}Nd = 0.7219 and ^{86}Sr$/$^{88}Sr = 0.1194 respectively. Detailed information on this analytical method can be found in: Thöni et al. (2008).

References:

Bartosova K. 2010. Geochemical, mineralogical, and petrographic investigations of the Eyreville drill cores from the Chesapeake Bay impact structure. Ph.D thesis, University of Vienna, Vienna, Austria, 433 pp.

Ehmann W. D. and Vance D.E. 1991. Radiochemistry and nuclear methods of analysis. New York, John Wiley and Sons, 531 pp.

Ferrière L. 2008. Shock metamorphism and geochemistry of impactites from the Bosumtwi impact structure: A case study of shock-induced deformations and transformations in quartz and associated methodology. Ph.D thesis, University of Vienna, Vienna, Austria, 279 pp.

Gill R. 1997. Modern analytical geochemistry: an introduction to quantitative chemical analysis techniques for earth, environmental and materials scientists. Longman, Harlow, 329 pp.

Govindaraju K. 1989. 1989. Compilation of working values and sample description for 272 geostandards. Geostandards Newsletter 13, 1–113.

Govindaraju K. 1994. 1994 compilation of working values and sample description for 383 geostandards. Geostandards Newsletter 18, 1–158.

Huber H. 2003. Application of gamma, gamma-coincidence spectrometry for the determination of iridium in impact related rocks, glasses, and microtekites. Ph.D thesis, University of Vienna, Vienna, Austria, 326 pp.

Jarosewich E., Clarke R. S. J., and Barrows J. N. 1987. The Allende meteorite reference sample. Smithsonian Contributions to Earth Sciences 27, 1–49.

Jenkins R. 1999. X-ray fluorescence spectrometry. Second edition. USA: John Wiley and Sons, Inc, 207 pp.

Koeberl C. 1995. Neutron activation analysis. In Methods and instrumentations: results and recent developments, Advanced mineralogy, Vol 2, edited by Marfunin A. S. Berlin, Heidelberg, New York, Springer-Verlag 322–329.

Mader D. and Koeberl C. 2009. Using instrumental neutron activation analysis for geochemical analyses of terrestrial impact structures: Current analytical procedures at the University of Vienna Geochemistry activation analysis laboratory. Applied Radiation and Isotopes 67, 2100–2103.

Markam B. and Barker J. 1986. Landsat MSS and TM post-calibration dynamic ranges, exoatmospheric reflectances and at-satellite temperatures. EOSAT Landsat Technical Notes 1, 3–8.

Muzein B.S. 2006. Remote Sensing and GIS for Land Cover/ Land Use Change Detection and Analysis in the Semi-Natural Ecosystems and Agriculture Landscapes of the Central Ethiopian Rift Valley. Ph.D thesis. Dresden, Germany, 166 pp.

Potts P. J. 1987. A handbook of silicate rock analysis. Glasgow, Blackie, 622 pp.

Potts P. J., Bowles J. F. W., Reed S. J. B., and Cave M. R. 1995. Microprobe techniques in the earth sciences. London, Chapman and Hall, 419 pp.

Son T. H. and Koeberl C. 2005. Chemical variation within fragments of Australasian tektites. Meteoritics and Planetary Sciences 40, 805–815.

Thöni M., Miller C., Blichert-Toft J., Whitehouse M.J., Konzett J., and Zanetti A. 2008. Timing of high-pressure metamorphism and exhumation of the eclogite type-locality (Kupplerbrunn–Prickler Halt, Saualpe, south-eastern Austria): constraints from correlations of the Sm–Nd, Lu–Hf, U–Pb and Rb–Sr isotopic systems. Journal of metamorphic geology 26, 561–581.

Vandecasteele C. and Block C. B. 1993. Modern methods for trace element determination. Chippenham, Wiltshire, UK, John Wiley and Sons, 330 pp.

Waltham T. 2005. Extension tectonics in the Afar Triangle. Geology Today 21, 101–107.

Watt I. M. 1997. The principles and practice of electron microscopy, 2nd ed. Cambridge, Cambridge University Press, 484 pp.

CHAPTER 4

CHAPTER 4: KINEMATIC ANALYSIS OF THE NORTHERN AND CENTRAL AFAR DEPRESSION: FROM CONTINENTAL BREAKUP TO MID-OCEANIC RIDGE TYPE RIFT AXIS

Abstract– The northern– to central Afar Depression, the volcano-tectonically most active region of the east African rift system, is a region of extensional tectonics that has undergone varying degrees of extension and counterclockwise rotation of its axial rift. Both field evidence from structural measurements and Landsat image data indicate that the rift axes of the northern Afar (Erta'Ale Range) and central Afar (Tendaho graben) Depressions are obliquely oriented (~20°−30°) to the Oligocene – Miocene-age western Afar border faults and marginal grabens. The western Afar border faults are relics of the incipient breakup of the Danakil Microplate from the Nubian part as the Red Sea rift started propagating southward to the central Afar. To evaluate the Afar Depression kinematics, the Nubian, Arabian, and Somalian plates, and the Danakil Block are reconstructed to their original position based on the existing paleomagnetic data and best-fit model hypothesis. In many cases, observations and the paleo stress-field show that the Danakil Microplate translated obliquely to the NE and the paleo rift-axis of Afar remained parallel with the boundary faults till the middle–late Miocene (~11 Ma). The major change in the geometry and kinematics of the Afar Depression and the Danakil Microplate occurred concurrent with the development of the new oceanic crust in the southcentral Red Sea, westward propagation of the Gulf of Aden, and NE motion of the Afar triple junction.

4.1 Introduction

The Arabian plate is migrating to the NE at a rate of ~16 mm/yr from Africa (Chu and Gordon, 1998), forming the Gulf of Aden rift between Arabia and Somalia and the Red Sea rift between the Nubian plate and Arabia (Fig. 4.1; Tesfaye et al., 2003). The Gulf of Aden rift and SE–trending Red Sea rift are currently heading toward each other, leaving a region of highly attenuated transitional crust in the Bab El Mendab Strait (Courtillot et al., 1987; Manighetti et al., 1997). The southern Red Sea rift has split into two and the western segment has jumped into Afar forming the NNW–trending Erta'Ale Range and leaving the elevated Danakil Microplate between the southern Red Sea and the Afar Depression (Fig. 4.1; Tesfaye et al., 2003). Southward spread of the volcano-tectonically active segments of the southern Red Sea rift propagators end in central Afar Depression near the arcuate accommodation zone (AAZ) at about 10° N, and then the Main Ethiopian Rift (MER) trend continues up to ~5°N to the south. The Gulf of Aden rift, on the other side, has been propagating westwards

into the central Afar Depression through a series of discontinuous en-echelon arrangement of ridges at a velocity of ~30 mm/yr at least since Pliocene (e.g., Courtillot et al., 1984; Manighetti et al., 2001; Thurmond et al., 2006).

The Afar Depression, a triple-plate junction above a hot mantle plume, is an area of active extensional deformation and basaltic volcanism from which the Red Sea, the Gulf of Aden, and the Ethiopian rift radiate (Abbate et al., 1995; Audin et al., 2004). These three rift arms superimpose in a complex zone within the central Afar Depression, producing the archetypal ridge–ridge–ridge-type sub-aerial triple junction associated with the raising of the Afar mantle plume (McKenzie et al., 1970; Wolfenden et al., 2004). The kinematic and geometric patterns of the Afar Depression is, however, mainly the result of the interaction between these three geodynamically distinct rifts, which form highly attenuated continental crust characterized by block rotations and bookshelf faulting (Mohr, 1972; Tapponier et al., 1990; Manighetti et al., 2001).

Paleomagnetism, structural, and geophysical data, constrain the timing and magnitude of migration of the Afar triple junction and the Danakil Microplate rotation; however, the relationship between the geometry of initial faulting in the northern– to central Afar escarpment (western escarpment) and the axial zones (e.g., Erta'Ale Range and Tendaho graben) in the depression and the Danakil Microplate were only loosely constrained. Thus, the kinematic analyses of the rift bounding faults and axial zones, and the role of the migrating Afar triple junction for the current structural setup of Afar Depression and counterclockwise rotation of the Danakil Microplate are the 'missing pieces' in our understanding of the geodynamics of the Afar region.

This chapter aims to determine the variation in orientation of the rift-bounding western Afar border faults and the northern (Erta'Ale axial range) and central (Tendaho graben) Afar rift axis, and their implications for the counterclockwise rotation of the Danakil Microplate. Structural measurements, remote sensing, geochemical studies, and existing data were undertaken from the entire Danakil Depression. The specific objectives of this study were to establish a structural setup for the northern and central Afar Depression by (1) collecting data on, and analyzing, the structural elements; (2) using remote sensing imagery to understand the spatial relationship, and to map faults and other structures through the entire Afar Depression.
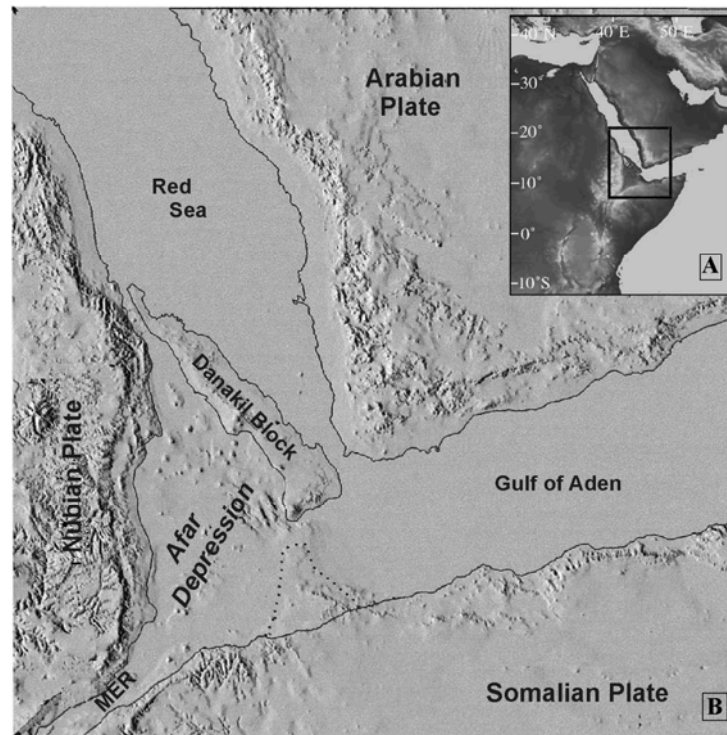
Figure 4.1 Regional view of the Afar Depression and associated rift zones. (A) Inset map (after Beyene and Abdelsalam, 2005). (B) Location map of the four major plates/blocks and the three axial rift zones merging together in the Afar Depression (modified after Collet et al., 2000).

4.2 An Overview of the Afar Depression

The East African Rift System (EARS) is the youngest (Late Oligocene–Quaternary) intracontinental extensional deformation system composed of several interacting rift segments, from highly evolved (Afar Depression) to the less evolved (Tanzanian and Mozambique) rifts (e.g., Davidson and Rex, 1980; Ebinger et al., 1989; Hayward and Ebinger, 1996; Bosworth and Strecker, 1997; Acocella and Korme, 2002; Eagles et al., 2002; Abebe et al., 2007). The Afar Depression is the only rift segment in the EARS and one of the few localities worldwide where one may study the complete process of mantle plume, rift-rift-rift triple junction and microplate formation on land (Eagles et al., 2002). The morphotectonics of the Afar Depression are currently under control of pure extensional movements induced by the upwelling Afar mantle plume (Chorowicz, 2005) and the northeast oriented far-field stress at Zagros Orogenic Front (Bosworth et al., 2005). The upper crust has reacted by brittle deformation and subsidence, forming elongated narrow rifts, whereas the lower crust and lithospheric mantle is subjected to sharply define ductile thinning, inducing ascension of asthenospheric mantle (Chorowicz, 2005).

At Afar Depression, the MER, northern segment of the EARS, connects with the Red Sea and Gulf of Aden rifts, both characterized by matured ridge segmentation (McKenzie et

al., 1970; Manighetti et al., 2001) and have achieved full oceanization stage since the middle Miocene–Pliocene period (Acocella and Korme, 2002) (Fig. 4.2). Northeast–oriented seafloor spreading in the Gulf of Aden and Red Sea commenced at ~16 Ma and ~4 Ma, respectively (D'Acremont et al., 2005; Cochran and Martinez, 1988). Seafloor spreading has not yet started in the MER (Wolfenden et al., 2004), but the current crustal extension direction is orthogonal to the NNE–trending axial fault zones, the Wonji fault belt (Acocella and Korme, 2002).

The Red Sea rift branches southward into two (Fig. 4.2): with one branch (eastern) running linearly along the southern Red Sea to the Ba El Mendab, while the other branch (SSW–trend) runs along the Gulf of Zula, steps onto land within the Danakil Depression and produces an almost NNW–oriented chains of volcanic centers (Abbate et al., 1995; Beyene and Abdelsalam, 2005). Volcano-tectonic processes are active in three segments of the SSW–trending Red Sea rift (Erta'Ale Range, Alyata–Manda Hararo, and Tendaho rift). The MER also funnels out in a slightly diverging manner as it approaches the triple junction, where it joins the Red Sea and Gulf of Aden rift systems (Tendaho–Goba'ad rifts) near Lake Abhe (Abbate et al., 1995). The Gulf of Aden rift, which does not directly join the other two arms of the triple-junction, infiltrates landwards within the rifts of Asal and Manda Inakir and nearly parallels the Red Sea rift for hundreds of kilometers, and then dies out as a NW–trending horsetail structure merging into the complex zone of the northeastern part of the Afar Depression (Abbate et al., 1995) (Fig. 4.2).
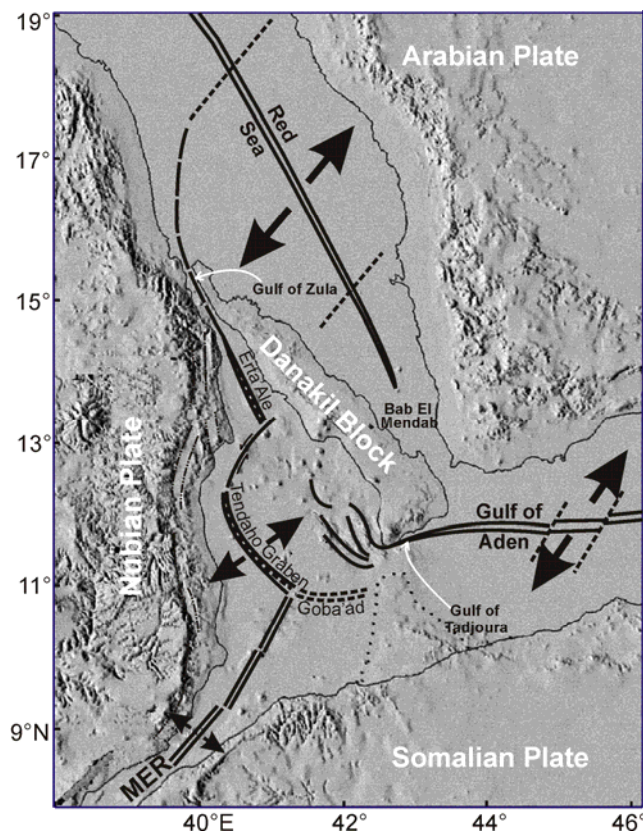
Figure 4.2 Outline of the tectonic setup of the Afar Depression. Oceanic and continental rift segments of the Red Sea, Gulf of Aden and Main Ethiopian ridge propagators. The Red Sea rift bifurcates southward into the western and eastern rift segments. Double dark lines: oceanic ridges, dashed double lines: Goba'ad graben, single dashed lines: transform structures, and dark arrows: extension direction of the ridges (modified after Collet et al., 2000).

The region constituting the three arms of the spreading centers (the Red Sea, Gulf of Aden and the MER) is not uniformly evolved. The northern Afar Depression is formed by the NNW–trending Erta'Ale Range shield basalts, typical of mid oceanic ridge-type constituting the deepest depression of the transitional Afar lithosphere (Barberi and Varet, 1975). The eastern zone of the depression is an oceanic rift but disappeared west of the Asal rift, marking the western end of seafloor propagation of the Gulf of Aden (Chorowicz, 2005). Only the southwestern zone of the Afar Depression (northeastern extension of the MER) completely belongs to continental rifting. It is an asymmetric rift dominated by NNE– to NE–trending structures manifesting a series of right-laterally offset grabens and horsts accompanied by ESE–dipping tilted fault blocks forming plateaus, which are parallel to the axial grabens (Tesfaye et al., 2003; Chorowicz, 2005).

4.3 Tectonic Setting of Afar Depression

4.3.1 The Afar Depression

The triangular-shaped Afar Depression is bounded on the west by the Ethiopian highland (Nubian plate), on the northeast by the Danakil Microplate, and on the south by the eastern Plateau (Somalian plate) (Fig. 4.2; Tesfaye et al., 2003). It is characterize by lowland plains ribbed by grabens and horsts and linearly aligned high relief peaks representing the axial shield volcanoes or volcanic edifices (Fig. 4.3). Elevation drops significantly from the Ethiopian Plateaus that stand well above 3500 m (western Plateau) to the lowest point in northern Afar Depression at ~146 m below sea-level (Dallol Depression) (Tesfaye et al., 2003). This depression, which is characterized by intense tectonic and volcanic processes, is still active (Barberi and Varet, 1975; Barrat et al., 1998; Harris et al., 2005). Wright et al. (2006) estimated that ~2.4–2.6 km^3 of magma was intruded along the Dabbahu rift segment (northern Afar Depression) during the 2-week rifting episode in September 2005, which also produced a total crustal rupture of ~60 km (Sigmundson, 2006).

In the newly developed basins, early Miocene– to early Pliocene syn-rift Red-bed series (sandstones) and lacustrine sediments were deposited (Redfield et al., 2003). The deposition of shallow water limestones, marine clays, and submarine volcanoes (Tiercelin et al., 1980) indicate that large area of the Danakil Depression was once covered by marine environments for at least some part of Miocene time. In east and west sides of the axial range, the Afar Stratoid series and underlying Red bed series are found in tilted fault-bounded blocks (Abbate et al., 1995).

The Afar Depression is divided into northern, central, and southern zones on the basis of similar tectonic domains (Hayward and Ebinger, 1996). The northern zone of the Afar Depression also called the Danakil Depression, with a mean elevation of ~200 m above sea level, is dominated by NNW–trending tectonically controlled axial volcanic ranges. The Quaternary volcanic edifices of the Danakil Depression are produced by basaltic shield and fissure eruptions along the NNW-SSE–trending ridge, parallel to the mean structural trend of the Red Sea rift (Varet and Gasse, 1978; Tesfaye et al., 2003). The elevation of the Danakil Depression gets gradually lower towards the northern part known as Dallol Depression (Fig. 4.3). At Dallol the elevation drops to ~146 m below sea level (CNR-CNRS, Afar team, 1973). Even though the Danakil Depression has generally low elevation, it is characterized by a number of shield volcanoes such as: Erta'Ale, Tat'Ali, and Alyata (Beyene and Abdelsalam, 2005), which can rise to an elevation of ~1300 m above sea level (Figs. 3 and 4a).

The central Afar Depression is bordered on the southwest by the Tendaho-Goba'ad Discontinuity (TGD), on the northwest by the Tat'Ali–Alyata shield volcanoes, and on the northeast by the southern parts of the Danakil Microplate (Fig. 4.3). It covers an area of lowland plains dominated by rigorously faulted E–W to NW trending grabens and horsts making an average elevation of ~450 m above sea level (Tesfaye et al., 2003). There is no adjacent segment and the grabens terminate in a broad area of more diffuse faulting (Hayward and Ebinger, 1996) called the horse-tail structures. This kinematically distinct zone does not show any sign of recent volcanic centers.
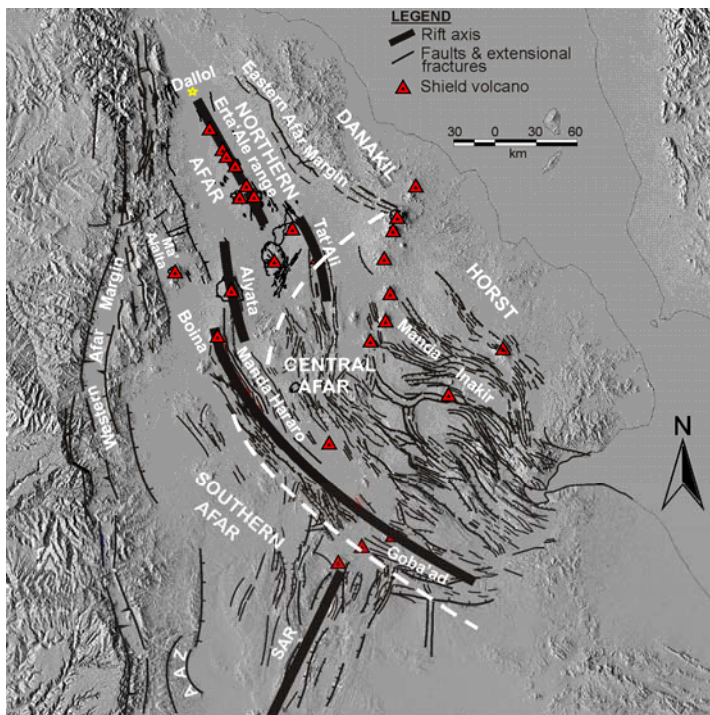
Figure 4.3 Shaded relief image of Afar Depression and surrounding plateaus (modified after Tesfaye et al., 2003). Possible spreading centers (the Red Sea and Main Ethiopian rift trends) of the depression are marked by thicker lines; normal faults and extensional fractures are represented by thinner lines; the Afar tectonic domains are separated by dashed white lines. AAZ-arcuate accommodation zone, SAR-southern Afar rift.

The southern Afar Depression, tectonically subdued zone compared to the other two domains, is a direct continuation of the MER that is interrupted by the TGD (Beyene and Abdelsalam, 2005). The depression is a funnel-shaped structure, which is dominated by parallel sets of horsts and grabens. Unlike central Afar, the grabens and horsts in southern Afar strike north-northeast, parallel to the axial rift zone of the MER, and has a mean elevation of ~700 m above sea level (Tesfaye et al., 2003).

4.3.1.1 *The Erta'Ale Axial Range*

Erta'Ale Range is located in the south of the Dallol Depression, and is composed of seven shield volcanoes, roughly NNW-SSE aligned: Hayli'Gub, AleBagu Erta'Ale, Borale'Ale, Dalaffilla, Alu, and Gada'Ale, from south to north (Fig. 4.4a; Barrat et al., 1998). The Ethiopian highland (mean elevation ~2500 m above sea level) and the Danakil Microplate (mean elevation ~400 m above sea level) lie to the west and east, respectively, of the highly attenuated crust in the depression (Acocella, 2006). Towards the central region (south of Tat'Ali), the NNW–trending tectonic elements related to the Red Sea bends counterclockwise to a more E-W trend (Fig. 4.3; Beyene and Abdelsalam, 2005). The Erta'Ale Range axial zone is characterized by extensional fractures or normal faults and fissure-fed lavas, which are mainly transitional– to tholeiitic in composition, although some felsic derivatives are also inter-bedded with the basaltic lava flows (Fig. 4.4a; Acocella, 2006).

The central part of the Erta'Ale Range (Erta'Ale shield volcano) is characterized by intense tectonic and volcanic activities. At the 1600 x 700 m summit elliptical caldera, Erta'Ale features two pit craters (both hosted active lava lakes) and many superimposed subcircular collapse structures (Oppenheimer and Francis, 1998). Holocene eruptions of lava have poured out mostly from the NNW–trending fractures on the caldera margins and from the craters on the caldera (Waltham, 2005).

The Erta'Ale Range as a whole is characterized by an attenuated continental crust (thickness <15 km) and intense tectonic and volcanic activity, analogous to the continental crust of the Red Sea before 4 Ma. The main volcano-tectonic features are intermittent axial volcanic edifices and fissure basalts, open extensional fractures and vertical step-faulting. The volcanic activity in the Danakil Depression is important since the Pliocene, and is today mostly restricted to the axial zone forming three spectacular volcanic shields: the Erta'Ale, Alyata and Tat'Ali (Barrat et al., 1998).
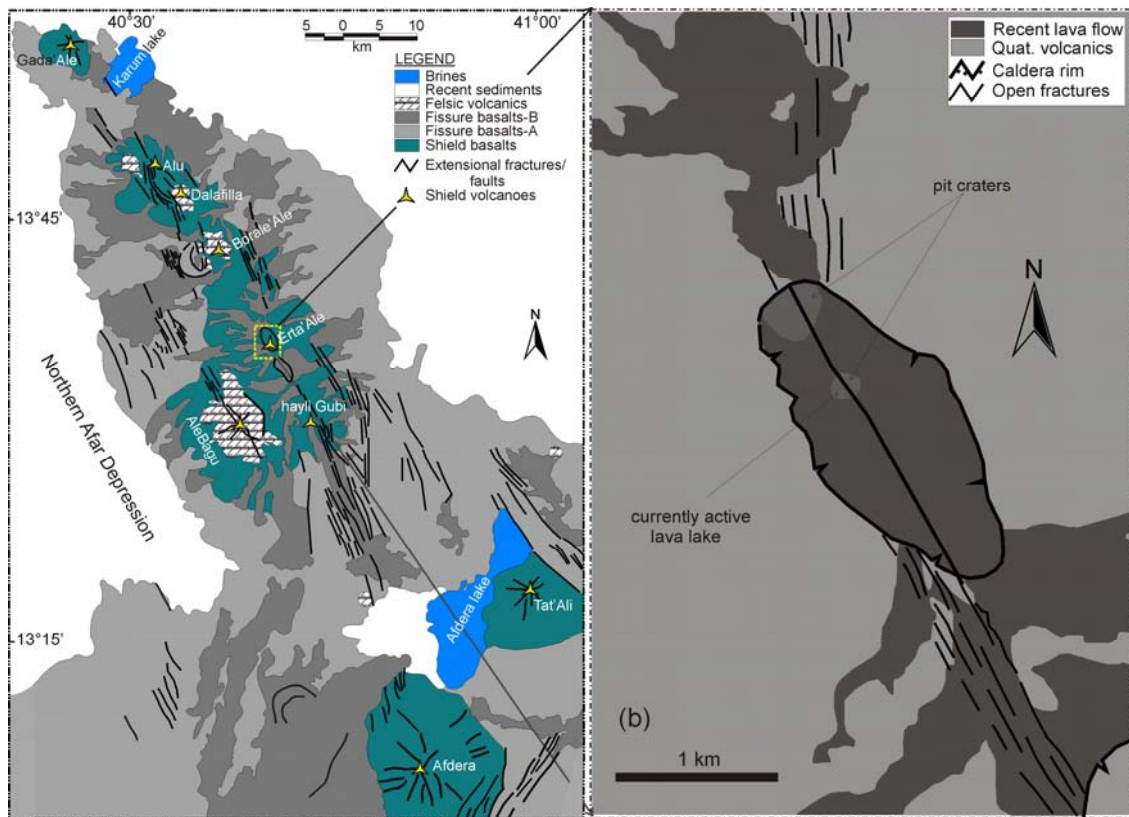
Figure 4.4 (a) Geology and structure of the northern part of the Afar Depression (Danakil Depression), the Erta'Ale Range; (b) Main features of the NNW-SSE–trending elongated Erta'Ale caldera (modified after Acocella, 2006).

4.3.1.2 *The Manda Hararo–Tendaho Graben*

The Red Sea propagator south of 17°30' N splits into a SE and a SSW trends (Chu and Gordon, 1998; Beyene and Abdelsalam, 2005). The SE–trending rift axis continues along the Red Sea and ceases in a tectonically inactive zone around the Bab El Mendab area (Barberi and Varet, 1975). The SSW–trending rift propagates through the Gulf of Zula in the north, jumps onto land within the northern Afar Depression and continues south in a right-stepping en-echelon configuration along the Erta'Ale axial volcanic ranges to Manda Hararo–Tendaho graben (Figs. 4.2 and 4.3; Beyene and Abdelsalam, 2005). In central Afar, the Red Sea propagator is mainly represented by the NW-SE–trending Tendaho graben (Tapponnier et al., 1990; Manighetti et al., 2001), the largest basin in the area, with a distinctive topographic expression (Acocella, 2010). The Tendaho graben, including the Manda Hararo rift in the north and the Goba'ad rift in the south, is ~250 km long and its width varies from ~25 km near its endpoints to >50 km in its center (Acocella, 2010). The Tendaho–Goba'ad graben, with a width of ~50 km in its center, is comparable to that of matured continental rift zones (Abbate et al., 1995). It is the second young axial structure formed in the region during the last ~1.8 Ma (Acton et al., 1991), and the floor of the graben is mainly filled with Stratoid

series and Quaternary deposits (Lahitte et al., 2003). Although, large part of the graben is covered by widespread Stratoid series and lacustrine sediments, Lahitte et al. (2001) identified ~30 ka volcanic products at the tip of Manda Hararo rift.

The Tendaho rift joins or intersects with the NNE–trending Wonji Fault Belt (WFB) in a zone marked by axial volcanic centers and crosscutting fault patterns (Abbate et al., 1995). This ridge constitutes multi-trend structures: N-S–striking Alyata ridge, NW-SE striking Tendaho/Manda Hararo graben and WNW-ESE striking Goba'ad graben (Fig. 4.3). The axial zones within the Afar Depression are segmented into 50- to 80-km-long volcanic ridges (Beyene and Abdelsalam, 2005). The size, morphology, and spacing of this magmatic and/or tectonic segmentation are similar to the 30- to 80-km-long, second order segmentation of slow spreading mid-oceanic ridges (Hayward and Ebinger, 1996).

4.3.1.3 *The Southern Afar Rift (Main Ethiopian Rift trend)*

The architectural setup of the southern Afar Depression is more or less similar with that of the central Afar Depression. It is dominated by Pliocene–Pleistocene horst and graben structures and highly spaced volcanic shields. Unlike central Afar, however, the geometry of structures and the physiography of the surface are different. In southern Afar, all the extensional features are the direct continuation of the NNE–trending structures of the WFB. Because of this direct continuity, the tectonic boundary between the southern Afar Depression and the northern MER is not readily identifiable within the rift floor (Tesfaye et al., 2003). On a broader view, however, the funneling out of the northern MER from a width of ~80 km to >300 km in the vicinity of the arcuate accommodation zone, near the Ayelu-Abida volcano, is interpreted to define a physiographic boundary between the southern Afar Depression and the MER (Tesfaye et al., 2003). The axial zones of both tectonic domains are dominated by Pleistocene WFB. The major lithologies of the region include Afar Stratoid series and lacustrine deposits (Pliocene– Pleistocene), and very young axial volcanic and associated sedimentary rocks (Pleistocene–Recent).

4.3.2 *The Main Ethiopian Rift*

The Main Ethiopian Rift (MER) constitutes the northernmost segment of the intracontinental rift system (EARS), connecting the rift system with the high evolved oceanic rifts (i.e., Red Sea and Gulf of Aden rifts) at the Afar triple junction (Abebe et al., 2007). The MER is a magmatic rift segment that imprints all the different phases of rift development from incipient continental breakup to the emergent seafloor spreading (Ebinger, 2005). It is thus an ideal place to investigate the development of continental stretching, new plate formation, and the

dynamics by which disseminated continental extensional deformation is increasingly focused at oceanic spreading centers (Corti, 2009).

The MER developed within a N-S–running pre-existing fabrics or suture zone called the Mozambique Belt, a major late Proterozoic mobile belt that extends from Arabian-Nubian shield south through Tanzania, and Mozambique (Keranen and Klemper, 2008). The MER is a well-defined and narrow (~60–100-km-wide) depression with an overall northeasterly orientation (Tesfaye et al., 2003). However, global positioning system (GPS) measurements show that almost all recent extensional deformation across the MER is accommodated in a ~20-km-wide zone of intense faulting and magmatism within Wonji tectonic segment (Billham et al., 1999). This narrow and highly deformed axial fault zone along the MER (Fig. 4.5) is referred to as the Wonji Fault Belt (WFB). The WFB is characterized by segmentation and NNE-SSW–trending active normal faults and open fractures, which in many places are associated with Quaternary–Recent fissure-fed basalts or central shield volcanoes (e.g., Mohr, 1987; Chorowicz et al., 1994; Korme et al., 1997).

Quaternary volcano-tectonic activity along the southern Afar Depression and MER is mainly located on the WFB (e.g., Mohr, 1968; Bilham et al., 1999; Ebinger and Casey, 2001; Tesfaye et al., 2003). The tectonic elements along the WFB are represented by normal faulting, extensional fractures, and fissure-fed basalt flows, and volcanic centers spaced by ~30 km- to 50 km (Fig. 4.5; Mohr, 1967; Kazmin et al., 1980). These NNE– to NE–oriented Quaternary rift segments of the WFB form areas of active extensional deformation obliquely cutting the MER rift floor (Abebe et al., 2007). The average width of the WFB in the MER part is ~5–12 km (Mohr and Woods, 1976). However, in southern Afar, near the triple junction, the width of the axial fault zone reaches 60 km (Mohr, 1967; Kazmin et al., 1980; Tesfaye et al., 2003). Like the highly evolved axial fault zones of the northern and central Afar, the WFB is systematically segmented and set in an en-echelon arrangement. Segment length ranges between ~40 and 80 km and offset or gap between adjacent segments ranges from a few kilometers up to 40 km (Mohr, 1967; Mohr and Woods, 1976; Tesfaye et al., 2003), with a general northward increase (Fig. 4.5).
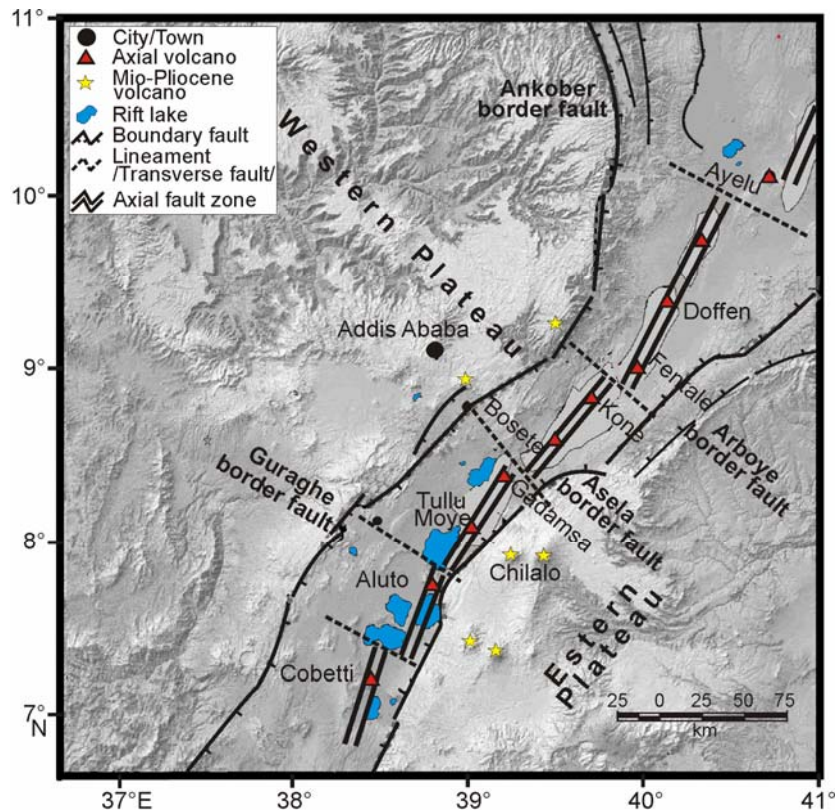
Figure 4.5 Structural outline of the Main Ethiopian Rift. Important features shown include the axial Wonji Fault Belt–Double line, Border faults–thick dark lines, Transverse faults–dashed lines, and major volcanic centers–yellow stars (modified after Keranen and Klemper, 2008).

4.4 Tectonic and Magmatic segmentation

All mid oceanic ridges and matured continental rift zones (e.g., Afar Depression and MER) are characterized by magmatic and tectonic segmentation, with segments ranging in size from tens to several hundreds of kilometers. Segmentation of oceanic and continental ridges is hierarchical and that tectonic and magmatic segmentations are linked and related by mantle convection and upwelling patterns (Batiza, 1996). The tectonically and magmatically active Ethiopian rift comprise systematic along-axis variation in volcanism and rate of extension, making it practical to investigate the relation between magmatism, strain rate, and the length scale of segmentation during rift evolution (Hayward and Ebinger, 1996).

All mid oceanic ridges and the well known continental rift zones (e.g., EARS and the Basin and Range Province of North America) are not ruler-drawn structures. Batiza (1996) pointed out that rate of spreading exerts an important control on ridge segmentation pattern, although this is probably not the only determining factor. Bell and Buck (1992) proposed that ridge segmentation is controlled by differences in the thermal state of the crust managed by magma supply rather than by spreading rate-dependent mantle convection processes.

In well-developed mid oceanic ridges, the overriding transform structures are represented by the first-order discontinuity/ segmentation. The first-order discontinuity has the greatest temporal stability, with transform faults lasting stably for ~10^7 years or more (Batiza, 1996). Macdonald et al. (1988) identified smaller scale segmentations (2° to 4°) associated with the first-order (1°) discontinuities. These segmentations divide the ridge into progressively smaller and shorter-lived segments.

Figure 4.6 Simplified geological map and major tectonic structures (segments) of the Afar Depression (after Hofstetter and Beyth, 2003). The following acronyms represent: AG, Asal Ghoubbet; AL, Alyata; BM, Bab El Mendab straits; ER, Erta'Ale; MH, Manda Hararo; MH-G, Manda Hararo-Goba'at; MI, Manda Inakir; TA, Tat'Ali; and TGD, Tendaho-Goba'ad discontinuity; HA, Ayelu, which mark the along axis segmentation of the newly evolved mid-oceanic ridge-type structures of the Afar Depression.

The seismically and volcanically active northern MER and southern Red Sea rift in the Afar Depression are two such regions, offering the opportunity to trace the evolution of along-axis segmentation during the complete process of rifting. The Afar Depression has an incoherent along-axis depth profile and the scale of segmentation is more erratic, most probably because there are many hotspots (magma chambers) with different thermal state near the ridge (Batiza, 1996). The northern and central Afar is affected by NE–trending sinistral strike-slip faults, which obliquely cut the axial range. These newly formed transverse structures could serve as local breaks and later would evolve to a more stable first order (1°) tectonic discontinuities (Batiza, 1996) (Fig. 4.6). Now, it is generally accepted that spreading rates control the chemistry of oceanic and continental ridges. Slower spreading ridge lavas (e.g., the WFB volcanics) have more geochemical variability than faster spreading ridges (e.g., the Erta'Ale Range volcanics) (Langmuir et al., 1992).

Quaternary–Recent crustal extension in Danakil Depression (northern Afar) occurs in a seismically quite zone between the Ethiopian escarpment and the Danakil Microplate (Hayward and Ebinger, 1996). From the kinematic models of Joffe and Garfunkel (1987), and Jestin et al. (1994), the extension rate between Nubian and Arabian plates is ~18–22 mm/yr to the NE–SW direction. Some of the active rift segments in the Afar Depression that can accommodate optimum extension rate are the Erta'Ale, Tat'Ali, Alyata, and Manda Hararo axial ranges. The shield volcanoes within the Erta'Ale range are spaced at ~10–15 km intervals, however, this interval gradually increases to 40–50 km to the south, the MER segments (Mohr, 1967; Tesfaye et al., 2003) (Figs. 4.4 and 4.5).

4.5 The Marginal Areas of the Afar Depression

4.5.1 Western Margin/Ethiopian Escarpment

The low-lying Afar Depression is separated from the Ethiopian highland by the Ethiopian escarpment; N-S–running border faults, right-stepping marginal basins and titled fault-blocks (Figs. 3 and 7). Most of the marginal faulted blocks are tilted to the east and dissected by east flowing drainage networks that resulted in the formation of a terrain dominated by relics of hogback-like features (Beyene and Abdelsalam, 2005). The elevation drops sharply from 3500–2500 m at the water-shade-line of the Ethiopian escarpment to 800–100 m and in places to ~146 m below sea level, the northern Afar Depression lowlands (Mohr, 1983).

Tectonically active, right-stepping, en-echelon systems of discontinuous marginal basins/ grabens are developed at the base of the western Afar escarpment (Tesfaye et al., 2003). These N-S–running marginal basins are Borkena, Menebay–Hayk, Raya, Dergaha–Sheket, and Maglala–Renda Coma listed from south to north (e.g., Mohr and Rogers, 1966; Mohr, 1967; Tesfaye et al., 2003; Beyene and Abdelsalam, 2005) (Fig. 4.7). The basins are supposed to have been commenced during the middle Oligo-Miocene that provoked the construction western Afar margin (Chorowicz et al., 1999; Tesfaye et al., 2003) formed mainly due to gravity collapse (Collet et al., 2000).

4.5.2 The Danakil Microplate (Northeastern–Eastern Margin)

The NW-SE–trending Danakil Microplate/Block, which extends from the Gulf of Zula in the northwest to the Gulf of Tadjoura in the southeast (Fig. 4.7b), separates the Afar Depression from the Red Sea. It is an elongated, ~500-km-long and ~100-km-wide, landmass with a mean elevation of ~400 m (e.g., Courtillot et al., 1984; Boccaletti et al., 1999; Collet et al., 2000; Manighetti et al., 2001; Eagles et al., 2002; Tesfaye et al., 2003; Beyene and

Abdelsalam, 2005), but rises to ~2100 m above sea level in its center. The Microplate is subjected to different scale of extensional and strike-slip faulting, to a much greater degree than the Nubian plate.

Kinematic models and paleomagnetic data point out that the Danakil Microplate has undergone an overall ~30° counterclockwise rotation (Le Pichon and Francheteau, 1978) with respect to Nubia since the late Oligocene (Fig. 4.7a). Manighetti et al. (2001) suggested that the Danakil Microplate had to break away from the Ethiopian Plateau ~20 Ma ago so as to attain a 30° counterclockwise rotation.

From the western margin fault-trace and the regional stress-field analyses, the Danakil Microplate had moved/translated to the NE with low angular rotation till middle Miocene. The aggregate magnitude and rate of rotation, however, is uncertain. Here below are few estimates of the magnitude of rotation proposed by various authors. Burek (1970) proposed ~25° of counterclockwise rotation since the Miocene, whereas Schult (1974), and Souriot and Brun (1992) suggested 10° of rotation since the early Pliocene. From the geological and structural analysis of the Ethiopian Plateau and Danakil Microplate, Tazieff et al. (1972) proposed ~18° counterclockwise rotation. Chu and Gordon (1998) computed a counterclockwise angular velocity of 1.22°/My for the Danakil Microplate with respect to the stable Nubian Plate. Even though the angular velocity of the Danakil Microplate is not uniform since its breakup, it takes ~25 Ma to achieve a 30° counterclockwise rotation.

It is assumed that counterclockwise rotation of the Danakil Microplate started since its separation from Nubia, but at the same (slow) angular velocity as the Arabian plate. Faster rate of rotation commenced most probably in the Pliocene period as the Gulf of Aden propagated westward through the Gulf of Tadjoura to the central Afar; and hence Souriot and Brun (1992) computed a 10° rotation for the last ~4 Ma that led to a higher rate of rotation. Based on the crank-arm model (Sichler, 1980), Souriot and Brun (1992) proved that accelerated counterclockwise rotation of the Danakil Microplate for the last 4 Ma caused concentrated extension in the Danakil Depression, subtle extension and clockwise rotation in the central Afar, oblique extension in the Gulf of Tadjoura and right-lateral strike-slip faulting in the southern Afar Depression.
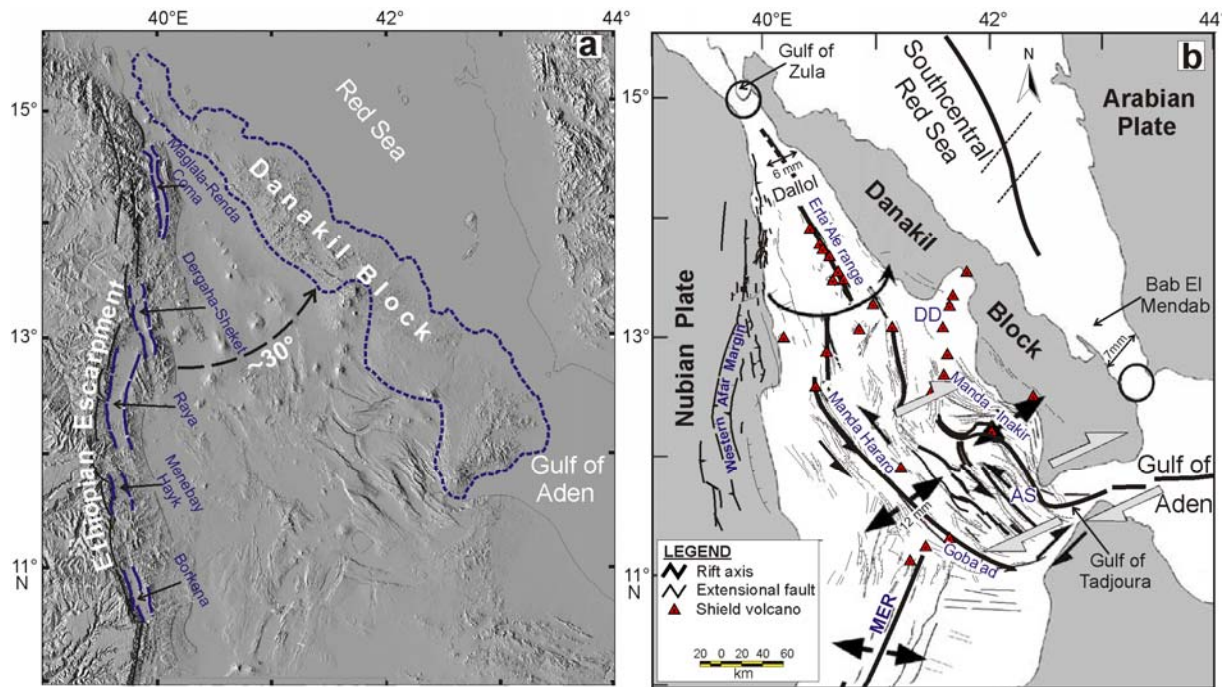
Figure 4.7 Outline of the western and eastern margins of the Afar Depression. N-S oriented but arcuate-shaped marginal grabens characterize the western Afar margin. (a) Shaded relief image showing the positions of the Danakil Microplate and western Afar marginal basins (modified after Tesfaye et al., 2003). (b) Strike-slip and oblique faulting associated with extensional tectonics; DD-Dadar graben, AS-Asal rift (modified after Manighetti et al., 2001).

4.5.3 Southern Afar Margin

The E-W–running Somalian escarpment (southern Afar escarpment) limits the southern propagation of the Afar Depression. The southern escarpment is characterized by book-shelf type faulted blocks tilting away from the Afar Depression (Beyene and Abdelsalam, 2005). It is a wide zone, intensely faulted by the westward propagators of the Gulf of Aden and reactivated NNW–oriented Marda faults, and with steeply tilted book-shelf type faulted blocks. No marginal grabens are developed adjacent to the Somalian escarpment. Instead E-W aligned local half-grabens, bounded by bedding and fault planes constitute the middle–lower portions of the southern margin.

4.6 Extensional Structures along the Western Margin and Active Rift Axes of the Afar Depression

Most of the Oligocene–Present extensional deformation structures constituting the EARS have been interpreted as reactivated features of the mobile Mozambique belt and the Arabian-Nubian shield (Korme et al., 2004, and references therein). The junction of the north-northwest–trending western Afar margin and the northeast–trending northern MER is an

intensely faulted and deformed zone. The arcuate accommodation zone (concave eastward opening fault zone) marks the boundary between the two tectonically distinct fault patterns.

4.6.1 The Erta'Ale Range

The Erta'Ale Range is one of the volcano-tectonically active segments of the Afar Depression, which is the onland southern termination of the Red Sea rift (Tazieff et al., 1972; Manighetti et al., 1998) and is composed of roughly NNW-SSE aligned seven volcanic centers: Gada'Ale, Alu, Dalaffilla, Borale'Ale, Erta'Ale, AleBagu and Hayli'Gub, from north to south (Barrat et al., 1998). The axial zone of Erta'Ale Range is characterized by active normal faulting and diffuse volcanism, which is mainly basaltic in composition, but with minor felsic derivatives inter-bedded with the tholeiitic basalts (Barberi and Varet, 1970; Barrat et al., 1998; Amelung et al., 2000).

In order to evaluate the Pleistocene–Recent rift-axis kinematics and geometry of the Erta'Ale Range, structural data have been collected along the entire western part of the range. In the eastern part of the depression, structural data have been acquired from well-georeferenced and processed Landsat-5 ETM image, as the area is difficult to access. Most of the structures are extension fractures and elliptical caldera collapses of various sizes and, in some places, normal faults with throws not exceeding 10 m. An extension fracture is a structural feature where the separation between the two blocks is commonly the result of tectonic stresses normal to the fracture surface (Acocella and Korme, 2002). Because of the location (axial range of the northern Afar Depression), trend (parallel to the Erta'Ale Range trend), and age (Pleistocene–Present) of the open fractures, their extension directions result from the existing kinematics of the Ethiopian plateau and Danakil Microplate in the depression. A total of ~60 fracture orientations and 23 asperities were measured from the western side of the Erta'Ale Range. All measured open fractures have an opening between 0.05 and 3 m and a length between 5 and 600 m; their depth of penetration, ~700 m, is inferred from mechanical considerations (Acocella and Korme, 2002, and references therein). The asperities along the walls of open fractures were sharp, fresh and unaffected by erosion and other secondary deformation, as for example shown in Figure 4.8a. This physical property, together with the late Pleistocene–Recent age of the rocks, confirms that the fractures are active features in the Erta'Ale Range. About 23 open fractures, which have clear asperities, were measured and all consistent with an overall ENE-WSW (066°) extension direction of the open fractures orthogonal to the mean NNW-SSE (337°) trend of the Erta'Ale Range rift axis (Fig. 4.8b–d). Moreover, the alignment of the six shield volcanoes, except the

AleBagu (Fig. 4.4a), and the trend of their elliptical calderas overlap with the mean trend of the extension fractures and normal faults of the Erta'Ale Range.
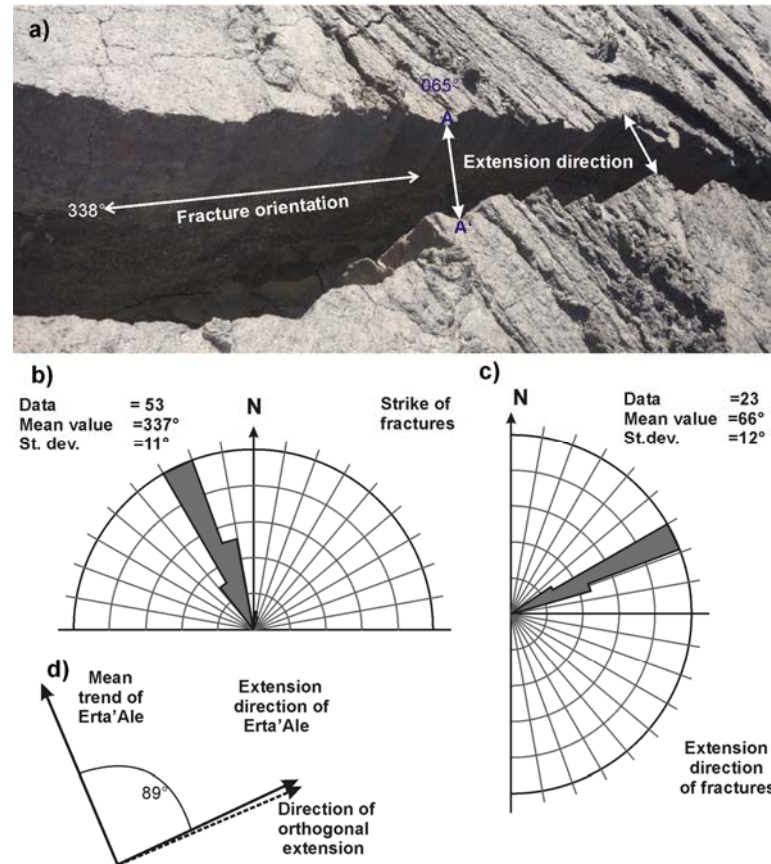
Figure 4.8 Determination of the trend and extension direction of open fractures of the Erta'Ale Range, northern Afar Depression. (a) Active open fracture whose asperities A and A' match to give the opening direction of the Erta'Ale Range (arrow). (b) Orientation, and (c) Opening direction of the Erta'Ale Range fractures. (d) The 89° angle between the fracture strike and extension direction suggests extension orthogonal to the fractures.

4.6.2 The Tendaho–Manda Hararo Rift

The NNW– to NW–trending Tendaho–Manda Hararo graben is the southern section of the Danakil Depression, which represents the southern end of the Red Sea propagator (Figs. 4.3 and 4.7b). Tendaho graben is ~150 km long and its width varies from ~25 km near its northern and southern tips to >50 km in its center (Acocella, 2010). The Tendaho–Manda Hararo is a concave eastward graben that encompasses N-S–trending axial faults at the Manda Hararo area, NW-SE–trending central graben, and ESE-WNW–trending Goba'ad rifts (Fig. 4.11; Tesfaye et al., 2003). Because of this unique geometric setup, the Tendaho graben does not directly merge into the MER; instead it bends to the east and joins the Gulf of Aden–trend structures. The Afar Stratoid series constitutes the edges of the Tendaho rift; the rift basin is filled with Holocene lacustrine and alluvial deposits and with post-Stratoid basalt flows (Abbate et al., 1995) as young as ~ 0.3 Ma (Acocella, 2010). The Tendaho–Manda

Hararo rift is at the center of the Afar triple junction and the influence of the other two arms of the junction (the Gulf of Aden and MER) for the geometric alignment of the Tendaho rift is significant.

In order to evaluate the Pleistocene axial zone trend of the Tendaho graben, structural data have been collected in the field along the asphalted road leading to the town of Semera, and from the Landsat-5 ETM image. The trends of the graben bounding faults are variable, from a nearly N-S trend at the northern end of the graben to NW-SE trend at the central part and WNW-ESE trend near the triple junction (Fig. 4.11). To avoid the geometric complexity all measurements were taken from the NW-SE–trending central Tendaho graben. About 44 fracture orientations and 21 fracture extensions are computed to assess the general view of the central Tendaho graben. The measured fractures range from few meters to several kilometers and their opening ranges from 0.05 to 10 m. The asperities along the walls of fractures were still sharp, fresh and easily measurable, as for example shown in Figure 4.9a. The average trend of the Tendaho rift is 328°, deviated by about 9° to the west from the average trend of Erta'Ale Range rift axis (Figs. 8b and 9b) and the average extension direction, 053°, is still nearly orthogonal (Fig. 4.9c and d).
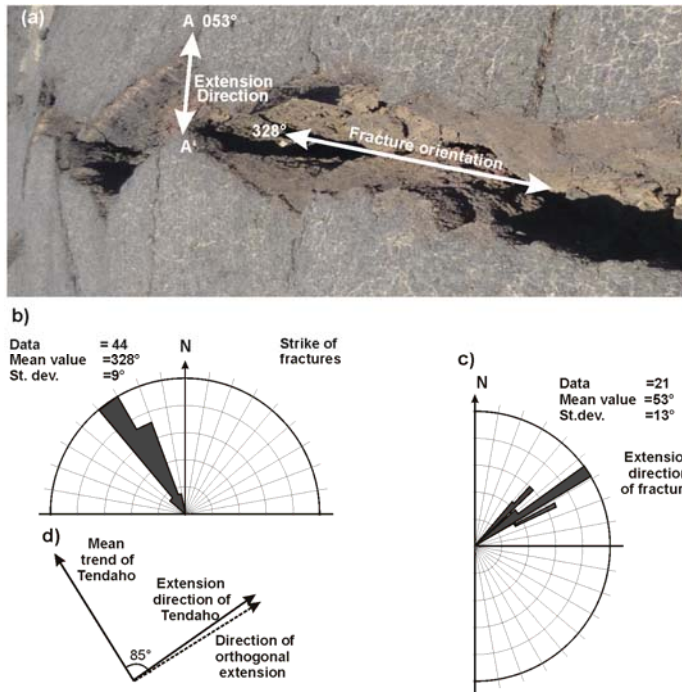
Figure 4.9 Determination of the trend and extension direction of extensional fractures of the Tendaho graben, central Afar Depression. (a) A stratoid series with an active extension fracture whose asperities A and A' match to give the best fit of the fracture (double arrow). (b) Average trend of fractures; and (c) Average extension direction of the Tendaho graben fractures. (d) The 85° angle between the fracture trend and extension direction suggesting extension still orthogonal to the trend.

4.6.3 The Western Afar Margin

The western Afar margin also called the Ethiopian escarpment is a N-S–running physiographic feature that marks the incipient breakup of the Afar Depression. The fault-plane escarpment is eroded and dissected by eastward-flowing rivers and few transverse structures (Wolfenden et al., 2005) (Fig. 4.10a). At the base of the escarpment, there are series of tectonically and seismically active marginal grabens arranged in an en-echelon

manner (Fig. 4.7a; Morton and Black, 1975; Tesfaye et al., 2003; Wolfenden et al., 2005). Structural and remote sensing analyses revealed that the western Afar margin evolved by gradual pure extensional deformation along the border faults (Asfaw et al., 1990). In contrast, Chorowicz et al. (1999) proposed that the western Afar margin developed as a result of pure strike-slip motion. Field observation and Remote Sensing data of this study, however, revealed that in the western margin there are series of step-faults and tilted fault-blocks, which are common characteristics of dip-silp or oblique-slip deformation. But, it has been still difficult to analyze the contribution of strike-slip component for the development of the western Afar margin.
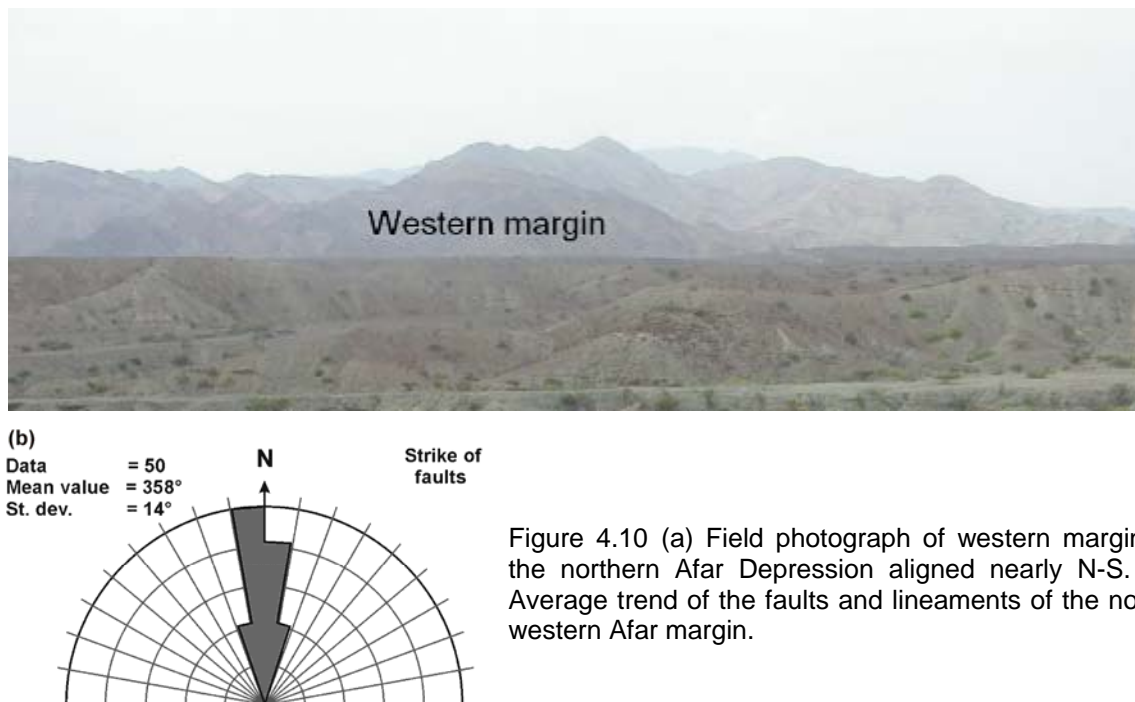
Figure 4.10 (a) Field photograph of western margin of the northern Afar Depression aligned nearly N-S. (b) Average trend of the faults and lineaments of the north-western Afar margin.

Most of the structural measurements of the western escarpment were taken from the Landsat-5 ETM image. The western Afar margin exhibits an arcuate structure in its center (Fig. 4.11) that comprises N-S, NNE, and SSW oriented border faults. More than 50 structural data (fault strike) have been collected from field measurements and landsat-5 images. Even though the structural alignment of western Afar margin is not uniform, the structural analysis reveals that this ~500-km-long margin has an average N-S trend (Fig. 4.10b). The lack of slickensides and other subsidiary structures (i.e., asperities) make the kinematics of the marginal structures still indistinct. The direction of extension in this study is extracted from previous works (e.g., Collet et al., 2000).

The structural setup of the Afar Depression and the Ethiopian escarpment is illustrated in Figure 4.11. The strike and extension direction of open fractures/normal faults of Erta'Ale

and Tendaho-Manda Hararo axial rift zones vary by about 009° and 13°, respectively. The deviation in the general orientation of the central Tendaho graben by about 009° to the west from the average trend of the Erta'Ale Range shows that the involvement of the Gulf of Aden rift (E-W–oriented ridge) is higher than the MER. Extension is orthogonal to the NW-SE– trending fractures. The Ethiopian escarpment, on the other hand, shows distinct geometry: a N-S–trending border faults accommodating dip-slip or oblique extension (Fig. 4.10).
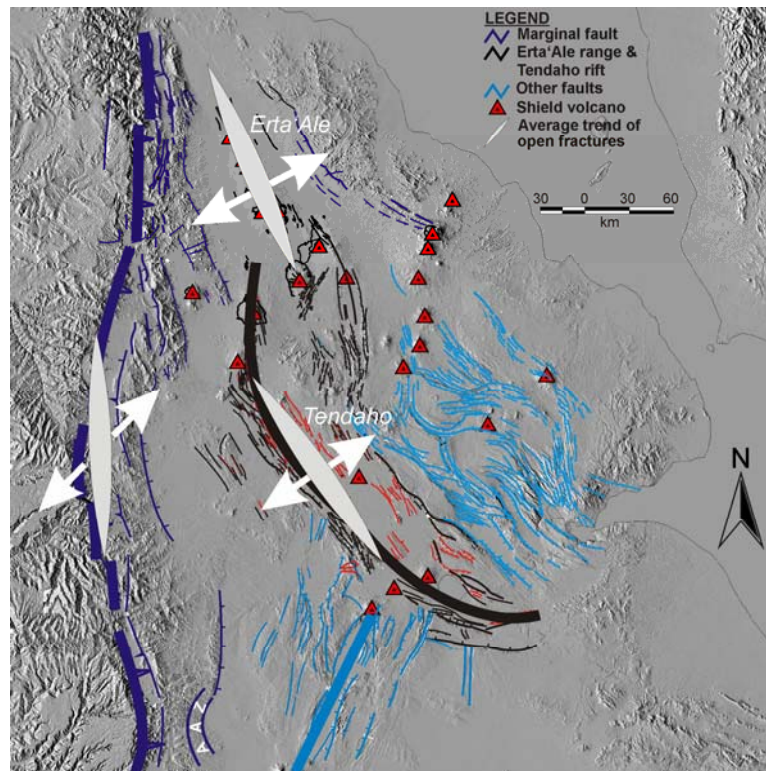
Figure 4.11 Outline of the structural setup of the Afar Depression with their respective extension direction. The Erta'Ale Range and the Manda-Hararo–Tendaho rifts, southern limit of the Red Sea rift, are aligned oblique to the western Afar margin. AAZ-arcuate accommodation zone. Extension direction for the western Afar margin (after Collet et al., 2000).

4.7 Reconstruction of the Nubian-Arabian-Somalian Plates

The triangular-shaped Afar Depression was formed as a result of disintegration of the Nubian plate immediately after or contemporaneous with the massive outpouring of the Afar plume magmatism at ~30 Ma (Hofmann et al., 1997; Beyene and Abdelsalam, 2005). When the Red sea and Gulf of Aden ridges arrived near the triple junction (~20 Ma; Courtillot et al., 1987) through the Gulf of Zula and Gulf of Tadjoura, respectively, the Afar Depression started to open (Audin et al., 2004). The relative motions of the Arabian and Somalian plates with respect to the stable Nubian plate were first studied by McKenzie et al. (1970) based on simple observations on the Red Sea coast lines and associated transform faults. Following the

previous studies, the Nubian, Arabian, Somalian, and Danakil plates were reconstructed to their pre-rift positions based on various paleomagnetic data and best fit hypothesis (e.g., Le Pichon and Francheteau, 1978; Jestin et al., 1994; Chu and Gordon, 1998; Collet et al., 2000; Eagles et al., 2002).

From the regional paleo-stress analysis, the Arabian plate commenced its movement towards the northeast during the Oligocene, (Collet et al., 2000). The northeast movement of the Arabian plate, as a result of the slab pull at Zagros Orogenic Front, generated continental rifting along the Gulf of Aden and Red Sea with a N45°E direction of the extension (Beyene and Abdelsalam, 2005). Various authors (e.g., Hofmann et al., 1997; Watchorn et al., 1998; D'Acremont et al., 2005; Wolfenden et al., 2005) estimated that continental rifting in the Gulf of Aden and Red Sea rifts commenced at ~35–28 Ma, just prior or contemporaneous with the Ethiopian flood volcanism at ~30 Ma. The faunal age estimated from the northern Somalia initial sy-nrift clastic sequences (southern margin of Gulf of Aden) is ~35 Ma (Watchorn et al., 1998), which is in good agreement with the age estimates of the above authors.

In reconstructing the Nubian, Arabian, Somalian and Danakil plates, the timing of incipient breakup was taken to be Oligocene (35–30 Ma). The aggregate angle of rotation of the Arabian and Danakil plates are -7° and -30°, respectively. In the Oligocene period, all the plates had one thing in common; they all met at the current Afar Depression (Fig. 4.12a). With time, the Gulf of Aden and Red Sea rift propagators directed onland to Afar, and detached the Danakil Microplate from the Nubian plate along the current western Afar margin. The direction of extension, NE-SW, for both the Red Sea and Gulf of Aden rifts remained the same throughout their formation, despite some differential rate of extension along the rift-axes. As a result of simple kinematic history, reconstructions of the pre-rift condition of the Nubian, Arabian, and Somalian plates have been rather straightforward. Plate reconstruction of the region becomes more complex when the geodynamically active Danakil Microplate is included.

To reconstruct the Nubian-Arabian-Somalian plates, the exact geometry and dynamics of the Danakil Microplate should be assessed first. The compilation of structural measurements, best-fit model hypothesis and other previous data allow to consider that the Danakil Microplate, originally had located to the southwest near the arcuate accommodation zone (Tesfaye et al., 2003), was connected with all the three major plates (Fig. 4.12a). Throughout Oligocene–middle Miocene, the evolution of the Afar Depression has been controversial due to poor constraints on the kinematics of the Danakil Microplate with regard to the Nubia–Somalia–Arabia plate motions (Manighetti et al., 2001; Eagles et al., 2002).

Some models show that the Arabian plate and the elongated Danakil Microplate rotate counterclockwise since the Oligocene about a pole fixed in the northern Red Sea region (Sichler, 1980; Souriot and Brun, 1992). When the pole of rotation is fixed fur to the north, it would favors pure dextral-slip deformation in the western Afar margin and counterclockwise rotation for the Danakil Microplate at ~31 Ma (Wolfenden et al., 2004). A bit earlier, Eagles et al. (2002) proposed an oblique-slip motion for the northwestern Afar Depression, which was determined from poles of rotation studies. From the interpretations of Eagles et al. (2002) and the regional stress-field, the whole region of Afar including the Danakil Microplate was under the influence of the far-field stress generated along the Zagros Orogenic Front until the middle Miocene. Throughout the Oligocene–middle Miocene, the N40°E oriented extensional motion formed 'pull-part basin' west of the Danakil Microplate, the Afar Depression, and the Microplate translated to the northeast without significant counterclockwise rotation (Fig. 4.12b; Collet, et al., 2000), but at a slower angular rate similar with that of the Arabian plate.
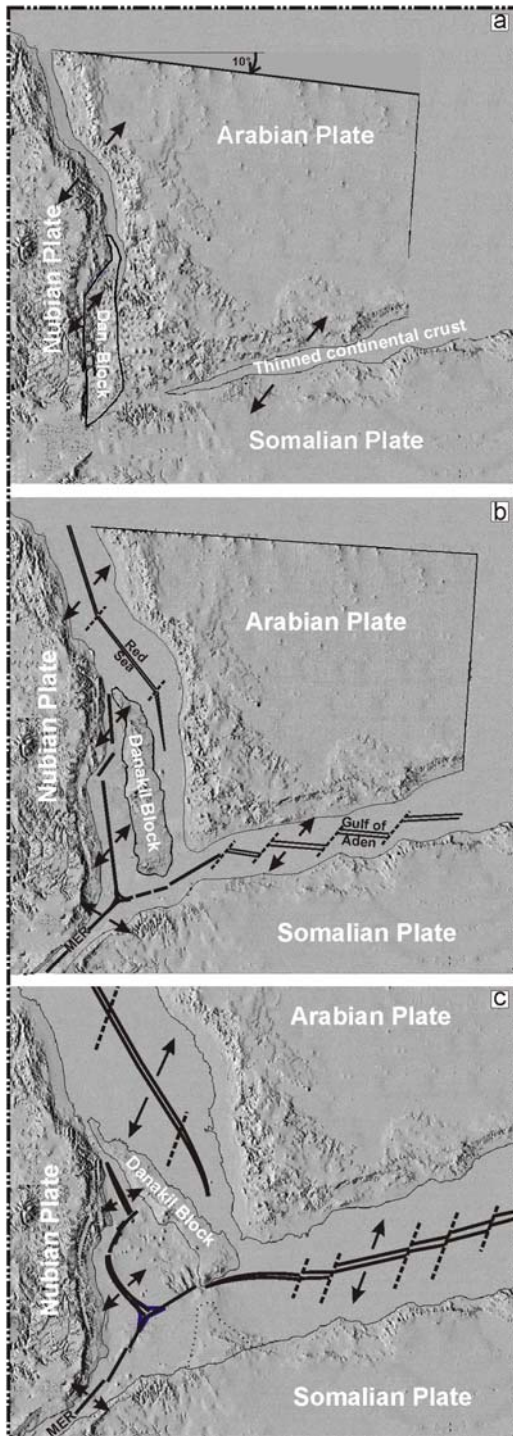
Figure 4.12 Nubian, Arabian, Somalian plate and the Danakil Microplate. The arrows show the relative motion of the plates at different stage of rifting. (a) Reconstruction of these plates to pre-rifting positions (Oligocene) based on the Red Sea and Gulf of Aden coastlines and the paleomagnetic data. (b) Middle-Late Miocene period; the commencement of northern MER and birth of the Afar triple junction. (c) The present geometric setup of the Red Sea – Gulf of Aden and MER. (modified after Collet et al., 2000).

The major change in the kinematics of the Danakil Microplate occurred when intense faulting and dyking in the central Afar Depression, rapid seafloor spreading in the southcentral Red Sea, and onland propagation of the Gulf of Aden affected the region (Fig. 4.12c). The uneven involvement of forces has produced different rate of extension along the

interior Afar Depression. The central Afar Depression accumulates higher rate of extension (12 mm/yr), while the northern Afar owed for lower rate of extension (6 mm/yr).

4.8 Birth and Growth of the Afar Triple Junction

The Gulf of Aden–Red Sea–MER triple junction, the only active continental rift-rift-rift junction, lies in a broad and tectonically complex zone within the central Afar Depression (Acton et al., 2000; Tesfaye et al., 2003) (Fig. 4.13b). The development of the junction, however, is disputable due to poor constraints on the timing of incipient breakup of the northern MER (third arm of the triple junction) and the kinematics of Danakil Microplate motion (Manighetti et al., 2001; Eagles et al., 2002; Wolfenden et al., 2004). The NNW–trending southern Red Sea rift and the NNE–trending MER converge at the southern end of the Tendaho graben, but the WSW–trending Gulf of Aden Rift fails to directly merge with the other two rift trends. Instead, it bifurcates in the eastern part of central Afar (Tesfaye et al., 2003) forming horse-tail type sub-parallel grabens. Because of the interaction of these three rifts in one region, a tectonically complex zone of extensional deformation is present in central Afar Depression (Manighetti et al., 1998, 2001). Tesfaye et al. (2003) proposed that the triple junction is not a narrow zone in the depression, instead it is a wide region around the Tendaho–Goba'ad grabens bounded by lat 11°–11°48'N and long 40°45'–41°42'E. So far, there is no sub-aerial triple junction recorded in the globe to compare the Afar triple junction with, and hence references are always from the ocean triple junctions.

From the middle–late Miocene geometric reconstruction of the Nubian–Somalian–Arabian–Danakil plates, the Paleo-triple junction (i.e., the birth place of the Afar triple junction) was positioned ~160 km to the SW from the current triple junction near the Addo-do graben (Fig. 4.13a; Wolfenden et al., 2004). Tesfaye et al. (2003) postulated that the Oligocene triple junction (paleo-triple junction) of Afar was located at about lat 10°N, in an arcuate accommodation zone (arcuate pattern of faults seen in high resolution imagery) farther SSW of its present location (Fig. 4. 13b). However, the actual timing for the initiation of the triple junction is still a controversy. Geological and remote sensing data from the northern MER indicate that initial crustal extension commenced in the middle Miocene between 12 and 10 Ma (Woldegabriel et al., 1990; Ebinger et al., 2000; Wolfenden et al., 2004). The late commencement of rifting in the third arm (northern MER) hindered the birth of the triple junction until the middle Miocene (~11 Ma). Wolfenden et al. (2004), instead, proposed that in the middle Miocene, the MER spread NE via the Arboye border fault as the marginal faults of the southern Afar Depression migrated southward via the Ankober border

fault (Fig. 4.5). This region effectively links the border faults of the southern Red Sea, the Gulf of Aden and the MER and gives a clue about the existence of the paleo-triple junction near this area.
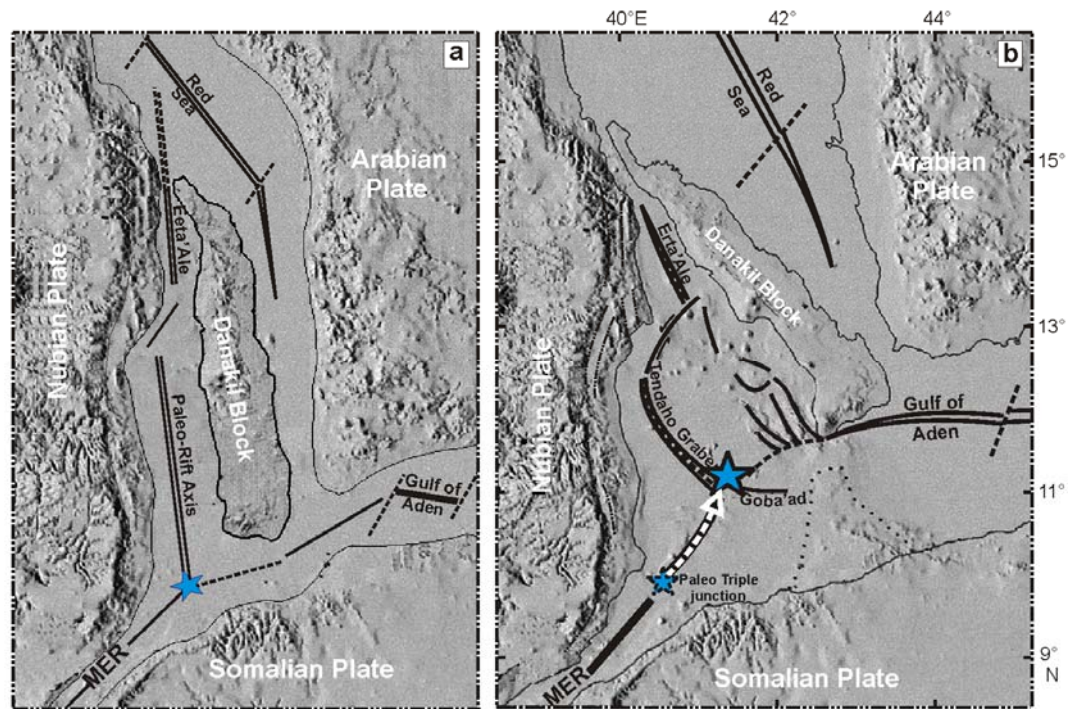
Figure 4.13 Structural reconstruction of the Afar triple junction. (a) Location of the birth of Afar triple junction (~11 Ma, Wolfenden et al., 2004). (b) The present location of the triple junction and geometric setup of the Afar Depression (modified after Collet et al., 2000).

Now the paleo-triple junction would clearly separate the entire Afar Depression from the MER and is serving as a tectonic boundary between these two regions. The movement vector of the triple junction is to the NE, which is parallel to the major extension direction of the Red Sea and Gulf of Aden rifts, implying that the separation of Arabia from the Nubian and Somalian plates is the main cause for the migration of the triple junction. The Afar triple junction has migrated over a distance of ~160 km to the NE for the last 11 Ma (Tesfaye et al., 2003; Wolfenden et al., 2004), with an average rate of ~14 mm/yr. This rate of movement of the triple junction is analogous with the average rate of extension (12–18 mm/yr) of the central Afar Depression, Red Sea and Gulf of Aden.

4.9 Discussion and Conclusions

The location of the Afar Depression in a geodynamically complex region, where both the far-field stress and upwelling mantle plume take part in the volcano-tectonic activities of the region, constrains to poorly trace the pre-rift position of the Afar province. The development of the Afar Depression has, therefore, been considered as active and/or passive rifting,

depending on the timing and progression of the rifting process related to the Gulf of Aden, the Red Sea, and the MER, the raise of the Ethiopian dome and associated continental flood volcanism (Beyene and Abdelsalam, 2005). Even though the detail of the evolution of the Afar Depression is still being disputed, the Red Sea and Gulf of Aden rifts have been developed as a result of the collision of Arabia with the Eurasian plate that generated initial crustal extension along these rifts during the early Oligocene (~35 Ma; Watchorn et al., 1998; D'Acremont et al., 2005; Wolfenden et al., 2005), just prior to the outpouring of the Ethiopian flood basalts at ~30 Ma (Hofmann et al., 1997).

Joffe and Garfunkel (1987) proposed that the incipient crustal deformation in the Ethiopian escarpment (western Afar margin) might have occurred as scattered faulting progressed in response to the passive rifting due to the convergence of Arabian plate along the Zagros Orogenic Front. With all these favorable conditions for rifting, the uprising Afar hotspot added further extensional stress that facilitates the lithospheric extension in the Afar Depression (Beyene and Abdelsalam, 2005). The combined effect of the stress fields (i.e., the far-field stress and upwelling mantle plume) of the region might have accelerated the evolution of the Afar Depression with strong extension parallel to the far-field stress.

Although the existing constraints on the exact timing of the initial Nubia-Arabia disintegration are sparse (Wolfenden et al., 2005), the Afar Depression started to open in the late Oligocene–early Miocene as a result of the far-field stress field along the Zagros Orogenic belt and/or the rising mantle plume over central Afar. Before the Afar breakup (early–middle Oligocene), the Danakil Microplate was located along the western Afar margin (Collet et al., 2000) firmly attached with the Nubian plate (Fig. 4.13a). Shortly after the breakup, between the late Oligocene and the middle Miocene, the motion vectors of the Danakil Microplate indicated a direction towards the NE (Collet et al., 2000), which was nearly parallel to the regional stress-field vector. This NE-SW–oriented stress field separated the Danakil Microplate from the Nubian plate along most probably a weak N-S–running suture zone (Korme et al., 2004), the western Afar escarpment. The Danakil Microplate then moved/translated obliquely to the NE direction, forming a pull-apart basin-type depression between the Ethiopian escarpment and the block itself until the middle–upper Miocene (Fig. 4.12b). Until then, the kinematic of the Afar Depression and the Danakil Microplate was analogous to that of the rift-bounding western Afar margin. The geometric setup and kinematics of the region were simple; nearly N–S oriented transtensional structures with oblique extension parallel to the regional stress-field. The elongated Danakil Microplate and

the paleo-rift axes of the newly formed depression were parallel to the western border faults and marginal grabens (Figs. 12b and 13a).

Contradicting to the oblique motion, Chorowicz et al. (1999) described en-echelon arrangement of sinistral strike-slip faults and releasing-bend basins parallel to the western Afar margin. These authors proposed a left-lateral strike-slip motion with the minimum principal stress oriented N20°E. Pure sinistral strike-slip motion for the Danakil Microplate is, however, poorly adequate to explain the geometric relationship between the western Afar border/marginal faults and the Danakil Microplate. The western Afar margin is characterized by N-S–trending antithetic normal/oblique faults and a right-stepping en-echelon system of marginal grabens. Such structural elements can be developed under tensile and/or transtensional stress fields. However, the regional stress-field in the Afro-Arabian region (i.e., Zagros Orogenic Front) did not favor pure tensile structures/dip-slip faults to occur along the western Afar margin. Instead, the most probable motion during the incipient breakup of the Danakil Microplate from the Nubian plate would be transtensional/oblique-slip motion.

During the middle Miocene, the drastic increase in displacement of the Arabian plate initiated the oceanization of the Gulf of Aden and the southcentral Red Sea (Collet et al., 2000). As a result, the oceanization of the Red Sea and the westward propagation of the Gulf of Aden through the Gulf of Tadjoura to the central Afar brought to halt the oblique-slip motion of the Danakil Microplate, and the block started to rotate in a counterclockwise motion. The NE spreading of the southcentral Red Sea (i.e., north of the Microplate) and the ENE–directed Afar expansion (Fig. 4.14) depicted a mechanical coupling effect, which was responsible for starting the rotation of the Danakil Microplate (Collect et al., 2000).

Although the Arabian plate and the Danakil Microplate shared in many respects a common tectonic history during the Oligocene–middle/late Miocene, the current kinematics and dynamics of these plates are different. The major change in kinematics of the region occurred when intense faulting and dyking in the central Afar Depression (i.e., Manda Hararo-Goba'ad, Manda Inakir, Asal rifts) and rapid oceanic spreading in the southcentral Red Sea affected the region (Fig. 4.14). Moreover, the development of new oceanic crust in the Red Sea and NE migration of the Afar triple junction imposed the Danakil Microplate to change its kinematics from translational/oblique-slip to rotational movements. During the onset of the Danakil Microplate breakup (Oligocene-Miocene) the regional stress field was oblique to the N-S–oriented western Afar border/marginal fault structures (Fig. 4.12b) and most of the deformation took place in the form of oblique-slip movement. This oblique-slip motion didn't change the kinematic of the Afar Depression; the paleo-rift axes (Figs. 4.12b

and 4.13a) remained nearly parallel to the border faults of the western Afar margin until the initiation of the Afar triple junction (~11 Ma; Wolfenden et al., 2005) at ~10°N. South of this paleo-triple junction, boundary faults developed concurrently with the deposition of felsic shields at 12–11 Ma (Wolfenden et al., 2005). These faults effectively linked the southern Afar and central MER.

Plate reconstructions envisage high stretching factors (ß ~3) in the southern– to central Afar Depression, suggesting that the dyke injected and densely faulted rift segments (Fig. 4.14) mark the beginning of formation of crust transitional between continental and oceanic (Wolfenden et al., 2005). Although the Red Sea rift and Afar Depression shared a common volcano-tectonic history until the middle–late Miocene, the current kinematics and dynamics of these rifts are very different. The aggregate rate of extension in the Afar Depression generally increases from ~6 mm/yr at the Gulf of Zula, north end of Afar Depression, to ~12 mm/yr in the Manda Hararo/Inakir rift, central Afar. In central Afar, the coupled lithospheric extension effect (the Red Sea and Gulf of Aden) enhances the rate of extension in the region. This rate of extension is equivalent with the rate of extension of the southcentral Red Sea (Fig. 4.14); however, they differ in that the Red Sea has experienced oblique rifting since its formation, whereas at the Afar Depression (i.e., the Erta'Ale Range and the Tendaho-Manda Hararo rift), the incipient oblique continental rifting changed to orthogonal (Figs. 4.8 and 4.9), most probably in the late Miocene–Pliocene indicating greater involvement of the upwelling mantle plume. This stress-field might have dominated the geodynamics of the region since the Pliocene. The greater rates of extension in the central Afar and southcentral Red Sea, therefore, enabled the Danakil Microplate to rotate in counterclockwise direction at greater angular speed (~2.5°/Ma) than the Arabian plate, which has experienced a total of ~7° since the incipient breakup of the Red Sea and Gulf of Aden rifts.

The Afar Depression, though it is the youngest continental–oceanic-type rift, adopts most of the common characteristics of matured oceanic ridges. The depression consists of a system of discontinuous en-echelon arrangement of basaltic ridges, flourished by linearly aligned volcanic edifices, which rise 700–1500 m from the rift floor. The NNE-SSW–trending axial zone within the Afar Depression is segmented into three parts. These are: the Erta'Ale Range, the Alyata and the Manda Hararo-Tendaho rift axes, which are arranged in an en-echelon, right-stepping array (Fig. 4.14). Convection of magma chambers underneath the ridge-axis and differences in spreading rate exert important control on rift segmentation pattern (Batiza, 1996), which are common characteristics of oceanic ridges.

In conclusion:

i. Continental breakup in the Afar Depression commenced in the form of oblique extension along the current N-S–trending western Afar margin.

ii. Oblique extension in the Afar Depression axial zone was gradually replaced by orthogonal extension between the middle/late Miocene–Pliocene.

iii. The Danakil Microplate had experienced simple translational motion until the end of middle Miocene and rotational motion afterwards.

iv. The major change in the kinematics and dynamics of the Danakil Microplate occurred concurrent with the introduction of new oceanic crust in the southcentral Red Sea, westward propagation of the Gulf of Aden to the central Afar, and the NE migration of the Afar triple junction.

v. Though the central Afar Depression has the highest extension rate in the entire Afar, the extension rate per unit width is smaller (~5 mm/yr/100 km), where as the Danakil Depression has the highest rate per unit width (12 mm/yr/100 km).
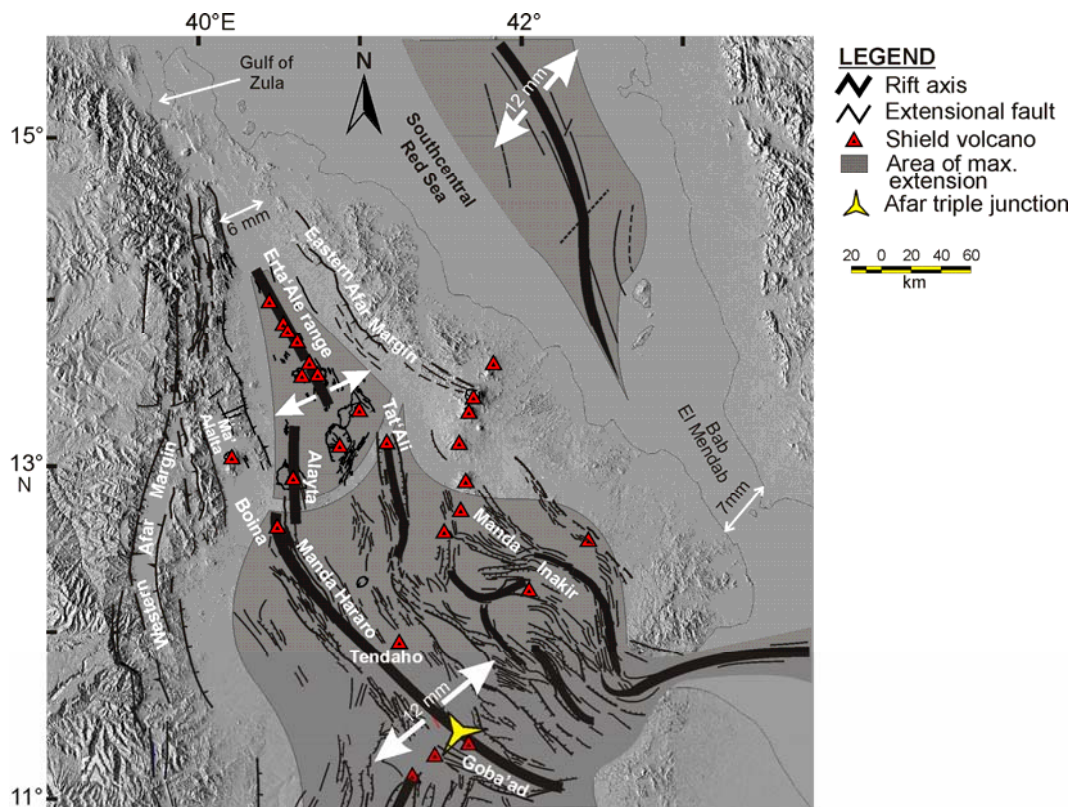
Figure 4.14 Structural outline of the Afar Depression and the southcentral Red Sea. Maximum extension rate, >12 mm/year, at the merger of the three rift axes and the southcentral Red Sea (modified after Tesfaye et al., 2003).

References:

Abbate E., Passerini P., and Zan L. 1995. Strike-slip faults in a rift area: A transect in the Afar Triangle, east Africa. Tectonophysics 241, 67–97.

Abebe B., Acocella V., Korme T., and Ayalew D. 2007. Quaternary faulting and volcanism in the Main Ethiopian Rift. Journal of African Earth Sciences 48, 115–124.

Acocella V. 2006. Regional and local tectonics at Erta'Ale caldera, Afar (Ethiopia). Journal of Structural Geology 28, 1808–1820.

Acocella V. 2010. Coupling volcanism and tectonics along divergent plate boundaries: Collapsed rifts from central Afar, Ethiopia. Geological Society of America Bulletin 122, 1717–1728.

Acocella V. and Korme T. 2002. Holocene extension direction along the Main Ethiopian Rift, East Africa. Terra Nova 14, 191–197.

Acton G.D., Stein S., and Engeln J.F. 1991. Block rotation and continental extension in Afar: A comparison to oceanic microplate systems. Tectonics 10, 501–526.

Acton G., Tessema A., Jackson M., and Bilham R. 2000. The tectonic and geomagnetic significance of paleomagnetic observations from volcanic rocks of central Afar. Earth and Planetary Science Letters 180, 225–241.

Amelung F., Oppenheimer C., Segall P., and Zebker H. 2000. Ground deformation near Gada Ale volcano, Afar, observed by radar interferometry. Geophysical Research Letters 27, 3093–3096.

Asfaw B., Ebinger C., Harding D., White T., and Woldegabriel G. 1990. Space-based imagery in paleo-anthropological research: An Ethiopian example. National Geographic Research 6, 418–434.

Audin L., Quidelleur X., Coulie E., Courtillot V., Gilder S., Manighetti I., Gillot P. Y., Tapponnier P., and Kidane T. 2004. Palaeomagnetism and K-Ar and ^{40}Ar/^{39}Ar ages in the Ali Sabieh area (Republic of Djibouti and Ethiopia): constraints on the mechanism of Aden ridge propagation into southeastern Afar during the last 10 Myr. Geophysical Journal International 158, 327–345.

Barberi F. and Varet J. 1970. The Erta'Ale Volcanic Range (Danakil depression, northern Afar, Ethiopia). Bulletin Volcanologique 34, 848–917.

Barberi F. and Varet J. 1975. Recent volcanic units of Afar and their structural significance. In: Pilger A. and Rösler A. (Eds.), Afar Depression of Ethiopia. Schweizerbart, (Inter-Union Commission on Geodynamics Scientific Report 14), Stuttgart, Germany, 174–178.

Barrat J.A., Fourcade S., Jahn B.M., Cheminee J.L., and Capdevila R. 1998. Isotope (Sr, Nd, Pb, O) and trace-element geochemistry of volcanics from the Erta'Ale Range (Ethiopia). Journal of Volcanology and Geothermal Research 80, 85–100.

Batiza R. 1996. Magmatic segmentation of mid-ocean ridges: a review. In: MacLeod C.J., Tyler P.A., and Walker C.L. (Eds), Tectonic, Magmatic, Hydrothermal and Biological Segmentation of Mid-Oceanic Ridges. Geological Society, London, Special Publication 118, 103–130.

Bell R.E. and Buck R. 1992. Crustal control of ridge segmentation inferred from observations of the Reykjanes Ridge. Nature 357, 583–586.

Beyene A. and Abdelsalam M. G. 2005. Tectonics of the Afar Depression: A review and synthesis. Journal of African Earth Sciences 41, 41–59.

Bilham R., Bendick R., Larson K., Mohr P., Braun J., Tesfaye S., and Asfaw L. 1999. Secular and tidal strain across the Main Ethiopian Rift. Geophysical Research Letters 26, 278–292.

Boccaletti M., Mazzuoli R., Bonini M., Trua T., and Abebe B. 1999. Plio-Quaternary volcanotectonic activity in the northern sector of the Main Ethiopian Rift; relationships with oblique rifting. Journal of African Earth Sciences 29, 679–698.

Bosworth W., Huchon P., and McClay K. 2005. The Red Sea and Gulf of Aden Basins. Journal of African Earth Sciences 43, 334–378.

Bosworth W. and Strecker M.R. 1997. Stress field changes in the Afro-Arabian rift system during the Miocene to Recent period. Tectonophysics 278, 47–62.

Burek P.J. 1970. Paleomagnetic evidence for a counterclockwise rotation of the Danakil horst: Eos (Transactions, American Geophysical Union) 51, 271.

Chorowicz J. 2005. The East African Rift System. Journal of African Earth Sciences 43, 379–410.

Chorowicz J., Collet B., Bonavia F.F., and Korme T. 1994. Northwest to north-northwest extension direction in the Ethiopian Rift deduced from the orientation of extension structures and fault-slip analysis. Geological Society of America Bulletin 105, 1560–1570.

Chorowicz J., Collet B., Bonavia F., and Korme T. 1999. Left-lateral strike-slip tectonics and gravity induced individualisation of wide continental blocks in the western Afar margin. Eclogae Geologicae Helvetiae 92, 149–158.

Chu D. and Gordon R.G. 1998. Current plate motions across the Red Sea. Geophysical Journal International 135, 313–328.

CNR-CNRS, Afar team, 1973. Geology of northern Afar (Ethiopia). Revue de Géographie Physique et de Geologie Dynamique 2, 343–390.

Cochran J. and Martinez F. 1988. Evidence from the northern Red Sea on the transition from continental to oceanic rifting. Tectonophysics 153, 25–53.

Collet B., Taud H., Parrot J.F., Bonavia F., and Chorowicz J. 2000. A new kinematic approach for the Danakil Block using a digital elevation model representation. Tectonophysics 316, 343–357.

Corti G. 2009. Continental rift evolution: From rift initiation to incipient breakup in the Main Ethiopian Rift, East Africa. Earth Science Reviews 96, 1–53.

Courtillot V., Achache J., Landre F., Bonhommet N., Montigny R., and Feraud G. 1984. Episodic spreading and rift propagation; new paleomagnetic and geochronologic data from the Afar nascent passive margin. Journal of Geophysical Research 89, 3315–3333.

Courtillot V., Armijo R., and Tapponnier P. 1987. Kinematics of the Sinai triple junction and a two phase model of Arabia-Africa rifting. In: Coward M.P., Dewey J.F., and Hancock P.L.

(Eds.), Continental extensional tectonics. Geological Society of America Special Paper 28, 559–573.

Davidson A. and Rex D.C. 1980. Age of volcanism and rifting in southwestern Ethiopia. Nature 283, 657–658.

D'Acremont E., Leroy S., Beslier M.O., Bellahsen N., Fournier M., Robin C., Maia M., and Gente P. 2005. Structure and evolution of the eastern Gulf of Aden conjugate margins from seismic reflection data. Geophysical Journal International 160, 869–890.

Eagles G., Gloaguen R., and Ebinger C. 2002. Kinematics of the Danakil Microplate. Earth and Planetary Science Letters 203, 607–620.

Ebinger C. 2005. Continental breakup: the East African perspective. Astronomy and Geophysics 46, 2.16–2.21.

Ebinger C.J. and Casey M. 2001. Continental breakup in magmatic province. An Ethiopian example. Geology 29, 527–530.

Ebinger C.J., Bechtel T.D., Forsyth D.W., and Bowin C.O. 1989. Effective elastic plate thickness beneath the East African and Afar plateaus and dynamic compensation of the uplifts. Journal of Geophysical Research 94, 2883–2901.

Ebinger C., Yemane T., Harding D., Tesfaye S., Rex D., and Kelley S. 2000. Rift deflection, migration, and propagation: linkage of the Ethiopian and Eastern rifts, Africa. Geological Society of America Bulletin 102, 163–176.

Harris A., Carniel R., and Jones J. 2005. Identification of variable convective regimes at Erta'Ale Lava Lake. Journal of Volcanology and Geothermal Research 142, 207–223.

Hayward N.J. and Ebinger C.J. 1996. Variations in the along-axis segmentation of the Afar rift system. Tectonics 15, 244–257.

Hofmann C., Courtillot V., Feraud G., Rouchett P., Yirgu G., Ketefo E., and Pik R. 1997. Timing of the Ethiopian flood basalt event and implications for plume birth and global change. Nature 389, 838–841.

Hofstetter R. and Beyth M. 2003. The Afar Depression: interpretation of the 1960-2000 earthquakes. Geophysical Journal International 155, 715–732.

Jestin F., Huchon P., and Gaulier J.M. 1994. The Somalia plate and the East African Rift System: present-day kinematics. Geophysical Journal International 116, 637–654.

Joffe S. and Garfunkel Z. 1987. Plate kinematics of the Circum Red Sea – A re-evaluation. Tectonophysics 141, 5–22.

Kazmin V., Seife M.B., Nicoletti M., and Petrucciani C. 1980. Evolution of the northern part of the Ethiopian rift. Atti dei Convegni Lincei 47, 275–292.

Keranen K. and Klemperer S.L. 2008. Discontinuous and diachronous evolution of the Main Ethiopian Rift: Implications for development of continental rifts. Earth and Planetary Science Letters 265, 96–111.

Korme T., Chorowicz J., Collet B., and Bonavia F.F. 1997. Volcanic vents rooted on extension fractures and their geodynamic implications in the Ethiopian Rift. Journal of Volcanology and Geothermal Research 79, 205–222.

Korme T., Acocella V., and Abebe B. 2004. The Role of Pre-existing Structures in the Origin, Propagation and Architecture of Faults in the Main Ethiopian Rift. Gondwana Research 7, 467–479.

Lahitte P., Coule M., Mercier N., Kidene T., and Gillot P.Y. 2001. K–Ar and TL volcanism chronology of the southern ends of the Red Sea spreading in Afar since 300 ka. Earth and Planetary Science Letters 332, 13–20.

Lahitte P., Gillot P., Kidane T., Courtillot V., and Bekele A. 2003. New age constraints on the timing of volcanism in central Afar, in the presence of propagating rifts. Journal of Geophysical Research, B 108, ECV 10.1–10.17.

Langmuir C.H., Klein E. M., and Plank T. 1992. Petrological systematics of mid-ocean ridge basalts: constraints on melt generation beneath ocean ridges. In: Morgan P. J., Blackman D. K. and Sinton J. M. (Eds.), Mantle flow and melt generation at Mid-Ocean Ridges. AGU Geophysical Monographs 71, 183–280.

Le Pichon X. and Francheteau J. 1978. A plate-tectonic analysis of the Red Sea–Gulf of Aden area. Tectonophysics 46, 369–406.

MacDonald K.C., Fox P.J., Perram L.J., Eissen M.F., Haymon R.M., Miller S.P., Carbotte S.M., Cormier M. H., and Shor, A.N. 1988. A new view of the mid-ocean ridge from the behavior of ridge-axis discontinuities. Nature 335, 217–225.

Manighetti I., Tapponnier P., Courtillot V., Gruszow S., and Gillot P.Y. 1997. Propagation of rifting along the Arabia Somalia plate boundary: The Gulf of Aden and Tadjoura. Journal of Geophysical Research 102, 2681–2710.

Manighetti I., Tapponnier P., Gillot P.Y., Jacques E., Courtillot V., Armijo R., Ruegg J.C., and King G. 1998. Propagation of rifting along the Arabia–Somalia plate boundary; into Afar. Journal of Geophysical Research 103, 4947–4974.

Manighetti I., Tapponier P., Courtillot V., Gallet Y., Jacques E., and Gillot P.Y. 2001. Strain transfer between disconnected, propagating rifts in Afar. Journal of Geophysical Research 106, 13613–13665.

McKenzie D.P., Davies D., and Molnar P. 1970. Plate tectonics of the Red Sea and East Africa. Nature 226, 243–248.

Mohr P. 1967. The Ethiopian Rift System. Bulletin of the Geophysical Observatory, Haile Selassie I University 11, 1–65.

Mohr P. 1968. Transcurrent faulting in the Ethiopian Rift System. Nature 218, 938–941.

Mohr P.A. 1972. Surface structure and plate tectonics of Afar. Tectonophysics 15, 3–18.

Mohr P. 1983. Volcanotectonic aspects of the Ethiopian Rift evolution. Bulletin Centre Recherches Elf Aquitaine Exploration Production 7, 175–189.

Mohr P. 1987. Patterns of faulting in the Ethiopian Rift Valley. Tectonophysics 143, 169–179.

Mohr P. and Rogers A.S. 1966. Gravity traverses in Ethiopia. Bulletin of the Geophysical Observatory, Haile Selassie I University 9, 7–58.

Mohr P. and Woods 1976. Volcano spacings and lithospheric attenuation in the eastern rift of Africa. Earth and Planetary Science Letters 126–144.

Morton W.H. and Black R. 1975. Crustal attenuation in Afar. In: Pilger A. and Rösler A. (Eds.), Afar Depression of Ethiopia. Schweizerbart, (Inter-Union Commission on Geodynamics Scientific Report 14), Stuttgart, Germany, 55–61.

Oppenheimer C. and Francis P. 1998. Implications of longeval lava lakes for geomorphological and plutonic processes at Erta'Ale volcano, Afar. Journal of Volcanology and Geothermal Research 80, 101–111.

Redfield T.F., Wheeler W.H., and Often M.2003. A kinematic model for the development of the Afar Depression and its paleogeographic implications. Earth and Planetary Science Letters 216 383–398.

Schult A. 1974. Paleomagnetism of Tertiary volcanic rocks from the Ethiopian Southern Plateau and the Danakil block. Journal of Geophysics 40, 203–212.

Sichler B. 1980. La biellette Danakile; un modele pour l'evolution geodynamique de l'Afar Colloque rift d'Asal. Reunion extraordinaire de la Societe Geologique de France. Bulletin de la Societe Geologique de France 22, 925–932.

Sigmundsson F. 2006. Magma does the splits. Nature 442, 251–252.

Souriot T. and Brun J.P. 1992. Faulting and block rotation in the Afar triangle, East Africa; the Danakil ''crank-arm'' model. Geology 20, 911–914.

Tapponier P., Armino R., Manighetti I., and Courtillot V. 1990. Bookshelf faulting and horizontal block rotations between overlapping rifts in southern Afar. Geophysical Research Letters 17, 1–4.

Tazieff H., Varet J., Barberi F., and Giglia G. 1972. Tectonic significance of the Afar (or Danakil) depression. Nature 235, 144–147.

Tesfaye S., Harding D.J., and Kusky T.M. 2003. Early continental breakup boundary and migration of the Afar triple junction, Ethiopia. Geological Society of America Bulletin 115, 1053–1067.

Thurmond A. K., Abdelsalam M. G., and Thurmond J. B. 2006. Optical-radar-DEM remote sensing data integration for geological mapping in the Afar Depression, Ethiopia. Journal of African Earth Sciences 44, 119–134.

Tiercelin J.J., Taieb M., and Faure H. 1980. Continental sedimentary basins and volcano-tectonic evolution of the Afar Rift. In: Carrelli A. (Eds.), Geodynamic Evolution of the Afro-Arabian Rift System. Atti dei Convegni Lincei, Accademia Nazionale dei Lincei 47, 491–504.

Varet J. and Gasse F. 1978. Geology of central and southern Afar (Ethiopia and Djibouti Republic). Editions du Centre National de la Recherche Scientifique Report, Paris, 124 pp. and map, scale 1:500,000.

Waltham T. 2005. Extension tectonics in the Afar Triangle. Geology Today 21, 101–107.

Watchorn F., Nichols G.J., and Bosence D.W.J. 1998. Rift related sedimentation and stratigraphy, southern Yemen (Gulf of Aden). In: Purser B.H. and Bosence D.W.J. (Eds.), Sedimentation and Tectonics of Rift Basins: Red Sea–Gulf of Aden. Chapman and Hall, London, 165–189.

WoldeGabriel G., Aronson J.L., and Walter R.C. 1990. Geology geochronology and rift basin development in the central sector of the Main Ethiopian Rift. Geological Society of America Bulletin 102, 439–458.

Wolfenden E., Ebinger C., Yirgu G., Deino A., and Ayalew D. 2004. Evolution of the northern Main Ethiopian rift: birth of a triple junction. Earth and Planetary Science Letters 224, 213–228.

Wolfenden E., Ebinger C., Yirgu G., Renne P., and Kelley S.P. 2005. Evolution of the southern Red Sea rift: birth of a magmatic margin. Geological Society of America Bulletin 117, 846–864.

Wright T.J., Ebinger C., Biggs J., Ayele A., Yirgu G., Keir D., and Stork A. 2006. Magma-maintained rift segmentation at continental rupture in the 2005 Afar dyking episode. Nature 442, 294–297.

CHAPTER 5

CHAPTER 5: GEOLOGY, PETROLOGY, AND GEOCHEMISTRY OF THE BASALTIC ROCKS OF AXUM AREA, NORTHERN ETHIOPIA

Miruts Hagos[1], Christian Koeberl[1], Kurkura Kabeto[2], Friedrich Koller[1]*

[1]Department of Lithospheric Research, University of Vienna, Althanstrasse 14, A-1090 Vienna, Austria
[2]Department of Earth Sciences, Mekelle University, P.O. Box 231 Tigray, Ethiopia
* corresponding author: Tel: +43-1-4277-53308; E-mail: miruts2005@yahoo.com (M. Hagos)

Abstract– The Axum volcanic rocks constitute an important outcrop of trap basalts at the northern end of the great Ethiopian flood basalt province. They are about 5–480-m-thick sequences exposed around Axum and Shire regions covering a total area of about 900 km^2. Even though the Axum volcanic rocks were previously assigned to the low-Ti (LT) tholeiitic basalts of the northwestern Ethiopian volcanic province, our geochemical studies on rocks from the region reveal that these rocks are alkaline to transitional in composition with distinct geochemical characteristics. Their petrologic diversity is very significant, the lavas ranging from basanites to tephrites and trachy-andesites. The variation in the major element (TiO_2 and Fe_2O_3) concentrations, incompatible trace elements, and the rare earth element (REE) concentrations and ratios (e.g., $(La/Yb)n$ = 5.0–14.0) indicate a complex petrogenetic evolution of the flood basalts. The Axum volcanic rocks are entirely alkaline to transitional in nature and are classified here into the Lower Sequence (Low-Ti) basalts and the Upper Sequence (High-Ti) basalts. Both these sub-divisions are also reflected in their unique chondrite-normalized REE patterns and multi-element diagrams: the Lower Sequence basalts show enhanced REE fractionation and higher concentrations of the highly incompatible trace elements; whereas the Upper Sequence basalts exhibit less REE fractionation and relatively high concentrations of the moderately incompatible trace elements. The mineralogical and geochemical variations among the basalts of Axum provide clues about the complexity of the Northern and North-western Ethiopian flood basalts and their petrogenetic evolution.

Keywords: Ethiopia; flood basalt; Axum; basanite; tephrite

5.1 Introduction

Most continental flood basalts are entirely associated with lithospheric extensions resulting from distant and/or local stress fields. The Ethiopian volcanic province is one of the youngest and well preserved flood basalt provinces on Earth, and is related to the opening of the Gulf of Aden and the Red Sea rifts (Baker et al., 1996; George et al., 1998). These two emerging oceanic rift segments are connected to the less evolved East African Rift at the center of Afar Depression. This depression is the site of a large and young magmatic province that is mainly exposed in the northwestern Ethiopia, Eritrea, Yemen, and the Republic of Djibouti (Pik et al., 1998).

The study area, Axum, is located in the northern part of the Ethiopian highlands and is mainly covered by Tertiary fissural basalts and the post-trap, east–west aligned Adwa–Axum phonolite and trachyte plugs. These volcanic rocks are exposed in the north-northwestern part of the Tigray region, northern Ethiopia, and are isolated from the major Ethiopian flood basalts by the deeply cut Tekeze basin and from the Eritrean highland basalts by the Mereb basin (Fig. 5.1). However, little attention has been paid to the petrologically important volcanic rocks of the erosion remnants in northern Ethiopia (Axum area).

The southern, central, and northwestern part of the Ethiopian flood basalts have been the focus of numerous studies (e.g., Mohr, 1983; George et al., 1998; Pik et al., 1998, 1999; Ebinger and Sleep, 1998; Ayalew et al., 1999, 2002; Kieffer et al., 2004). Most of the studies (e.g., Alemu, 1998; Alene et al., 2000; Asrat et al., 2003, 2004; Tadesse, 1996, 1997) in the northern region have focused on the Precambrian basement and Pan-African plutons. The only work dealing with the volcanics of the area was conducted during the regional mapping by the Ethiopian Institute of Geological Survey (1999). According to this study, the volcanic rocks of Axum are classified on the basis of the locality names as the Koyetsa volcanics (stratified flood basalt) and the Adwa trachyte formation (trachytic and phonolitic plugs). The petrologic and geochemical classifications of the volcanics were done on the basis of the rock samples analyzed from the nearby Maichew and northwestern Ethiopian flood basalts. Pik et al. (1998) collected only one sample (i.e., their number E210) from the southwestern part of the Axum volcanics and the whole interpretation was made with regard to the single data that represented about 900 km^2. As a result of incomplete exploration, the petrographic and geochemical characteristics of the volcanic rocks of Axum area remained unsolved. Our aim here is to investigate the petrography, geochemistry, and genesis of the Axum flood basalts, which has remained unknown and unexplored until now.

In this study we have focused on the geochemical (major and trace element) variations between the Axum basalts and the earlier well-defined northwestern tholeiitic basalts, and the possible petrogenetic relationships among them. We have also traced the spatial and temporal geochemical variation of the basaltic rocks of the area with that of the central and northwestern part of the Ethiopian flood basalts.

5.2 Geological Background

The Ethiopian volcanic province covers over an area of at least 600,000 km^2 with a layer of mafic and felsic volcanic rocks (Baker et al., 1996; Ukstins et al., 2002; Kieffer et al., 2004). An area close to 750,000 km^2 must have existed before domal uplift and resulting massive erosion that occurred during Pleistocene time (Mohr, 1983) removing about 150,000 km^2. Most Ethiopian flood basalts were unconformably emplaced on regionally lateritized sandstone surfaces (Ukstins et al., 2002) and few on deeply eroded Precambrian basement complexes. Lavas of this province erupted ~30 Ma, during a short 1–2 My period, to form a huge volcanic plateau (Baker et al., 1996; Hofmann et al., 1997; Kieffer et al., 2004). However, rift-triggered Miocene–Pliocene magmatism with an age of 14–5 Ma and pre-rift, Eocene–Oligocene (Stewart and Rogers, 1996) volcanic rocks are common to the east and south of the main Ethiopian flood basalts, respectively. The flood basalts are partly overlain by younger shield volcanoes and rhyolitic/trachytic and phonolitic volcanic rocks (Ayalew et al., 1999).

The northwestern Ethiopian flood basalts have relatively uniform mineralogical and chemical composition (Kieffer et al., 2004). According to these authors, most of the flood basalts are aphyric to sparsely phyric, and contain significant amount of phenocrysts of plagioclase and clinopyroxene and sometimes olivine. Interbedded with the flood basalts, particularly at upper eruptive levels, are ignimbrites and trachytes with variable textures ranging from porphyritic through sparsely porphyritic to glassy (6–20 vol% of phenocrysts) (Ayalew et al., 2002; Kabeto et al., 2004). Despite their compositional similarities, the Tertiary flood basalts of Ethiopia are divided into four types based on their ages (Mohr, 1983). From bottom to top these are called the Ashange, Aiba, Alage, and Tarmaber formations. In contrast to the above classification, the flood basalts are geochemically classified into three distinct magma types: as low-Ti basalts (LT), high-Ti 1 basalts (HT1) and high-Ti 2 basalts (HT2) (Pik et al., 1998, 1999) (Fig. 5.1). These authors recognized a group of LT basalts distinguished by low concentrations of Ti and highly incompatible trace elements and flat rare earth element (REE) patterns. These magma groups are defined on the basis of

incompatible trace element and TiO$_2$ with MgO concentrations (Rogers, 2006). The LT rocks are confined to the northwestern part of the volcanic province (Fig. 5.1). The HT (HT1 and HT2) basalts with elevated incompatible trace element contents and more fractionated REE patterns are found to the south, southeast and east of the volcanic province (Pik et al., 1998). Kieffer et al. (2004), however, disagreed with this simple subdivision and their sampling indicated a slightly wide distribution of the LT rocks. The HT2 basalts are more magnesium-rich than the HT1 basalts and commonly showing olivine + clinopyroxene phenocryst accumulations rather than primitive characteristics (Pik et al., 1999; Kieffer et al., 2004). The HT2 basalts have higher incompatible trace element content and show extreme fractionation of the REE (Kieffer et al., 2004).
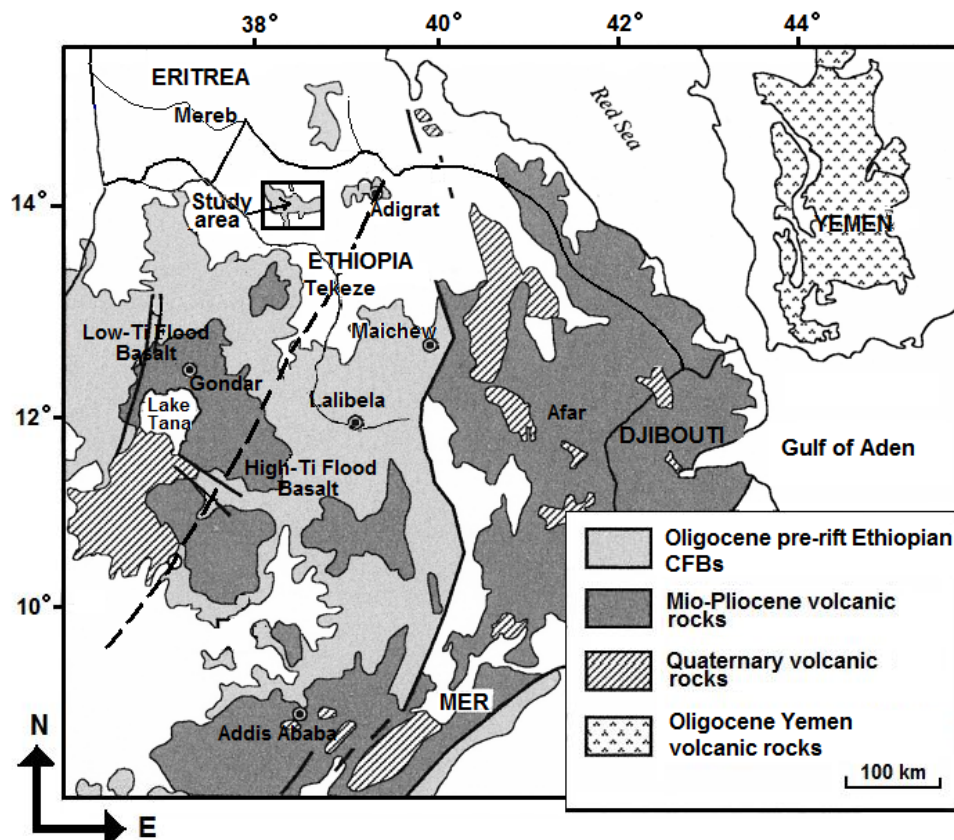
Figure 5.1 Sketch map of the central, northwestern and northern parts of the Ethiopian flood basalt province and the Afar triple junction with a box showing the location map of the Axum volcanics. Dividing line between high-Ti and low-Ti basalt province is marked by a dashed line (modified after Merla et al. 1979; Pik et al., 1998, and Küster et al., 2005).

The Oligocene flood basalt magmatism was followed by the Mio–Pliocene rift-triggered Afar volcanism, widespread transitional–tholeiitic basaltic suites and crustal uplift (Küster et al., 2005). The evolution of the Main Ethiopian rift (MER) was accompanied by the middle Miocene widespread bimodal volcanism that erupted both within the rift floor and on its margins (Gasparon et al., 1993). The Axum–Adua, Yerer–Tullu Wellel, and Goba–

Bonga lineaments (Mohr, 1987; Beyth, 1991; Abebe et al., 1998) are important E–W trending regional structures, transverse to the MER axis that dissect the rift. The rift-related uplift of the Ethiopian dome continued until the optimum thinning of the Afar Depression lithosphere and led to considerable erosion of the volcanic piles of the Ethiopian highlands (Küster et al., 2005). In the northern part of the Ethiopian volcanic province (Axum, Adigrat, and central Eritrean highlands) only erosional remnants of flood basalts and erosionally resistant post-Tertiary silicic rocks remain and the subvolcanic phonolites are widely exposed.

5.3 Sampling Strategy and Analytical Techniques

One hundred and twelve (112) rock samples (each weighing 0.75–1 kg) were collected during two field seasons (December 2006 and April 2007) from the entire area of the Axum volcanics but because of weathering and similarity in some of the samples only 33 of them were selected for this study. From these 33 analyzed samples only 19 samples come from the flood basalts and their data are used in this chapter. The remaining 14 samples come from the phonolitic rocks of the Bete-Giorgis and Gobo-Dura ridges.

The basaltic rock samples were first crushed at the University of Vienna in a stainless steel jaw crusher and then powdered in an agate mill in order to avoid contamination by the transition elements (such as Co, Ta, and Nb). Contents of major element oxides, minor and trace element (Nb, Zr, Y, Rb, Sr, Ga, Zn, Cu, Ni, Co, Cr, Sc, V, Ce, Ba, La) abundances were determined using wavelength dispersive X-ray fluorescence (XRF) spectrometry at the Department of Lithospheric Research, University of Vienna, Austria. For this, 1.2 g of powdered rock was mixed with 6 g of lithium tetra-borate to prepare fused pellets used for the analyses of the major element oxides, and 10 g of powdered rock was used to prepare pressed pellets for the analyses of the trace elements.

Contents of the rare earth elements (REE) and other trace elements, namely Sc, Cr, Co, Ni, Zn, As, Se, Br, Rb, Sr, Zr, Sb, Cs, Ba, Hf, Ta, W, Ir, Au, Th, and U, were analyzed by instrumental neutron activation analysis (INAA) at the Department of Lithospheric Research, University of Vienna. For this, samples weighing between about 115 and 130 mg were sealed into polyethylene capsules and, together with the rock standards AC-E (granite), Allende (carbonaceous chondrite), and SDO1 (shale) were irradiated for 8 hours at the Triga Mark II reactor of the Institute of Atomic and Subatomic Physics, Vienna, at a neutron flux of 2.10^{12} n cm^{-2} s^{-1}. Details of the INAA method, including standards, correction procedures, precision, and accuracy, are reported in Koeberl (1993) and Son and Koeberl (2005).

5.4 Rock Type Classification

The Axum volcanics are classified in the field into the fissure-fed continental flood basalts and the phonolite–trachyte plugs. Large parts of the fissure-fed alkali basalts overlie the undifferentiated clastic Mesozoic sedimentary rocks of the region and small parts of the basalts overlie the deeply eroded meta-volcano-sedimentary complexes of the Arabian–Nubian shield (ANS) (Fig. 5.4). The Mio–Pliocene phonolite–trachyte plugs on the other hand are exposed intruding the basalt flows and/or the clastic sedimentary rocks of the area.

During the Tertiary Period, large parts of the present landmass of Ethiopia were flooded by successive lava flows, and a few pyroclastic falls and flows. In the study area, the Mesozoic sedimentary rocks are unconformably overlain by Oligocene basaltic lava flows and syn–post trap pyroclastic rocks (Beyth, 1972; Zanettin et al., 2006). After a prolonged period of erosion of the uplifted landmasses, the volcanic rocks of the Axum area, range in thickness from a thin veneer (<5 m) at its peripheries to about 500 m in some of the ridges and mountains of the area (e.g., Ferasit and Moror). Based on the field observations and mineral compositions, we subdivide these volcanic rocks broadly into the following three major sequences (Fig. 5.2).

Sequence-1: The lowermost samples of the basalts were collected from the southern Axum town or the west and northwest of Deigo village at altitudes of 2020–2130 m. This gently inclined (dip not >5 degrees) basaltic outcrop, 5–60 m. thick, and unconformably overlying the basement rock, is vesicular, columnar-jointed, and commonly slightly weathered. Unlike the other sequences, which are flat lying, these rocks are linear and convex downward exposures filling valleys in the underlying basement complexes. Such rocks are laterally discontinuous but well exposed along the big canyons of the southern part of the area.

Petrographically, the basalts are commonly aphyric to phyric/porphyritic, plagioclase-laths with significant phenocrysts constituting of about 20–25 vol%. The phenocryst minerals are olivine, clinopyroxene, and plagioclase with a few opaques. Most of the phenocrysts are rounded with some angular grains, and in some thin-sections extremely large and zoned phenocrysts of clinopyroxene are observed (Fig. 5.3a, b and c). These pyroxenes are pentagonal–hexagonal in shape, light-colored under crossed polarizers and show two obliquely (~120 degrees) aligned cleavage surfaces.
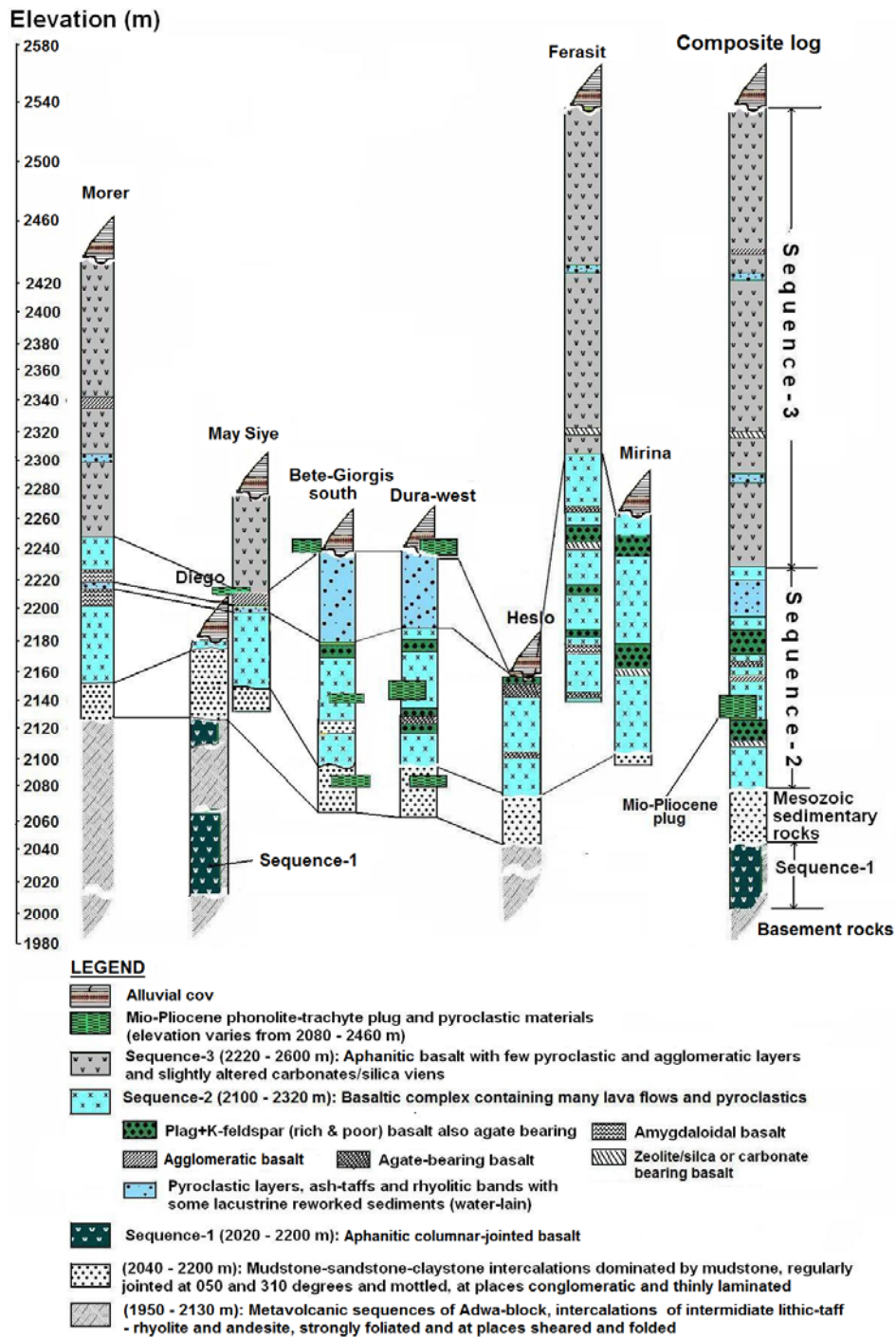
Figure 5.2 Eight column sections and one composite section (right) of the stratigraphy of the Axum area constructed from different traverses; outcrops are logged based on their altitude in the area.

Sequence-2: The second sequence, about 50–140 m thick and commonly exposed at an altitude between 2080–2240 m, is invariably weathered and intercalated with thin pyroclastic (ash fall) materials and basaltic agglomerate in its top part. The vesiculated and weathered basalts of this sequence also contain some calcite veins in addition to silica and zeolites. Even though it is not more than 140 m thick, this sequence covers a large portion of

the mapped area and is emplaced directly over the horizontally lying, clastic Mesozoic sedimentary rocks. This sequence is uniformly made up of coarse-grained, Carlsbad-twinned, plagioclase-phyric, ± K-feldspar bearing (rich and poor) basalts, and grading upwards to agate- and zeolite-bearing amygdaloidal. Samples of this sequence show significant accumulation of the opaque minerals, but fewer phenocrysts of olivine, clinopyroxene, and other minerals (Fig. 5.3d and e).

Sequence-3: These rocks are essentially aphyric to micro-phenocrystic basalts exposed between 2200–2600 m with rare ash-fall layers intercalated with them. This sequence is the thickest, 300–400 m thick, and forms the highest peaks of the area. These rocks are extensive in area and form a shield-volcano-type edifice, the Ferasit and Morer ridges. This sequence is relatively fine-grained with few phenocrysts. The phenocryst minerals are clinopyroxene, olivine, and plagioclase without opaques. The groundmass of these basalts consists of dominantly altered plagioclase with the above-mentioned phenocrysts phases, accessory glass, and few zircons (Fig. 5.3f). For a complete petrographic description of the samples, see Table 5.1 below.

Table 5.1: Detailed petrographic descriptions of the Axum alkali basalts, Northern Ethiopia.

Sample code	Sample type	Location (in UTM)	Description
AX004	Porphyritic basalt	472099E 1562095N	Needle-like, medium-grained plagioclase-laths and hornblende (>60 vol%) with few anhedral shape micro–mega phenocrysts of olivines, clinopyroxenes and very few opaque minerals. The plagioclases are carlsbad twinned but irregularly aligned. No flow texture.
AX08	Aphanitic basalt	479601E 1564013N	Fine-grained plagioclase (ground-mass) incorporating very few phenocrysts of pyroxenes and some secondary quartz crystals (agate). No olivine crystals were observed.
AX20	Aphanitic basalt	472639E 1551783N	Fine-grained matrix (dominated by plagioclase) and all size (micro–mega) phenocrysts of olivines, clinopyroxenes and some plagioclases. Phenocrysts constitute about 30 vol%. Few opaques are present.
AX21	Columnar basalt	472805E 1551143N	Plagioclase-laths dominated matrix. Euhedral–subhedral shaped, medium-grained phenocrysts of olivine. No opaque minerals.
AX24	Porphyritic basalt	474185E 1550132N	Medium-grained, elongated plagioclase and tabular hornblende (ground-mass) with medium size phenocrysts of olivines and few but very large and perfectly zoned phenocrysts of clinopyroxenes. Opaque minerals are not common.
AX29	Dolerite/ diabase	464013E 1557294N	Coarse-grained plagioclase-laths interfingering with the anhedral shaped, olivine mega-phenocrysts. The plagioclase shows Carlsbad-type twinning but poor flow texture.
AX31	Vesicular basalt	464206E 1557432N	Needle-like, medium-grained plagioclase (ground-mass) with very few pyroxene micro-phenocrysts. The matrix constitute >90 vol% and the plagioclase in the ground mass shows good flow texture.
AX32	Aphanitic basalt	463129E 1560422N	Carlsbad twinned medium-grained plagioclase (ground-mass). No phenocryst minerals found but medium-grained (the same size as the plagioclase) olivines and few opaque minerals are common.
AX34	Aphanitic basalt	473529E 1552248N	Carlsbad twinned, fine-grained plagioclase-laths matrix with varying size (micro–mega) phenocrysts of olivines and pyroxenes. The plagioclases show good flow texture and the phenocrysts are euhedral –anhedral in shape.
AX38	Aphanitic basalt	474033E 1556172N	Fine–medium-grained, elongated–equant plagioclase-laths (50–60 vol%). Micro–mega, Euhedral–subhedral shaped phenocrysts of olivines and zoned and un-zoned phenocrysts of pyroxenes.
AX43d	Columnar basalt	466516E 1564320N	Tabular, medium-grained plagioclase with few olivine phenocrysts. The phenocrysts are subhedral – anhedral in shape. Some opaque minerals are present.
AX44	Basalt	465459E 1563351N	Euhedral–subhedral shaped olivine phenocrysts (about 5–8 vol%) embedded in fine-grained matrix of equant – elongated plagioclase-laths and few olivines.
AX46	Aphanitic basalt	469365E 1562236N	Needle- like plagioclase and hornblende constituting about 90 vol% with very few olivine micro-phenocrysts. No opaques.
AX47b	Aphanitic basalt	474973E 1555646N	Needle-like equant shape, fine–medium-grained plagioclase-laths with medium-size olivine phenocrysts.
AX63	Aphanitic basalt	460147E 15520044N	Extremely large, euhedral–anhedral shaped pyroxene and olivine phenocrysts. The pyroxenes are multiply zoned and some altered/secondary minerals are developed at the rims of the phenocrysts. The ground-mass is still dominated by very fine-grained plagioclase with very few of the above- mentioned minerals.
AX79	Basalt	479293E 1560281N	Needle-like, Medium–course-grained plagioclase with few olivine micro-phenocrysts. No visible pyroxene and opaque minerals.
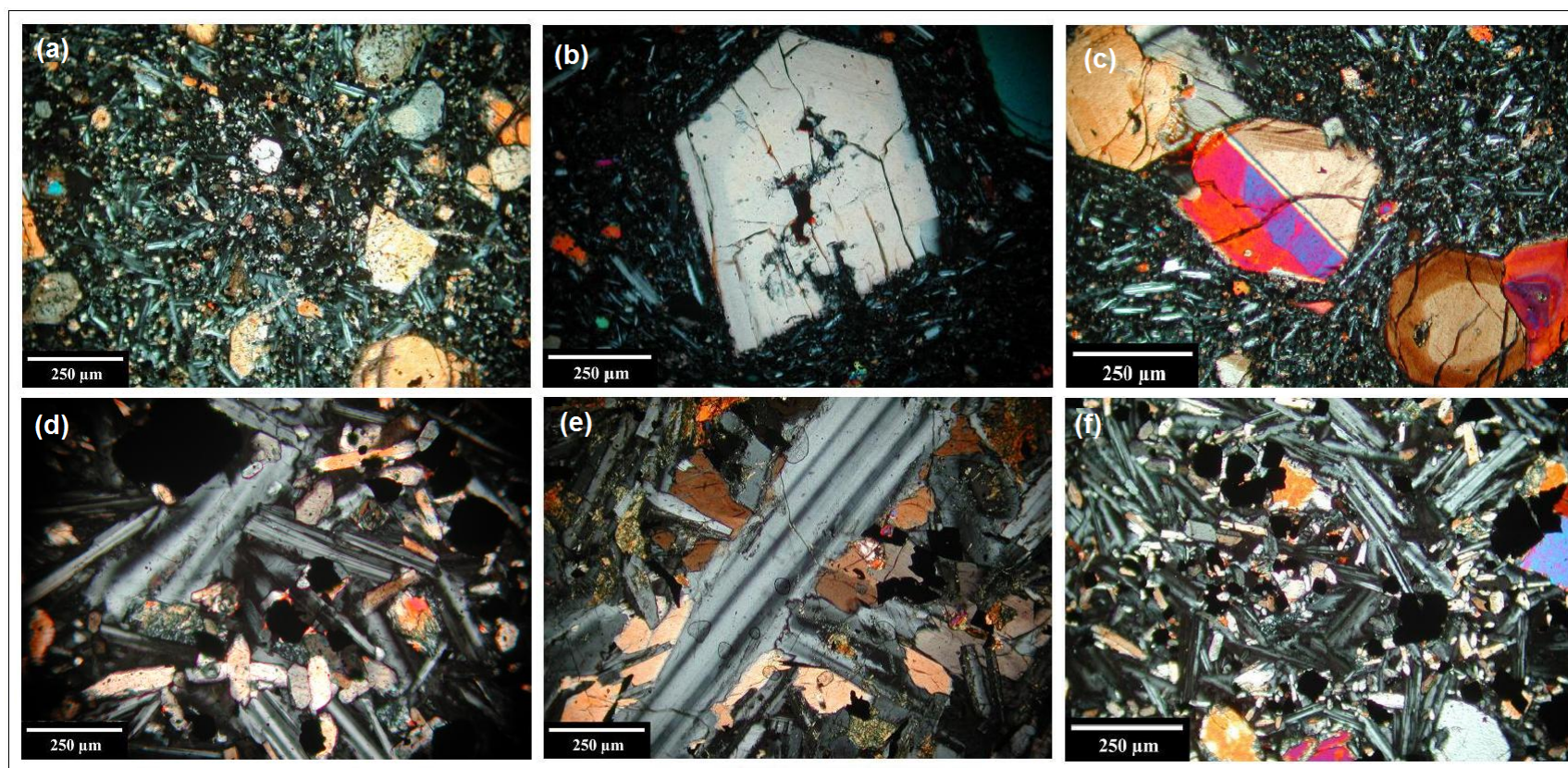
Figure 5.3 Petrography of the volcanic rocks of the Axum area showing various mineralogical and textural features. All images are taken under crossed polar with a magnification of 125x. (a) Very fine-grained plagioclase rich (ground mass) alkali basalts with coarse-grained olivine and some clinopyroxenes phenocrysts; the plagioclases are lathlike but with poor flow texture, where as the phenocrysts are rounded to angular and of varying size. (b) Large grain of zoned clinopyroxene embedded in fine-grained and altered groundmass of plagioclase. (c) Zoned plagioclase and clinopyroxenes imbedded in fine-grained matrices of the same compositions. Thin-sections a, b and c represent the lower basaltic sequence (sequence-1) of the study area. (d) Randomly aligned, medium–course-grained plagioclase-laths with few grains of pyroxenes. (e) Coarse-grained plagioclase, clinopyroxene and olivine are intruded by extremely large, NE aligned plagioclase crystal; isotropic minerals are few in this image. (f) Medium-grained, plagioclase-laths rich alkali basalt with clinopyroxene and some olivine phenocrysts; dark-colored minerals of Ti oxides and Mg oxides are filling the interstices of other grains. Thin-sections d, e, and f represent the mineralogy and texture of alkali basalts of the upper sequences (sequences 2 and 3).
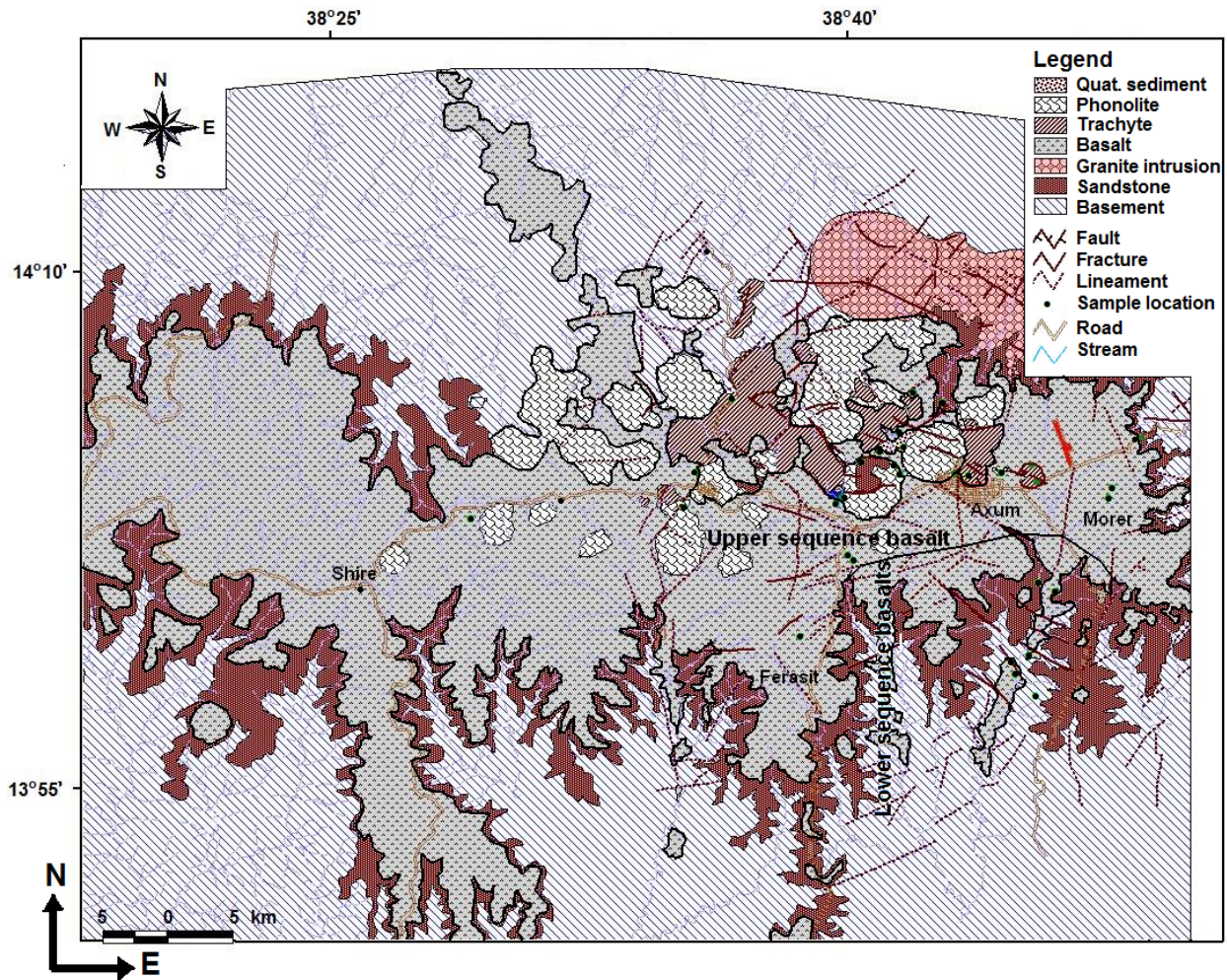
Figure 5.4 Geological map of the volcanic rocks of Axum area. The 1:50,000 scale topographic maps of Axum, Adwa, Enda-Silasie and Chila were taken as a base map. The spatial variations of rocks, lithologic contacts and the structures were extracted from 1:50,000 scale aerial photographs (Eth94), Landsat ETM[+] 2002, and ASTER. Color composite images of Landsat band 7, 5 and 2 are commonly used to differentiate between the clastic Mesozoic sedimentary rocks and the overlaying flood basalts, but geologic structures such as: faults, fractures and lineaments were drawn from aerial photographs. In some areas the high spatial resolution image, the ASTER image was used.

Table 5.2: Major and trace element contents of alkali basalts from the Axum area, Northern Ethiopia

	Basalt AX004	TB AX08	Basalt AX20	Basalt AX21	Basalt AX24	Basalt AX29	Basalt AX31	Basalt AX32	Basalt AX34	Basalt AX38	Basalt AX42	Basalt AX43d	Basalt AX44	TB AX46	Basalt AX47b	Basalt AX63	TB AX79	Basalt AX09	Basalt AX12
(wt.%)																			
SiO_2	43.05	54.37	43.63	44.06	49.20	48.32	48.19	46.82	48.65	44.32	50.68	48.76	47.06	51.60	45.75	44.82	50.96	45.13	45.77
TiO_2	4.39	1.85	2.56	2.95	2.10	3.50	2.12	3.25	2.25	2.44	2.90	2.23	2.85	1.54	2.17	3.07	1.58	3.97	1.99
Al_2O_3	13.88	15.67	15.49	14.85	15.87	15.32	19.22	16.51	15.93	15.58	16.24	16.67	16.38	16.92	14.57	14.32	16.68	15.16	15.53
Fe_2O_3	17.32	9.71	12.94	12.85	10.82	15.39	10.85	14.89	11.12	11.64	13.42	14.57	15.84	12.55	11.68	16.26	12.61	16.58	12.90
MnO	0.21	0.17	0.22	0.20	0.19	0.20	0.21	0.17	0.20	0.20	0.19	0.15	0.14	0.24	0.20	0.24	0.25	0.18	0.17
MgO	7.22	2.01	7.73	7.89	7.68	4.60	3.32	5.22	7.92	6.82	3.63	3.84	3.52	2.45	11.02	5.66	2.64	5.44	10.18
CaO	7.90	5.46	10.59	9.90	9.42	7.08	7.90	6.87	9.35	11.69	7.22	5.16	4.71	4.93	10.72	7.68	5.48	7.07	9.25
Na_2O	4.17	4.01	4.13	4.36	3.96	3.87	5.30	3.86	3.69	4.28	3.35	6.19	5.94	6.87	2.85	5.34	6.38	3.46	2.49
K_2O	1.59	2.97	1.71	1.12	1.93	1.05	2.08	1.12	1.84	1.04	1.74	0.96	0.58	1.50	1.53	1.47	1.54	1.37	0.45
P_2O_5	0.96	0.66	0.69	0.76	0.55	0.53	0.80	0.48	0.53	0.84	0.80	0.67	0.59	1.51	0.57	1.30	1.53	0.60	0.19
LOI	0.72	4.13	1.93	2.81	0.17	1.89	1.41	1.53	0.24	2.57	1.18	2.29	3.08	0.91	0.63	1.05	1.44	2.88	4.02
Total	**101.41**	**101.01**	**101.62**	**101.75**	**101.89**	**101.75**	**101.40**	**100.72**	**101.72**	**101.42**	**101.35**	**101.49**	**100.69**	**101.02**	**101.69**	**101.21**	**101.09**	**101.83**	**102.92**
Mg#	**49.4**	**35.8**	**58.27**	**58.9**	**64.1**	**41.1**	**43.5**	**46.9**	**64.2**	**57.8**	**40.5**	**40.7**	**35.9**	**33.7**	**68.8**	**46.7**	**35.3**	**43.4**	**64.9**
(ppm)																			
Sc	13.7	15.4	22.3	18.2	17.7	19.2	6.70	20.6	21.9	24.3	19.5	6.81	6.14	5.42	24.0	10.9	5.42		
V	199	126	254	227	201	207	142	266	212	240	225	79	76	48	242	139	47	384	321
Cr	14.9	17	106	128	273	11.0	9.7	39.3	386	226	23.6	97.1	28.7	9.06	579	8	7.06	39.5	307
Co	44.2	17.9	40.9	33.5	31.9	35.5	20.7	52.0	43.9	40.7	34.6	31.9	38.5	14.3	49.9	32.0	14.3	--	--
Ni	34	14	71	90	143	22	5	52	161	112	27	17	46	10	245	12	8	19	5
Cu	25	17	6	41	66	29	6	30	57	70	36	13	19	2	73	9	4	--	--
Zn	165	137	115	97.8	99.0	140	90.4	165	124	112	171	132	136	155	115	192	150	--	--
Ga	29	22	16	18	18	24	16	24	18	16	22	21	22	25	16	32	25	24	18
As	1.04	0.18	<1.5	1.71	0.45	<1.5	0.45	<1.5	<2.1	<2.3	0.32	<3.2	<1.5	1.36	0.48	1.17	<1.9	--	--
Se	<1.7	<1.64	0.26	2.19	2.19	<2.9	<2.2	3.05	<3.1	<2.4	<2.8	<2.5	<2.3	<2.5	<3.8	<2.8	<2.5	--	--
Br	<0.7	<0.75	<1	1.50	1.37	<3.86	1.91	<1.5	<4.9	<5.2	<3.5	<5.3	<4	<5.1	<3	<5.1	<4.4	--	--
Rb	41.0	37.4	64.7	35.9	36.7	12.3	48.3	19.6	41.7	16.1	51.8	26.7	16.2	25.1	30.0	21.3	29.5	17.7	20.2
Sr	989	559	786	983	796	619	1163	680	737	927	760	704	1020	1776	789	1207	1760	614	349
Y	30	44	31	34	28	39	29	36	28	31	45	16	23	61	27	36	62	37	26
Zr	321	389	192	258	197	212	222	208	190	211	269	209	315	637	173	389	621	267	128
Sb	0.10	<0.14	0.09	0.04	0.02	<0.13	0.07	<0.2	0.21	0.10	0.09	<0.1	<0.2	<0.2	<0.1	0.85	0.14	--	--
Nb	34	23	69	84	70	12	77	15	65	73	20	10	20	37	60	40	35	19	5
Cs	0.42	0.34	0.64	0.54	0.26	<0.2	0.89	0.36	0.43	0.74	0.61	0.22	3.18	0.91	0.33	0.48	0.38	--	--
Ba	110	640	523	378	363	221	433	270	431	664	460	178	65.4	176	453	116	150	504	57.7
La	30.4	38.3	46.8	60.8	47.4	15.2	55.5	20	47.4	55.9	31.1	20.9	15.1	42.7	41.1	38.4	41.1	--	--
Ce	72.6	84.2	86.1	110	80.8	38.2	102	47.4	86.5	98.2	72.0	53.6	44.8	108	71.7	90.3	104	47.3	20.2
Nd	46.8	45.2	31.5	45.9	32.5	27	42.3	30.6	34.8	44.3	42.1	38.7	38.5	70.8	35.8	56.9	68.4	--	--
Sm	11.3	9.91	7.29	8.86	6.33	7.27	7.91	8.38	7.62	8.80	10.4	10.3	10.6	17.3	7.24	14.3	16.6	--	--
Eu	4.25	3.79	2.46	3.02	2.24	2.62	2.70	2.85	2.44	2.70	3.27	3.37	3.49	5.73	2.35	4.59	5.66	--	--
Gd	9.0	9.13	6.76	7.69	6.18	9.20	9.07	10.2	9.52	9.81	11.2	9.07	12.4	19.4	8.82	15.1	15.6	--	--
Tb	1.46	1.43	1.07	0.93	0.84	1.16	1.03	1.39	1.03	1.08	1.56	1.22	1.33	2.26	0.86	1.71	2.18	--	--
Tm	0.37	0.68	0.59	0.56	0.47	0.67	0.73	0.75	0.7	0.67	0.82	0.38	0.36	1.08	0.59	0.54	1.08	--	--
Yb	1.80	3.93	2.57	2.69	2.18	2.81	2.63	2.85	2.37	2.76	3.63	1.34	1.37	5.18	2.23	2.03	4.89	--	--
Lu	0.22	0.62	0.37	0.38	0.31	0.43	0.38	0.45	0.32	0.4.0	0.54	0.15	0.17	0.75	0.32	0.24	0.70	--	--
Hf	8.63	10.6	4.16	5.81	4.02	5.23	4.67	6.08	4.49	4.63	7.33	8.27	8.04	17.0	3.52	10.3	16.7	--	--
Ta	2.51	1.33	4.97	5.55	4.53	0.62	5.61	1.13	4.90	4.67	1.32	1.36	1.00	3.12	4.07	2.84	2.86	--	--
W	3.10	<3.42	<4.39	0.41	0.38	<2.4	0.15	<2	<3.6	<4.1	<2.1	2.14	<2.2	<3.6	<1.7	<3.5	<3	--	--
Ir (ppb)	<1.6	<1.6	<1.4	2.99	3.05	<2.4	<1.7	<2.6	<2.9	<2.1	<2.1	<2.3	<2.2	<1.9	<2	<3.2	<2.3	<2	--
Au (ppb)	2.02	0.98	0.8	0.82	0.78	<2.1	1.1	<2.2	<2.3	<0.01	<0.01	<0.01	<0.01	<2.3	<0.01	<1.8	<2.5	<0.01	--
Th	2.53	1.76	5.72	7.14	4.78	0.69	6.58	1.15	4.78	5.79	1.36	1.52	1.07	3.28	3.88	2.92	3.05	2.06	43.4
U	0.67	0.53	1.28	1.92	1.37	<3.86	1.80	<3.6	1.20	1.80	<0.7	<0.6	<0.8	1.12	0.98	<0.9	<0.8	--	--

All major elements, and the trace element contents of V, Ni, Cu, Ga, Sr, Y, Zr, and Nb were determined using XRF spectrometry, and the contents of remaining trace elements and all rare earth elements were determined using INAA, both at the Department of Lithospheric Research, University of Vienna. Mg-number (Mg#) = $100*Mg^{2+} / (Mg^{2+} + Fe^{2+})$, where Mg^{2+} and Fe^{2+} are in atomic units (Rollinson, 1993). Samples AX09 and AX12 are from K. Kabeto (unpublished data).

Table 5.3: CIPW normative composition in wt% for the alkaline basalts of Axum, Northern Ethiopia.

	Basalt AX004	Basalt AX20	Basalt AX21	Basalt AX24	Basalt AX29	Basalt AX31	Basalt AX32	Basalt AX34	Basalt AX38	Basalt AX42	Basalt AX43D	Basalt AX44	Basalt AX47B	Basalt AX63	Basalt AX09
qz	0	0	0	0	0	0	0	0	0	2.47	0	0	0	0	0
or	9.47	10.3	6.80	11.3	6.29	12.4	6.76	10.8	6.28	10.4	5.79	3.56	9.04	8.79	8.30
ab	17.2	6.32	14.2	22.1	33.2	26.4	33.3	22.2	11.6	28.6	42.3	44.3	11.0	23.7	29.7
an	14.6	18.9	18.1	19.7	21.6	22.7	24.9	21.3	20.7	24.4	15.4	16.9	22.4	10.9	22.3
ne	9.96	15.8	12.8	6.01	0	10.2	0	4.78	13.8	0	6.02	4.25	7.09	11.9	0.16
en	8.81	15.4	14.2	13.2	4.20	4.90	3.08	12.3	17.1	2.67	2.58	1.19	15.9	8.54	4.07
fs	6.50	8.86	8.00	5.46	4.54	4.70	2.42	4.97	9.81	2.75	2.82	1.59	5.89	7.22	3.90
di	15.3	24.3	22.2	18.7	8.74	9.59	5.49	17.2	26.9	5.42	5.40	2.78	21.8	15.8	7.97
Hy	0	0	0	0	10.0	0	3.32	0	0	17.2	0	0	0	0	0
fo	9.84	8.67	9.53	8.99	3.64	4.26	7.07	9.76	6.60	0	6.00	5.99	14.1	7.22	8.41
fa	9.17	6.29	6.79	4.69	4.98	5.16	7.02	5.00	4.79	0	8.30	10.1	6.59	7.72	10.2
ol	19.0	15.0	16.3	13.7	8.62	9.42	14.1	14.8	11.4	0	14.3	16.1	20.7	14.9	18.6
mt	3.86	2.90	2.92	3.31	3.45	3.37	4.68	3.41	2.63	4.17	5.16	5.07	2.58	5.07	3.76
il	8.40	4.93	4.78	3.95	6.75	4.06	6.30	4.25	4.74	5.56	4.32	5.62	4.12	5.90	7.73
ap	2.24	1.62	1.81	1.26	1.25	1.87	1.14	1.22	1.99	1.87	1.58	1.42	1.32	3.05	1.43

qz: quartz; or: orthoclase; ab: albite; an: anorthite; ne: nepheline; en: enstatite; fs: ferrosilite; di: diopside; hy: hypersthene; fo: forsterite; fa: fayalite; ol: olivine; mt: magnetite; il: ilmenite; ap: apatite. $Fe_2O_3/Fe_2O_{3T} = 0.15$; $FeO/Fe_2O_{3T} = 0.85$.

Table 5.4: Average concentrations and ranges of the contents of selected major elements, trace elements and ratios of the lower sequence and upper sequence basalts of the Axum area, Northern Ethiopia.

	Lower sequence		Upper sequence	
	Range	**Average values**	**Range**	**Average values**
TiO_2	1.54 - 2.56	**2.26 (9)**	2.60 – 4.40	**3.42 (10)**
SiO_2	44.1 – 49.2	**46.8 (9)**	43.0 – 48.3	**46.2 (10)**
Fe_2O_3	10.8 – 14.6	**12.1 (9)**	13.4 – 17.3	**15.7 (10)**
MgO	3.32– 11.0	**7.33 (9)**	3.53 – 7.22	**5.04 (10)**
CaO	5.16 – 11.7	**9.17 (9)**	4.71 – 7.90	**6.93 (10)**
P_2O_5	0.19 – 0.84	**0.61 (9)**	0.48 – 1.3	**0.75 (10)**
$Y(ppm)$	16.0 – 34.0	**27.4 (8)**	23 – 45	**34.0 (7)**
$La(ppm)$	21.0 – 61.0	**47.0 (8)**	15.0 – 38.0	**24.8 (7)**
$Ce(ppm)$	20.0 - 118	**75.0(8)**	13.0 – 104	**49.6 (7)**
$Ta(ppm)$	1.36 – 5.61	**4.38 (8)**	0.62 – 2.84	**1.35 (7)**
$Nb (ppm)$	10.0 – 84.0	**61.7 (8)**	12.0 – 40.0	**22.8 (7)**
CaO/Al_2O_3	0.31 – 0.75	**0.66 (9)**	0.29 – 0.57	**0.40 (10)**
Ti/Y	434 – 853	**508 (8)**	391 – 866	**630 (7)**
Nb/Y	0.63 – 2.66	**2.16 (8)**	0.30 – 1.13	**0.70 (7)**
Nb/La	0.47 – 1.49	**1.27 (8)**	0.64 – 1.36	**0.82 (7)**

5.5 Whole Rock Geochemistry

The general characteristics of the Axum volcanic rocks are illustrated in the total alkali-silica (TAS) classification of Le Bas et al. (1986) (Fig. 5.5). In this classification the rocks are basanites, tephrites, trachybasalts, basalts, and basaltic trachy-andesites. All the analyzed rocks have SiO_2 contents ranging from 43 to 55 wt% and also show a wide range in concentrations of other major and minor element oxides (Table 5.2). The Axum volcanics have compositions that plot, with the exception of sample AX12 showing tholeiitic affinity, in the alkaline field and few samples (AX08, AX29, AX42) within the transition field. All the basaltic rocks of the area have low (<49 wt%) SiO_2 contents, zero normative quartz (except AX42, 2.5 wt%), and high normative olivine contents (9–20 wt%) (Tables 5.2 and 3). However, slight differences in the alkalinity of the Axum volcanic rocks are observed. All the samples from sequence-1 are highly alkaline (silica-undersaturated), whereas, samples from sequences-2 and 3 are a bit stretched, and cover highly–mildly alkaline and transitional fields.
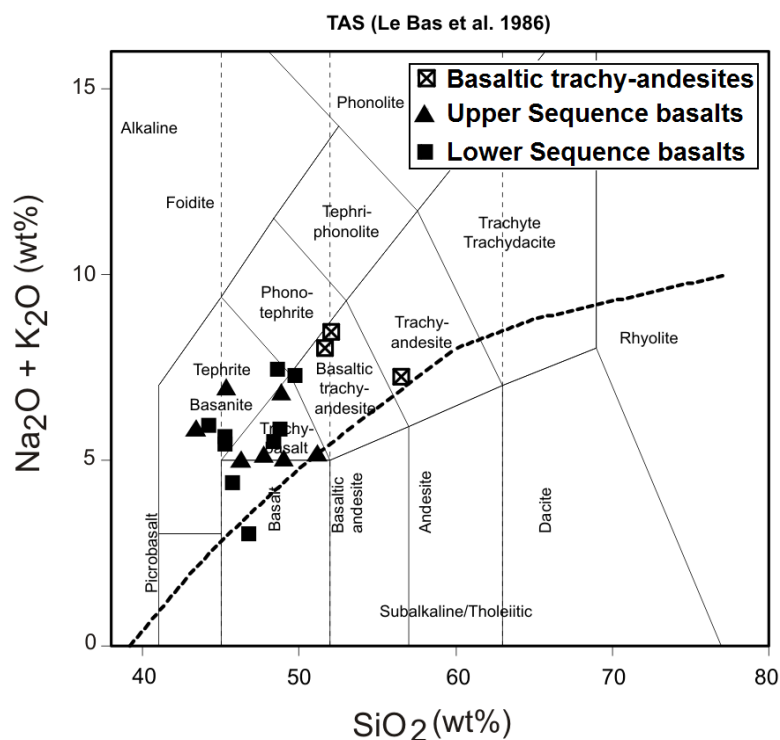
Figure 5.5 Total alkalis-silica (TAS) diagram comparing the geochemical characteristics of the volcanic rocks of Axum. Oxides are recalculated (on a LOI-free basis) using the SINCLAS program of Verma et al. (2002) for obtaining the TAS names, Mg numbers, and also the normative compositions. The TAS diagram is plotted using the Geochemical Data Toolkit (GCDkit 2.3). The dashed line distinguishes alkaline from subalkaline basalts (after Le Bas et al., 1986).

Almost all samples from the sequence-2 and sequence-3 basalts are fractionated mafic rocks with MgO values between 2 and 7.9 wt% and Mg# between 35.3 and 58.3 (Table 5.2). However, sequence-1 basalts (AX12 AX24, AX34, and AX47b) from the Lower Sequence have more primitive compositions with MgO values between 7.7 and 11 wt% and Mg# between 64.1 and 68.8. The distribution of the TiO_2 contents in the basaltic, tephritic, and basanitic rocks of the area is not uniform. Nearly half of the basaltic samples have 2.6–4.4 wt% TiO_2, and the remaining samples from the Lower Sequence have 1.5–2.6 wt% TiO_2. However, the TiO_2 concentrations correlate well with the Fe_2O_3 contents in the rocks. The high-TiO_2 basalts have high Fe_2O_3 content but low MgO and CaO contents (Fig. 5.6). In the binary plot (Harker variation diagram), the distribution of Fe_2O_3 in the basaltic rocks (tephrites, basanites, trachybasalts, and basalts) shows two well defined patterns: the Lower Sequence (sequence-1) is characterized by gently sloping low Fe_2O_3 and the Upper Sequence (sequence-2 and sequence-3) by moderately sloping high Fe_2O_3 patterns (Fig. 5.6c). To simplify our discussion, those samples from sequence-1 are called Lower Sequence basalts and those from sequence-2 and sequence-3 are called Upper Sequence basalts.

The Lower Sequence basalts have the lowest TiO_2 contents (2–2.6 wt%) and are confined to the south and southeastern parts of the mapped area. In contrast, the Upper Sequence basalts display much higher TiO_2 contents (2.6–4.4 wt%) and are widely distributed in the central, western, and northwestern part of the mapped area. Generally, the Lower Sequence basalts exhibit low Fe_2O_3 (10.8–14.6 wt%, average: 12.1 wt%), low P_2O_5 (0.18–0.84 wt%, average: 0.61 wt%), low Ti/Y (average: 508) and low concentrations of the high field strength trace elements (Zr, Hf, Ga, Tb, Y). However, the Lower Sequence basalts are characterized by significantly higher contents of CaO (5.2–11.7 wt%, average: 9.2 wt%) and MgO (3.3–11 wt. %, average: 7.3 wt%), high CaO/Al_2O_3 ratios, and very high contents of Ba, Rb, Th, Nb, Ta, La, and Ce. The Upper Sequence basalts on the other hand display contrasting characteristics, with high contents of Fe_2O_3 (13.4–17.3 wt%, average: 15.7 wt%), P_2O_5 (0.48–1.3 wt%, average: 0.75 wt%), Ti/Y (average: 630), the moderately incompatible trace elements (Sm, Eu, Gd, Zr, Hf, Tb, Y) and low contents of MgO, CaO, low ratios of CaO/Al_2O_3, Nb/Y, Nb/La (Table 5.4), and low concentrations of highly incompatible elements (Ba, Rb, Nb, Ta, La, Ce).
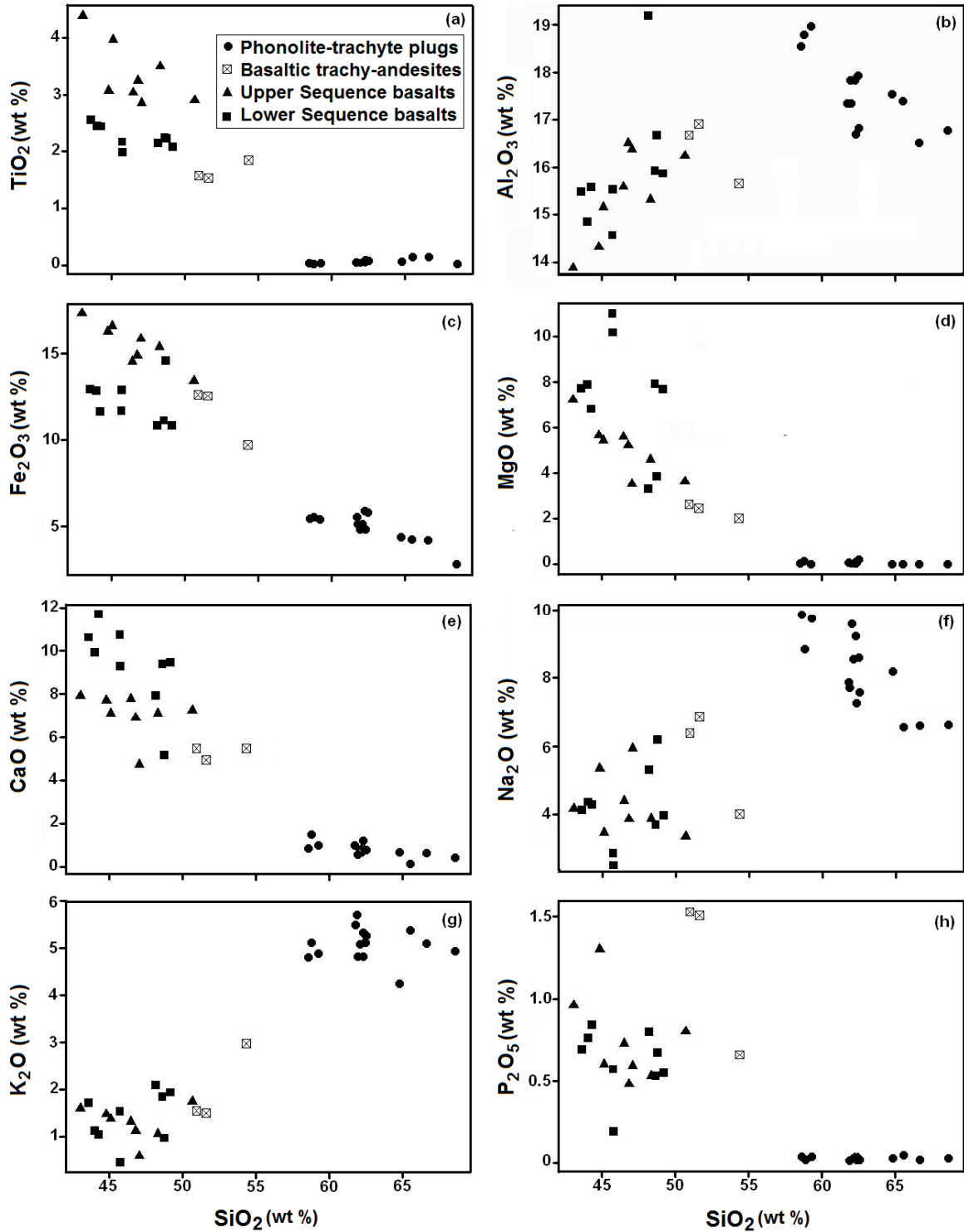
Figure 5.6 Harker variation diagrams for the volcanic rocks of Axum area. All the major oxides are characterized by their trends as SiO_2 ranges from 43–67 wt%.

The chondrite-normalized trace element patterns for the mafic rocks of the area show some variation between the various samples (Fig. 5.7a and c). The basaltic rocks show two different REE patterns. The Lower Sequence basalts have highly sloping light REE (LREE) and relatively flat heavy REE (HREE) patterns; in contrast the Upper Sequence basalts have a

comparatively flat LREE and moderately sloping HREE pattern. The samples AX21, AX24 and AX31 from the Lower Sequence basalts exhibit very high chondrite-normalized light to heavy REE, (La/Yb)n, ratios of 15.3, 14.7, and 14.3 respectively. The average chondrite-normalized La/Yb ratios (13.1) of the Lower Sequence basalts are higher than the value for Upper Sequence basalts, which is 7.7 (Fig. 5.7a and c). This relatively high (La/Yb)n ratio of the Lower Sequence basalts shows that basalts of such type are highly fractionated compared with the Upper Sequence basalts. However, both basalts show similar, slightly positive Eu anomalies (average 1.13), and also have similar middle REE (MREE) patterns. There is one sample, AX43d, from the Lower Sequence basalts that has a REE pattern similar to that of the HT basalts.

The geochemical variation of the Lower Sequence and Upper Sequence basalts is highly amplified in the normalized multi-element diagrams. The primitive mantle-normalized incompatible trace element diagrams (Fig. 5.7b and d) show generally coherent behavior with enriched low-field strength elements (Ba, Rb, K, Th) and depleted high-field strength elements (Zr, Eu, Ti) throughout the Lower Sequence suite; however, such behavior in the incompatible trace elements is reversed for the Upper Sequence basalts. In the primitive mantle-normalized multi-element diagram the contents of the elements Th and Nb from the Lower Sequence basalts are enriched by a factor of 3 compared to the Upper Sequence basalts, but the Sr, Nd, and Yb concentrations in both rocks are similar (Fig. 5.7b and d).

5.6 Results and Discussion

The field relations and geochemical data for the Axum volcanics reveal that there are spatially and temporally different volcanic sequences at the northern end of the Ethiopian flood basalts. The Axum volcanics, in this case, appear to be distinct from the northwestern Ethiopian flood basalts in that, first, they consist predominantly of alkaline to transitional basalt sequences; second, they show two mineralogically and geochemically distinct categories of basalts (Lower Sequence and Upper Sequence basalts).
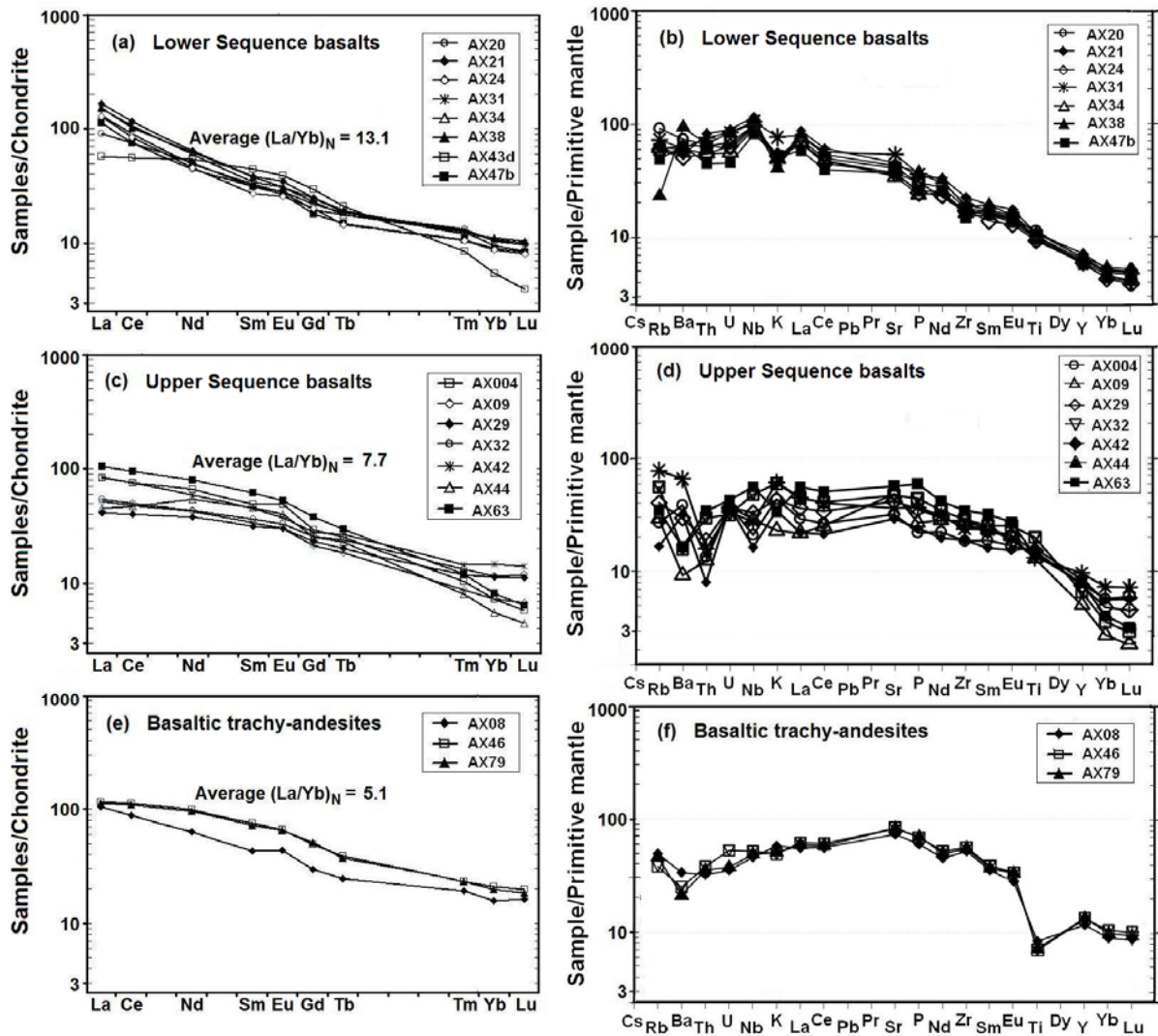
Figure 5.7 Chondrite-normalized rare earth and primitive mantle-normalized incompatible trace element abundance patterns of the Axum volcanic rocks. Normalization factors after Taylor and McLennan (1985) for the chondrite-normalization, and Sun and McDonough (1989) for the primitive mantle normalization.

Although Pik et al. (1998, 1999) grouped the Axum volcanics as transitional to tholeiitic low-Ti basalts, our detailed geochemical study on the northern end of the Ethiopian flood basalt confirmed that the Axum basaltic sequences are not tholeiitic in character, but instead they are entirely alkaline to transitional in character and plot along the trachybasalt/basanite boundary in the TAS plot (Le Bas et al., 1986) (Fig. 5.5). The other distinct feature of these flood basalts is their wider range in TiO$_2$ content. Previously, Pik et al. (1998, 1999) and Küster et al. (2005) proposed that rocks of the transitional to alkali basalts from the northwestern Ethiopian flood basalts were restricted to high-Ti (HT2 and HT1) suites with a TiO$_2$ ranging from 2.4–5 wt%; however, the Axum alkaline to transitional basalts cover a wider range (1.5–4.4 wt%) in TiO$_2$ content. They also exhibit a wider range in

concentration of the highly incompatible trace elements (Ba, Th, U, Nb, Ta, and La). The concentrations of Ba and Th range from 65 to 664 ppm and from 0.7 to 7.1 ppm, respectively. Based on the field relations, TiO_2 contents and incompatible trace element concentrations, the Axum alkali basalts are grouped into two parts as Lower Sequence alkali basalts (1.5–2.6 wt% TiO_2) and Upper Sequence alkali basalts (2.6–4.4 wt% TiO_2). These LT alkali basalts with their unique geochemical signature are not present in any other part of the Ethiopian flood basalt province, but Zanettin et al. (1999, 2006) and Kieffer et al. (2004) documented the existence of low-Ti alkali basalts in the central Eritrean highlands (Adi-Ugri and Asmara basalts) and in the central part of the northwestern Ethiopian volcanic province (Choke and Guguftu shield volcanoes), respectively.

The majority of the basaltic suites of the area (Upper Sequence) are HT type basalts; however, all samples from elongated outcrops in the southern part of the mapped area (Lower Sequence) are LT type basalts (Fig. 5.4). Generally, the Upper Sequence basalts of the area exhibit high TiO_2, Fe_2O_3, P_2O_5, and Y contents and Ti/Y ratios. In contrast, the Lower Sequence basalts exhibit high MgO and CaO contents, and CaO/Al_2O_3, Nb/Y, and Nb/La ratios (Table 5.3). Despite all the major and trace element variations, these two rock suites have similar SiO_2 contents.

The Axum volcanic rocks display a wide range in incompatible trace element abundances that are probably the result of variations in both source composition and melting conditions. The chondrite-normalized REE patterns and the multi-element spider diagram for the basaltic suites of Axum also confirm the existence of these two major groups of alkaline flood basalts. The geochemical characteristics of the Lower Sequence and Upper Sequence basalts of Axum are very different from those of the low-Ti and high-Ti basalts of the north-western Ethiopian flood basalts reported by Pik et al. (1998). According to the authors, the HT basalts were characterized by higher concentrations of incompatible elements and more fractionated REE patterns; however, in our study the opposite is observed.

The Lower Sequence basalts of Axum are characterized by higher concentration of the more incompatible elements (Ba, Rb, K, Nb, Ta, La, and Ce), steeply sloping LREE patterns, and more fractionated REE patterns. These rocks are much more similar with the Choke and Guguftu volcanoes in their trace element characteristics and TiO_2 contents. The Choke and Guguftu volcanoes consist of high contents of the highly incompatible trace elements, steeply sloping trace element patterns, low TiO_2 contents and positive Nb anomalies (Kieffer et al., 2004). Zanettin et al. (2006) believed that, during the early Miocene (24–22 Ma), the entire region of northern Ethiopia extending from Adi-Ugri (Mendefera)

through Axum–Adwa to Senafe (southeastern Eritrea) was involved in mafic and felsic volcanic activities, but with a considerable spatial variation in the ratio between basalt and trachyte or rhyolite. Kieffer et al. (2004) also confirmed that the Choke and Guguftu shield volcanoes erupted around 22 Ma ago contemporaneously with the central Eritrean Alkali basalts. Therefore, during the early Miocene period, not only the central Eritrea and Tigray regions were flooded by the alkaline magmatism but also extensive region extending to the central part of the northwestern Ethiopian volcanic province (Choke and Guguftu area) was involved in such magmatism.

Figure 5.7c and d show that, in terms of their trace element contents, the Upper Sequence basalts of Axum resemble Pik et al.'s (1998) HT1 type of flood basalt. The Upper Sequence basalts are characterized by relatively high concentrations of the less incompatible elements (Sm, Zr, Hf, and Tb), nearly flat LREE patterns and moderately sloping HREE patterns. The chondrite-normalized light to heavy REE ratio, (La/Yb)n, of the Upper Sequence basalts of Axum is 7.7, showing the relatively less fractionated nature of the basalts. According to Pik et al. (1998), the ages of HT1 rocks range from about 30 Ma in the north of the province to far younger in the south.

The distinct geochemical signatures of the Lower and Upper Sequence basalts of Axum indicate that the petrogenetic processes that formed these two rock types were different. One of the major element binary plots that can show differences in the petrogenetic processes is the CaO/Al_2O_3 vs. SiO_2. At a given SiO_2 content, most of the Lower Sequence basalts are displaced towards higher CaO/Al_2O_3 ratios (Fig. 5.8a). At a given Zr content, the Lower Sequence samples have higher Nb contents than do the Upper Sequence samples (Fig. 5.8b). Kamber and Collerson (2000) have indicated that Nb is more sensitive to variations in degrees of partial melting than Zr, and hence can be used to decipher the influence of variable degrees of melting. The Zr/Nb ratio of the Lower Sequence basalts is very low (2.8–3.1), except for sample AX43d, which has an abnormally high ratio of 21.1; whereas the Zr/Nb ratios of the Upper Sequence basalts are very high (9.4–18.1). A variation of trace element ratios between the Lower and Upper Sequence samples (e.g., Zr/Nb; Fig. 5.8c) is often cited as strong evidence that fractional crystallization has not been the dominant process in their evolution (Weaver, 1977; Wilson et al., 1985).
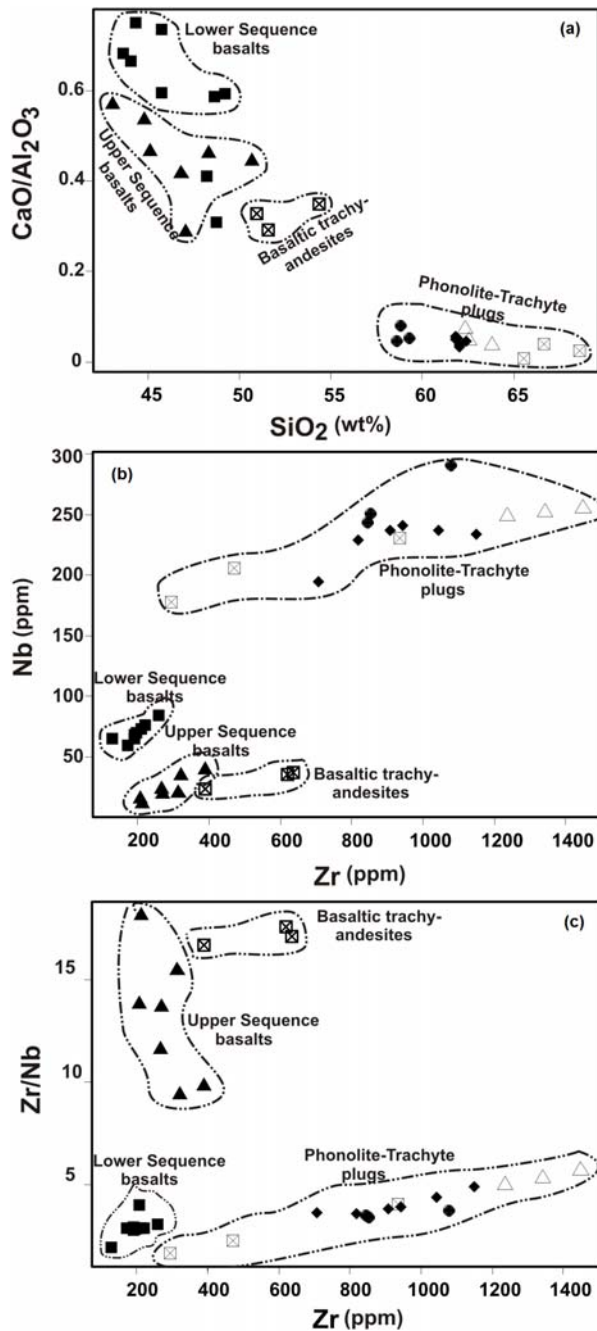
Figure 5.8 (a) Plot of CaO/Al_2O_3 ratio against SiO_2, showing the two apparent evolution trends for the Axum volcanic rocks. All the Upper Sequence basalts plot at lower ratios and most of the Lower Sequence basalts plot at higher ratios. (b) Linear correlation between Zr and Nb contents. Samples generally plot along Zr/Nb = 3 and Zr/Nb = 14, which may indicate different petrogenetic processes. (c) Zr/Nb vs Zr plot for the Axum volcanic rocks: the Upper Sequence rocks show expanded (7–18) Zr/Nb ratios and the Lower Sequence rocks with narrower and lower (2–5) Zr/Nb ratios.

The MnO–TiO₂–P₂O₅ and Zr–Nb–Y discrimination diagrams for basalts and basaltic andesites indicate that both the Lower and Upper Sequence basalts of Axum have similar source compositions, namely ocean-island alkali basalt (OIA) and/or within-plate alkali basalt (AI and AII), respectively (Fig. 5.9a and b). Although the primitive mantle-normalized incompatible trace element diagram for both the Lower and Upper Sequences shows some deviation from OIB composition, the average of all alkali basalts belongs to the OIB trend except the trace element Sr, which has relatively higher concentrations than those of normal OIB (Fig. 5.10c). The source reservoirs for both the Lower and the Upper Sequence basalts seem to be the same and resemble those of the OIB, but the main petrogenetic change may be most probably in the degree and mechanism of partial melting of the mantle plume. The comparatively small areal extent and volume of the Lower Sequence basalts in the study area suggests the outpouring of small volume of magma influx during the late-stage of flood basalt volcanism and these basalts are confined to post-volcanic depressions in the basement complex, with clastic sedimentary rock between the volcanics and the basement in some places. The laterally discontinuous but petrologically important rock suites at the base of the Axum volcanic piles are the basis for the classification of Axum basalts into Lower Sequence

basalts and Upper Sequence basalts. The Lower Sequence basalts of Axum provide also important clues for further study the temporal variations of the northwestern Ethiopian flood basalts.
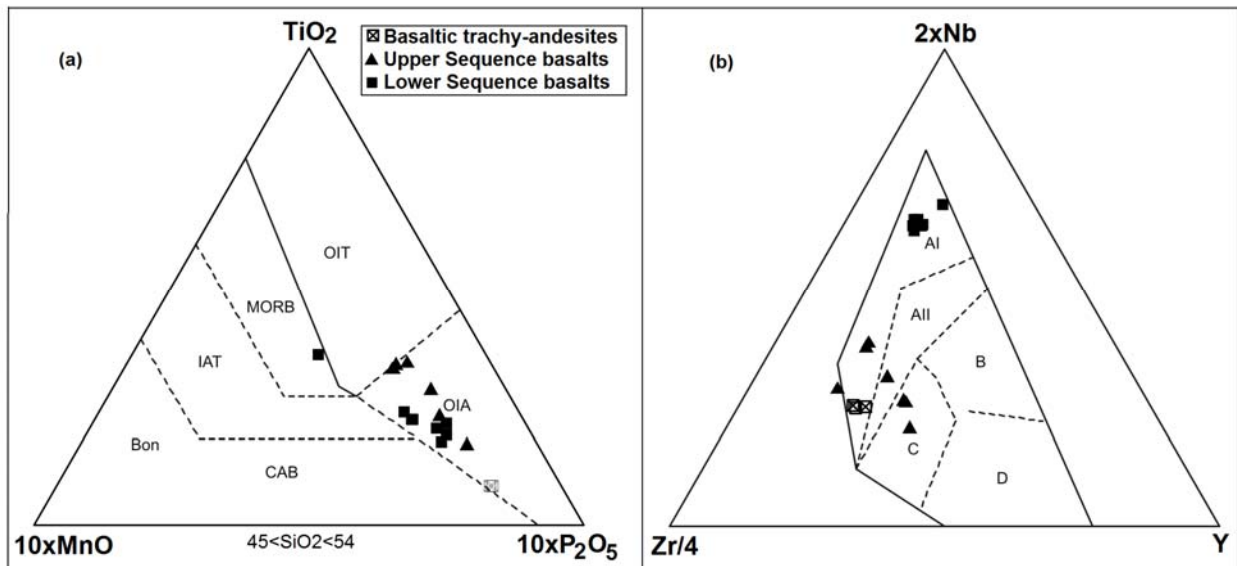
Figure 5.9 Selected major and trace elements for plotting discrimination diagrams. (a) The MnO–TiO_2–P_2O_5 discrimination diagram for basalts and basaltic andesites (45-54 wt% SiO_2) (after Mullen, 1983). The fields are MORB – mi-oceanic-ridge basalt; OIT – ocean-island tholeiite; OIA – ocean-island alkali basalt; CAB – island-arc calc-alkaline basalt; IAT – island-arc tholeiite; Bon – boninite. (b) The Zr-Nb-Y discrimination diagram for basalts (after Meschede, 1986). The fields are defined as follows: AI – within-plate alkali basalts; AII – within-plate alkali basalts and within-plate tholeiites; B – E-type MORB; C – within-plate tholeiites and volcanic-arc basalts; D – N-type MORB and volcanic-arc basalts.

5.7 Conclusions

Many petrologically different volcanic sequences in the northern Ethiopian plateau have been indistinctly categorized as the low-TiO_2 (LT) transitional to tholeiitic basalt suites of the northwestern flood basalts (Pik et al., 1998, 1999). One of these volcanic sequences are comprised by the Axum volcanics, a geochemically complex and lithologically varied part of the northwestern Ethiopian flood basalt province erupted in a narrow time span. The Axum volcanics are highly alkaline to transitional in composition, with distinctive geochemical signatures among the Ethiopian flood basalts.
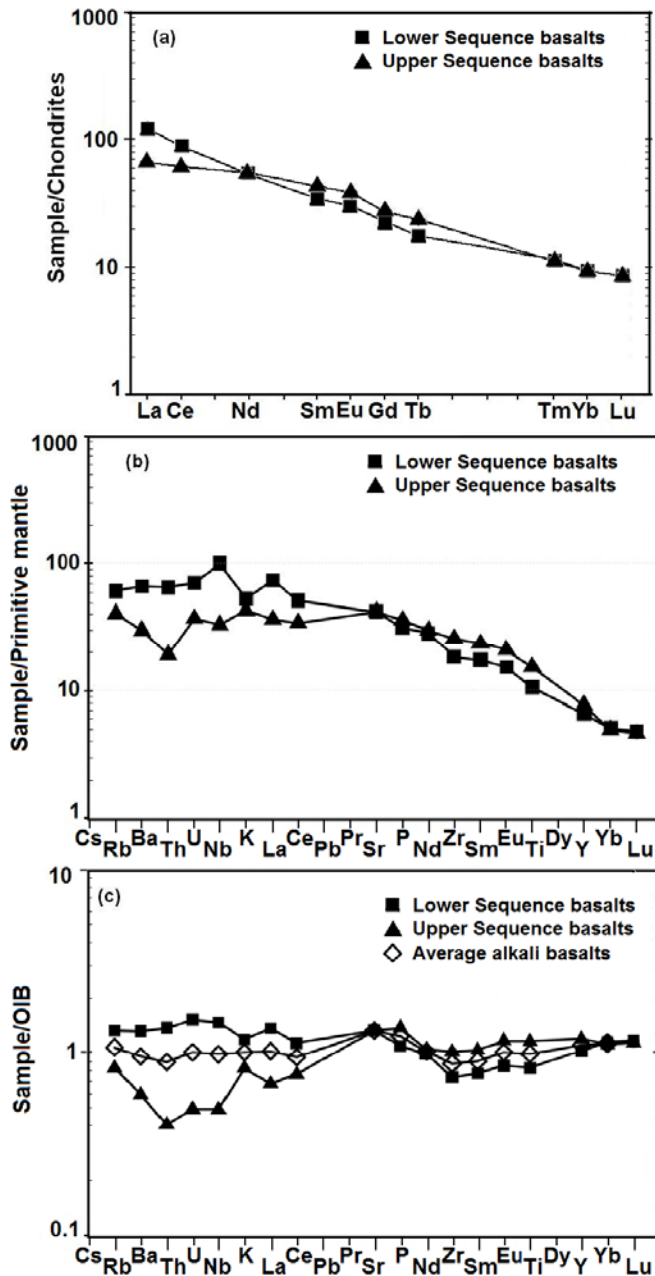
Figure 5.10 Average plots of the Lower Sequence and Upper Sequence basalts of Axum area. (a) Plot of average chondrite-normalized rare earth element abundances (normalizing factors from Taylor and McLennan, 1985); (b) plot of average primitive mantle-normalized incompatible trace element contents (normalizing factors from Sun and McDonough, 1989), and (c) plot of ocean island basalt (OIB)-normalized incompatible trace elements (normalizing factors from Sun and McDonough, 1989). From the primitive mantle-normalized multi-element plot the Lower Sequence basalts show higher concentrations of the highly incompatible (mobile) trace elements especially Ba, Th and Nb, however the less incompatible trace elements (Zr, Sm, Eu, Ti) are slightly higher in the Upper Sequence basalts. To see further differences between these two suites, the incompatible traces are projected in the OIB normalized plot. The unique character of the chondrite- and primitive mantle-normalized plots is also observed here, but the average of all alkali basalts of Axum agrees well with the composition of OIB, except for the element Sr, which is slightly high for alkali basalts.

The Axum volcanic rocks have been subdivided here based on their petrography and geochemistry into two main groups: the Lower Sequence basalts and the Upper Sequence basalts. The Lower Sequence basalts are aphyric–phyric with sparse phenocrysts of clinopyroxene and olivine. They have high MgO and CaO contents, high CaO/Al_2O_3, Nb/Y,

Nb/La ratios, and high large ion lithophile (LIL) or low field strength incompatible trace element contents. The Upper Sequence basalts, which are plagioclase-phyric, ± K-feldspar bearing (rich and poor), display high TiO_2, Fe_2O_3, P_2O_5 contents and Ti/Y ratio, and relatively high low field strength (LFS) incompatible trace element contents.

The basaltic rocks of Axum area are, therefore, different from the northwestern LT tholeiitic basalts both in mineralogy and geochemistry. The Lower and Upper Sequences of Axum are silica-undersaturated (negative saturation index, SI), alkaline–transitional basalts with basanitic–basaltic-trachyandesitic affinity. The basaltic rocks of Axum are characterized by wide ranges of TiO_2, trace element and REE contents, which helps to obtain information about the mineralogical, geochemical composition and the age variations of the northern Ethiopian volcanic rocks.

Acknowledgements

References:

Abebe T., Mazzarini F., Innocenti F., and Manetti P. 1998. The Yerer–Tullu Wellel volcanotectonic lineament: a transtensional structure in central Ethiopia and the associated magmatic activity. Journal of African Earth Sciences 26, 135–150.

Alemu T. 1998. Geochemistry of Neoproterozoic granitoids from the Axum Area, Northern Ethiopia. Journal of African Earth Sciences 27, 437–460.

Alene M., Secco L., Dal Negro A., and Sacchi R. 2000. Crystal chemistry of clinopyroxene in Neoproterozoic metavolcanic rocks of Tigrai, Northern Ethiopia. Bollettino della Societa Geologica Italiana 119, 581–586.

Asrat A., Gleizes G., Barbey P., and Ayalew D. 2003. Magma emplacement and mafic - felsic magma hybridisation: structural evidence from the Pan-African Negash pluton, Northern Ethiopia. Journal of Structural Geology 25, 1451–1469.

Asrat A., Barbey P., Ludden N.J., Reisberg L., Gleizes G., and Ayalew D. 2004. Petrology and isotope geochemistry of the Pan-African Negash pluton, Northern Ethiopia: Mafic-felsic magma interactions during the construction of shallow-level calc-alkaline plutons. Journal of Petrology 45, 1147–1179.

Ayalew D., Yirgu G., and Pik R. 1999. Geochemical and isotopic (Sr, Nd and Pb) characteristics of volcanic rocks from south-western Ethiopia. Journal of African Earth Sciences 29, 381–391.

Ayalew D., Barbey P., Marty B., Reisberg L., Yirgu G., and Pik R. 2002. Source, genesis and timing of giant ignimbrite deposits associated with Ethiopian continental flood basalts. Geochimica et Cosmochimica Acta 66, 1429–1448.

Baker J., Snee L., and Menzies M. 1996. A brief Oligocene period of flood volcanism in Yemen: implications for the duration and rate of continental flood volcanism at the Afro-Arabian triple junction. Earth and Planetary Science Letters 138, 39–55.

Beyth M. 1972. The geology of central and western Tigray. Ph.D thesis: Rheinische Friedrich-Wilhelms Universtät, Bonn, Germany, 200 pp .

Beyth M. 1991. ''Smooth'' and ''rough'' propagation of spreading, southern Red Sea – Afar depression. Journal of African Earth Sciences 13, 157–171.

Ebinger C.J. and Sleep N.H. 1998. Cenozoic magmatism throughout East Africa resulting from impact of a single plume. Nature 395, 788–791.

Ethiopian Institute of Geological Survey 1999. Aksum map sheet ND 37-6 (scale 1:250,000). Geological Survey of Ethiopia, Addis Ababa, Ethiopia.

Gasparon M., Innocenti F., Manetti P., Peccerillo A., and Tsegaye A. 1993. Genesis of the Pliocene to Recent bimodal mafic-felsic volcanism in the Debre Zeyt area, central Ethiopia: volcanological and geochemical constraints. Journal of African Earth Sciences 17, 145–165.

George R.M., Rogers N., and Kelley S. 1998 Earliest magmatism in Ethiopia: Evidence for two mantle plumes in one flood basalt province. Geology 26, 923–926.

Hofmann C., Courtillot V., Feraud G., Rochette P., Yirgu G., Ketefo E., and Pik R. 1997. Timing of the Ethiopian flood basalt event and implications for plume birth and environmental change. Nature 389, 838–841.

Kabeto K., Sawada Y., Bussert R., and Küster D. 2004. Geology and geochemistry of Maychew volcanics, northwestern Ethiopian Plateau. International Conference on East African Rift system, Addis Ababa, Ethiopia. Extended Abstracts 1, 110–114.

Kamber B.S. and Collerson K.D. 2000. Zr/Nb systematics of ocean island basalts reassessed – the case for binary mixing. Journal of Petrology 41, 1007–1021.

Kieffer B., Arndt N., Lapierre H., Bastien F., Bosch D., Pecher A., Yirgu G., Ayalew D., Weis D., Jerram A.D., Keller F., and Meugniot C. 2004. Flood and shield basalts from Ethiopia: magmas from the African superswell. Journal of Petrology 45, 793–834.

Koeberl C. 1993. Instrumental neutron activation analysis of geochemical and cosmochemical samples: A fast and reliable method for small sample analysis. Journal of Radioanalytical and Nuclear Chemistry 168, 47–60.

Küster D., Dwivedi S.B., Kabeto K., Mehary K., and Matheis G. 2005. Petrogenetic reconnaissance investigation of mafic sills associated with flood basalts, Mekelle basin, Northern Ethiopia: implication for Ni-Cu exploration. Journal of Geochemical Exploration 85. 63–79.

Le Bas M.L., Le Maitre R.W., Streckeisen A., and Zanettin B. 1986. A chemical classification of volcanic rocks based on the total alkali – silica diagram. Journal of Petrology 27, 745–750.

Meschede M. 1986. A method of discriminating between different types of mid-ocean ridge basalt and continental tholeiites with the Nb-Zr-Y diagram. Chemical Geology 56, 207–218.

Merla G., Abbate E., Azzaroli A., Bruni P., Canuti P., Fazzuoli M., Sagri M., and Tacconi P. 1979. Comments to the geological map of Ethiopia and Somalia. Consiglio Nazionale delle Ricerche, Firenze, 89–95.

Mohr P. 1983. Ethiopian flood basalt province. Nature 303, 577–584.

Mohr P. 1987. Patterns of faulting in the Ethiopian Rift Valley. Tectonophysics 143, 169–179.

Mullen E.D. 1983. MnO/TiO2/P2O5: a minor element discriminant for basaltic rocks of oceanic environment and its implications for petrogenesis. Earth and Planetary Science Letters 62, 53–62

Pik R., Deniel C., Coulon C., Yirgu G., Hoffmann C., and Ayalew D. 1998. The northwestern Ethiopian Plateau flood basalts: classification and spatial distribution of magma types. Journal of Volcanology and Geothermal Research 81, 91–111.

Pik R., Deniel C., Coulon C., Yirgu G., and Marty B. 1999. Isotopic and trace element signatures of Ethiopian basalts: evidence for plume-lithospheric interactions. Geochimica et Cosmochimica Acta 63, 2263–2279.

Rogers N.W. 2006. Basaltic magmatism and the geodynamics of the East African Rift System. In: Yirgu G., Ebinger C.J., and Maguire P.K.H. (Eds.), The Afar Volcanic Province within the East African Rift System. Geological Society, London, Special Publication 259, 77–93.

Son T.H. and Koeberl C. 2005. Chemical variations within fragments of Australasian tektites. Meteoritics and Planetary Science 40, 805–815.

Stewart K. and Rogers N. 1996 Mantle plume and lithosphere contributions to basalts from Southern Ethiopia. Earth and Planetary Sciences Letters 139, 195–211.

Sun S. and McDonough W.F. 1989. Chemical and isotopic systematics of oceanic basalts: implications for mantle composition and processes. In Saunders A.D. and Norry M.J. (Eds.), Magmatism in the ocean basins. Special Publication of Volcanology. Geological Society of London 42, 313–345.

Tadesse T. 1996. Structure across a possible intra-oceanic suture zone in the low-grade Pan-African rocks of Northern Ethiopia. Journal of African Earth Sciences 23, 375–381.

Tadesse T. 1997. The Geology of Axum area (ND 37-6). Memoir no. 9, Ethiopian Institute of Geological Survey, Addis Ababa, Ethiopia, 184 pp.

Taylor S.R. and McLennan S.M. 1985. The continental crust: Its composition and evolution. Blackwell, Oxford, 312 pp.

Ukstins I., Renne P., Wolfenden E., Baker J., Ayalew D., and Menzies M. 2002. Matching conjugate volcanic rifted margins: $^{40}Ar/^{39}Ar$ chronostratigraphy of pre- and syn-rift bimodal flood volcanism in Ethiopia and Yemen. Earth and Planetary Science Letters 198, 289–306.

Verma S.P., Torres-Alvarado I.S., and Sotelo-Rodriguez Z.T. 2002. SINCLAS: standard igneous norm and volcanic rock classification system. Computers and Geosciences 28, 71–715.

Weaver S.D. 1977. The Quaternary caldera volcano Emuruangogolak, Kenya Rift, and the petrology of a bimodal ferrobasalt-pantelleritic- trachyte association. Bulletin of Volcanology 40, 209–230.

Wilson M., Downes H., and Cebriá J. 1995. Contrasting fractionation trends in coexisting continental alkaline magma series. Cantal, Massif Central, France. Journal of Petrology 36, 1729–1753.

Zanettin B., Bellieni G., Visentin J.E., and Haile T. 1999. The volcanic rocks of the Eritrean plateau: stratigraphy and evolution. Acta Volcanology 11, 183–193.

Zanettin B., Bellieni G., and Visentin J.E. 2006. New radiometric age of volcanic rocks in the Central Eritrean plateau (from Asmara to Adi Quala): considerations on stratigraphy and correlations. Journal of African Earth Sciences 45, 156–161.

CHAPTER 6

CHAPTER 6: GEOCHEMICAL CHARACTERISTICS OF THE ALKALINE BASALTS AND THE PHONOLITE–TRACHYTE PLUGS OF THE AXUM AREA, NORTHERN ETHIOPIA

Miruts Hagos[1]*, Christian Koeberl[1], Kurkura Kabeto[2], Friedrich Koller[1]

[1]Department of Lithospheric Research, University of Vienna, Althanstrasse 14, A-1090 Vienna, Austria
[2]Department of Earth Sciences, Mekelle University, P.O. Box 231 Tigray, Ethiopia

* corresponding author: Tel: +43-1-4277-53104; E-mail: miruts2005@yahoo.com (M. Hagos)

Abstract– The Axum volcanic rocks constitute important deposits of trap (Oligocene) and post-trap (Miocene- to Pliocene) volcanic rocks at the northern end of the great Ethiopian flood basalt sequence. The petrologic diversity of lavas erupted in the Axum area is significant, ranging from basanites to tephrites and phonolites to trachytes. The variation in the concentration of major elements (Fe_2O_3, TiO_2, CaO), rare earth elements (REE), and incompatible element ratios (Zr/Nb, Nb/Y) in the volcanic rocks of Axum demonstrates the heterogeneous character for their source region. Such heterogeneity can be interpreted by the involvement of a mantle reservoir to different degrees and mechanisms of partial melting. The geochemical data show that the Axum volcanic rocks represent two magma series, which we designate as the flood basalt sequence and the post-trap basalt sequence. The flood basalt sequence, which erupted contemporaneously with the Oligocene Ethiopian flood basalts, exhibit high TiO_2 (2.6–4.4 wt%), Fe_2O_3 (13.4–17.4 wt%), and high Zr/Nb ratio (9–18). In contrast, the post-trap basalt sequence, which has a slight tendency towards the composition of the northcentral Ethiopian shield volcanoes (Guguftu shield volcano) and the central and southeastern Eritrean volcanics suites, exhibit low TiO_2 (2.0–2.6 wt%), Fe_2O_3(10.5–14.6 wt%), Zr/Nb ratio (2.8–3.1), and high Nb (60–84 ppm), Th (3.9–7.2 ppm), and Nb/Y ratio (2.2–2.7). The acidic rocks, on the other hand, are indistinguishable from each other and values of their trace element ratio are comparable with the trace element ratios of the post-trap basalt sequence. The acid volcanics (phonolites and trachytes) might, therefore, have formed mostly through fractional crystallization of the post-trap basalt sequence magmas.

Keywords: Ethiopian flood basalts; Axum; Basanite; Tephrite; Phonolite

----

6.1 Introduction

The Axum study area is located in the northern part of the Ethiopian highlands and it is mainly covered by Tertiary fissure basalts and the post-trap, east–west aligned Adwa–Axum phonolite and trachyte plugs (Hagos et al., 2010). These volcanic rocks were emplaced in the north–northwestern portion of the Tigray region, northern Ethiopia, isolated from the major Ethiopian flood basalts by the deeply cut Tekeze basin and from the Eritrean highland basalts and trachytes by the Mereb basin (Fig. 6.1).

The Oligocene–Present Ethiopian volcanic province is one of the youngest flood basalt deposits on Earth and is a classic example to study young hot mantle plume processes underneath the Afar Depression. This province is particularly favorable for the understanding of magmatism related to all phases of rift evolution (Barrat et al., 1998). Magmatism in this region commenced in southwestern Ethiopia around 45 Ma (George et al., 1998), followed by massive outpouring of flood basalt activity in northwestern Ethiopia, Eritrea and Yemen at ~30 Ma (Hofmann et al., 1997; Furman et al., 2004). Subsequent volcanic or magmatic activity, from early Miocene–Present, occurs as large shield volcanoes overlying the Ethiopian flood basalts (Kieffer et al., 2004) or is associated with lithospheric extension and is localized to the tectonically active rift segments of Afar Depression (Pik et al., 1999). The Ethiopian landmass has experienced volcanic activities for a wide time span, from the Eocene to present and in northern Ethiopia, in the Axum area, at least two phases of eruptive activity have taken place; the first during the Oligocene period ~30 Ma (part of the Ethiopian flood basalt) and the second during the Miocene–Pliocene periods (post-trap basalts and phonolite/trachyte plugs).

The northwestern, central, and southern part of the Ethiopian flood basalts and associated shield volcanoes have been the subject of numerous studies (e.g., Mohr, 1983; Ebinger and Sleep, 1998; George et al., 1998; Pik et al., 1998, 1999; Ayalew et al., 1999, 2002; Ukstin et al., 2002; Kieffer et al., 2004). The existing studies in the Axum region (e.g., Alemu, 1998; Alene et al., 2000; Asrat et al., 2003, 2004; Tadesse, 1996, 1997) have mainly focused on the Precambrian basement and Pan African plutons of the area. The only study dealing with the volcanics of the Axum area was conducted during the regional mapping by the Ethiopian Institute of Geological Survey (1999). In this study, the volcanic rocks of Axum were classified on the basis of the locality names as the Koyetsa volcanic (stratified flood basalt) and the Adwa trachyte formation (trachytic and phonolitic plugs). However, detailed geological investigations are still rare in the Axum region. Petrologic and

geochemical classifications of the area were made based on sample analyses collected from Mai-chew area and northwestern flood basalts. As a result of poor extrapolation the geological classifications were not representing the actual volcanic rocks of the Axum area.

In this topic we have focused on the geochemical (major and trace element) characteristics of the Axum alkali basalts, phonolites and trachytes, and possible petrogenetic relationships among them. We have also compared the spatial and temporal variation of the Axum volcanic rocks with the central– to northwestern Ethiopian shield volcanoes and the central– to southeastern parts of the Eritrean volcanic rocks.

6.2 Geological Background

Most continental volcanism represent huge volume of fissure fed basaltic lava flows and, in some cases, felsic lavas and pyroclastic products, mostly with volumes greater than one million km^3 (Baker et al., 1996). The Ethiopian volcanic province is one of the well preserved and youngest flood basalt provinces resulting from the mantle plume head centered on the present day Afar Depression (e.g., Baker et al., 1996; George et al., 1998; Audin et al., 2004). These flood basalts were unconformably deposited on a regionally lateritized clastic Mesozoic sedimentary surfaces (Ukstins et al., 2002) and some on deeply eroded Precambrian basement complexes. Basaltic lavas of this province erupted at ~30 Ma, during a short 1–2 My period, to form a thick pile (~2000 m) of vast volcanic highland (e.g., Baker et al., 1996; Hofmann et al., 1997; Kieffer et al., 2004). However, younger phases of intraplate and rift-triggered magmatism with an age range of 14–5 Ma and pre-rift, Eocene–Oligocene (Stewart and Rogers, 1996) volcanic rocks are common to the east and southwestern portion of the Ethiopian volcanic province, respectively.

The mineralogical and chemical composition of the Oligocene Ethiopian flood basalt is comparatively uniform and most rocks are aphyric to sparsely phyric, and contain phenocrysts of plagioclase and clinopyroxene with minor olivine (Kieffer et al., 2004). Despite their compositional similarities, the flood basalts of Ethiopia were divided into three types based on their temporal variations (Mohr, 1983). In ascending stratigraphic order, these are called the Ashange, Aiba, and Alage basalts. Subsequent studies (Pik et al., 1998, 1999) have shown that the old classification was not vindicated from petrology and geochemistry analyses. The lowermost sequence, the so called 'Ashange basalts', is characterized by tholeiitic basalts found with inter-layered felsic lavas and pyroclastic products towards its top (Coulie et al., 2003).

Interbedded with the flood basalts, particularly at upper eruptive levels, are trachytes and/or ignimbrites with variable textures ranging from glassy through sparsely porphyritic to porphyritic (6–20 vol% of phenocrysts) (Ayalew et al., 2002; Kabeto et al., 2004). In the northern Ethiopia and Eritrea (Senafe area), magmatism began somewhat later, at about 24 Ma, with the deposition of felsic volcanics (trachyte and rhyolite), coeval with the basaltic rocks of the region (Zanettin et al., 2006a).

The volume and aerial coverage of these felsic rocks substantially increase towards the northern end (Tigray and Eritrea) of the Ethiopian volcanic province. The trachytes occur as plugs (steep-sided conical hills), and lie within an E–W belt extending from the eastern margin of the Ethiopian plateau, between Adigrat and Senafe, via Adwa and Axum, westward to the middle Tekeze river valley. Along this belt, the trachytic/phonolitic domes reach their highest frequency and dimension and lie indistinguishably on the Arabian-Nubian shield, Mesozoic sandstone, and Oligocene volcanic rocks of the region (Zanettin et al., 2006b).
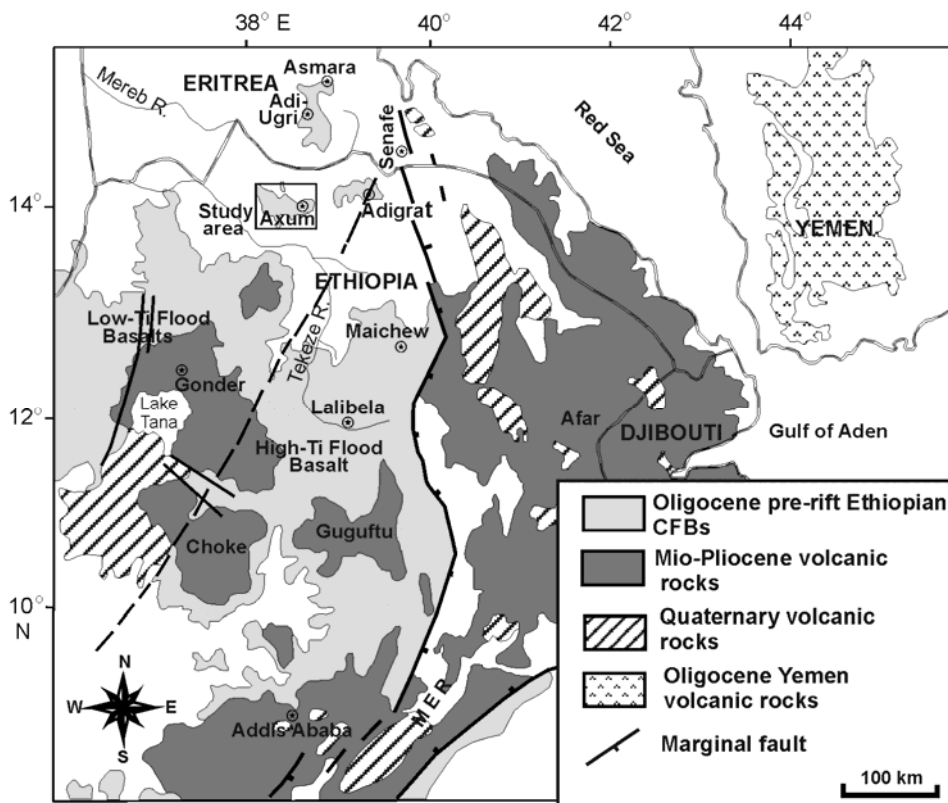
Figure 6.1 Simplified sketch map of the central– to northern parts of the Ethiopian volcanic province and the Quaternary Afar Depression basalts with a box showing the location map of the Axum bimodal volcanics. The dashed line divides the eastern high-Ti and western low-Ti basalts (modified after Merla et al., 1979; Pik et al., 1998, and Küster et al., 2005).

The felsic rocks of Axum–Adwa area and, by analogy, those of the Senafe domes (southeastern Eritrea) were coeval with the ignimbritic layers intercalated with the late stage

trap series occurring in both Tigray and in the central Eritrean plateau (Dainelli, 1943). The geochemical data shows that the felsic rocks of the region are highly diversified, ranging from the rhyolite field to the phonolitic tephrites (Zanettin et al., 2006b). According to these authors, the domes and dykes existing in the Axum–Adwa and Senafe area correspond to different volcanic series: transitional, mildly alkaline, and strongly alkaline.

6.3 Geology and Petrography of the Axum Volcanic Rocks

The Axum volcanic rocks constitute an important outcrop of trap basalts and post-trap basalts and phonolite trachyte plugs at the northern end of the Ethiopian flood basalt province. They are about 5–500-m-thick sequences exposed around Axum and Shire regions covering a total area of about 1200 km^2. The Axum volcanics are visually classified in to the Axum basaltic sequences and the phonolite–trachyte plugs.

6.3.1 The Axum Basaltic Sequences

In the study area, the Mesozoic sedimentary rocks and/or basement complexes are unconformably overlain by the Ethiopian Plateau flood basalts erupted between 31–29 Ma (Hofmann et al., 1997) and the later phase basaltic rocks. Based on field observations and mineralogy, these volcanic rocks are broadly subdivided into two major sequences. These are the post-trap basalt sequence and the flood basalt sequence.

6.3.1.1 Post-trap Basalt Sequence

This sequence is located about 5–10 km south of the town of Axum, mainly unconformably overlying the sheared, deformed and deeply weathered basement complex of Deigo and Adi-Tsehafi villages at an altitude of 2020–2130 m. The rocks are gently inclined (<5°), 5–60 m thick, and show southwest lava flow direction. They are rarely vesicular, columnar jointing, and commonly less weathered than the adjacent flood basalt sequence. The lava flows of this basaltic sequence are thicker but less continuous than the neighboring flood basalt sequence. Normally, such rocks are laterally discontinuous and usually exposed along the deep canyons of the southern and northern part of the area (Fig. 6.3).

The basalts are commonly aphyric to highly phyric with a significant amount of phenocrysts (Fig. 6.2a). The phenocryst minerals constitute about 25 vol% and comprise euhedral to subhedral pyroxene, olivine, and plagioclase-lath. More over opaque minerals (ilmenite, magnetite) constitute up to 20 vol%. The groundmass is dominated by plagioclase and pyroxene.

6.3.1.2   Flood Basalt Sequence

This sequence, about 350–400 m thick and commonly exposed in the central and western part of the area at an altitude between 2080–2600 m, is invariably weathered and intercalated with thin pyroclastic (ash-tuff fallout) materials. This basaltic sequence, unconformably overlying the clastic Mesozoic sedimentary rocks of the region, is the western extension of the Adigrat basaltic sequence, but is isolated from the Adigrat basalts by the Adwa basin. The vesiculated and weathered parts of this sequence contain some secondary minerals like calcite veins in addition to silica and zeolites. These rocks show extensive areal distribution but with contrasting thickness. This volcanic deposit comprises coarse-grained, plagioclase-phyric, ± K-feldspar-bearing basalts. The feldspars are well aligned and show well-preserved flow texture. In most of the samples the pyroxenes exist as euhedral to subhedral mega-phenocrysts. The pyroxene phenocrysts constitute ~5–10 vol% (Fig. 6.2b).

6.3.2   Miocene– to Pliocene-age Axum Phonolite–Trachyte Plugs

Widespread silica-poor igneous materials, forming steep sloped plugs and ridges, were produced probably during middle–late Miocene (20–7 Ma) (Beyth, 1972), when they punctured and partially extruded/intruded the upper part of the clastic Mesozoic sedimentary and the Tertiary flood basalt Sequence. These, silica-poor volcanic to hypabyssal rocks belong to the Axum-Adwa phonolite–trachyte volcanic field and are exposed mostly at the north side of the study area (Fig. 6.3). The variation in mineralogy is gradational and ranges from nepheline-rich phonolite (Bete-Giorgis phonolites)– to nepheline-poor phonolitic-trachyte (Adi-Tsehafi trachytes) and trachytes (Mai-Koho trachytes).

6.3.2.1   Bete-Giorgis Phonolites

These rocks are emplaced directly at the northwestern end of the town of Axum and about 4 km to the northeast of the Gobo-Dura ridge. The exposure is in the form of a large, completely exposed, circular (~3.2 km in diameter) dome rising about 300 m above the alkaline basalts. Only few primary structures and secondary features: some columnar joints along the hilly parts of the dome and weak spheroidal-type weathering in some of the rounded blocks are observed in the dome. The phonolitic rocks are still massive, but moderate weathering along fracture surfaces and complete alteration along contacts and weak zones occur. The Bete-Giorgis phonolite plugs show a zoned texture with a light colored and fine-grained rim at the contact with the trachytes, and a dark-colored, medium- to coarse-grained core. The uphill part of the dome is relatively flat and covered by debris of the fine-grained phonolites. This is because during the early (~150 BC–AD 150) and typical Axumite

(AD 150–350) civilization periods, settlements in the region were dense and concentrated around Axum and Bete- Giorgis areas (Schmid et al., 2008).

The Bete-Giorgis phonolites have variable texture. They are porphyritic with phenocrysts of alkali pyroxene, nepheline, and feldspars. Under plane polarized light, the pyroxenes have high-relief, brownish- to greenish color, with needle-like to skeletal form. The nephelines are rectangular- to hexagonal in shape and some exist in the form of inclusion inside the alkali pyroxene phenocrysts (Fig. 6.2c). In some of the samples (AX43 and AX111) the nephelines are highly altered to zeolites and they mask the existence the other minerals. The aegerines are tabular- to elongated and in places they grew at the rims of other minerals.

6.3.2.2   Gobo-Dura Phonolites

Five km west of Axum, along the road to Shire, there is an about 200–250 m thick, circular (3.5 km in diameter) and dome-shaped phonolite outcrops. They are dark-gray to pink in color, extremely massive, unweathered and occur in places as 35-m-long single blocks. Most of the blocks are tabular and elongated, but few form spherical outcrops. Despite its unique lithologic setup the Gobo-Dura ridge constitutes various relics reflecting the ancient architecture of the Axumite Empire. At the northeastern part of the dome, there is ancient, (~1700 years old) quarry-site hosting dozens of semi-finished obelisks. To further study the mineralogical and geochemical characteristics of these archaeologically important rocks, five samples were collected for analyses.

Petrographically, the Gobo-Dura phonolites are also dominated by phenocrysts of pyroxene, nepheline, and some early crystallized sanidine. The pyroxenes are light-brown to green with distinct relief under plane polarized light. Very large grains of partly altered, subhedral to anhedral nephelines mask other low-relief minerals (Fig. 6.2d). Highly altered mafic minerals and some intergrowths of aegerines surround the nepheline phenocrysts. Tightly locked needle-like feldspars filled the interstices of the pyroxenes.

6.3.2.3   Adi-Tsehafi Trachyte

About five km to the north of the town of Axum, where the river Gwada turns to the north, the great unconformity that separates the late-Proterozoic granitic intrusion and the clastic Mesozoic sedimentary rocks is injected by the Miocene- to Pliocene rocks of the area. These are subvolcanic bodies (sills) exposed along the Gwada river after intense erosion of the overlying rocks (the sandstone and the trap basalts). These sills are about 15 m thick, and comprise massive, partially weathered and fine- to medium-grained rocks. The second-largest quarry-site operated during the time of King Kaleb (~520 AD) is situated at this outcrop. The

length of a single block of rock does not exceed 15 m, but this quarry site was mainly used as a source for rock inscriptions and various underground and gravestone works during the time of King Kaleb of the Axumite Empire. To study the geochemical characteristics of these rocks, three samples were analyzed for their major and trace element contents. The Adi-Tsehafi trachytes constitute needle-like- to elongated, holocrystalline, medium-grained feldspars (orthoclase) and sparsely distributed dark-green sodic pyroxenes/aegerines. Most of the minerals are highly weathered but some subhedral- to anhedral nepheline crystals filled the interstices of the feldspars (Fig. 6.2e).

6.3.2.4   Mai-Koho Trachytes

At the northern and northwestern part of Axum, trachyte flows cut by phonolites plugs are widely distributed and at places they formed mountain-chains as high as 500 m. They are considered to be the western extension of the Senafe – Adwa trachytic plugs (Zanettin et al., 2006b) but with a remarkable shift in their morphology. The Senafe–Adwa trachytic plugs are steeper and taller (~1000 m) than the Axum trachytic plugs, which are dome-shaped and not >400–500 m tall. The Mai-Koho trachytes are whitish-grey in color, soft, moderately weathered, thinly layered and intensely fractured. These rocks are commonly emplaced adjacent to the phonolites, but they are steep plugs and form chain-like exposures.

Fine– to coarse-grained (inequigranular) elongated and in some cases euhedral K-feldspars with well developed trachytic textures are the main constituents of the outcrop. The feldspars occur both as groundmass and as phenocrysts. Some of the phenocrysts show simple twinning and others have spherulitic texture. Some mafics (dark minerals) exist, but they are highly oxidized (Fig. 6.2f).

6.4   Geochemical Data

6.4.1 Sampling and Analytical Methods

Our sampling attempted to include both the mafic and felsic volcanic rocks of Axum. Thirty-three samples were carefully selected from 112 samples collected from the entire Axum area and prepared for X-Ray Fluorescence (XRF) spectrometry and Instrumental Neutron Activation Analysis (INAA). 100–200 g of clean, unaltered interior chips were selected from approximately one kg sample for crushing and preparation of powders for chemical analyses. Petrographic thin-sections were also prepared for 32 samples from each of the basaltic, trachytic and phonolitic rocks, and detailed mineralogical analyses were made under an optical (petrographic) microscope. For some of the minerals, the semiquantitative modes were determined by visually estimating the mineral proportions in thin sections

From the 33 analyzed samples 19 were from the two types of basalts and the remaining samples were from the phonolitic–trachytic rocks of the Bete-Giorgis, Gobo-Dura, Adi-Tsehafi, and Mai-Koho ridges. All rock samples were first crushed in a stainless steel jaw crusher and then powdered in an agate mill in order to avoid contamination of transition elements (such as Co, Ta, and Nb) for the chemical analyses. Contents of major oxides, minor and trace element (Nb, Zr, Y, Sr, Ga, Cu, Ni, V) abundances were determined using wavelength-dispersive XRF spectrometry at the Department of Lithospheric Research, University of Vienna, Austria. 1.2 g of powdered rock was mixed with 6 g of lithium tetra-borate to prepare fused pellets used for the analyses of the major oxides, and 10 g of powdered rock was used to prepare pressed pellets for the analyses of the trace elements.

Contents of the rare earth element (REE) and other trace elements (i.e., Sc, Cr, Co, Zn, As, Se, Br, Rb, Sb, Cs, Ba, Hf, Ta, W, Ir, Au, Th, and U) were analyzed by INAA at the Department of Lithospheric Research, University of Vienna. For this, samples weighing between 115 and 130 mg were sealed into polyethylene capsules, as well as 60- to 100 mg of three of the following international rock standards: carbonaceous chondrite Allende (Smithsonian Institute, Washington DC, USA; Jarosewich et al., 1987), the granite AC-E (Centre de Recherche Pétrographique et Géochimique, Nancy, France: Govindaraju, 1989), and the Devonian Ohio shale SDO-1 (United States Geological Survey, Govindaraju, 1989) were irradiated for 8 hours at the Triga Mark II reactor of the Institute of Atomic and Subatomic Physics, Vienna, at a neutron flux of 2.10^{12} n cm^{-2} s^{-1}. Details of the INAA method, including standards, correction procedures, precision, and accuracy, are reported in Koeberl (1993), Son and Koeberl (2005), Mader and Koeberl (2009)

Table 6.1: Major and trace element contents of the phonolites and trachytes from Axum, Northern Ethiopia.

	Trachyte AX002	Trachyte AX008	Phonolite AX011	Phonolite AX012	Trachyte AX41	Phonolite AX43	Phonolite AX45	Phonolite AX45c	Trachyte AX51	Phonolite AX111	Phonolite AX112	Phonolite AX06	Trachyte AX07	Phonolite AX10a	Trachyte AX10b
(wt.%)															
SiO_2	66.65	68.61	62.32	62.21	62.81	59.28	62.03	62.41	65.53	58.82	58.62	61.92	62.53	61.80	62.35
TiO_2	0.15	0.03	0.04	0.06	0.06	0.03	0.04	0.06	0.15	0.03	0.03	0.05	0.08	0.06	0.09
Al_2O_3	16.52	16.78	17.83	17.84	17.84	18.97	17.84	17.93	17.40	18.81	18.55	17.35	16.82	17.36	16.70
Fe_2O_3	4.19	2.83	4.82	5.14	4.39	5.44	4.87	4.87	4.26	5.51	5.46	5.19	5.83	5.57	5.92
MnO	0.14	0.18	0.24	0.21	0.21	0.30	0.24	0.21	0.14	0.30	0.29	0.22	0.22	0.22	0.24
MgO	0.01	0.01	0.01	0.01	0.01	0.01	0.01	0.01	0.01	0.14	0.01	0.10	0.19	0.08	0.10
CaO	0.64	0.40	0.66	0.88	0.65	0.99	0.60	0.84	0.14	1.50	0.87	0.89	0.79	0.97	1.21
Na_2O	6.60	6.62	9.23	8.57	8.58	9.77	9.60	8.58	6.57	8.85	9.88	7.71	7.57	7.89	7.27
K_2O	5.10	4.93	4.82	5.09	4.74	4.89	4.82	5.14	5.38	5.12	4.82	5.70	5.26	5.51	5.33
P_2O_5	0.02	0.03	0.03	0.04	0.03	0.04	0.03	0.04	0.05	0.03	0.04	0.02	0.02	0.02	0.02
LOI	1.01	0.76	0.83	1.05	1.79	1.07	0.84	0.88	1.16	1.94	2.13	3.04	2.65	4.97	3.50
Total	**101.03**	**101.18**	**100.83**	**101.1**	**101.11**	**100.79**	**100.92**	**100.97**	**100.79**	**101.05**	**100.70**	**102.20**	**101.94**	**104.44**	**102.74**
(ppm)															
Sc	1.34	0.76	0.97	0.87	0.74	0.83	0.86	0.67	1.23	0.86	0.88	--	--	--	--
V	38	41	38	38	39	38.0	39	38	43	30	38	1	6	3	2
Cr	8.23	9.49	10.3	8.85	6.09	8.30	8.68	5.64	6.77	9.41	9.08	<0.01	5.1	2.14	<0.01
Co	0.35	0.24	<0.04	0.47	0.34	0.23	0.2	0.35	1.96	0.18	0.38	--	--	--	--
Ni	15	8	17	12	15	14	18	17	24	18	16	202	252	192	260
Cu	<2	<2	<2	<2	<2	<2	<2	<2	<2	<2	<2	--	--	--	--
Zn	209	153	250	182	204	264	272	198	190	278	285	--	--	--	--
Ga	41	29	48	42	42	42	49	52	45	52	54	39	51	38	51
As	3.93	1.9	6.59	4.18	3.9	2.66	5.71	4.99	4.57	3.65	6.76	--	--	--	--
Se	1.93	2.31	4.31	0.31	0.31	1.16	0.20	<2.6	<2.1	0.88	1.48	--	--	--	--
Br	<1.1	<1	2.91	2.21	<6.2	8.92	6.73	3.60	<5.2	<2.8	5.74	--	--	--	--
Rb	235	208	321	232	264	283	350	249	277	285	290	239	298	237	293
Sr	13	23	9	3	6	3	<2	49	10	17	3	7.84	1.77	3.48	55.4
Y	94	47	113	83	92	152	115	113	91	120	122	79	114	71.0	127
Zr	471	295	908	707	1236	1079	944	817	935	846	853	1148	1449	1042	1552
Sb	0.23	0.17	0.56	0.34	0.20	0.19	0.34	0.24	11.2	0.93	0.44	--	--	--	--
Nb	206	128	237	195	249	290	241	229	231	243	251	202	252	192	260
Cs	1.30	2.01	4.00	2.91	2.82	3.46	4.25	2.58	2.27	3.83	4.05	--	--	--	--
Ba	47.6	92.7	30.1	20.7	25.4	26.4	39.5	23.6	51.8	32.3	32.3	16.2	20.3	19.9	21.1
La	144	75.1	183	134	160	171	194	142	129	203	195	--	--	--	--
Ce	282	142	346	240	270	323	352	255	275	338	352	358	433	326	443
Nd	103	44.5	119	97.9	89.1	121.1	127	95.9	76.8	132	132	--	--	--	--
Sm	17.5	7.89	22.4	18.3	17.1	23.7	24.9	19.1	16	28.1	26.2	--	--	--	--
Eu	1.16	0.82	1.72	1.41	0.87	2.19	1.69	1.43	0.63	2.33	2.32	--	--	--	--
Gd	15.6	5.82	26.8	16.0	16.9	19.9	22.9	19.6	15.6	23.0	25.5	--	--	--	--
Tb	2.73	1.16	3.6	2.52	2.27	3.37	3.53	2.77	2.56	3.65	3.71	--	--	--	--
Tm	1.69	0.83	2.24	1.62	1.85	2.02	2.28	1.63	1.77	2.11	2.19	--	--	--	--
Yb	9.49	5.43	12.1	8.51	8.92	10.8	12.2	9.73	10.3	12.4	12.2	--	--	--	--
Lu	1.47	0.85	1.77	1.28	1.32	1.59	1.80	1.38	1.51	1.69	1.73	--	--	--	--
Hf	19.5	14.1	32.6	23.7	40.0	31.7	35.2	27.4	34.8	33.3	30.1	--	--	--	--
Ta	15.3	14.3	20.9	16.3	20	20.85	23.5	15.7	17.8	22.0	22.3	--	--	--	--
W	3.71	1.49	1.28	5.56	<6.2	3.51	3.5	<4.5	1.65	5.75	2.62	--	--	--	--
Ir (ppb)	<1.1	<1	3.04	<1.1	<1.8	<1.6	<1.7	<2	<1.7	<1.7	<1.8	--	--	--	--
Au (ppb)	<1.7	<1.7	<2	<1.2	<2	<2.3	<3.2	<2.2	<2.5	<0.01	<2.7	--	--	--	--
Th	28.1	21.5	39.2	19.6	32.1	27.3	38.0	26.7	30.4	31.9	33.9	24.6	24.1	21.7	26.5
U	4.74	4.56	8.79	6.66	7.11	9.13	10.7	7.76	6.6	12.1	9.77				

Samples AX06, AX07, AX10a, and AX10b are from K. Kabeto (unpublished data); --, not analyzed

Table 6.1: Contn'd. Data from Hagos et al. (2010)

	Basalt AX004	Basalt AX08	Basalt AX20	Basalt AX21	Basalt AX24	Basalt AX29	Basalt AX31	Basalt AX32	Basalt AX34	Basalt AX38	Basalt AX42	Basalt AX43d	Basalt AX44	Basalt AX46	Basalt AX47b	Basalt AX63	Basalt AX79	Basalt AX09
(wt.%)																		
SiO_2	43.05	54.37	43.63	44.06	49.20	48.32	48.19	46.82	48.65	44.32	50.68	48.76	47.06	51.60	45.75	44.82	50.96	45.13
TiO_2	4.39	1.85	2.56	2.95	2.10	3.50	2.12	3.25	2.25	2.44	2.90	2.23	2.85	1.54	2.17	3.07	1.58	3.97
Al_2O_3	13.88	15.67	15.49	14.85	15.87	15.32	19.22	16.51	15.93	15.58	16.24	16.67	16.38	16.92	14.57	14.32	16.68	15.16
Fe_2O_3	17.32	9.71	12.94	12.85	10.82	15.39	10.85	14.89	11.12	11.64	13.42	14.57	15.84	12.55	11.68	16.26	12.61	16.58
MnO	0.21	0.17	0.22	0.20	0.19	0.20	0.21	0.17	0.20	0.20	0.19	0.15	0.14	0.24	0.20	0.24	0.25	0.18
MgO	7.22	2.01	7.73	7.89	7.68	4.60	3.32	5.22	7.92	6.82	3.63	3.84	3.52	2.45	11.02	5.66	2.64	5.44
CaO	7.90	5.46	10.59	9.90	9.42	7.08	7.90	6.87	9.35	11.69	7.22	5.16	4.71	4.93	10.72	7.68	5.48	7.07
Na_2O	4.17	4.01	4.13	4.36	3.96	3.87	5.30	3.86	3.69	4.28	3.35	6.19	5.94	6.87	2.85	5.34	6.38	3.46
K_2O	1.59	2.97	1.71	1.12	1.93	1.05	2.08	1.12	1.84	1.04	1.74	0.96	0.58	1.50	1.53	1.47	1.54	1.37
P_2O_5	0.96	0.66	0.69	0.76	0.55	0.53	0.80	0.48	0.53	0.84	0.80	0.67	0.59	1.51	0.57	1.30	1.53	0.60
LOI	0.72	4.13	1.93	2.81	0.17	1.89	1.41	1.53	0.24	2.57	1.18	2.29	3.08	0.91	0.63	1.05	1.44	2.88
Total	101.41	101.01	101.62	101.75	101.89	101.75	101.40	100.72	101.72	101.42	101.35	101.49	100.69	101.02	101.69	101.21	101.09	101.83
(ppm)																		
Sc	13.7	15.4	22.3	18.2	17.7	19.2	6.7	20.6	21.9	24.3	19.5	6.81	6.14	5.42	24	10.9	5.42	
V	199	126	254	227	201	207	142	266	212	240	225	79	76	48	242	139	47	384
Cr	14.9	17	106	128	273	11.0	9.7	39.3	386	226	23.6	97.1	28.7	9.06	579	8	7.06	39.5
Co	44.2	17.9	40.9	33.5	31.9	35.5	20.7	52.0	43.9	40.7	34.6	31.9	38.5	14.3	49.9	32.0	14.3	--
Ni	34	14	71	90	143	22	5	52	161	112	27	17	46	10	245	12	8	18.6
Cu	25	17	6	41	66	29	6	30	57	70	36	13	19	2	73	9	4	--
Zn	165	137	115	97.8	99.0	140	90.4	165	124	112	171	132	136	155	115	192	150	--
Ga	29	22	16	18	18	24	16	24	18	16	22	21	22	25	16	32	25	24
As	1.04	0.18	<1.5	1.71	0.45	<1.5	0.45	<1.5	<2.1	<2.3	0.32	<3.2	<1.5	1.36	0.48	1.17	<1.9	--
Se	<1.7	<1.64	0.26	2.19	2.19	<2.9	<2.2	3.05	<3.1	<2.4	<2.8	<2.5	<2.3	<2.5	<3.8	<2.8	<2.5	--
Br	<0.7	<0.75	<1	1.50	1.37	<3.86	1.91	<3.9	<4.9	<5.2	<3.5	<5.3	<4	<5.1	<3	<5.1	<4.4	--
Rb	41.0	37.4	64.7	35.9	36.7	12.3	48.3	19.6	41.7	16.1	51.8	26.7	16.2	25.1	30.0	21.3	29.5	17.7
Sr	989	559	786	983	796	619	1163	680	737	927	760	704	1020	1776	789	1207	1760	614
Y	30	44	31	34	28	39	29	36	28	31	45	16	23	61	27	36	62	37
Zr	321	389	192	258	197	212	222	208	190	211	269	209	315	637	173	389	621	267
Sb	0.10	<0.14	0.09	0.04	0.02	<0.13	0.07	<0.2	0.21	0.10	0.09	<0.1	<0.2	<0.2	<0.1	0.85	0.14	--
Nb	34	23	69	84	70	12	77	15	65	73	20	10	20	37	60	40	35	19
Cs	0.42	0.34	0.64	0.54	0.26	<0.2	0.89	0.36	0.43	0.74	0.61	0.22	3.18	0.91	0.33	0.48	0.38	--
Ba	110	640	523	378	363	221	433	270	431	664	460	178	65.4	176	453	116	150	504
La	30.4	38.3	46.8	60.8	47.4	15.2	55.5	20	47.4	55.9	31.1	20.9	15.1	42.7	41.1	38.4	41.1	--
Ce	72.6	84.2	86.1	110	80.8	38.2	102	47.4	86.5	98.2	72.0	53.6	44.8	108	71.7	90.3	104	47.3
Nd	46.8	45.2	31.5	45.9	32.5	27	42.3	30.6	34.8	44.3	42.1	38.7	38.5	70.8	35.8	56.9	68.4	--
Sm	11.3	9.91	7.29	8.86	6.33	7.27	7.91	8.38	7.62	8.80	10.4	10.3	10.6	17.3	7.24	14.3	16.6	--
Eu	4.25	3.79	2.46	3.02	2.24	2.62	2.70	2.85	2.44	2.70	3.27	3.37	3.49	5.73	2.35	4.59	5.66	--
Gd	9	9.13	6.76	7.69	6.18	9.20	9.07	10.2	9.52	9.81	11.2	9.07	12.4	19.4	8.82	15.1	15.6	--
Tb	1.46	1.43	1.07	0.93	0.84	1.16	1.03	1.39	1.03	1.08	1.56	1.22	1.33	2.26	0.86	1.71	2.18	--
Tm	0.37	0.68	0.59	0.56	0.47	0.67	0.73	0.75	0.7	0.67	0.82	0.38	0.36	1.08	0.59	0.54	1.08	--
Yb	1.80	3.93	2.57	2.69	2.18	2.81	2.63	2.85	2.37	2.76	3.63	1.34	1.37	5.18	2.23	2.03	4.89	--
Lu	0.22	0.62	0.37	0.38	0.31	0.43	0.38	0.45	0.32	0.4	0.54	0.15	0.17	0.75	0.32	0.24	0.70	--
Hf	8.63	10.6	4.16	5.81	4.02	5.23	4.67	6.08	4.49	4.63	7.33	8.27	8.04	17.0	3.52	10.3	16.7	--
Ta	2.51	1.33	4.97	5.55	4.53	0.62	5.61	1.13	4.90	4.67	1.32	1.36	1.00	3.12	4.07	2.84	2.86	--
W	3.10	<3.42	<4.39	0.41	0.38	<2.4	0.15	<2	<3.6	<4.1	<2.1	2.14	<2.2	<3.6	<1.7	<3.5	<3	--
Ir (ppb)	<1.6	<1.6	<1.4	2.99	3.05	<2.4	<1.7	<2.6	<2.9	<2.1	<2.3	<2.2	<1.9	<2	<3.2	<2.3	<2	--
Au (ppb)	2.02	0.98	0.8	0.82	0.78	<2.1	1.1	<2.2	<2.3	<0.01	<0.01	<0.01	<2.3	<0.01	<1.8	<2.5	<0.01	--
Th	2.53	1.76	5.72	7.14	4.78	0.69	6.58	1.15	4.78	5.79	1.36	1.52	1.07	3.28	3.88	2.92	3.05	2.06
U	0.67	0.53	1.28	1.92	1.37	<3.86	1.80	<0.8	1.20	1.80	<0.7	<0.6	<0.8	1.12	0.98	<0.9	<0.8	--

All major element and trace element contents of: V, Ni, Cu, Ga, Sr, Y, Zr and Nb were determined using the XRF spectrometry, and the contents of remaining trace elements and all rare earth elements were determined using INAA at the Department of Lithospheric Research, University of Vienna. Total Fe as Fe_2O_3.

Table 6.2: CIPW norm calculation in wt% for the volcanic rock of Axum, Northern Ethiopia. The norm calculation was from the CIPW software.

SAMPLE	Rock Name	Qz	or	ab	an	ne	di	hy	ol	ac	mt	il	ap	nms
AX43	**Phonolite**		28.9	37.5		17.8	4.1		2.6	7.9		0.1	0.1	0.8
AX111	**Phonolite**		30.3	37.0		16.9	6.4		1.5	5.9	1.0	0.1	0.1	
AX112	**Phonolite**		28.5	37.3		16.9	3.6		2.8	7.9		0.1	0.1	1.4
AX011	**Phonolite**		28.5	49.5		8.4	2.7		2.6	7.0		0.1	0.1	1.2
AX012	**Phonolite**		30.1	47.5		8.6	3.7		2.4	7.4		0.1	0.1	0.2
AX45	**Phonolite**		28.5	48.2		9.1	2.5		2.8	7.0		0.1	0.1	1.9
AX45C	**Phonolite**		30.4	48.1		8.4	3.5		2.3	7.0		0.1	0.1	0.2
AX06	**Phonolite**		28.5	37.3		17.0	3.6		2.8	7.9		0.1	0.1	1.4
AX10a	**Phonolite**		32.6	45.4		7.2	4.2		2.5	7.2	0.4	0.1	0.1	
AX41	**Trachyte**		28.0	53.9		6.2	2.7		2.9	5.1		0.1	0.1	0.3
AX07	**Trachyte**		31.1	50.9		3.5	3.3		4.0	6.0	0.4	0.2	0.1	
AX10b	**Trachyte**		31.5	50.8		3.0	5.2		2.8	4.7	1.1	0.2	0.1	
AX002	**Trachyte**	6.5	30.1	55.9	0.4		2.4	2.0			2.4	0.3	0.1	
AX008	**Trachyte**	9.4	29.1	56.0	1.5		0.3	2.4			1.6	0.1	0.1	
AX51	**Trachyte**	5.0	31.8	55.6	0.4	0.6	3.3				2.5	0.3	0.1	
AX004	**Basalt**		9.4	16.8	14.5	10.0	15.2		19.3		5.0	8.3	2.2	
AX09	**Basalt**		8.1	28.7	21.8	0.3	7.8		18.5		4.8	7.5	1.4	
AX29	**Basalt**		6.2	32.8	21.3		8.6	9.5	9.1		4.5	6.7	1.2	
AX32	**Basalt**		6.6	32.7	24.4		5.4	1.1	17.5		4.3	6.2	1.1	
AX42	**Basalt**	1.4	10.3	28.4	24.1		5.4	19.4			3.9	5.5	1.9	
AX44	**Basalt**		3.4	41.3	16.3	4.9	2.7		17.6		4.6	5.4	1.4	
AX63	**Basalt**		8.7	24.4	10.4	11.7	15.8		12.9		7.6	5.8	3.0	
AX20	**Basalt**		10.1	6.0	18.7	15.7	24.0		15.0		3.8	4.9	1.6	
AX21	**Basalt**		6.6	14.1	17.6	12.4	21.6		15.6		3.7	5.6	1.8	
AX24	**Basalt**		11.4	21.4	19.8	6.6	19.0		15.2		3.1	4.0	1.3	
AX31	**Basalt**		12.3	25.2	22.5	10.7	9.6		10.8		3.2	4.0	1.9	
AX34	**Basalt**		10.9	21.4	21.5	5.3	17.4		16.3		3.2	4.3	1.2	
AX38	**Basalt**		6.2	11.2	20.2	13.6	26.4		11.4		3.4	4.6	2.0	
AX43D	**Basalt**		5.7	39.7	14.9	6.9	5.4		16.8		4.2	4.2	1.6	
AX47B	**Basalt**		9.0	10.9	22.5	7.2	21.8		20.9		3.4	4.1	1.3	

Qz: quartz; or: orthoclase; ab: albite; an: anorthite; ne: nepheline; di: diopside; hy: hypersthenes; ol: olivine; ac: acmite; mt: magnetite; il: ilmenite; ap: apatite; nms: metasilcate. The Fe^{2+}/Fe^{3+} ratios for basalts, trachytes and phonolites are 4:1, 3:2 and 1:1, respectively.
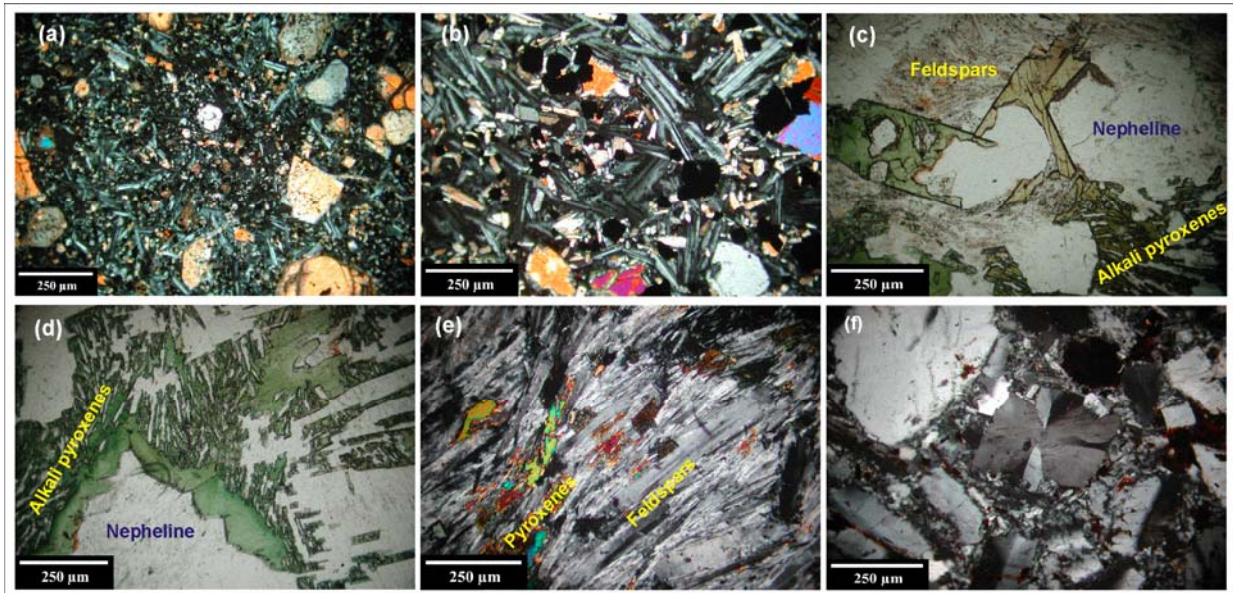
Figure 6.2   Petrography of the volcanic rocks of Axum area showing various mineralogical and textural features. Images (a), (b), (e) and (f) were taken under crossed polarizers, whereas (c) and (d) were taken under plane polarized light. (a) Aphyric–phyric, plagioclase rich alkali basalts with medium–coarse-grained phenocrysts of olivines and clinopyroxenes; the plagioclase are lath-like but randomly aligned, where as the phenocrysts are rounded to angular of varying size. (b) Coarse-grained, plagioclase-phyric, ± K-feldspar bearing basalts. Dark-colored minerals of Ti oxides and Mg oxides are filling the interstices of other grains. (c) Highly porphyritic with phenocrysts of alkali pyroxene, nepheline, sodic pyroxene/aegerine and feldspars. (d) Phenocrysts of pyroxene, nepheline, sodic pyroxene, and some early crystallized feldspars. Highly altered mafic minerals and some intergrowths of aegerines surround the nepheline phenocrysts. (e) Dark-colored, well aligned, elongated- to needle-like, tightly packed grains of K-feldspar with few anhedrally shaped nephelines. This sample is transitional between trachytes and phonolites (Gobo-Dura phonolites). (f) Fine– to coarse-grained (inequigranular) elongated and in some cases euhedral-shaped K-feldspars with well-developed trachytic textures are the main constituents. Most of the phenocrysts show simple twinning and others spherulitic texture.
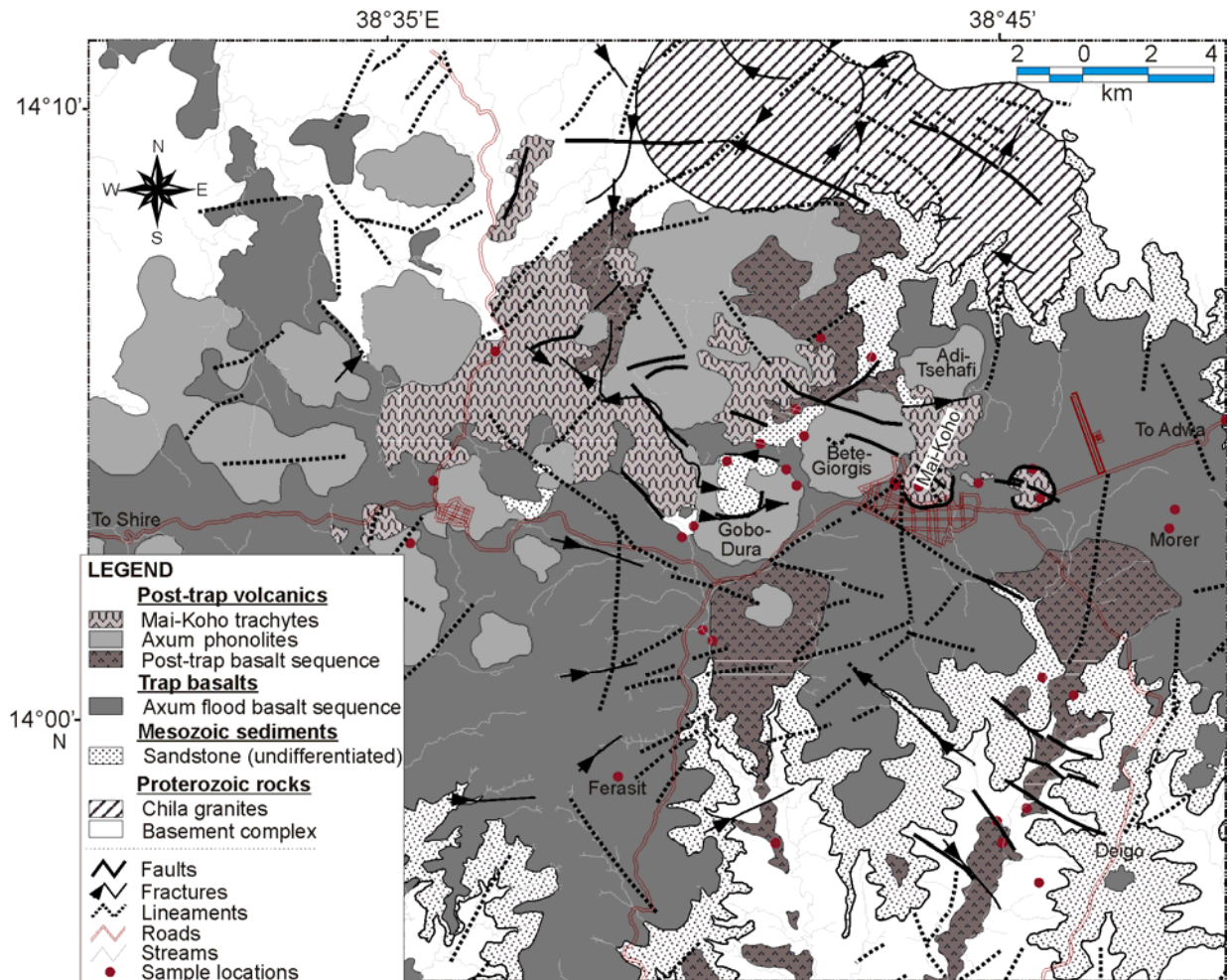
Figure 6.3 Geological and structural map of the of Axum area. 1:50,000 scale topographic maps and aerial photographs (Eth94), Landsat ETM[+] 2002, and ASTER images of the Axum–Shire areas were commonly used to produce the geological and structural maps of the area.

6.4.2 Results

6.4.2.1 Major Elements

According to the total alkali-silica (TAS) classification of Le Bas et al. (1986) (Fig. 6.4) the volcanic rocks of the Axum–Shire area belong to phonolites, trachytes, basaltic-trachyandesites, basalts, trachybasalts, basanites and tephrites ranging from 43 to 69 wt% SiO_2 contents (Table 6.1). The Axum volcanic rocks plot in the alkaline field or slightly within the transition field with the exception of one sample (AX12). All the basaltic rocks have <49 wt% SiO_2 contents and high (~4.3–7.4 wt%) $Na_2O + K_2O$ contents. The phonolitic–trachytic rocks of the area have 58–69 wt% SiO_2 contents. The Bete-Giorgis phonolites are silica-undersaturated (58.6–59.3 SiO_2 wt%), with very high Al_2O_3 (18.5–19 wt%) and Na_2O (8.9–9.9 wt%) contents. The CIPW normative compositions of the Axum volcanics (Table 6.2) reflect these geochemical variations. All samples from the Axum volcanic rocks, except the samples from the Mai-Koho trachytes, are normative quartz-free (Table 6.2). Mai-Koho trachytes (silica-oversaturated) contain a significant amount of normative quartz (5–9.5 wt%). All rocks of the post-trap basalt sequence and some of the flood basalt sequence are basanites and/or alkali-olivine basalts. However, an olivine tholeiite tendency is observed for the flood basalt sequence group (e.g., AX12, AX29, and AX32).
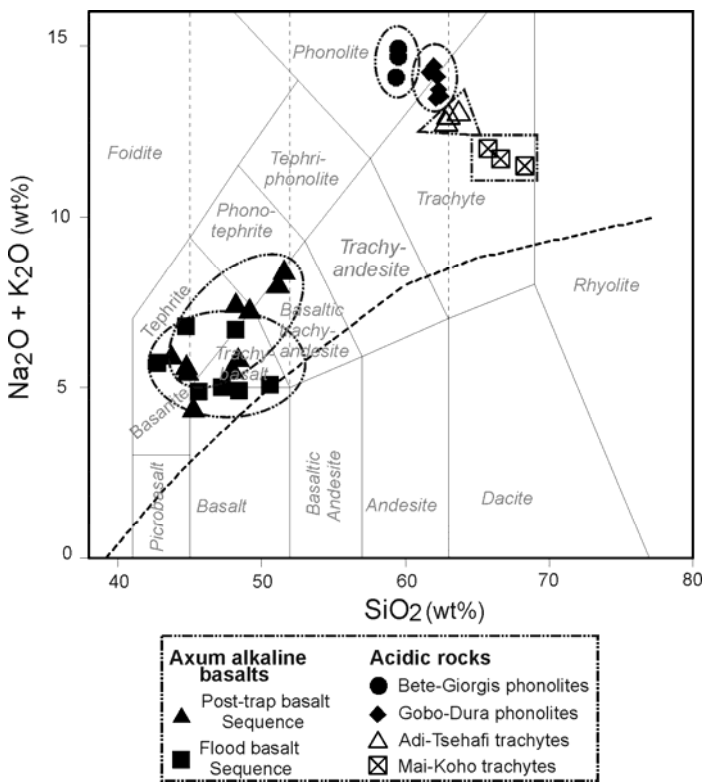
Figure 6.4 Total alkali-silica diagram comparing the geochemical characteristics of the volcanic rocks of Axum. The dashed line distinguishes tholeiitic from alkaline basalts (after Le Bas et al., 1986).

Alkali contents of the Gobo-Dura phonolites vary between 13.4 and 14.5 wt % $Na_2O + K_2O$. Samples AX11, 12 and 45 correspond to the Bete-Giorgis phonolites; whereas samples AX06, 10a and 45c are analogous to the foid-bearing trachytes (the Adi-Tsehafi trachytes). The Adi-Tsehafi trachytes on the other hand do not show a wide range in alkalinity; however, all samples plot close to the phonolite-trachyte boundary (Fig. 6.4). The compositions of the felsic rocks from Axum, therefore, correlate linearly in the TAS diagram

and their total alkali ($Na_2O + K_2O$) contents or their alkalinities decrease systematically from the Bete-Giorgis phonolite to the Mai-Koho trachytes, whereas the SiO_2 (wt%) contents increase (Fig. 6.4).

Almost all basalt samples, except sample AX47b, are highly–moderately fractionated mafic rocks with MgO values between 2 and 8 wt% (Hagos et al., 2010). The distribution of TiO_2 in the basaltic, tephritic, and basanitic rocks of the area covers a wide range (1.5–4.4 wt%) and shows two well- defined trends: the low-Ti post-trap basalt sequence and the high-Ti flood basalt sequence (Fig. 6.5a). The MgO and TiO_2 contents in the phonolite–trachyte rocks are very low (0.01–0.14 wt% MgO and 0.03–0.15 wt% TiO_2). Instead, the content of Al_2O_3 is very high (16.5–19 wt%), which exceeds the contents of $Na_2O + K_2O + CaO$ and follows the same trend as that for the total alkalis (Fig. 6.5c). Generally, the Axum phonolitic–trachytic rocks have very low but nearly identical contents of TiO_2, MgO, and CaO. The Al_2O_3, Na_2O, K_2O, and MnO contents are very high (Fig. 6.5a–h). Most of the samples from the Bete-Giorgis and Gobo-Dura phonolites have significant Cl contents (0.12–0.34 wt%), in contrast to the low contents in the basalts and trachytes of the region.

6.4.2.2   Trace Elements

The trace element contents of the Axum basaltic sequences are highly variable. The post-trap basalt sequence displays the highest incompatible trace element contents. In contrast, the flood basalt sequence is less enriched. This is illustrated in Figures 6b, d, e, and h, where selected trace element contents are plotted against SiO_2 contents.

Inverse relations in the plots of the contents of some incompatible trace elements vs. SiO_2 (wt%) are observed in the basaltic sequences (Fig. 6.6a and f) and the alkaline acidic rocks (Fig. 6.6b, d and e) of Axum. Negative correlations are also observed for the V and Ni vs. SiO_2 contents (not plotted). The contents of incompatible trace elements, such as Nb, Zr, and the REE, increase with the silica content up to the phonolitic-trachytes (Adi-Tsehafi trachytes), but are slightly lower again in the Mai-Koho trachytes. The content of Y increases slightly from the basanites to the basaltic trachy-andesites, shows very high values in the Bete-Giorgis phonolites, and decreases sharply from the Gobo-Dura phonolites to the Mai-Koho trachytes.

The chondrite-normalized REE patterns for the post-trap basalts and the flood basalt sequence are different (Fig. 6.7a). The post-trap basalt sequence has highly sloping light REE (LREE) and relatively flat heavy REE (HREE) patterns; in contrast the flood basalt sequence has a comparatively flat LREE and moderately slopping HREE pattern. The average

chondrite-normalized La/Yb ratios (13.1) of the post-trap basalt sequence are higher than the value for flood basalt sequence, which is 7.7 (Hagos et al., 2010).
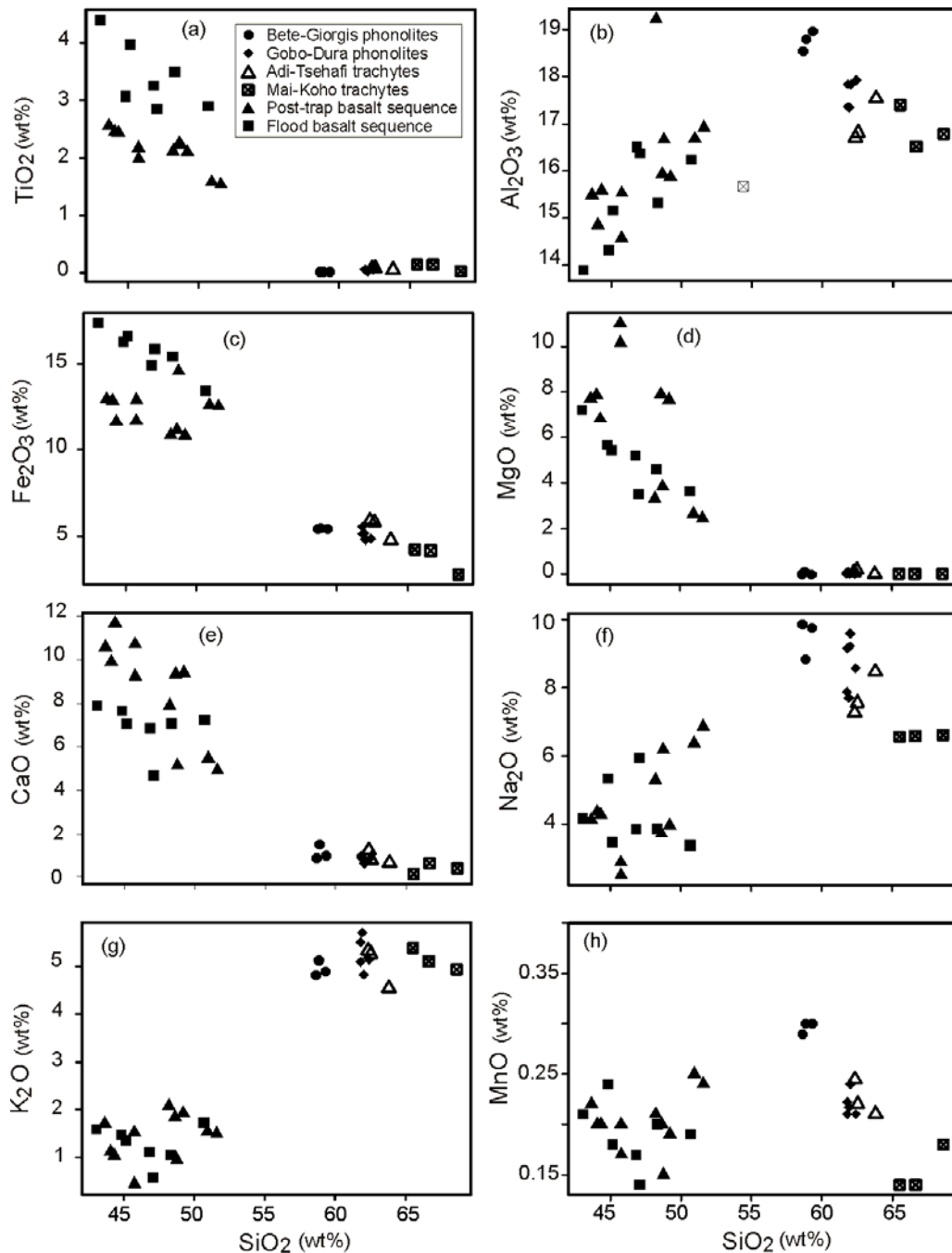
Figure 6.5 Harker variation diagrams for the bimodal volcanic rocks of Axum area. All the major oxides are characterized by their unique trend as SiO_2 progress from 43–69 wt%.

Chondrite-normalized incompatible trace element diagrams (Fig. 6.7b) show generally a coherent behavior with enriched low-field strength elements (Ba, Rb, K) and depleted high-field strength elements (Zr, Hf, Y) throughout the post-trap basalt sequence; however, such behavior is reversed for the flood basalt sequence. In the normalized multi-

element diagram the elements Nb and Ta from the post-trap basalt sequence are enriched by a factor of 3 compared to the flood basalt sequence, but the Sr, Nd, and Yb concentrations in both rocks are similar (Hagos et al., 2010).
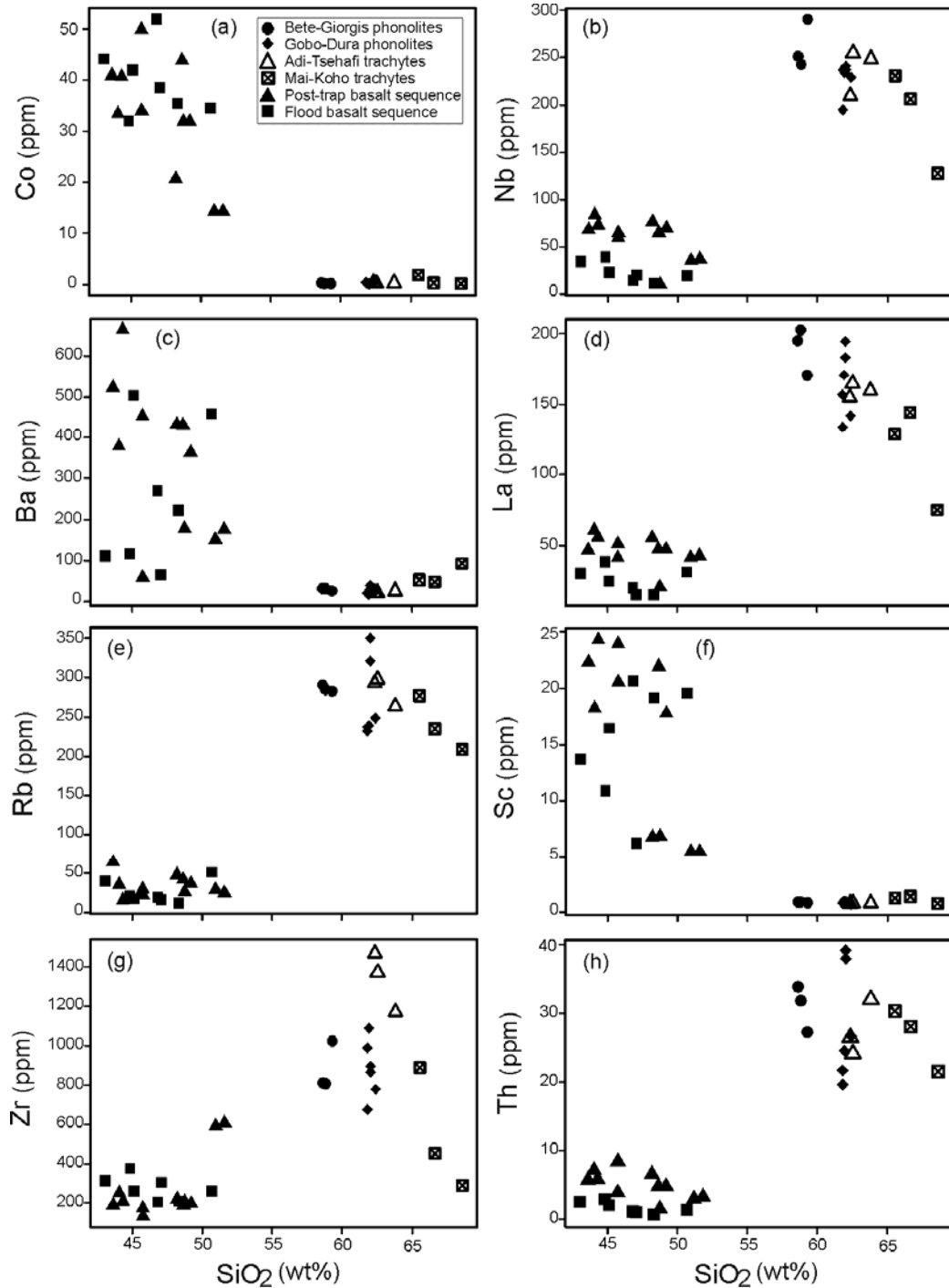
Figure 6.6 Plots of selected trace elements (ppm) against differentiation index (SiO_2 wt%) for the Axum volcanic rocks. The binary plots of the contents of Sc, Co, Rb, Th, Zr, Nb, Ba, and La versus SiO_2 illustrate the compositional variation among the Axum volcanic rocks.

The phonolite–trachyte rocks have similar chondrite-normalized REE patterns. All have steep LREE and flat HREE patterns. They also show strong negative Eu anomalies with

152

(Eu/Eu*)$_n$ ratios ranging from 0.21 to 0.30 for the Bete-Giorgis and Gobo-Dura phonolites and 0.12 to 0.33 for the Adi-Tsehafi and Mai-Koho trachytes. The trachytes have a wider range of the (Eu/Eu*)$_n$ ratio and this shows that there is a relatively broader compositional range than for the phonolites.
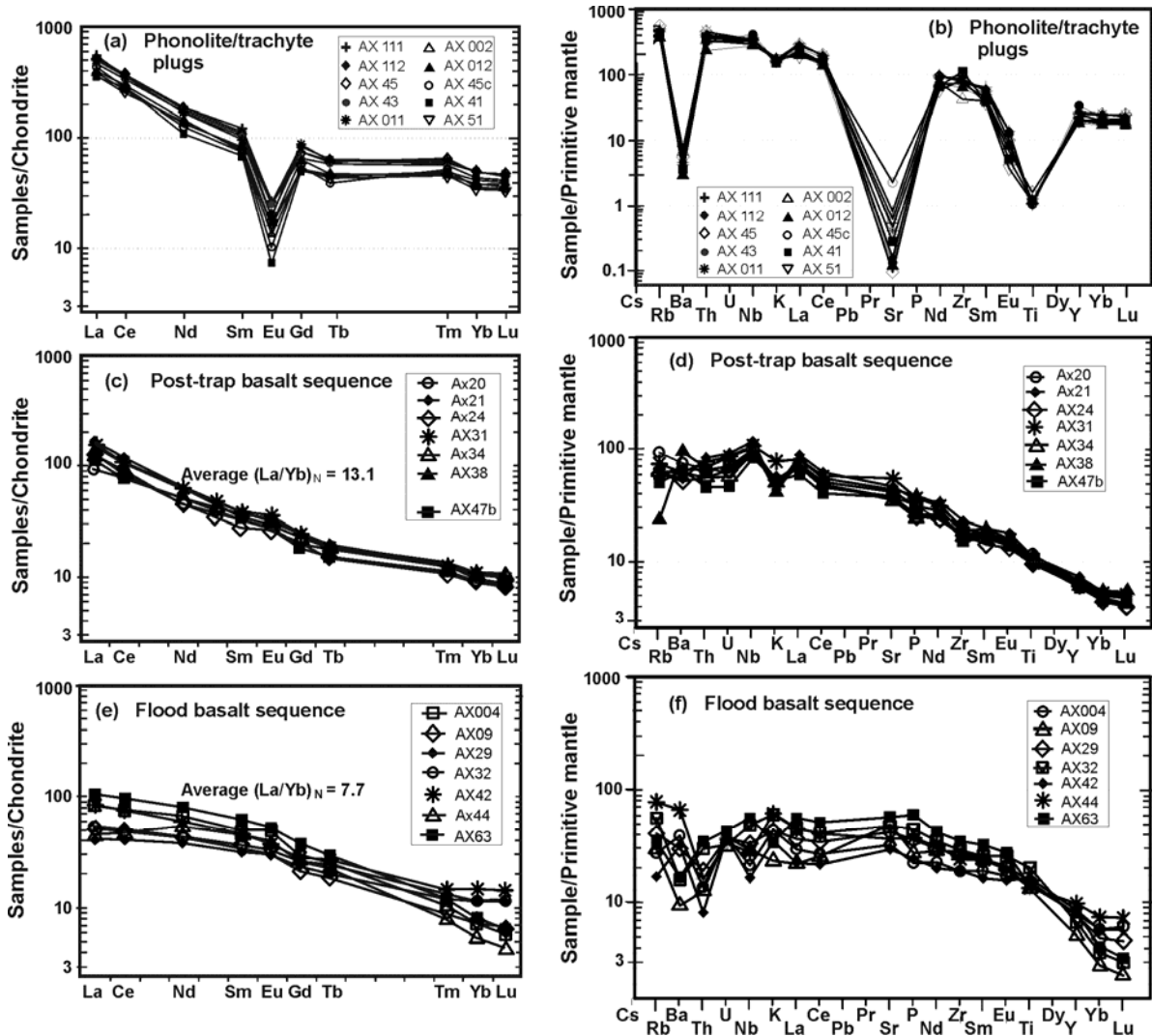
Figure 6.7 Chondrite-normalized rare earth and primitive mantle-normalized incompatible trace element abundance patterns of the Axum volcanic rocks. Normalization factors after Taylor and McLennan (1985) for the chondrite-normalization, and Sun and McDonough (1989) for the primitive mantle normalization. (a) Steeply inclined light REE, strong negative Eu anomaly and gently inclined heavy REE. (b) Strong negative anomalies are observed at Ba, Sr, and Ti.

6.5   Discussion

The volcanic rocks of the northern Ethiopia in general, and the Axum volcanic rocks in particular, are among the least studied parts of the Ethiopian flood basalts. The Axum volcanics are highly diversified and cover the range from basanites/tephrites, basalts, trachybasalts, and basaltic trachy-andesites to phonolites and trachytes. Hagos et al. (2010) conducted a geochemical study on the Axum basalts and found two groups (post-trap basalt and flood basalt sequences) of mildly to highly alkaline basaltic rocks.

6.5.1 The Alkaline Basalts of Axum

Pik et al. (1998, 1999) grouped the Axum volcanics as transitional to tholeiitic low-Ti basalts, but our study on the northern end of the Ethiopian flood basalt confirmed that the Axum volcanic rocks are not tholeiitic in character; instead they are alkaline constituting a wide range in the TiO_2 content and highly diversified rocks (trachybasalts–basanites–tephrites) (Fig. 6.4).

Based on the TiO_2 content and the incompatible trace element concentration variations, the Axum basalts are grouped in to two parts as post-trap basalt sequence (1.5–2.6 TiO_2 wt%) and flood basalt sequence (2.6–4.5 TiO_2 wt%) (Hagos et al., 2010). The different elemental compositions of post-trap basalt and flood basalt sequences are clearly evident on TiO_2 vs. SiO_2, Nb vs. La, Hf vs. Th, Nb/Y vs. Zr, and La/Sm vs. Gd/Yb plots (Fig. 6.8). At given La contents the post-trap basalt sequence samples have higher Nb contents than do the flood basalt sequence samples. In contrast, the rocks of the post-trap basalt sequence have lower Hf contents than those of the flood basalt sequence.

The rocks from the post-trap basalt sequence, with their unique geochemical signature, are unlike those in any other part of the Ethiopian flood basalt province (Fig. 6.8); however, Kieffer et al. (2004) and Zanettin et al. (1999, 2006b) documented the existence of low-Ti alkali basalts in the central part of the northwestern Ethiopian volcanic province (Guguftu and Choke shield volcanoes) and in the central– to southeastern Eritrean highlands (i.e., Adi-Ugri, Asmara, and Senafe basalts), respectively. Zanettin et al. (2006a) proposed that during the early Miocene (24–22 Ma) this alkaline magmatism extended from Adi-Ugri (Mendefera), and perhaps also from Axum–Adwa to Senafe. Kieffer et al. (2004) also confirmed that the Choke and Guguftu shield volcanoes erupted around 23 Ma contemporaneously with the central Eritrean Alkali basalts.

The lack of geochronological data in the Axum area constrains the absolute age determination of the post-trap basalt sequence; however, from its properties and emplacement,

it appears to be much younger than the Choke and Guguftu shield basalts. The post-trap basalt sequence is fresh, unaltered, undeformed and overlies a deeply and newly eroded basement complex, indicating the relatively young time of emplacement of these basalts. Several authors confirmed that the post-trap alkaline rocks span a wide time of eruption. In some of the shield volcanoes, the strongly alkaline rock types (tephrites, tephri-phonolites and phonolites) are even younger (early Miocene–Pliocene; Zanettin et al., 2006b). Kieffer et al. (2004) have also pointed out that the post-trap magmatism in the Ethiopian highland is getting younger north or southwards of the Choke and Guguftu shield basalts. Mt. Guna, which erupted to the north of the Choke and Guguftu shields, has an age of 10.7 Ma (Kieffer et al., 2004). Although the absence of geochronological data constrains the study of temporal relationship of Axum post-trap basalt sequence with the other post-trap basaltic rocks of Ethiopia, our geochemical analyses of rocks from the Axum area reveal that there is a similarity with the composition of the Guguftu shield volcano (Fig. 6.8b, d, e, and f). In several binary element plots the post-trap basalt sequence of Axum is tightly clustered, with very high contents of Nb, La, Th, Ta, and high Nb/Y and La/Sm ratios. In contrast, the composition of the Guguftu shield basalt is less tightly clustered and has moderate to high contents of Nb, La, Th, as well as moderate Nb/Y and La/Sm ratios. These alkaline post-trap basalts of Axum display extremely high incompatible trace element contents that are characteristic of magmas formed by low degrees of partial melting, most probably during the last phase of the Ethiopian plateau volcanism.

The Axum flood basalt sequence shows broad geochemical characteristics ranging from highly to mildly alkaline basaltic suites. Based on the normative proportions of nepheline, olivine, diopside, hypersthenes, and quartz (not plotted), these basalts fall in the tephrite–basanite series and some samples progressed to the olivine tholeiite. This flood basalt does not share any geochemical characteristics with the Axum post-trap basalt sequence, except their alkalinity (Fig. 6.8a-f). Instead, our geochemical data of the flood basalt sequence from the Axum area complement the Adigrat data (Samples: E215–E217) reported by Pik et al. (1998, 1999).

The flood basalt sequence of Axum and the HT1 flood basalts of Adigrat areas are located in the same geographic zone in the northern Ethiopia at nearly the same altitude, except that these two patches of basaltic suites are now isolated by the ~15 km wide Adwa basin. Figure 6.8 shows that in terms of their trace element contents and ratios, the flood basalt sequence from the Axum area resemble Pik et al.'s (1999) HT1 flood basalt from the Adigrat area. Both basalts share an alkaline–mildly alkaline magmatic character with

relatively moderate concentrations of the highly incompatible trace elements and moderately fractionated trace element patterns. In most of the binary plots (Fig. 6.8b, c, e, and f) both basaltic suites cluster in the same region and it is difficult to differentiate them.

The flood basalt sequence of Axum displays trace element compositions in between those of HT2 and LT basalts (Fig. 6.8b, c, and d). Some of the samples of this sequence exhibit lower La/Nb, Ba/Nb, and Ba/Th ratios (not plotted) similar to those of the HT2 flood basalts. The other samples exhibit a shift towards higher La/Nb, Ba/Nb, and Ba/Th ratios similar to those of the LT flood basalts. The strongly differentiated nature of the Axum flood basalt sequence indicated that the contribution of the lower–upper crustal materials to the mantle-drived magmas was significant (Pik et al., 1999) (Fig. 6.8).
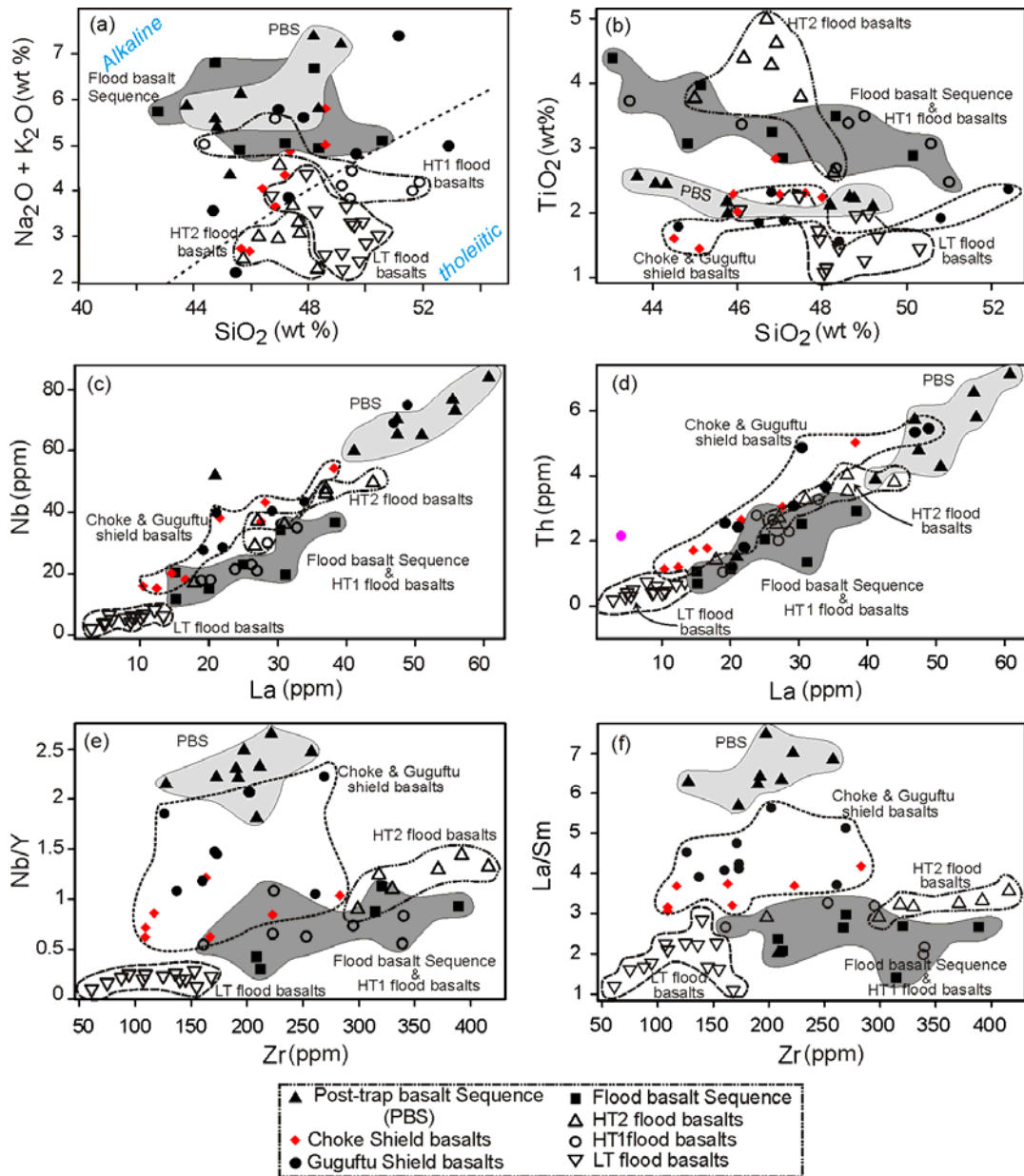
Figure 6.7 Binary plots of major element, trace element, and ratio comparing the Axum alkaline basalts with the northwestern Ethiopian flood basalts and shield volcanoes; (a and b) major oxides vs. SiO$_2$ (wt %); (c and d) highly incompatible trace elements (Nb and Th) vs. La, and (e and f) ratios of the important trace elements (Nb/Y and La/Sm) vs. Zr contents.

6.5.2 The Axum Miocene– to Pliocene Phonolite–Trachyte Plugs

There is no concrete evidence whether or not the Axum phonolite–trachyte plugs are coeval with the Ethiopian shield volcanoes or if they are Miocene- to Pliocene alkaline acidic rocks that extruded/intruded the trap along the ENE–trending northern Afar lineament. It is evident from the field observation that the Axum phonolites and trachytes do not interfinger with the Axum flood basalt sequence, but instead they are overlying these basalts and, at places, intrude and deform the basaltic flow layers. From our new $^{40}Ar/^{39}Ar$ dating, the phonolites and Phonolitic trachytes were emplaced at ~19 and 15 Ma, respectively. In this region, the phonolitic/trachytic plugs reach their optimum dimension and frequency, and overlie the Neoproterozoic basement rocks, Mesozoic sandstone, and the Oligocene flood basalts. According to Zanettin et al. (2006b, and references therein) the viscous and plug-forming lavas were erupted after a long erosive period, in the course of which both the late stage trap series and the clastic Mesozoic sedimentary rocks were removed, thus exposing the Arabian-Nubian shields. These authors assumed that the age of the plugs was rather recent, Quaternary or late Pliocene, and chronologically categorize with the acid domes in the Senafe area.

The silica-poor rocks at Axum constitute the Bete-Giorgis phonolites, the Gobo-Dura trachy-phonolites, and the Adi-Tsehafi phonolitic trachytes. Each of these rock types has distinct geochemical and petrographic characteristics. However, their trace element ratios (e.g., Zr/Nb, Nb/Y, La/Lu) show limited variation, which indicates a homogeneous source region. Geochemically, these alkaline rocks, including the peralkaline trachytes, correspond to the silicic rocks of the central and southeastern Eritrea (Zanettin et al., 2006b), which are characterized by very low contents of MgO (0.02–0.2 wt%); however, the Eritrean silicic rocks are slightly older (24–20 Ma) and cover relatively diversified suites, from tephri-phonolite to rhyolite. The Axum acidic rocks, on the other hand, are younger and less diverse, ranging from phonolites to trachytes, and exhibit gradual variation from the nepheline-rich to the nepheline-poor rocks.

6.5.3 The Alkaline Basalt–Phonolitic/Trachytic Magma Interactions of the Axum Volcanic Rocks

The post-trap and flood basalt of the Axum area exhibit major petrogenetic differences (Hagos et al., 2010). The accompanying phonolites and trachytes correspond to the incompatible element-enriched post-trap basalt sequence. The petrogenetic relationship between the basalts and the phonolite/trachyte rocks is inferred from binary and ternary plots of the contents of incompatible trace elements and their ratios (Fig. 6.9 and 6.10). The Zr vs.

Ta and Zr vs. Nb diagrams show a well-defined linear correlation among the post-trap basalt sequence and the phonolitic/trachytic rocks (Fig. 6.9a and b), and their incompatible element abundances progressively increase with increasing degree of fractionation. Similarity of the content of highly incompatible trace elements and their ratios is often cited as reliable evidence that fractional crystallization has been the dominant process in the evolution of the post-trap to phonolitic/trachytic magmatic suites (Weaver, 1977; Wilson et al., 1995). The Zr/Nb ratio of the Axum phonolites and trachytes and the post-trap basalt sequence is nearly constant (Fig. 6.9c; 3–4.5) with the exception of the Adi-Tsehafi trachytes, which have relatively higher Zr/Nb ratios ranging from 5–5.7, which are still much lower than in the Axum flood basalt (Zr/Nb 10–18; Fig. 6.9c).
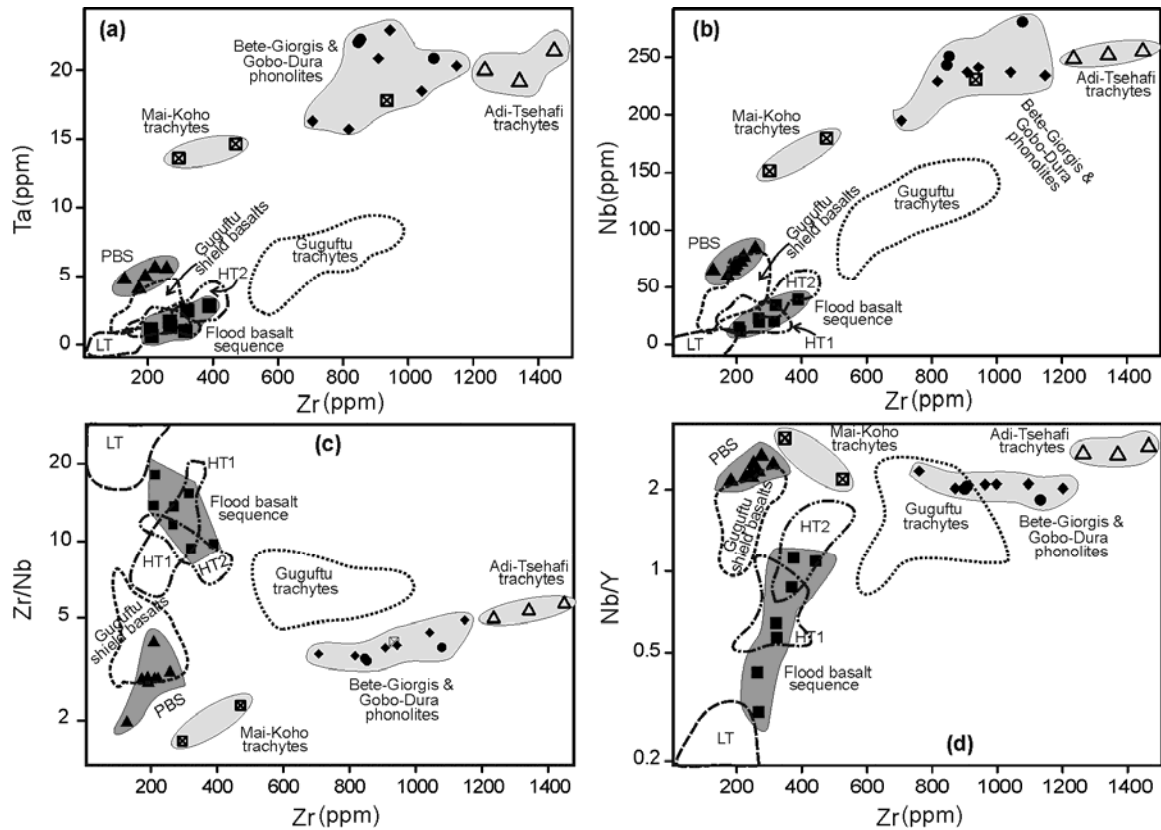
Figure 6.8 (a and b) Plots of Ta vs. Zr and Nb vs. Zr, showing the two apparent evolution trends for the Axum volcanics and the other Ethiopian flood basalts and shield volcanoes. Most Axum flood basalt sequence and the other Ethiopian volcanics rocks plot at lower Ta and Nb contents. (c) Zr/Nb vs Zr plot for the volcanic rocks. The post-trap basalt sequence with their cogenetic acidic rocks have the same low Zr/Nb ratio, however, the flood basalt sequence and other Ethiopian volcanics rocks have a higher and wider Zr/Nb ratio. (d) Nb/Y vs. Zr plot showing high Nb/Y ratios for the post-trap basalt sequence with their co-genetic acidic rocks.

Low Nb/La ratios (<1.0) in volcanic rocks are a reliable trace element index of crustal assimilation (Kieffer et al., 2004). The LT basalts of the Ethiopian flood volcanics and the overlying shield volcanoes are characterized by low Nb/La ratios, typical of crustal

assimilation, whereas alkali basalts from the Choke and Guguftu, and the underlying HT1 and HT2 basalts have high Nb/La ratios (Kieffer et al., 2004). Our data support this interpretation. The same behavior is seen in the Axum volcanics, where a persistent crustal signature is absent in the alkaline volcanic rocks.

The Zr/Nb ratio in volcanic sequences is also good indicator of crustal contamination or variation in degree of partial melting (Wilson et al., 1995; Kamber and Collerson, 2000). The Adi-Tsehafi trachyte is sandwiched between the Chila granite and the Mesozoic sandstone unit. The slight increase in the Zr/Nb ratio for the Adi-Tsehafi trachyte reflects crustal involvement either from the sandstone or late Proterozoic Chila granite.

At given Zr contents most of the post-trap basalt sequence samples have higher Ta, Nb, and Th contents and Nb/Y ratio (Fig. 6.9a, b and d) than do the flood basalt sequence. Kamber and Collerson (2000) have pointed out that Nb is more sensitive to variations in degrees of partial melting than Zr, and hence can be used to constrain the influence of variable degrees of melting. The discrimination diagrams Zr/4–2xNb–Y, Th–Hf/3–Ta, and Th–Zr/117–Nb/16 of Axum volcanic rocks form two clusters (Fig. 6.10a–c). The samples from the Axum flood basalt sequence fall within the enriched-MORB of within-plate basalts, and the samples from the post-trap basalt sequence and the phonolites/trachytes of Axum indistinguishably plot within the within-plate alkali basalt field. Hagos et al. (2010) stated that the source reservoirs for both the post-trap and the flood basalt sequences seems to be one and the same and resembles those of the OIB, but the main petrogenetic change between these two basaltic rocks of Axum would be most probably in the degree and mechanism of partial melting of the rocks in the mantle plume.
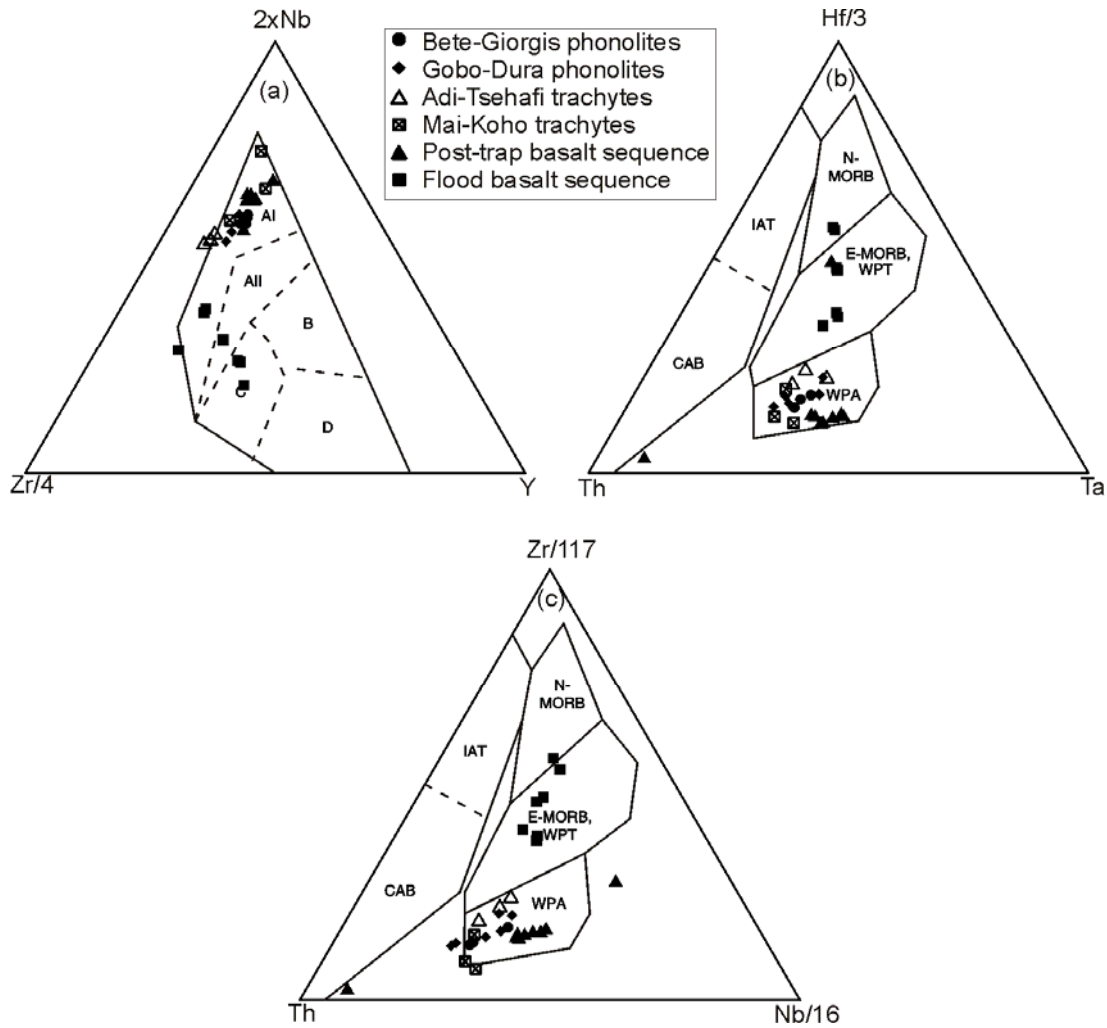
Figure 6.9 Discrimination diagrams, showing that the Axum volcanic rocks plot into two clusters all three diagrams: (a) The Zr-Nb-Y discrimination diagram for the Axum basalts and phonolites. Volcanic rocks from various tectonic provinces generally fall into these fields: AI–AII: within-plate alkali basalts; AII-C: within-plate tholeiitic basalts; B: P-type mid-oceanic ridge basalts; D: N-type mid-oceanic ridge basalts; C-D: volcanic arc basalts (Meschede, 1986). (b) The Th-Hf-Ta discrimination diagram divides the triangle into; N-MORB: normal-type mid-oceanic ridge basalt; E-MORB (WPT): enriched mid-oceanic ridge basalt (with-in-plate tholeiite; WPA: within-plate alkali; and IAT; island-arc tholeiite (Wood, 1980). (c) The Th-Zr-Nb discrimination diagram also divides the triangle into: N-MORB, E-MORB (WPT), WPA, and IAT(Wood, 1980) .

6.6   Conclusions

All possible combinations of the REE, trace element contents and their ratios confirmed that the Axum area experiences two volcanic episodes. The first volcanic episode, Axum flood basalt sequence, erupted contemporaneously with the northwestern Ethiopian flood basalts. The second magmatic episode, Axum post-trap basalt sequence and associated felsic rocks, happened most probably during the last phase of the Ethiopian shield basalts. The flood basalt sequence displays high TiO_2, Fe_2O_3, contents and Zr/Nb, Ti/Y ratios, and relatively high heavy incompatible trace element contents. The post-trap basalt sequence is characterized by aphyric- to phyric, plagioclase-laths with sparsely distributed coarse-grained

clinopyroxene and olivine phenocrysts. This sequence has high Nb and Th contents, high CaO/Al_2O_3, Nb/Y, Nb/La ratios, and high light incompatible trace element contents. From the geochemical analyses, the flood basalt sequence of Axum and the HT1 flood basalts of Adigrat are indistinguishable. However, the second group of basalts, the post-trap basalt sequence, exhibits different and distinct geochemical characteristics.

Unlike the alkaline basalts, the phonolites and trachytes of Axum exhibit similar geochemical characteristics. The contents of oxides (Al_2O_3, Fe_2O_3, Na_2O, MnO) and the trace elements (Nb, La, Rb, Zr) decrease linearly with increasing SiO_2 content from the Bete-Giorgis phonolites to the Mai-Koho trachytes. All these rocks have a similar degree of fractionation that is characterized by very low MgO and TiO_2 contents, ranging from 0.01 – 0.14 wt% and 0.03–0.15 wt%, respectively.

The Nb vs. Zr, Zr/Nb vs. Zr, and Nb/Y vs. Zr binary plots and the Zr/4–2xNb–Y, Th–Hf/3–Ta, and Th–Zr/117–Nb/16 discrimination diagrams confirmed that the post-trap basalt sequence, the phonolites, and the trachytes evolved from the same parental magma that invaded some parts of the westcentral Tigray and most probably the central and southeastern part of Eritrea (Adi-Ugri, Asmara, and Senafe volcanic rocks) ~8 to 6 My after the major Ethiopian flood basalts. The Axum flood basalt sequence is distinct from the remaining volcanic rocks of Axum and considered to be part of the HT1 basalts of Adigrat area that erupted during the major phase of the Ethiopian flood basalts.

References:

Alemu T. 1998. Geochemistry of Neoproterozoic granitoids from the Axum Area, Northern Ethiopia. Journal of African Earth Sciences 27, 437–460.

Alene M., Secco L., Dal Negro A., and Sacchi R. 2000. Crystal chemistry of clinopyroxene in Neoproterozoic metavolcanic rocks of Tigrai, Northern Ethiopia. Bollettino della Societa Geologica Italiana 119, 581–586.

Asrat A., Gleizes G., Barbey P., and Ayalew, D. 2003. Magma emplacement and mafic - felsic magma hybridisation: structural evidence from the Pan-African Negash pluton, Northern Ethiopia. Journal of Structural Geology 25, 1451–1469.

Asrat A., Barbey P., Ludden N.J., Reisberg L., Gleizes G., and Ayalew D. 2004. Petrology and isotope geochemistry of the Pan-African Negash pluton, Northern Ethiopia: Mafic-Felsic magma interactions during the construction of shallow-level calc-alkaline plutons. Journal of Petrology 45, 1147–1179.

Audin L., Quidelleur X., Coulie E., Courtillot V., Gilder S., Manighetti I., Gillot P. Y., Tapponnier P., and Kidane T. 2004. Palaeomagnetism and K-Ar and $^{40}Ar/^{39}Ar$ ages in the Ali Sabieh area (Republic of Djibouti and Ethiopia): constraints on the mechanism of Aden ridge propagation into southeastern Afar during the last 10 My. Geophysical Journal International 158, 327–345.

Ayalew D., Yirgu G., and Pik R. 1999. Geochemical and isotopic (Sr, Nd and Pb) characteristics of volcanic rocks from south-western Ethiopia. Journal of African Earth Sciences 29, 381–391.

Ayalew D., Barbey P., Marty B., Reisberg L., Yirgu G., and Pik R. 2002. Source, genesis and timing of giant ignimbrite deposits associated with Ethiopian continental flood basalts. Geochimica et Cosmochimica Acta 66, 1429–1448.

Baker J., Snee L., and Menzies M. 1996. A brief Oligocene period of flood volcanism in Yemen: implications for the duration and rate of continental flood volcanism at the Afro-Arabian triple junction. Earth and Planetary Science Letters 138, 39–55.

Barrat J.A., Fourcade S., Jahn B.M., Chemirke J.L., and Capdevila R. 1998. Isotope (Sr, Nd, Pb, O) and trace-element geochemistry of volcanics from the Erta'Ale range (Ethiopia). Journal of Volcanology and Geothermal Research 80, 85–100.

Beyth M. 1972. The geology of central and western Tigray. Ph.D thesis, Rheinische Friedrich-Wilhelms Universität, Bonn, W. Germany, 200 pp.

Coulié E., Quidelleur X., Gillot P.Y., Courtillot V., Lefèvre J.C., and Chiesa S. 2003. Comparative K-Ar and Ar/Ar dating of Ethiopian and Yemenite Oligocene volcanism: Implications for timing and duration of the Ethiopian Traps. Earth and planetary Science Letters 206, 477–492.

Dainelli G. 1943. Geologia dell' Africa orientale. Regia Accademia d'Italia Centro studi per l' Africa oriental Italiana, Rome, Italy, 1–4.

Ebinger C. J. and Sleep N.H. 1998. Cenozoic magmatism throughout East Africa resulting from impact of a single plume. Nature 395, 788–791.

Ethiopian Institute of Geological Survey, 1999. Aksum map sheet ND 37–6 (scale 1:250,000), Geological Survey of Ethiopia, Addis Ababa, Ethiopia.

Furman T., Bryce G.J., Karson J., and Lotti A. 2004. East African rift system (EARS) plume structure: Insights from Quaternary mafic lavas of Turkana, Kenya. Journal of Petrology 45, 1069–1088.

George R.M., Rogers N., and Kelley S. 1998. Earliest magmatism in Ethiopia: Evidence for two mantle plumes in one flood basalt province. Geology 26, 923–926.

Govindaraju K. 1989. 1989 combilation of working values and sample description for 272 geostandards. Geostandards Newsletter 13, 1–113.

Hagos M., Koeberl C., Kabeto K., and Koller F. 2010. Geology, petrology and geochemistry of the basaltic rocks of the Axum area, Northern Ethiopia. In: Ray J., Sen J.G., and Ghosh B. (Eds.), Topics in Igneous Petrology. A Tribute to Prof. Mihir K. Bose, Springer, Heidelberg, in press.

Hofmann C., Courtillot V., Feraud G., Rochette P., Yirgu G., Ketefo E., and Pik R. 1997. Timing of the Ethiopian flood basalt event and implications for plume birth and environmental change. Nature 389, 838–841.

Jarosewich E., Clarke R.S.J., and Barrows J.N. 1987. The Allende meteorite reference sample. Smithsonian Contributions to Earth Sciences 27, 1–49.

Kabeto K., Sawada Y., Bussert R., and Kuster D. 2004. Geology and geochemistry of Mai-chew volcanics, northwestern Ethiopian Plateau. International Conference on East African Rift system, Addis Ababa, Ethiopia. Extended Abstract 1, 110–114.

Kamber B.S. and Collerson K.D. 2000. Zr/Nb systematics of ocean island basalts reassessed - The case for binary mixing. Journal of Petrology 41, 1007–1021.

Kieffer B., Arndt N., Lapierre H., Bastien F., Bosch D., Pecher A., Yirgu G., Ayalew D., Weis D., Jerram A.D., Keller F., and Meugniot C. 2004. Flood and shield basalts from Ethiopia: magmas from the African superswell. Journal of Petrology 45, 793–834.

Koeberl C. 1993. Instrumental neutron activation analysis of geochemical and cosmochemical samples: A fast and reliable method for small sample analysis. Jouranl of Radioanalytical and Nuclear Chemistry 168, 47–60.

Küster D., Dwivedi S.B., Kabeto K., Mehary K., and Matheis G. 2005. Petrogenetic reconnaissance investigation of mafic sills associated with flood basalts, Mekelle basin, Northern Ethiopia: implication for Ni-Cu exploration. Journal of Geochemical Exploration 85, 63–79.

Le Bas M.L., Le Maitre R.W., Streckeisen A., and Zanettin B. 1986. A chemical classification of volcanic rocks based on the total alkali – silica diagram. Journal of Petrology 27, 745–750.

Mader D. and Koeberl C. 2009. Using instrumental neutron activation analysis for geochemical analyses of terrestrial impact structures: Current analytical procedures at the laboratory. Applied Radiation and Isotopes 67, 2100–2103.

Merla G., Abbate E., Azzaroli A., Bruni P., Canuti P., Fazzuoli M., Sagri M., and Tacconi P. 1979. Comments to the geological map of Ethiopia and Somalia. Consiglio Nazionale delle Ricerche, Firenze, 89–95.

Meschede M. 1986. A method of discriminating between different types of mid-oceanic ridge basalts and continental tholeiites with the Nb-Zr-Y diagram. Chemical Geology 56, 207–218.

Mohr P. 1983. Ethiopian flood basalt province. Nature 303, 577–584.

Pik R., Deniel C., Coulon C., Yirgu G., Hoffmann C., and Ayalew D. 1998. The northwestern Ethiopian Plateau flood basalts: classification and spatial distribution of magma types. Journal of Volcanology and Geothermal Research 81, 91–111.

Pik R., Deniel C., Coulon C., Yirgu G., and Marty B. 1999. Isotopic and trace element signatures of Ethiopian basalts: evidence for plume-lithospheric interactions. Geochimica Cosmochimica Acta 63, 2263–2279.

Schmid T., Koch M., DiBlasi M., and Hagos M. 2008. Spatial and spectral analysis of soil surface properties for an archaeological area in Aksum, Ethiopia, applying high and medium resolution data. Catena 75, 93–101.

Son T.H. and Koeberl C. 2005. Chemical variations within fragments of Australasian tektites. Meteoritics and Planetary Science 40, 805–815.

Stewart K. and Rogers N. 1996. Mantle plume and lithosphere contributions to basalts from Southern Ethiopia. Earth and Planetary Science Letters 139, 195–211.

Sun S. and McDonough W.F. 1989. Chemical and isotopic systematics of oceanic basalts: implications for mantle composition and processes. In Saunders A.D. and Norry M.J. (Eds.), Magmatism in the ocean basins. Special Publication of Volcanology. Geological Society of London 42, 313–345.

Tadesse T. 1996. Structure across a possible intra-oceanic suture zone in the low-grade Pan-African rocks of Northern Ethiopia. Journal of African Earth Sciences 23, 375–381.

Tadesse T. 1997. The Geology of Axum area (ND 37-6). Memoir no. 9, Ethiopia Institute of Geological Survey, Addis Ababa, Ethiopia, 184 pp.

Taylor S.R. and McLennan S.M. 1985. The continental crust: Its composition and evolution. Blackwell, Oxford, 312 pp.

Ukstins I., Renne P., Wolfenden E., Baker J., Ayalew D., and Menzies M. 2002. Matching conjugate volcanic rifted margins: $^{40}Ar/^{39}Ar$ chronostratigraphy of pre- and syn-rift bimodal flood volcanism in Ethiopia and Yemen. Earth and Planetary Science Letters 198, 289–306.

Weaver S.D. 1977. The Quaternary Caldera Volcano Emuruangogolak, Kenya Rift, and the Petrology of a Bimodal Ferrobasalt-Pantelleritic-Trachyte Association. Bullotin of Volcanology 40, 209–230.

Wilson M., Downes H., and Cebriá J. 1995. Contrasting fractionation trends in coexisting continental alkaline magma series; Cantal, Massif Central, France. Journal of Petrology 36, 1729–1753.

Wood D.A. 1980. The application of a Th-Hf-Ta diagram to problems of tectono-magmatic classification and to establishing the nature of crustal contamination of basaltic lavas of the British Tertiary volcanic province. Earth and Planetary Science Letters 50, 11–30.

Zanettin B., Bellieni G., Visentin J.E., and Haile T. 1999. The volcanic rocks of the Eritrean plateau: stratigraphy and evolution. Acta Volcanology 11, 183–193.

Zanettin B., Bellieni G., and Visentin J.E. 2006a. New radiometric age of volcanic rocks in the Central Eritrean plateau (from Asmara to Adi Quala): considerations on stratigraphy and correlations. Journal of African Earth Science 45, 156–161.

Zanettin B., Bellieni G., and Visentin J.E. 2006b. Stratigraphy and evolution of the trachy – rhyolitic volcanism of the Senafe area (eastern Eritrean plateau). Journal of African Earth Sciences 45, 478–488.

CHAPTER 7

CHAPTER 7: MINERALOGICAL, GEOCHEMICAL, AND ISOTOPIC INVESTIGATIONS OF THE NORTHERN AFAR/ DANAKIL DEPRESSION, NORTHEASTERN ETHIOPIA

Abstract– The Danakil Depression is the most important volcano-tectonically active portion of the Afar region and the East African Rift system. In its center, over an area that is ~120 km long and ~35 km wide, there are several volcanic edifices constituting seven major NNW-SSE aligned shield volcanoes and low-lying fissure-fed basalts. The petrology of the lavas in this area ranges from transitional alkali to tholeiitic basalts, with significant across-axis variation both in mineralogy and geochemistry. The variation in the contents of the major elements (TiO_2, Al_2O_3, and Fe_2O_3), incompatible trace elements (Nd, Hf, Th, Ta), and the contents and ratios of the rare earth elements (REE) (e.g., (La/Yb)n = 5.3–9.3) indicate some variation in the petrogenetic processes of the basalts.

However, the variation in isotopic compositions of the basalts is minimal ($^{87}Sr/Sr^{86}$ = 0.7036 - 0.7041, $^{143}Nd/Nd^{144}$ = 0.51286–0.51289), which suggests that there is only one source region for all the Danakil Depression basalts. The Ce/Pb, Ba/U ratios, and isotopic data indicate that continental crust is not a major component for the petrogenesis of the volcanic rocks; instead, depth and degree of melting of the source reservoir underneath the Danakil Depression played a major role for the production of incompatible element-enriched, transitional alkali basalts (e.g., AleBagu Shield basalts) and the incompatible element-depleted tholeiitic basalts (e.g., Erta'Ale Shield basalts).

Keywords: Danakil Depression, shield volcano, tholeiitic basalt, petrogenesis

7.1 Introduction

The Afar Depression (Fig. 7.1) is located at the junction of two vigorously spreading embryonic oceanic rifts (Gulf of Aden, Red Sea and) and an intra-continental rift (Ethiopian Rift). It is a region of extensional deformation tectonics and basaltic volcanism from which the three rift-axes radiate (Abbate et al., 1995). Though there is recent (Pliocene–Present) volcanism in the Afar Depression, the earliest magmatic activities in the East African rift system occurred in southern Ethiopia, northern Kenya, and southern Sudan at 40–45 Ma (e.g., Ebinger et al., 1993; George et al., 1998; Yirgu et al., 2006). During the late Oligocene–early Miocene (i.e., ~31 and 22 Ma), magmatism was extensive throughout northcentral Ethiopia, and Yemen where flood– to shield basalts and associated felsic lavas and pyroclastic products were deposited (Hofmann et al., 1997; Kieffer et al., 2004; Yirgu et al., 2006).

Volcanism in the Afar Depression occurred in four distinct episodes. The first, the eruption of the Adolei basalts, took place in the early Miocene between ~27 and 19 Ma (Barberie et al., 1975; Deniel et al., 1994), shortly after the initiation of widespread rifting in the Gulf of Aden and Red Sea (Wolfenden et al., 2004). A second and less voluminous phase (the Mabla rhyolites) took place between ~16 and 9 Ma (Varet, 1975). Rocks representing this magmatic episode outcrop on the eastern and southeastern edges of the Danakil Depression (Danakil and Ali Sabieh Microplates). The third phase of volcanism, the Dahla basalts, erupted during the late Miocene between 8 and 6 Ma (Lahitte et al., 2003b). These three magmatic events must originally have covered a wider area, but were since overlain by the younger and most important basaltic series present in Afar (Lahitte et al., 2003b). The fourth phase, the Stratoid and Aden series, began 4.4 Ma (Barberi et al., 1975) and continues to this day, covering an area of approximately 55,000 km^2 (Varet and Gasse, 1978). The total thickness of the Afar Stratoid series varies laterally and cannot be exactly determined because the lower sequence of the series is not well exposed (Lahitte et al., 2003b). In the northern part of the Afar Depression, Danakil, volcanism is more active and its floor is mainly covered by the Aden series basalts.

Although the Danakil Depression has been one of few places on earth that imprint a complete record of the volcano-tectonic evolution of a young ocean basin; it, however, lacks extensive field and geochemical investigations due to extremely difficult field conditions, as well as security problems that have prevented almost any access to the depression. This is apparent in the literatures, which show a clear gap between the 1970s and 1980s. After fieldwork conducted in the 1960s and 1970s (Barberi and Varet, 1970; Le Guern et al., 1979), most subsequently published work was based on the interpretation of remote sensing data (Harris et al., 2005). Thurmond et al. (2006), for example, used different types of remote sensing images and data for geological and structural mapping of the area. Because of such inconvenience, very important volcanic events, such as the vanishing of the northern lava lake in the Erta'Ale caldera, still have not been documented exactly (Harris et al., 2005). Even the available studies on the Afar Depression magmatism have been carried out at a regional scale (e.g., Barberi and Varet, 1970, 1975; Varet and Gasse, 1978; Barberi et al., 1980; Barrat et al., 1998), and detailed investigations on single magmatic segment and specific shield volcanoes are scarce. Only recently (since 2005) has fieldwork been possible again, allowing researchers to conduct detailed investigations within the Danakil Depression and understand its contribution to the volcano-tectonic history of the region as a whole.

Here, a petrological and geochemical study is presented of the Erta'Ale, Alu–Dalaffilla, and AleBagu shield volcanoes, and the Erta'Ale Range fissure-fed basalts (Fig. 7.1). Compositional data on whole rocks and minerals are discussed with the aim of placing constraints on the main cause for the distinct geochemical characteristics between the shields themselves and the fissure-fed basalts. As part of verifying the source characteristics for the Danakil Depression basalts, we explore their relationship to compositions attributed formerly to hot mantle plume underlying the Ethio-Afar dome (e.g., Barberi et al., 1980; Barrat et al., 1998; Pik et al., 1999; Rogers et al., 2000).
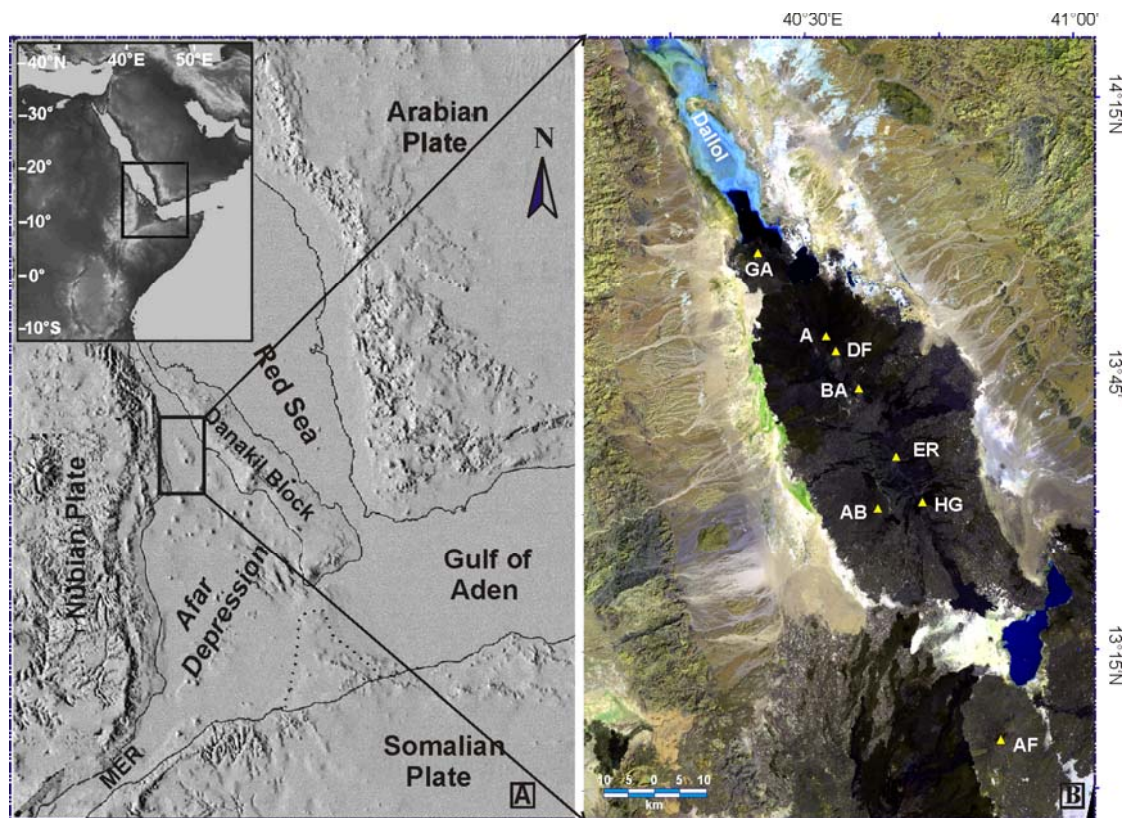
Figure 7.1 (A) Location map of the Afar Triple Junction, the two young oceanic ridges (Gulf of Aden and Red Sea), and the main Ethiopian rift (modified after Collet et al., 2000). (B) Landsat-5 ETM composite image (Bands 7, 5 and 2) of the northern Afar Depression showing the major shield volcanoes of the Erta'Ale Range: GA = Gada'Ale, A = Alu, DF = Dalaffilla, BA = Borale'Ale, EA = Erta'Ale, AB = AleBagu, HG = Hayli Gubi, and AF = Afdera. Inset map after Beyene and Abdelsalam (2005).

7.2 Geological Setting of Afar Depression

The Afar Depression is floored by volcanic rocks, which are dominantly of trap-like basalts and basaltic shields that range in age from Miocene–Pliocene (i.e., Adolei, Mabla, Dahla; 26–6 Ma), through Pliocene–Pleistocene (Afar Stratoid series; 4–1 Ma), to Quaternary (Aden series; <1 Ma) (e.g., Barberi et al., 1975; Hayward and Ebinger, 1996; Lahitte et al., 2003b).

The volcanic/basaltic rocks associated with the evolution of this depression show a relatively uniform compositional pattern than those from the Kenya depression, reflecting both thin lithosphere of homogeneous basement and the actively evolving tectonic regime (Vidal et al., 1991; Rogers, 2006). The Afar Depression basalts have lower $^{143}Nd/^{144}Nd$ and higher $^{87}Sr/^{86}Sr$ ratios than mid oceanic ridge basalts (MORB), and extend to values beyond that for the bulk silicate Earth (Rogers, 2006). Kenyan rift basalts, in contrast, are dominated by high $^{143}Nd/^{144}Nd$ and low $^{87}Sr/^{86}Sr$, typical of MORB (e.g., Furman et al., 2004; Rogers, 2006).

The Adolei basaltic formation, oldest volcanic units recognized within the eastern Afar Depression, erupted during the late Oligocene–early Miocene, from 27 to 20 Ma (Audin et al., 2004), shortly after pick of the Ethiopian flood basalt volcanism (30 Ma; Hofmann et al., 1997). They are found injected long fractures of variable orientations that dissect the sedimentary basement and are, in some cases, located on the edges of the sedimentary blocks (Black et al., 1975). The Afar Depression and the Main Ethiopian Rift (MER) have experienced eruptions of huge volumes of silicic volcanic rocks (i.e., trachytes and rhyolites), attributed to fractional crystallization (FC) of mafic magmas with little or no crustal assimilation (e.g., Barberi et al., 1975; Boccaletti et al., 1995; Ayalew et al., 2002). The Mabla series erupted between 25 and 12 Ma around the eastern blocks of the depression and consists of rhyolitic lavas, some ignimbrite deposits, and fissure-fed basaltic lava flows (Audin et al., 2004, and references therein).

The Afar Depression and its margins have experienced a long history of mafic lava dominated volcanism since early Miocene (at ~25 Ma), with the volumetrically largest eruptions (Stratoid series) tied to the onset of seafloor spreading of the Red Sea and Gulf of Aden ~4 Ma (Yirgu et al., 2006). In central Afar Depression, magmatism of the last 4 Ma has been bimodal, but with basaltic rocks predominating over silicic products (Lahitte et al., 2003b). Recent volcanism has mainly consisted of eruption of the 1-km-thick stratiform sequence of trap-like basalt to hawaiite lava flows, 'Afar Stratoid series' (Corti, 2009). This series with an aerial exposure of ~55,000 km^2 covers approximately two-thirds of the low-lying Afar Depression and has been dated at 3.5 to 0.6 Ma (Thurmond et al., 2006). The Afar Stratoid lavas, derived from flood-like volcanism, mainly consist of a series of fissure basaltic flows but are overlain by Quaternary shield volcanoes along the ridge, and are underlain by large amounts of silicic lavas (Lahitte et al., 2003a). This series, which is widespread in the central Afar both in volume and aerial coverage, is not found within the eastern blocks of the Afar Depression (Ali Sabieh block; Audin et al., 2004). Silicic central volcanoes (mainly represented by trachy-rhyolites to pantellerites) emerge locally on the

upper level of the Stratoid series and some younger volcanic units (Lahitte et al., 2003a, and references therein). Further to the north, Tendaho–Manda Hararo and Erta'Ale Range, the site of Quaternary magmatism and tectonism is marked by bunches of volcanic edifices and fissure-fed basalt flows (Corti, 2009).

Quaternary volcanism in Afar Depression is mainly confined to magmatic segments within the incipient seafloor spreading zones (Vidal et al., 1991; Schilling et al., 1992; Boccaletti et al., 1998). They are mainly composed of transitional–tholeiitic basalt flows and shields built along the NNW–trending Erta'Ale Range (Tefera et al., 1996). Towards this range, volcanism becomes increasingly tholeiitic. The Erta'Ale Range is the major volcanic chain within the northern Afar Depression. The range is composed of seven volcanic centers (Fig. 7.1b), roughly NNW-SSE aligned: Gada'Ale, Alu, Dalaffilla, Borale'Ale, Erta'Ale, AleBagu and Hayli Gub (Barrat et al., 1998; Thurmond et al., 2006). Erta'Ale volcano, 60-km-long and 30-km-wide sub-aerial shield, is located approximately in the middle of the magmatic range and rises ~500–700 m from the low-lands of Danakil Depression, reaching a peak of 613 m above sea level (Harris et al., 2005; Thurmond et al., 2006). The surface of the volcanic shield has a wide range of rock types, from mafic to felsic, and imprints the most important volcanic structures (Thurmond et al., 2006). The plume-tail lavas from Erta'Ale Range have slightly lower $^{87}Sr/^{86}Sr$ ratios than the plume-head lavas (Ethiopian high-Ti basalts), although the $^{143}Nd/^{144}Nd$ ratios of these two series overlap (Furman et al., 2004). It has been proposed that the portion of the plume that melted at ~30 Ma was compositionally distinct from the portion undergoing melting now (Furman et al., 2004).

7.3 Sampling, Rock Classification and Petrography

7.3.1 Sampling Methods

The northern Afar Depression volcanics are visually classified into the fissure-fed Quaternary basalts, and shield and composite type volcanoes. Our sampling attempted to cover the entire western part of the Erta'Ale Range and the eastern part of the region was excluded. Sampling in this area is difficult; only a single trail leads to the summit of the lava lake at the Erta'Ale volcano. Despite the poor accessibility and harsh weather conditions, 63 fresh and spatially well-distributed samples were collected and 50 of those were prepared for X-Ray Fluorescence (XRF) spectrometry and Instrumental Neutron Activation Analysis (INAA). Fifteen representative samples were selected and prepared for Sr and Nd isotope ratio measurements. Moreover, 6 samples from three shield volcanoes were treated for electron Microprobe analysis. In each case slightly less than a kilogram of material was collected and

about 100–200 grams of clean, unaltered interior chips were selected for crushing and preparation of powders for chemical analyses. Petrographic thin-sections were also prepared for 40 samples from the basaltic and andesitic rocks and detailed mineralogical analyses were made under an optical (petrographic) microscope.

7.3.2 *The Danakil Depression Basalts and their Petrography*

The northern Afar Depression, commonly called 'Danakil Depression', is a well-defined rift valley confined between the margins of the Nubian plate and the Danakil Microplate (Fig. 7.1a). It is the most volcano-tectonically active depression in the East African Rift System (EARS) and one of the most active places on Earth. The morphology of the Danakil Depression is similar to diverging ocean basins. Low-lying salt plains and lakes are analogous to the abyssal plains of the ocean floor, above which a NNW-SSE aligned chain of shield volcanoes rise 0.5 to 1 km. Quaternary volcanic deposits exposed in the depression are mostly fissure-fed basaltic lava flows and basaltic–trachytic shield volcanoes trending north-northwest, perpendicular to the regional extension direction and parallel to actively propagating Erta'Ale rift segment. The total volume of Quaternary volcanic products in the $\sim$4300-km^2 depression inferred from the digital elevation model (DEM) of Wiart and Oppenheimer (2005) is $\sim$2400 km^3. Although the spatial and temporal relationships of the Quaternary volcanic rocks in general and the basalts in particular, are indistinguishable, they are heterogeneous in nature and show across- and along-axis variations in petrography, geochemistry, and eruptive style. Previous attempts have been made to differentiate the depression's volcanic rocks into various suites. The axial range basalts are considered as MORB-type (Barberi and Varet, 1977), marginal volcanoes as silicic units (e.g., the Nabro and Ma'alalta, volcanoes), and the stratoid series basalts as continental flood basalts (Wiart and Oppenheimer, 2005). However, these classifications were more regional and lack detailed studies on the axial volcanic rocks of Erta'Ale Range.

Based on field observations, morphology, and mineralogy, the volcanic rocks of Erta'Ale Range can be subdivided into three major series:

7.3.2.1 *The Fissure-fed Basalt Series*

This series consists of piles of several meters-thick fissure lava flows, derived from flood basalt-like volcanism, that cover a large area of the Danakil Depression (Fig. 7.2). Their thickness varies laterally and cannot be exactly measured because the lower part of the series is not well exposed and in some places superimposed by the upper part of the axial shield volcanoes. This basaltic series is the youngest lava-flow in the Afar Depression and displays

both fresh pahoehoe and aa types (Fig. 7.2a, c). Except for the flatter peripheral part of the series, the fissure basalts are gently dipping (4–5°) and, in most cases, flow radially away from their respective shield volcanoes. A few randomly oriented small central volcanoes and/or cinder cones are also part of the series.

The majority of samples collected from this series are fresh and holocrystalline, and many are vesicular with ~6–8 vol% vesicles. The fabric of most samples is inequigranular with finely crystallized plagioclase-lath dominated to extremely porphyritic and glomeroporphyritic basalts. In some of the samples (e.g., ER04, ER06, and ER34), especially from north of the Danakil Depression, early crystallized olivine phenocrysts are common. The olivine phenocrysts (0.2–0.4 mm) are mostly zoned with core and rim compositions ranging from Fo_{69-75} and Fo_{62-69}, respectively. The matrix composition of olivine ranges from Fo_{65-71}. Plagioclase crystals in some of the flows exhibit trachytic textures, but in the majority of the samples crystals are not well aligned. Intergrowths of the two dominant phenocryst phases, plagioclase feldspar and clinopyroxene, are observed. Some of the phenocrysts are set in a fine-grained matrix of plagioclase feldspar, opaque oxides and, to a lesser extent, clinopyroxene and olivine. The phenocrysts of plagioclase (0.5–7mm) are euhedral to subhedral and often exhibit polysynthetic texture. Zoning is typical characteristic of the plagioclase phenocrysts in this series (Fig. 7.2d–f). The phenocryst compositions vary from core, An_{65-72}, to rim, An_{45-55}. Varying compositions of opaque minerals (<0.05 mm) form inclusions with in olivine and constitute some portion of the matrix. Chrome-rich spinels (≤30% Cr_2O_3) form the major inclusion in olivines. Scattered crystals of ilmenites (TiO_2 ~46%, and FeO_T ~47%) are inter-fingered with the matrix (Table Appendix 2).
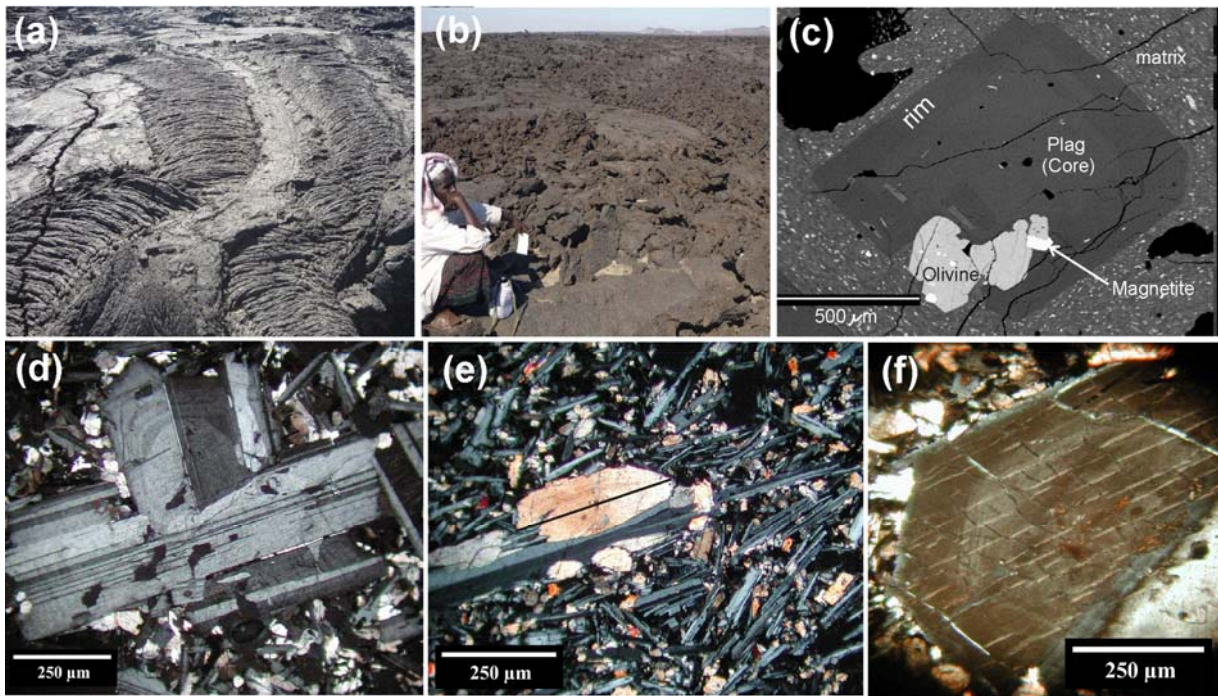
Figure 7.2 Representative outcrops of the fissure-fed basalts and their respective photomicrographs. (a) Pahoehoe lava flowing from small and newly-developed open fractures. (b) The fissure basalts are topped by very young aa lavas ranging in size from cm to meters.(c) Zoned plagioclase imbedded in fine-grained plagioclase-rich matrix. Inclusions of opaque minerals in olivine crystals. (d) Mega phenocrysts of zoned plagioclase, central, imbedded in a medium-grained groundmass of randomly aligned plagioclase, clinopyroxene, and a few opaque minerals; mega-phenocryst pyroxenes are rare. (e) Highly elongated medium- – coarse-grained plagioclase with some clinopyroxene. Phenocrysts of both plagioclase and pyroxene are rare. (f) Hexagonal and zoned phenocryst of plagioclase with two orthogonally aligned cleavage surfaces. All photomicrographs are taken under crossed polars.

7.3.2.2 *The Erta'Ale–Alu Shield Volcanoes*

Erta'Ale is a typical shield volcano at the center of the Erta'Ale Range with gentle slopes of basaltic pahoehoe and aa lavas, and almost no tephra. The summit of the shield is marked by an elliptical caldera ~600-m-wide and ~1700-m-long filled with very young pahoehoe and lava tubes. Inside the caldera, there are two craters (large and inactive northern crater and small and active central crater) both lie within the center of NNW aligned axial zone. The flanks of the volcano are gently sloping and fresh, whereas the inner walls of the caldera form ~30-m-high cliff constituting different layers of basalt flow. The lava dynamics of Erta'Ale is variable; few decades ago the older northern crater was the dominant vent that contained active lava lake fluctuating between ~150 m below the rim to overflowing for at least a century (Waltham, 2005) (Fig. 7.3a).

Of the 7 shield volcanoes in the Erta'Ale Range, Alu volcano is an ellipsoidal volcanic horst, elongated in the NNW-SSE direction, and formed primarily of older basaltic

lava flows. The sides of the shield volcano constitute fissure-type fresh pahoehoe and aa lavas, mostly vesiculated on their upper layers, associated with scoria cones and pyroclastic materials (Fig. 7.3b). Very recent extensional fractures parallel to the major axis of the Erta'Ale Range cut the main volcanic horst of Alu and other areas to the SSE. Dalaffilla is another small conical shield volcano at the southeastern end of Alu. Both shields constitute the central part of the Erta'Ale Range, and record the youngest volcanic eruption in the region.

Throughout the Erta'Ale Range, the basaltic outcrops are younger than 100 ka, fresh, and hypocrystalline. Most of the samples are inequigranular with finely crystallized plagioclase-lath dominated to moderately porphyritic (Fig. 7.3d and f). The majority of samples from these shield volcanoes are nonvesicular and nearly aphanitic, with <10 vol% phenocrysts (0.5–5mm) of plagioclase feldspar, clinopyroxene and, less commonly, olivine in a fine-grained matrix of plagioclase feldspar, clinopyroxene, and few opaque oxides dominated by Ti-magnetites. Although olivines are not the major mineral phases, they exhibit a narrow range of composition, Fo_{66-69}, in this series. Intergrowths of two phenocryst phases, plagioclase feldspar and clinopyroxene, are observed. Most plagioclase phenocrysts show radiating and polysynthetic textures with weak zoning. The plagioclase phenocrysts and matrixes are anorthite-rich (An_{81-89}), but there is no significant compositional variation from core to rim. Clinopyroxenes occur both as meso-phenocrysts (0.4–0.8 mm) and matrixes displaying a limited compositional range that straddles slightly the ferrosilite–augite boundary (MgO, 12.6%; CaO, 14.6%; FeO, 15.5).
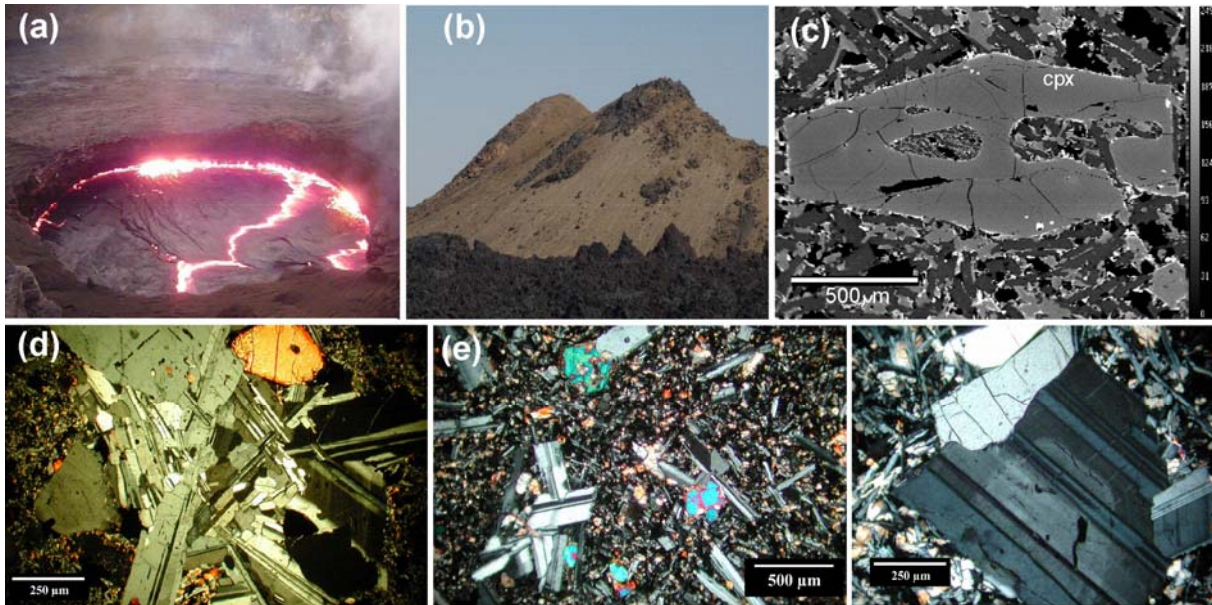
Figure 7.3 Two important outcrops from the Erta'Ale–Alu volcanic chain with photomicrographs of representative samples. (a) The prominent and long-lasting lava lake at the summit of the Erta'Ale shield volcano. (b) A mixture of aa lava, scoria and pyroclastic ash at the Alu-Dalaffilla volcanic shield. (c) Hexagonal cpx intruded by late plagioclase, cpx and few opaque. (d) Extremely porphyritic with mega-phenocrysts (5–8 mm) of euhedral-subhedral plagioclase. Clinopyroxene phenocrysts are rare or absent but significant amount of pyroxenes are found in the groundmass. Highly scattered olivines both as phenocrysts and in the groundmass. The groundmass is still dominated by randomly aligned plagioclase and pyroxenes. Phenocrysts account ~35 % by volume. (e) Fine-grained plagioclase-dominated groundmass of clinopyroxene, few olivine and some opaque. Tabular–elongated mesophenocrysts of polysynthetic plagioclase grains. Phenocrysts do not exceed 10 vol%. (f) Euhedral phenocrysts of plagioclase imbedded in a fine grained groundmass of plagioclase, pyroxene and some opaques. All photomicrographs are taken under crossed polars.

7.3.2.3 *The AleBagu–Afdera Shield Volcanoes*

AleBagu (elevation 1150 m) is an inactive shield volcano composed largely of basaltic lavas and trachytes with some rhyolite lavas and pyroclastic materials. It is a well preserved, steeply inclined, and elliptical strato-type volcano with the longest axis aligned parallel to the principal rift axis of the Erta'Ale Range. However, unlike the other shield volcanoes, AleBagu erupted outside of the major rift axis (i.e., off-axis volcano). At the crest, the large southern elliptical crater and the small northern circular crater both lie along the major axis of the volcano, parallel to the Erta'Ale Range rift axis. As seen from Landsat-5 ETM image (Fig. 7.15), two fresh trachytic lava flows have erupted along the major NNW-SSE–oriented fracture of the shield volcano.

Afdera is another shield volcano in the southern Danakil Depression, located at the intersection of three rift systems between the Erta'Ale, Tat Ali, and Alayta mountain ranges. It is the highest volcanic shield in the depression (~1330 m elevation) and is composed mainly of basalts, basaltic andesites, andesites, and some pyroclastic materials that range from basic to acidic. It is a well preserved, gently inclined circular shield volcano.

The pahoehoe and aa lavas have porphyritic textures with phenocrysts of plagioclase, clinopyroxene, and scattered olivine, embedded by finely-crystalline to hypocrystalline groundmass of the same minerals. Total phenocryst abundance is variable, from nearly aphanitic to moderately porphyritic, and mostly ranges between 2–15% by volume; however, some strongly porphyritic pockets of outcrops with up to 20–30 vol% phenocrysts and megacrysts are also present (Fig. 7.4d, e). The plagioclase phenocrysts, nearly always occur as euhedral, are generally large (~12 mm), compositionally anorthite-rich (An$_{77-89}$), and zoned (Fig. 7.4d–f). No significant compositional differences between the core and rim of the plagioclase. Opaques and other accessory (apatite) minerals form inclusions within plagioclase and pyroxene, and also found as groundmass (Fig. 7.4.c). Euhedral–subhedral olivine phenocrysts (0.3–0.5 mm) are observed in most samples, but the composition is dominated by fayalite (Fo$_{34-45}$).
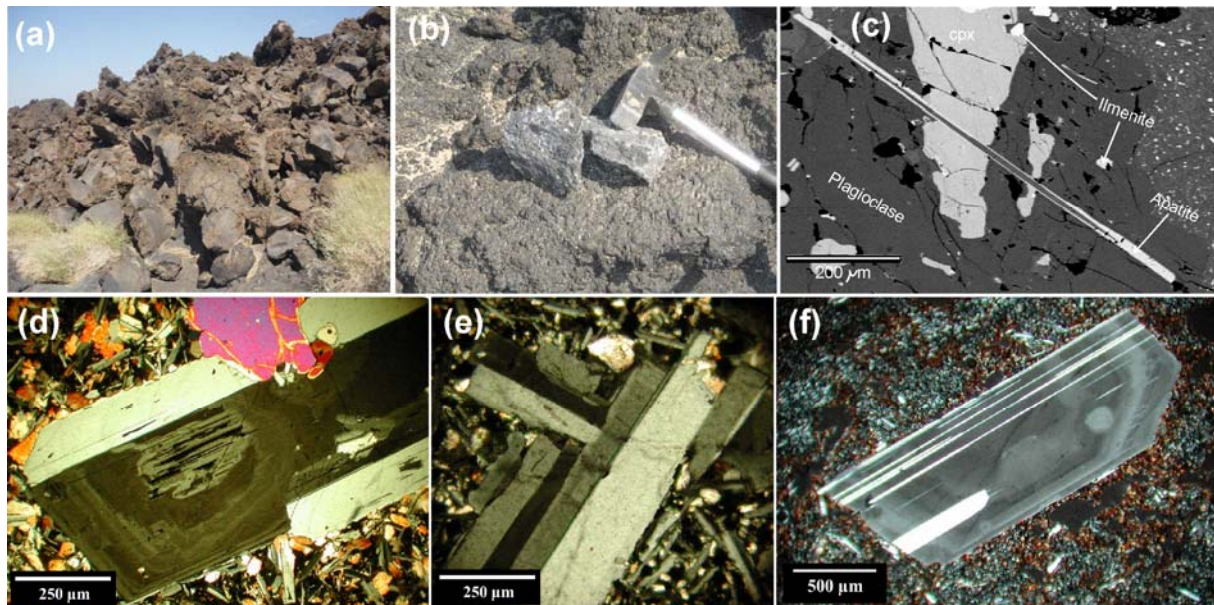
Figure 7.4 (a) Northern view of Afdera, the highest shield volcano in the Erta'Ale Range, surrounded by younger blocky- and aa lavas. (b) Blocky lava at the northern base of AleBagu. (c) Out-crop of fresh, dark-brown vesicular basalts from the northeastern base of Afdera shield volcano. (d) Large grain of zoned plagioclase embedded in medium-grained groundmass of plagioclase, pyroxene and few olivines. Mega-phenocrysts are all plagioclase, except very few meso-phenocrysts of olivine (upper center). The groundmass also contains a limited amount of pyroxene, very few olivines, and other accessories minerals. (e) Phenocrysts of plagioclase in a medium-grained plagioclase rich groundmass. Phenocrysts account 5–7 vol%. (f) Very fine-grained plagioclase- and pyroxene-rich groundmass. It is aphanitic, but a few zoned and polysynthetic mega-phenocrysts (0.7–1.1 cm) of euhedral plagioclase occur. Total amount of phenocrysts is very low (<3 vol%). Images d–f are taken under crossed polars.

7.4   Geochemistry

7.4.1 Analytical Methods

The samples analyzed in this study come from four shield volcanoes and the fissure basalts of the Danakil Depression. Fifty samples have been analyzed for major and trace element contents and 15 samples for Sr and Nd isotopic analyses. All rock samples were first crushed in a stainless steel jaw crusher and then powdered in an agate mill in order to avoid contamination of transition elements (such as Co, Ta, and Nb) for the chemical analyses. Contents of major oxides, minor and trace element (Nb, Zr, Y, Sr, Ga, Cu, Ni, V, Pb) abundances were determined using wavelength-dispersive XRF spectrometry at the Department of Lithospheric Research, University of Vienna, Austria. 1.2 g of powdered rock was mixed with 6 g of lithium tetra-borate to prepare fused pellets for the major oxides analyses, and 10 g of powdered rock was used to prepare pressed pellets for the trace elements analyses.
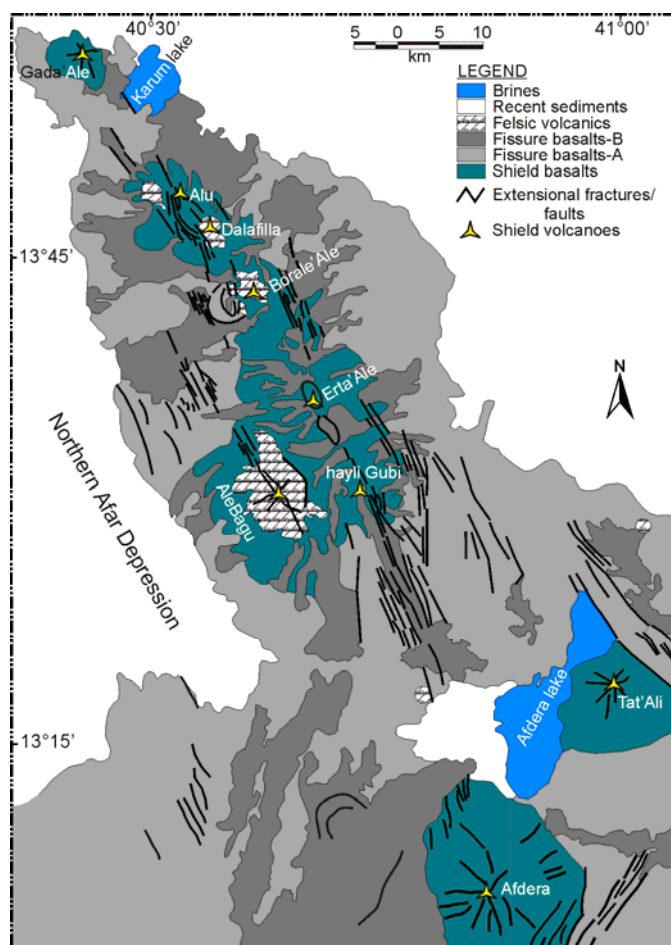
Contents of the rare earth elements (REE) and other trace elements (i.e., Sc, Cr, Co, Zn, As, Se, Br, Rb, Sb, Cs, Ba, Hf, Ta, Th, and U) were analyzed by INAA at the Department of Lithospheric Research, University of Vienna. For this, samples (115–130 mg) were sealed into polyethylene capsules, as well as 60–100 mg of three international rock standards: the carbonaceous chondrite Allende (Smithsonian Institute, Washington DC, USA; Jarosewich et al., 1987), the granite AC-E (Centre de Recherche Pétrographique et Géochimique, Nancy, France: Govindaraju, 1989), and the Devonian Ohio shale SDO-1 (United States Geological Survey, Govindaraju,

Figure 7.5 Geological map of the Northern Afar/Danakil Depression based on interpretation of Landsat-5 ETM and on reconnaissance fieldwork conducted in December 2008.

Table 7.1: Major and trace element contents of transitional-tholeiitic basalts from the Northern Afar Depression, northeastern Ethiopia

	ER01 Basalt	ER02 Basalt	ER03 Basalt	ER04 Basalt	ER06 Basalt	ER07 Basalt	ER08 Basalt	ER09 Basalt	ER10 Basalt	ER13 Basalt	ER14 Basalt	ER15 Basalt
(wt.%)												
SiO_2	49.23	48.05	49.78	48.13	48.31	49.73	50.74	50.97	50.99	50.85	48.99	49.10
TiO_2	2.72	1.88	2.77	2.56	2.60	2.36	2.63	2.62	2.59	2.58	2.52	2.43
Al_2O_3	13.58	13.80	13.74	13.92	14.11	14.41	14.05	14.11	14.21	14.25	15.61	15.76
Fe_2O_3	13.68	10.90	13.89	12.47	12.72	12.49	13.59	13.65	13.57	13.53	11.93	11.69
MnO	0.22	0.18	0.22	0.18	0.18	0.20	0.22	0.22	0.22	0.22	0.19	0.18
MgO	5.88	11.51	5.74	8.59	8.18	6.31	5.47	5.80	5.68	5.56	5.96	6.11
CaO	10.36	11.01	10.06	10.35	10.39	11.06	9.70	9.71	9.81	9.82	11.60	11.66
Na_2O	3.02	2.22	3.20	3.48	3.72	3.07	3.24	3.26	3.19	3.27	2.77	2.86
K_2O	0.49	0.45	0.57	0.49	0.35	0.54	0.63	0.60	0.60	0.60	0.64	0.64
P_2O_5	0.38	0.23	0.39	0.39	0.38	0.33	0.38	0.38	0.37	0.38	0.35	0.35
LOI	0.73	0.99	0.12	0.16	0.12	0.25	-0.11	-0.59	-0.40	-0.30	0.11	0.08
Total	100.29	101.22	100.48	100.72	101.06	100.75	100.54	100.73	100.83	100.76	100.67	100.86
Mg#	53.86	73.50	53.17	65.35	63.88	57.99	52.75	54.12	53.69	53.28	57.46	58.64
NORM												
Q	1.90	--	1.84	--	--	0.35	3.11	2.76	3.11	2.78	0.26	--
Or	2.90	2.65	3.35	2.87	2.05	3.17	3.69	3.49	3.49	3.50	3.75	3.75
Ab	25.61	18.72	26.92	28.99	29.90	25.79	27.17	27.16	26.60	27.31	23.26	23.97
An	22.10	26.26	21.32	20.75	20.53	23.78	21.74	21.75	22.36	22.15	28.06	28.00
Ne	--	--	--	0.13	0.66	--	--	--	--	--	--	--
Di	21.88	21.27	20.94	22.18	22.45	23.11	19.11	18.86	18.87	19.10	21.67	21.82
Hy	12.40	10.55	12.14	--	--	12.05	12.04	12.88	12.63	12.20	11.33	10.10
Ol	--	11.20	--	12.80	11.94	--	--	--	--	--	--	0.96
Mt	7.15	5.27	7.37	6.56	6.72	6.55	7.32	7.32	7.25	7.27	6.12	6.02
Il	5.18	3.56	5.23	4.82	4.88	4.45	4.95	4.90	4.85	4.84	4.75	4.57
Ap	0.88	0.53	0.90	0.90	0.87	0.76	0.87	0.87	0.85	0.87	0.80	0.80
(ppm)												
Sc	37.1	34.9	37.2	35.8	32.3	39.0	34.1	35.1	36.9	37.1	36.7	36.8
V	442	307	443	354	361	372	434	443	428	418	347	334
Cr	57.6	616	54.3	331	269	25.7	24.1	23.6	23.9	25.5	113	126
Co	41.1	49.2	40.7	50.0	42.0	44.1	37.9	39.1	41.3	41.7	38.9	38.9
Ni	39.1	211	36.9	144	120	23.9	25.7	26.6	28.0	24.6	43.1	47.8
Cu	134	46.6	116	122	94.0	77.3	123	126	120	120	150	136
Zn	168	134	140	120	108	143	143	139	148	153	135	140
Ga	17.6	14.4	17.4	14.5	17.0	16.9	17.8	17.4	17.6	18.1	17.2	16.6
As	<1.5	<1.9	<3.4	<3.3	<2.1	<3.3	<1.9	0.55	<3.3	<3.3	<3.0	<2.7
Se	<2.1	<2.1	<2.2	<2.2	<2.12	<2.22	<2.12	0.20	<2.12	<2.12	<2.1	0.76
Br	1.14	0.61	0.92	0.73	<0.55	<0.74	1.21	1.32	1.22	1.04	0.50	0.36
Rb	12.2	21.6	18.6	4.72	4.64	17.9	13.7	17.5	9.12	18.6	14.5	18.9
Sr	269	528	261	345	374	296	255	249	251	257	340	341
Y	43.5	30.0	55.5	45.9	46.5	49.4	54.7	72.8	52.6	48.2	36.6	39.5
Zr	223	198	356	315	316	351	331	553	320	261	207	261
Nb	32.5	20.0	33.0	37.1	35.8	31.6	34.9	34.0	33.2	33.2	34.1	33.5
Mo	1.5	0.7	1.2	2.2	2.2	1.3	1.5	1.2	1.0	1.0	1.6	1.1
Sb	<0.19	<0.25	<0.29	<0.29	<0.27	<0.30	<0.31	<0.24	<0.29	<0.28	<0.29	<0.27
Cs	0.15	0.34	0.18	<0.2	<0.19	0.15	0.14	0.14	0.13	0.18	0.19	0.22
Ba	88.1	59.8	94.5	124	92.2	79.5	85.9	87.1	78.2	83.3	106	103
La	23.9	16.2	25.0	31.0	27.2	27.0	24.3	25.6	26.0	26.0	28.6	28.2
Ce	52.3	34.4	53.4	64.7	56.6	56.3	52.8	53.9	55.1	56.4	59.7	58.9
Nd	25.5	17.5	28.1	31.0	28.2	26.2	26.1	26.4	26.1	29.5	30.0	30.6
Sm	7.73	4.23	6.72	7.06	5.92	6.74	5.94	6.34	6.44	6.90	6.62	6.61
Eu	2.22	1.44	2.25	2.38	2.18	2.24	2.21	2.23	2.32	2.33	2.29	2.19
Gd	7.50	3.76	7.84	7.93	6.98	7.28	6.26	9.85	6.87	6.40	7.16	6.95
Tb	1.01	0.73	1.00	1.05	0.93	1.02	1.14	1.05	1.07	1.11	0.99	0.94
Tm	0.71	0.47	0.73	0.74	0.67	0.74	0.72	0.71	0.75	0.80	0.69	0.69
Yb	3.11	1.67	3.33	2.99	2.45	2.96	3.19	3.11	3.34	3.40	2.60	2.63
Lu	0.50	0.26	0.51	0.43	0.38	0.43	0.51	0.51	0.52	0.54	0.40	0.40
Hf	6.86	6.03	10.8	10.4	9.03	12.2	9.68	15.6	9.82	8.61	6.62	8.39
Ta	2.47	1.76	2.55	3.02	2.58	2.85	2.49	2.51	2.70	2.74	2.76	2.79
Pb	3.7	3.8	3.0	3.0	3.8	3.2	3.2	3.8	4.5	6.0	4.4	3.7
Th	3.03	1.95	3.06	3.67	3.09	3.42	3.19	3.21	3.27	3.46	3.41	3.39
U	1.6	3.2	0.7	1.3	2.1	1.7	1.8	1.0	1.4	1.4	2.2	1.1

All major elements, and the trace element contents of V, Ni, Cu, Ga, Sr, Y, Zr, and Nb were determined using XRF spectrometry, and the contents of remaining trace elements and all rare earth elements were determined using INAA. Mg-number (Mg#) = 100*Mg^{2+} / (Mg^{2+} + Fe^{2+}), where Mg^{2+} and Fe^{2+} are in atomic units (Rollinson, 1993). CIPW normative composition in wt%; qz: quartz; or: orthoclase; ab: albite; an: anorthite; ne: nepheline; en: enstatite; fs: ferrosilite; di: diopside; hy: hypersthene; fo: forsterite; fa: fayalite; ol: olivine; mt: magnetite; il: ilmenite; ap: apatite. Fe_2O_3/Fe_2O_{3T} = 0.15; FeO/ Fe_2O_{3T} = 0.85.

Table 7.1: Continued

	ER16 Basalt	ER24 Basalt	ER25 Basalt	ER26 Basalt	ER27 Basalt	ER28 Basalt	ER29 Basalt	ER30 Basalt	ER17 Basalt	ER18 Trach	ER20 Basalt	ER21 Trach	ER22 Basalt	ER31 Trach
(wt.%)														
SiO_2	49.15	48.99	48.27	48.45	48.85	49.46	49.48	49.50	47.92	63.36	49.02	62.25	48.55	62.58
TiO_2	2.81	2.60	2.20	2.52	2.28	2.53	2.38	2.14	2.51	1.22	2.42	1.45	3.44	1.38
Al_2O_3	14.72	14.77	16.99	14.94	16.47	15.35	15.85	16.34	15.18	14.08	16.16	14.27	13.50	14.38
Fe_2O_3	12.56	12.39	11.21	12.31	11.28	12.34	12.02	11.15	11.62	8.77	11.28	7.86	14.19	8.33
MnO	0.19	0.19	0.17	0.19	0.18	0.19	0.18	0.17	0.20	0.17	0.18	0.17	0.22	0.19
MgO	6.31	6.50	5.95	6.08	6.01	6.05	6.50	6.34	6.43	1.13	6.39	1.83	6.05	1.73
CaO	11.15	10.62	11.62	11.48	12.00	11.40	11.62	11.98	12.15	3.77	11.56	4.24	10.55	4.13
Na_2O	3.02	2.62	2.63	2.75	2.79	2.79	2.73	2.69	2.66	4.52	2.76	5.08	2.79	4.76
K_2O	0.64	0.66	0.53	0.62	0.57	0.62	0.60	0.52	0.62	3.03	0.65	2.72	0.86	2.62
P_2O_5	0.38	0.39	0.30	0.34	0.31	0.34	0.31	0.29	0.36	0.34	0.35	0.28	0.49	0.32
LOI	-0.07	0.95	1.47	0.67	0.10	-0.10	-0.20	-0.28	0.82	0.07	-0.10	0.02	0.07	-0.15
Total	100.86	100.68	101.34	100.35	100.84	100.97	101.47	100.84	100.47	100.46	100.67	100.17	100.71	100.27
Mg#	57.81	58.55	58.63	57.07	58.97	57.07	59.43	60.51	59.68	31.57	60.50	45.49	53.67	42.31
NORM														
Q	--	1.55	--	0.00	--	0.77	--	0.08	--	16.96	--	12.81	1.22	14.98
Or	3.74	3.90	3.13	3.67	3.34	3.62	3.48	3.03	3.67	17.84	3.81	16.05	5.04	15.42
Ab	25.27	22.19	22.25	23.30	23.40	23.31	22.69	22.47	22.55	38.09	23.13	42.92	23.41	40.11
An	24.44	26.62	32.98	26.62	30.45	27.19	28.69	30.58	27.70	9.15	29.50	8.09	21.58	10.09
Ne	--	--	--	--	--	--	--	--	--	--	--	--	--	--
Di	22.44	19.04	18.36	22.82	21.44	21.42	20.94	21.17	24.48	6.00	20.18	8.92	21.97	6.68
Hy	10.87	14.52	11.83	11.70	8.69	11.84	12.77	12.35	6.91	2.51	11.19	2.08	11.84	3.42
Ol	0.56	--	0.94	--	1.94	--	0.20	--	3.20	--	1.06	--	--	--
Mt	6.53	6.35	5.64	6.31	5.74	6.33	6.09	5.65	5.88	6.36	5.77	5.73	7.34	5.95
Il	5.28	4.94	4.18	4.79	4.29	4.74	4.44	4.01	4.78	2.31	4.55	2.75	6.48	2.61
Ap	0.87	0.90	0.70	0.79	0.71	0.78	0.70	0.66	0.84	0.79	0.80	0.65	1.13	0.74
(ppm)														
Sc	34.9	36.9	37.7	40.5	33.0	36.3	41.0	34.4	35.0	13.9	36.2	11.8	38.5	16.4
V	392	353	304	358	318	365	339	315	331	12.0	321	8.0	411	72.6
Cr	59.7	160	168	146	128	127	187	146	90.1	10.9	91.4	8.38	45.1	21.8
Co	36.9	41.9	36.4	39.3	34.7	36.5	41.3	35.7	40.8	10.0	41.6	2.57	45.7	11
Ni	40.6	62.0	47.4	41.1	45.7	41.2	51.6	51.9	53.8	<1	54.2	<1	41.1	4.5
Cu	129	111	120	127	130	144	150	139	130	51.3	135	17.3	189	22.4
Zn	125	120	105	125	98	109	110	116	127	154	139	165	137	163
Ga	18.2	16.8	17.7	17.6	17.5	17.5	16.6	16.7	17.0	19.6	17.6	21.0	18.3	21.0
As	<2.7	2.01	<2.1	0.6	<1.0	<2.1	<1.3	<3	<2.8	2.09	<2.1	1.93	0.68	1.76
Se	<2.4	2.69	<2.5	0.68	<2.0	<2.2	<2.3	<1.8	<2,02	<1,53	<2,06	0.23	<2.5	<1.5
Br	0.58	1	0.6	0.6	0.6	0.5	0.7	0.4	0.60	1.09	0.49	1.25	0.7	1.1
Rb	14.7	20.4	14.5	17.7	11.5	13.1	14	10.5	18.3	93.5	17.30	89.16	17	76.9
Sr	346	351	330	321	337	324	320	328	394	232	408	228	405	263
Y	43.2	40.4	31.6	34.8	32.5	41.9	33.7	42.0	35.3	89.4	45.3	104	46.2	87.2
Zr	271	266	191	182	176	269	175	299	206	776	338	957	315	744
Nb	34.0	36.5	26.6	31.7	28.3	31.7	30.1	27.3	36.3	115	34.1	120	54.8	105
Mo	1.4	1.6	1.0	1.2	1.3	1.3	1.1	0.8	1.3	5.0	1.4	5.1	1.8	4.4
Sb	<0.26	<0.2	<0.2	0.15	<0.2	<0.2	0.07	<0.3	<0.27	0.24	<0.26	0.28	0.19	0.37
Cs	0.09	0.26	0.22	0.23	0.16	0.24	0.17	0.08	0.11	1.30	0.16	1.19	0.35	1.02
Ba	88.6	103	78	77	70	85	96	92	113	385	95.4	371	132	331
La	25.2	29.3	20.9	25.9	21.3	24.0	25.4	20.8	27.9	95.9	29.7	105	44.2	92.3
Ce	54.7	60.9	41.9	54.8	43.8	49.4	49.3	42.9	60.7	194	61.4	205	87.9	176
Nd	27.4	31.0	22.6	28.5	23.9	29.6	27.4	20.2	32.5	81.3	29.6	78.8	45.5	67.8
Sm	5.95	7.19	5.26	6.53	5.37	5.86	6.41	5.20	6.43	15.3	6.54	16.1	9.85	15.5
Eu	2.21	2.27	1.81	2.21	1.79	1.95	1.89	1.75	2.26	3.98	2.34	4.08	2.83	3.73
Gd	6.24	7.52	6.02	5.81	4.71	5.00	5.38	4.34	6.67	13.2	5.03	16.5	8.6	15.1
Tb	0.91	1.14	0.85	1.07	0.85	0.92	0.95	0.69	0.92	2.40	0.95	2.46	1.34	2.22
Tm	0.61	0.52	0.44	0.49	0.43	0.46	0.44	0.33	0.69	1.58	0.70	1.69	0.62	0.92
Yb	2.46	2.66	2.3	2.84	2.31	2.54	2.62	2.21	2.34	7.15	2.40	7.30	3.33	6.54
Lu	0.39	0.35	0.30	0.35	0.3	0.33	0.35	0.33	0.38	1.07	0.37	1.09	0.40	0.98
Hf	7.80	8.62	6.35	6.09	5.28	7.82	5.85	8.47	6.57	22.8	11.4	28.2	10.3	24.2
Ta	2.34	3.08	1.98	2.36	1.91	2.06	2.20	2.03	2.92	8.10	3.02	8.70	4.2	7.68
Pb	3.8	4.4	3.0	4.1	4.5	3.6	3.5	3.5	4.0	11.5	4.1	10.0	5.2	8.8
Th	2.90	3.85	2.73	3.03	2.41	2.71	2.86	2.48	3.58	12.6	3.56	18.0	5.27	15.5
U	2.0	2.2	1.5	2.0	2.9	1.7	1.5	2.3	2.0	7.1	2.0	7.0	3.2	6.1

Table 7.1: Continued

	ER33 Basalt	ER34 Basalt	ER35 Basalt	ER36 Basalt	ER37 Basalt	ER38 Basalt	ER39 Andes	ER41 Basalt	ER43 Basalt	ER44A Andes	ER44B Andes	ER45 Andes	ER47 Andes
(wt.%)													
SiO_2	47.65	47.10	48.59	47.73	46.71	47.76	53.50	47.22	48.08	58.14	57.61	56.23	47.14
TiO_2	3.40	2.74	3.43	2.64	2.82	3.82	1.90	4.29	2.45	1.57	1.60	1.64	3.62
Al_2O_3	13.49	14.33	14.20	15.39	13.71	13.67	17.19	13.58	16.43	15.48	15.31	15.52	13.56
Fe_2O_3	13.97	12.14	14.22	11.68	12.28	15.68	9.12	16.15	11.73	7.99	8.14	8.37	15.82
MnO	0.22	0.19	0.22	0.18	0.20	0.23	0.14	0.23	0.17	0.13	0.13	0.13	0.23
MgO	6.30	6.34	5.71	5.97	5.21	5.37	3.62	5.48	8.52	4.16	4.32	4.68	5.53
CaO	10.79	12.01	10.20	12.03	8.57	9.99	9.27	10.00	11.28	7.38	7.62	8.43	10.06
Na_2O	2.79	2.70	2.94	2.72	3.60	2.84	3.37	3.08	2.63	3.44	3.50	3.33	3.18
K_2O	0.88	0.67	0.92	0.65	1.16	0.54	1.29	0.62	0.44	2.07	2.06	1.87	0.56
P_2O_5	0.48	0.39	0.48	0.37	0.51	0.43	0.25	0.42	0.20	0.19	0.19	0.19	0.41
LOI	0.14	0.55	-0.33	0.51	5.48	0.43	0.80	-0.48	-0.14	0.75	0.16	0.44	-0.36
Total	100.11	99.16	100.58	99.87	100.25	100.76	100.45	100.59	101.79	101.30	100.64	100.83	99.75
Mg#	54.94	58.23	52.35	57.80	54.15	47.87	54.05	47.80	65.90	62.18	62.61	63.27	48.57
NORM													
Q	--	--	0.86	--	--	2.13	6.06	0.29	--	10.45	9.25	7.61	--
Or	5.19	4.01	5.38	3.86	7.21	3.17	7.65	3.62	2.57	12.17	12.12	11.01	3.30
Ab	23.57	23.13	24.60	23.13	32.04	23.90	28.62	25.72	21.94	28.95	29.48	28.07	26.82
An	21.64	25.31	22.57	27.99	18.74	22.83	28.07	21.12	31.28	20.57	19.88	21.80	21.00
Ne	--	--	--	--	--	--	--	--	--	--	--	--	--
Di	23.18	26.19	19.75	23.86	17.62	19.31	13.29	20.46	18.20	11.67	13.19	14.90	21.27
Hy	10.71	4.69	11.87	6.71	6.10	12.55	6.85	11.58	5.96	7.77	7.53	8.00	10.14
Ol	0.95	4.31	--	2.61	4.10	--	--	--	10.50	--	--	--	1.56
Mt	7.20	6.18	7.44	5.95	7.07	5.26	5.26	8.21	5.77	5.02	5.09	5.08	8.13
Il	6.45	5.27	6.44	5.04	5.63	7.21	3.62	8.04	3.33	2.97	3.02	3.10	6.85
Ap	1.11	0.92	1.10	0.86	1.49	0.99	0.58	0.96	0.46	0.44	0.44	0.44	0.95
(ppm)													
Sc	36.9	31.3	33	35.7	30.7	39.7	24.4	39.9	36.0	22.8	23.1	22.8	38.4
V	403	344	407	342	334	513	218	518	268	187	198	195	505
Cr	47.3	59.3	24.9	97.2	35.1	20.3	25.4	17.2	76.4	114	115	121	18.5
Co	48.3	37.5	42.3	41.1	35.4	49.6	28.7	49.6	53.6	27.1	27.0	27.6	48.2
Ni	46.6	47.7	34.9	44.7	20.7	14.5	17.3	17.4	93.9	43.4	43.4	46.6	21.7
Cu	198	165	182	153	111	93.2	101	84.1	133	91.7	70.4	86.7	191
Zn	143	120	126	130	131	161	103	161	110	96.5	95.4	88.1	149
Ga	17.7	16.9	18.4	17.2	17.3	19.7	18.6	21.2	16.8	17.9	17.7	18.1	20.4
As	<3.9	<3.3	<5	<3.1	0.82	<0.9	1.02	0.79	<0.87	0.95	1.16	1.34	1.76
Se	<2.2	<1.8	<1.9	<2	<1.67	1.12	<2,18	<2,5	1.09	<2.0	0.96	1.48	<2,5
Br	0.7	<0.3	0.5	0.7	1.01	0.60	1.19	0.64	0.61	1.11	0.87	0.94	0.73
Rb	28.0	10.3	21.1	11.1	31.3	11.7	36.2	12.9	11.9	57.2	50.4	47.1	10.2
Sr	415	406	426	429	447	396	373	418	336	275	280	291	390
Y	42.6	35.1	50.0	35.1	42.8	45.4	39.7	43.0	25.9	50.0	47.4	43.7	43.1
Zr	283	212	354	215	217	244	268	242	126	309	284	243	229
Nb	55.5	40.3	54.3	39.4	51.3	35.5	40.7	42.4	15.6	48.1	47.2	43.7	34.3
Mo	2.4	1.7	1.7	1.4	1.9	1.6	2.0	1.4	1.3	2.8	2.6	2.9	1.1
Sb	<0.4	<0.3	<0.4	<0.4	0.10	0.20	0.13	<0,2	<0,17	0.15	0.15	0.18	<0,19
Cs	0.27	0.12	0.22	0.15	0.43	0.42	0.44	0.32	0.25	0.72	0.67	0.58	0.98
Ba	135	85	125	148	140	106	165	129	59.0	201	183	183	235
La	49.1	30.4	42.3	33.2	38.22	29.15	37.99	30.61	13.49	45.32	45.01	39.11	26.37
Ce	94.7	60.9	84.1	68.8	83.25	64.36	79.90	67.79	31.44	94.53	91.23	78.59	57.90
Nd	39.4	26.3	37	31.2	41.30	35.27	37.23	32.33	18.25	41.43	38.18	34.99	29.98
Sm	9.87	6.45	8.60	7.09	8.64	8.12	7.92	8.02	4.24	8.47	8.21	7.76	7.73
Eu	3.14	2.2	2.73	2.45	2.83	2.86	2.21	2.92	1.61	1.91	1.93	1.76	2.57
Gd	8.33	5.43	8.48	6.6	7.70	8.99	8.03	7.72	5.10	9.37	8.62	7.60	6.98
Tb	1.28	0.95	1.18	0.98	1.37	1.42	1.29	1.39	0.82	1.39	1.34	1.31	1.34
Tm	0.59	0.38	0.51	0.45	0.59	0.54	0.56	0.57	0.38	0.59	0.59	0.61	0.54
Yb	3.27	2.30	2.89	2.52	3.23	3.05	3.30	2.93	2.30	3.93	3.82	3.36	2.81
Lu	0.46	0.34	0.42	0.40	0.50	0.46	0.49	0.44	0.30	0.62	0.59	0.51	0.42
Hf	9.54	6.24	10.8	7.45	6.94	8.24	9.42	7.94	4.36	11.18	10.10	8.26	7.32
Ta	4.48	2.77	3.87	3.06	3.66	2.84	3.49	3.47	1.34	4.01	3.82	3.76	2.80
Pb	4.8	4.5	4.4	4.7	4.8	7.7	5.8	5.0	4.7	7.0	6.7	7.6	3.1
Th	5.71	3.46	4.90	3.94	4.71	3.14	7.78	3.58	1.59	10.04	9.49	8.54	2.94
U	3.5	2.7	3.2	3.1	3.3	2.1	4.2	3.2	1.8	3.8	4.2	2.9	2.3

Table 7.2: Sr and Nd data for the rock samples from the Danakil Depression, northeastern Ethiopia

Sample No.	Danakil Depression	Rock type	$^{143}Nd/^{144}Nd$	$^{87}Sr/^{86}Sr$
ER06	Fissure	Basalt	0.512883	0.704095
ER16	Fissure	Basalt	0.512887	0.703699
ER20	Fissure	Basalt	0.512865	0.703679
ER02	Erta'Ale S.	Basalt	0.512887	0.705312
ER24	Erta'Ale S.	Basalt	0.512873	0.703695
ER26	Erta'Ale S.	Basalt	0.512886	0.703685
ER28	Erta'Ale S.	Basalt	0.512880	0.703690
ER22	AlebBagu	Basalt	0.512861	0.703705
ER33	AlebBagu	Basalt	0.512865	0.703829
ER35	AlebBagu	Basalt	0.512863	0.703767
ER41	Afdera	Basalt	0.512886	0.703629
ER44B	Afdera	Basalt	0.512893	0.703760
AS54	M. Basalt	Basalt	0.512883	0.703481
MB59	M. Basalt	Basalt	0.512897	0.703500
AX004	M. Basalt	Basalt	0.512991	0.703400

Govindaraju, 1989) were irradiated for 8 hours at the Triga Mark II reactor of the Institute of Atomic and Subatomic Physics, Vienna, at a neutron flux of 2.10^{12} n cm^{-2} s^{-1}. Details of the INAA method, including standards, correction procedures, precision, and accuracy, are reported in Koeberl (1993), Son and Koeberl (2005), and Mader and Koeberl (2009). Nd and Sr isotope analyses (Table 7.2) were carried out at the Laboratory of Geochronology, Department of Lithospheric Research, University of Vienna. All samples were leached for 10 min in 2N HCl in an ultrasonic bath, then a second time in dilute HF to remove secondary minerals. To evaluate the effects of leaching, two duplicate analyses were run on unleached samples.

7.4.2 Major Elements

The general characteristics of the volcanic rocks of Danakil Depression are illustrated in the total alkalis-silica (TAS) diagram (Fig. 7.6). All rocks from the depression have compositions that plot, with one or two exceptions, in the transitional–tholeiitic field. According to the TAS classification of Le Bas et al. (1986), the rocks are basalts, basaltic andesites, andesites, and trachytes. The Danakil Depression volcanic rocks show a range of SiO_2 contents from 46.5 to 63.5 wt%, although they are dominantly basaltic and clustered in a narrow region in the diagram (46.5 – 51.0 SiO_2 wt% and 3.2–4.1 Na_2O + K_2O wt%). The basalts, including those from the Alu-Dalaffilla and Erta'Ale shield volcanoes, have lower (<2.6 wt%) TiO_2 and (3.2–3.9 wt%) Na_2O + K_2O contents and plot in the subalkaline/tholeiitic field. The distinction appears to other major and incompatible trace elements. In contrast, the off-axis

shield/composite volcanoes, AleBagu and Afdera, for example, have moderately-high to high (3.27 and 3.91 wt% respectively) TiO_2 and relatively high (3.4–4.1 wt%) $Na_2O + K_2O$ contents compared with the along-axis shield volcanoes, Alu-Dalaffilla and Erta'Ale shield basalts (Table 7.1 and Figs. 7.6 and 7.7a, f, and g). Moreover, the Ale Bagu and Afdera volcanoes have distinct major and trace element characteristics: they exhibit high Fe_2O_3 and P_2O_5 wt% and low MgO and CaO wt% contents (Fig. 7.7c, d, e, and h).
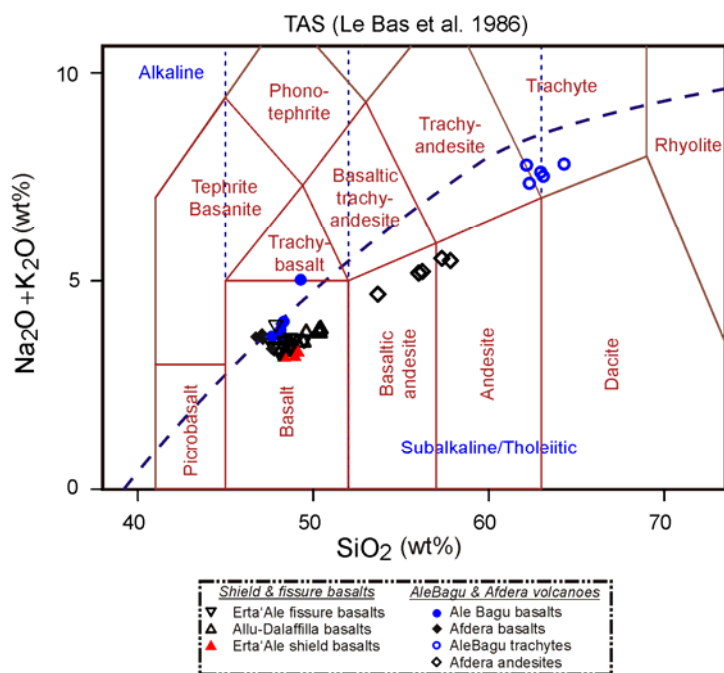
Figure 7.6 Total alkalis ($Na_2O + K_2O$) versus silica (SiO_2) variations in Danakil Depression lavas. Oxides are recalculated (LOI-free) using the SINCLAS program of Verma et al. (2002) for obtaining the TAS names. The dashed line distinguishes alkaline from subalkaline basalts (after Le Bas et al. 1986).

Major element variations show considerably less scattering for the basaltic rocks of the Danakil Depression. Overall there is an increase in Na_2O and K_2O contents and a decrease in MgO, TiO_2, CaO, P_2O_5, and Fe_2O_3 contents with increasing silica (Fig. 7.7). Primitive basaltic lavas with MgO >8 wt% are infrequent. All samples, except samples ER02, ER04, and ER06 have low MgO contents (<8 wt%) and consequently very low magnesium number (47–65 %). The presence of large amount of plagioclase in some samples (e.g., Erta'Ale Shield basalts) shows that the shield rocks of the Danakil Depression are evolved lavas (i.e., low-MgO, high-Al_2O_3). Almost all the samples from the depression are dominated by olivine- and quartz-normative compositions, whereas samples ER04 and ER06 from southern Gada'Ale are slightly nepheline-normative lavas (not plotted). The contents of Cr vary from 630 to 8 ppm, La from 13 to 104, and Nd from 17 to 96 ppm (Table 7.1). Such elemental variation in a suite of basaltic rocks indicates that fractional crystallization as a possible cause. However, it has to be noted that fractional crystallization alone cannot fully enlighten many geochemical features of the mafic lavas of the depression.
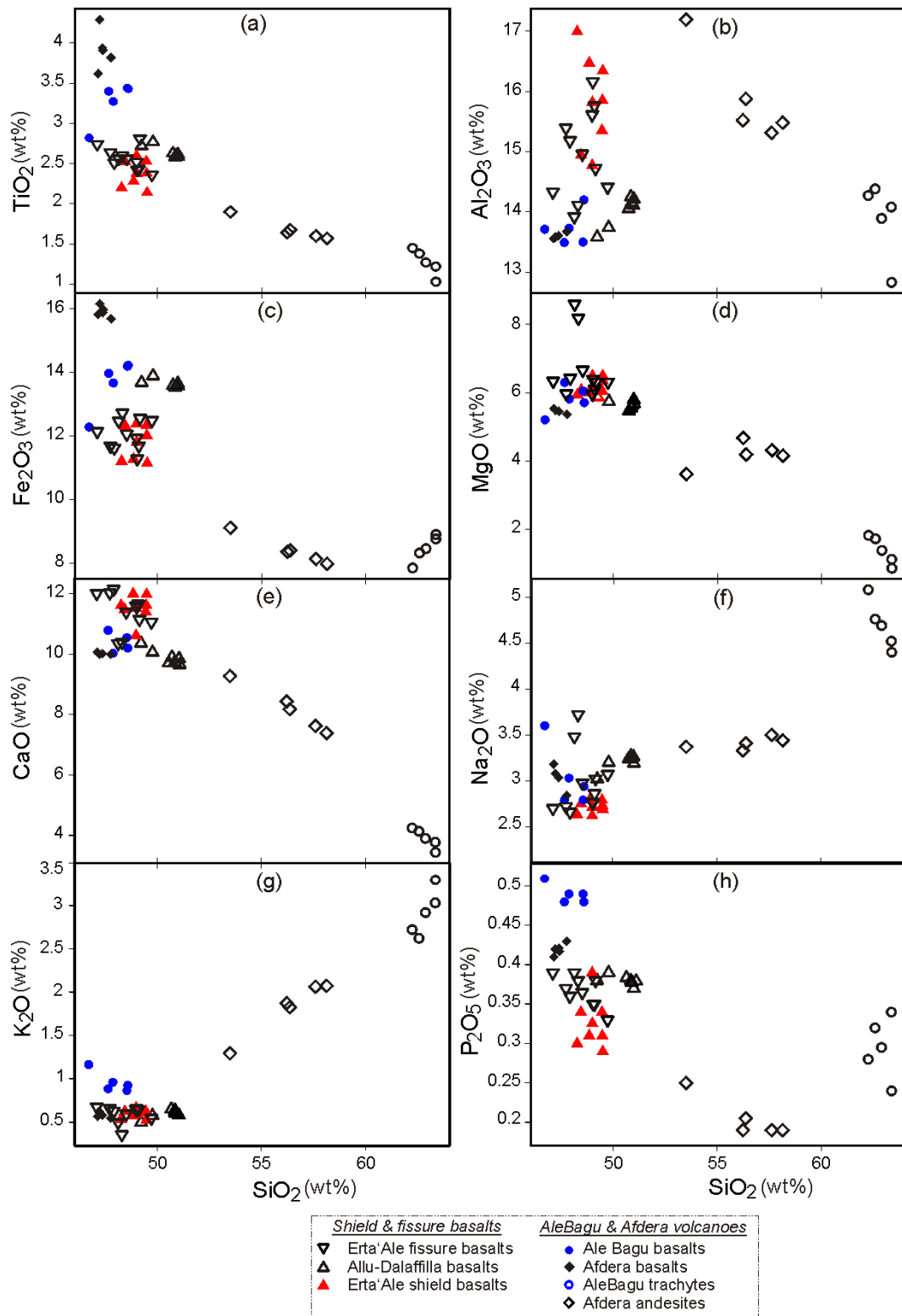
Figure 7.7 Harker variation diagrams for the Quaternary volcanic rocks of the Danakil Depression. All major oxides are characterized by their unique trends as SiO_2 ranges from 47–62 wt%.

7.4.3 Trace Elements

7.4.3.1 Incompatible Trace Elements

In the Danakil Depression (northern Afar Depression) basaltic lavas, abundances of the highly incompatible elements (Th, Ta, and Nb) and light rare earth elements (La, Ce, and Nd) greatly vary from one shield basalt to another when plotted against SiO_2 (Fig. 7.8). The young generations of the Danakil Depression basalts show distinct trace element abundance patterns. Of the samples analyzed, the AleBagu shield basalt, which lies beyond the main rift axis, shows the highest degree of incompatible trace element enrichment, whereas the Erta'Ale shield basalts show the least enrichment compared to primitive mantle. The highly incompatible element content of the AleBagu basalts is twice that of the Erta'Ale shield basalts. This difference between two adjacent shield volcanoes is enigmatic. The other shields and fissure-fed lavas tend to have intermediate trace element abundances (with greater tendency to the Erta'Ale shield basalts) compared to the two Danakil Depression shields. However, the primitive mantle-normalized trace element patterns for all the Danakil Depression basalts are somewhat similar to each other. Primitive mantle-normalized incompatible element plots display generally consistent pattern throughout the Danakil Depression, but few elements show substantial negative anomalies that requires interpretation in the petrogenesis. All of the samples from the Danakil Depression are characterized by positive U, La, and Nb and negative Ba, K, and Sr anomalies (Fig. 7.9).
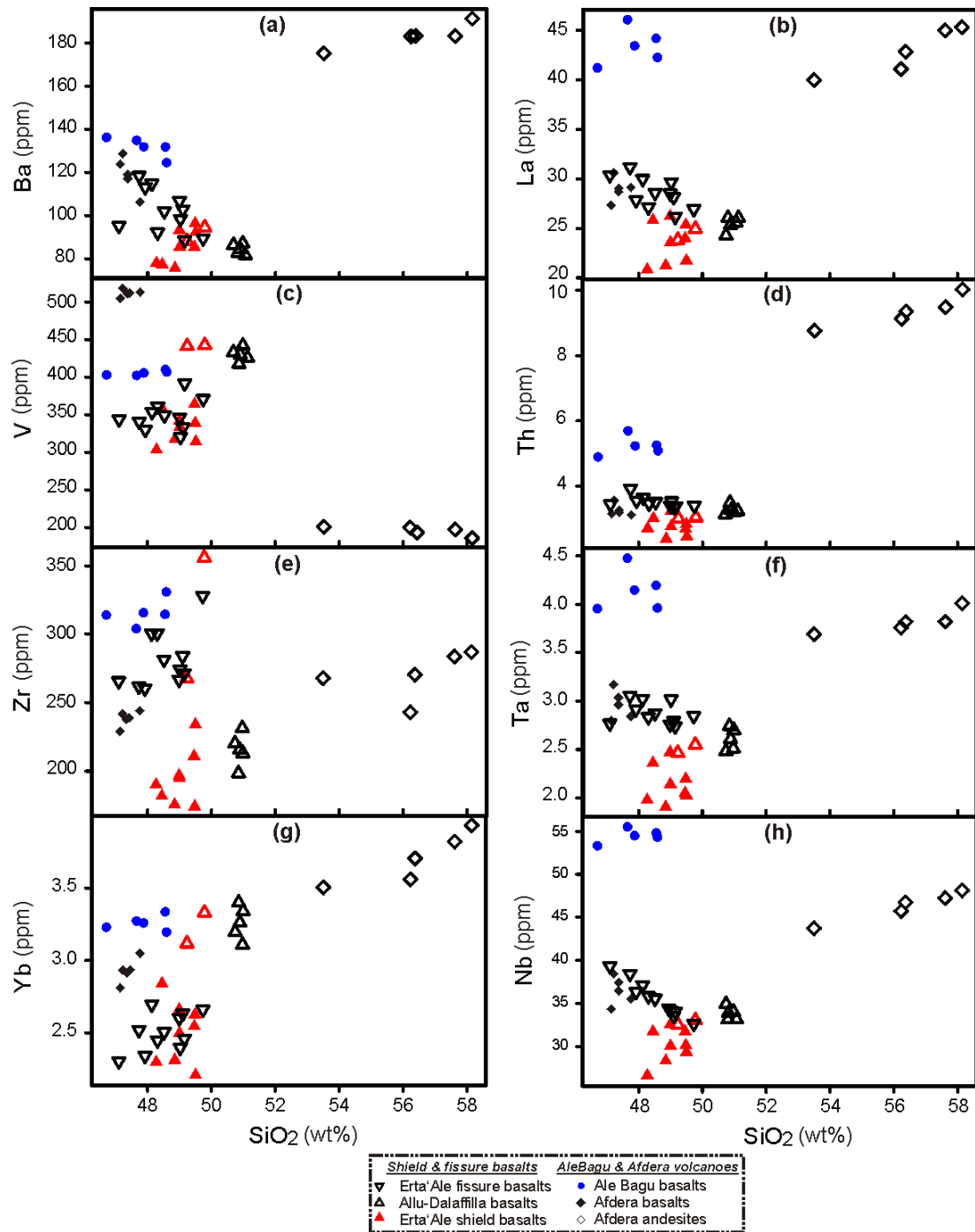
Figure 7.8 Plots of selected minor and trace elements (ppm) against differentiation index (SiO$_2$ wt%) for the Danakil Depression mafic lavas. The binary plots of the contents of Ba, V, Zr, Yb, La, Th, Ta, and Nb versus SiO$_2$ illustrate the compositional variation among the mafic rocks of the region.
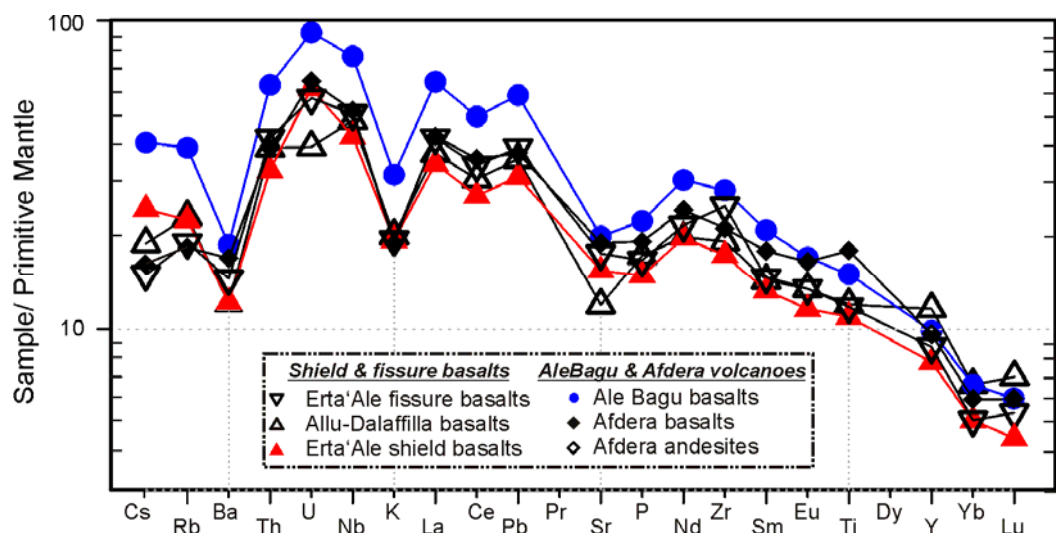
Figure 7.9 Primitive mantle-normalized incompatible trace element variations among Danakil Depression mafic lavas show well-defined ranges for each eruptive center. Normalization factors after Sun and McDonough (1989).

7.4.3.2   Rare Earth Elements

Chondrite-normalized REE diagrams for the Danakil Depression lavas display light REE enrichment relative to heavy REE. The basaltic rocks of the depression show three REE patterns. The Alu-Dalaffilla, Erta'Ale, and Afdera shield basalts have a comparatively flat LREE and HREE pattern. In contrast, the AleBagu shield basalts have highly sloping light REE (LREE) patterns. In contrast, the Erta'Ale fissure-fed basalts are characterized by moderately sloping LREE and flat HREE patterns (Fig. 7.10). The average chondrite-normalized La/Yb ratio of the AleBagu basalts (9.3) is higher than that for the other basalts (<7.7; Fig. 7.10). This ratio decreases greatly in rocks to the north (5.3), the Alu-Dalaffilla and Gada'Ale basalts. The relatively high $(La/Yb)_n$ ratio of the AleBagu shows that basalts of this type are highly fractionated compared with the other shield and fissure basalts of the area. Despite this inconsistency, all basalts of the Danakil Depression show similar, slightly positive Eu anomalies. The basaltic andesites and andesites from the Afdera shield show negative Eu anomalies (Fig. 7.10).

Values of $(La/Sm)_n$ and $(La/Yb)_n$ vary when plotted against La and with one another, in the Danakil Depression (Fig. 7.11). Chondrite-normalized Tb/Yb values for all except the Afdera and AleBagu are low and roughly constant among the Danakil Depression basaltic suite. $(Tb/Yb)_n$ values are difficult to fractionate in zones with low residual garnet, thus most of the Danakil Depression data suggest melting in the absence of garnet (Furman et al., 2004). The highest $(Tb/Yb)_n$ value (2.02) measured at Afdera is because of an anomalously low Yb content. All the Depression basalts are LREE-enriched, with LREE abundances ranging from a few tens to hundred times the chondritic abundance (e.g., AleBagu shield basalts). However,

insignificant differences are apparent in the fractionation of the HREE compared with overall LREE enrichment.
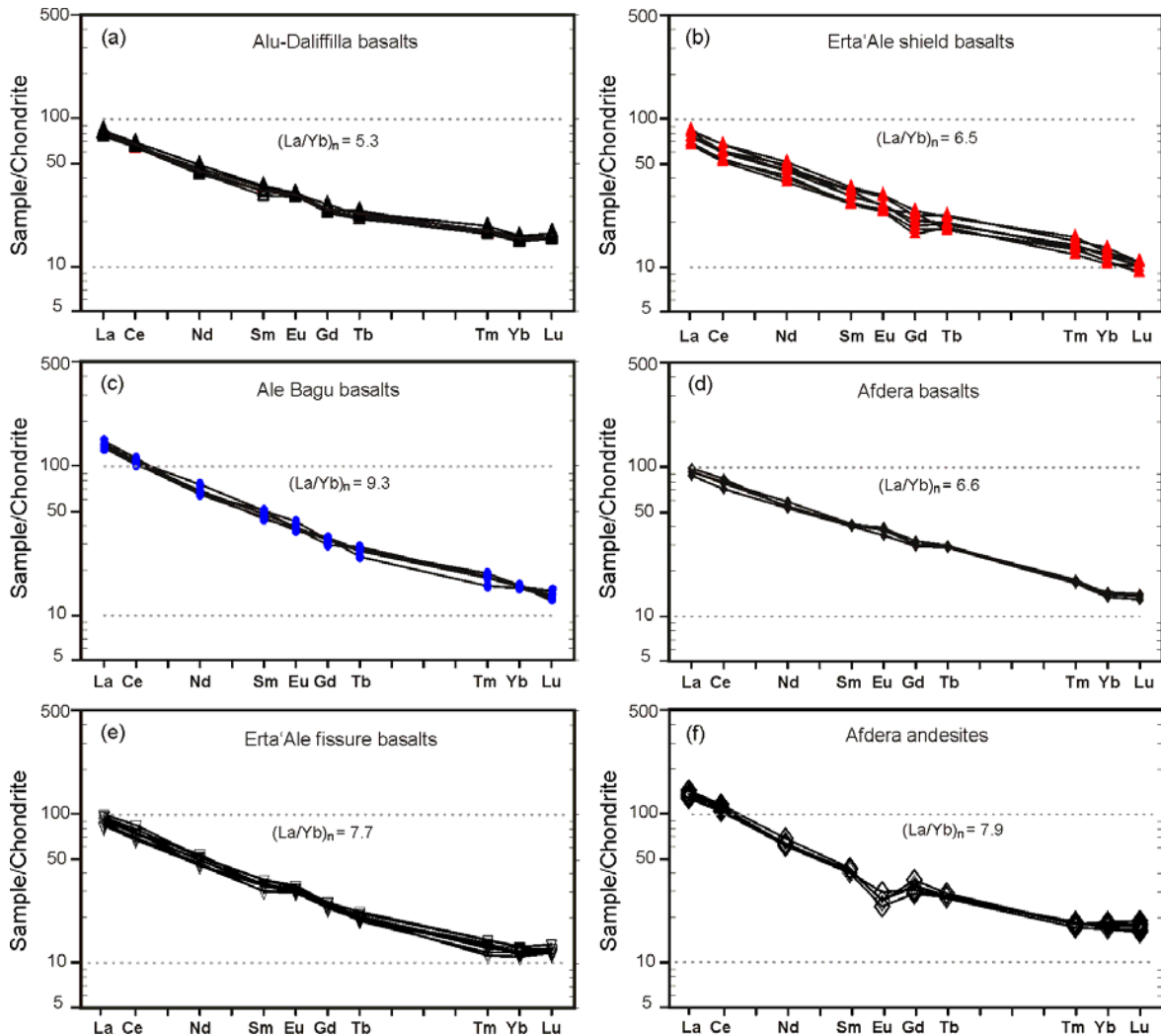
Figure 7.10 (a–f) Chondrite-normalized REE for samples from different shield volcanoes and fissure basalts. (a) The Alu-Dalaffilla basalts, least differentiated with $(La/Yb)_n$ = 5.3. (b) Erta'Ale shield basalts, depleted in the Heavy REE (c) AleBagu basalts have the highest degree of Heavy REE and are the most differentiated basalts in the Danakil Depression: $(La/Yb)_n$ = 9.3. (d) Afdera shield basalts; moderate enrichment in the Heavy REE and slight positive Eu anomaly. (e) Erta'Ale fissure basalt with moderate enrichment in the Light REE and moderate positive Eu anomalies. (f) Afdera andesites.
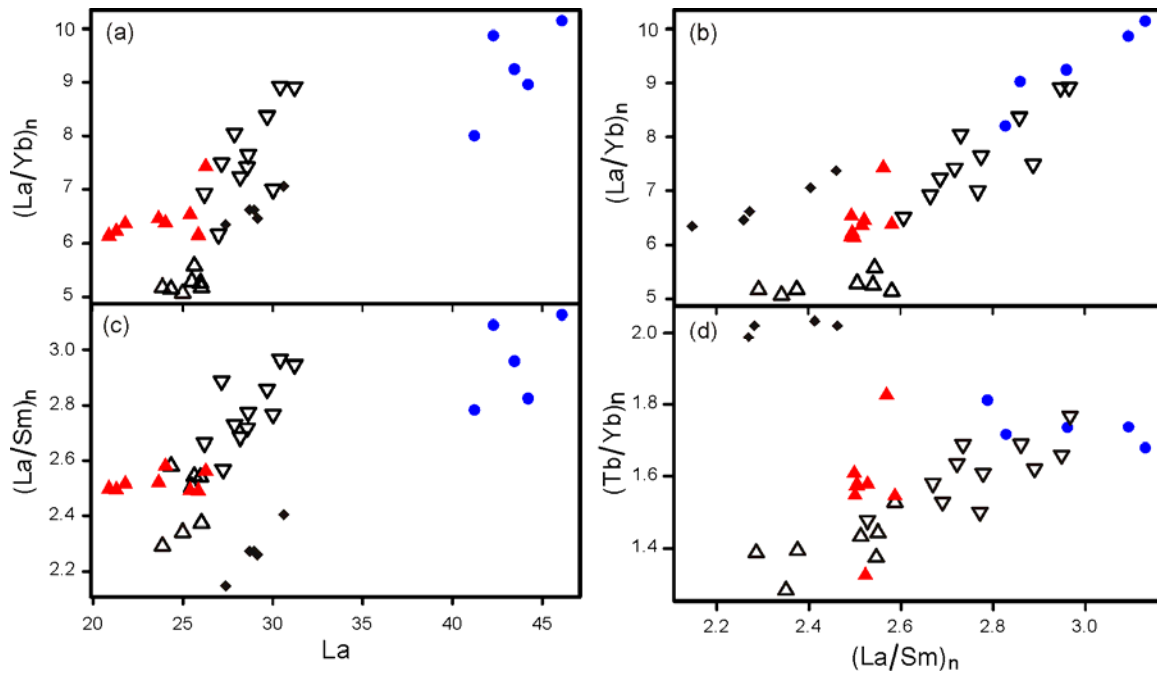
Figure 7.11 (a–d) Chondrite-normalized REE and ratios in Danakil Depression mafic lavas. (a, b, and c) Values of $(La/Yb)_n$ and $(La/Sm)_n$ correlate positively with La and $(La/Sm)_n$ within the Danakil Depression suite with AleBagu basalts showing the highest ratio. (d) $(La/Sm)_n - (Tb/Yb)_n$ variations in mafic lavas of the area.

7.4.3.3   *Sr and Nd Isotope Evidence*

As previously proposed (Barberi and Varet, 1970; Barrat et al., 1998, and references therein), the presence of a wide compositional spectrum from mafic to felsic lavas of the Afar Depression supports rhyolitic magma generation by means of fractional crystallization. The narrow range of Sr and Nd isotopic compositions of the Danakil Depression basaltic suite ($^{87}Sr/^{86}Sr$ 0.7036–0.7041, $^{143}Nd/^{144}Nd$ 0.51286–0.51289; Table 7.2) suggests that contamination by crustal materials or the overlying sediments is not significant. One outlier sample (ER02) from the northern part of the depression exhibits significant increment in the Sr isotopic composition (Fig. 7.12 and Table 7.2). Note that the Erta'Ale and AleBagu basalts with contrasting petrological and geochemical characters have similar $^{143}Nd/^{144}Nd$ and $^{87}Sr/^{86}Sr$ ratios, which indicates that the Danakil Depression basalts are derived from a single reservoir, prevalent mantle (PREMA), which is commonly called the hot mantle plume source.
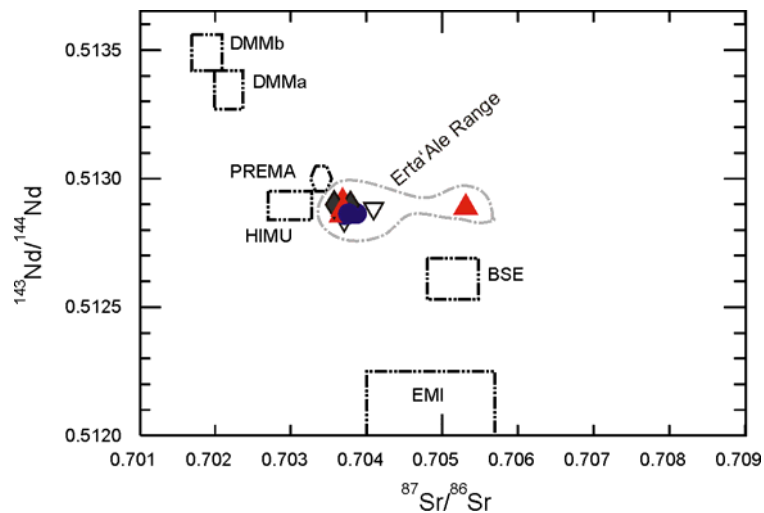
Figure 7.12 $^{87}Sr/^{86}Sr$ vs. $^{143}Nd/^{144}Nd$ plot for the recent basaltic rocks from the Erta'Ale Range. The Sr-Nd isotope range observed in rocks from the Danakil Depression is tightly clustered, except sample ER02, which has an abnormally high value (0.705312) of $^{87}Sr/^{86}Sr$.

7.5   Discussion

The presence of Danakil Depression (Afar Depression) at the merger of two embryonic oceanic rifts (Red Sea and Gulf of Aden) and one intra-continental rift (EARS) creates a complex geodynamic process to understanding the volcanic evolution of the region. Magmatism in the northern segment of the rift system (i.e., the Afar Depression, the Red Sea and Gulf of Aden) is characterized by mid-oceanic ridge-type tholeiitic basalts; whereas volcanism beneath most of the EARS is dominated by lithospheric melts of various compositions (e.g., Rogers et al., 2000; Furman et al., 2004). Due to differences in rift evolution and underlying basement lithosphere, the rift basalts are diverse in composition. Generally, EARS quaternary basalts display along-axis geochemical variations that likely reflect the evolution of rifting and consequently magma supply from the underlying magma chamber/s. In the southern EARS, the Kenyan rift, mafic lavas comprise a wide compositional spectrum (i.e., transitional-tholeiites through alkali basalts to basanites and tephrites) that can be influenced by various petrogenetic processes (Macdonald et al., 2001; Rogers, 2006). On the other hand, basalts at the northern end of the EARS, the Afar/Danakil Depression, are entirely transitional alkali to tholeiitic and are resemble the Oligocene flood basalts of northwestern Ethiopia and mid-oceanic ridge basalts.

The Main Ethiopian Rift basalts are characterized by transitional tholeiites, falling close to the boundary between the Kenyan rift and Afar Depression basalts (Hart et al. 1989; Rogers, 2006). The high degree of tectonic and magmatic activities in the northern end of the EARS favors the production of voluminous and nearly tholeiitic lavas. The Pliocene– to Quaternary basaltic lavas linked with the evolution of the Afar tectonics show a relatively

homogeneous compositional makeup than that of the Kenyan rift basalts, reflecting both the greater uniformity of the attenuated lithosphere and the developing tectonic domain (Vidal et al., 1991). However, even in the Afar Depression, compositional differences are significant ranging from transitional alkali to tholeiitic and from incompatible element-enriched to depleted basalts. In the Danakil Depression (Erta'Ale Range), mineralogical and geochemical variations are evident especially for the adjacent, Erta'Ale and AleBagu shield volcanoes. They are separated by only ~11 km, with the Erta'Ale shield situated at the center of the rift-axis and the AleBagu located about 10 km west of the present rift-axis. Their spatial and temporal variation is minimal; however, their overall compositional make-up is distinct. The trace element contents of the AleBagu basalts are as much twice as high as in the Erta'Ale shield basalts. Such a wide compositional difference in a geographically-restricted setting suggests that the basaltic character of fast spreading rift segments is not homogenous. On the basis of TiO_2 and incompatible trace element contents, the basaltic suites of the Northern Afar Depression can be broadly divided into three magma groups: (1) Low-TiO_2 tholeiitic basalt characterizes the Erta'Ale and Alu–Dalaffilla shield basalts. (2) High-TiO_2 transitional alkali basalt characterizes the AleBagu and Afdera shield basalts. (3) Erta'Ale fissure-fed basalt lies in between (1) and (2).

7.5.1 Crustal Contamination

Crustal contamination is thought to be greatest in less-evolved continental rift zones where crustal thicknesses are considerably large and magma supply rates are low, resulting in greater residence times for individual magma batches within the lithospheric crust (Furman, 2007). However, unlike many other continental rift zones, the center of Danakil Depression is floored by thin (~14 km) oceanic-type lithosphere and bordered by fragments of attenuated continental crust along the plate margins, (Barberi et al., 1980). Accordingly, no persuasive evidence for assimilation of lithospheric crustal materials is expected for most Danakil Depression lavas. Ce/Pb ratios of mafic lavas are sensitive to contamination and well-defined for primary mantle-derived magmas (25 ± 5, Hofmann et al., 1986), making it a useful signal of crustal assimilation (Furman, 2007). Most of the samples from the Danakil Depression plot within the range of mantle values (20 ≤ Danakil Depression ≤ 30) (Fig. 7.13). However, there are few exceptions, such as samples ER13, ER14, ER30, and ER43, which have slightly lower Ce/Pb ratios (<20) than mantle values. This may be explained by interactions between parent magmas and the thin continental crust or abnormally low cerium content. Minor crustal material involvements cannot be completely avoided from the mantle originated

magma in the depression, such magma–country rock interaction is almost negligible in the
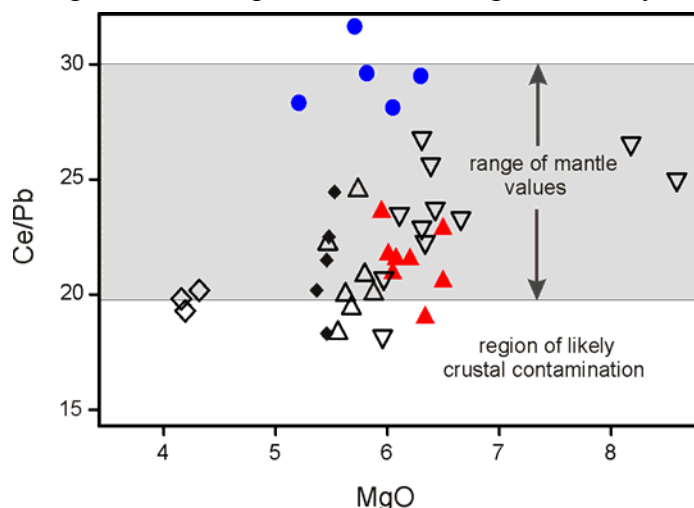
petrogenetic processes of the lava; geochemical variations between the depression's mafic lavas likely reflect primarily heterogeneities in the mantle source region rather than crustal contamination (Furman et al., 2004).

Figure 7.13 Values of Ce/Pb are sensitive to crustal contamination. Most lavas from the Erta'Ale Range have Ce/Pb values within the range of mantle derived melts (20–30; Hofmann et al., 1986).

7.5.2 *Identifying the Source Region for the Danakil Depression Mafic Lavas*

The low-land plain of the Afar Depression, area between the axial ranges and margins, may be interpreted as oceanic crust that formed during Pliocene–Pleistocene oceanic spreading or, alternatively, as attenuated continental crust covered by fissure-fed flood basalt flows (Barberi and Varet, 1977). The thickness of the lithosphere is estimated to be ~26 km in the southern and central Afar and gradually decreases towards the Red Sea and Gulf of Aden, reaching a minimum of 14 km in the Dallol area, northern Afar (Makris and Ginzburg, 1987; Maguire et al., 2006). This thickness is comparable with the thickness of the newly formed oceanic lithosphere. However, the geophysical and geochemical data, in this case, are inconsistent in suggesting the true nature for large parts of the inner Afar. Geophysical studies in the central part of the depression point out that Afar is evolving towards an oceanic type lithosphere, similar to that of the sub-aerial oceanic crust in Iceland or close to the Mid-Atlantic Ridges, with abnormally shallow asthenospheric material beneath the depression (Barberi et al., 1980, and references therein).

On the other hand, the geochemical and isotopic results reveal that the Afar Depression and/or Danakil Depression is not in a state of complete oceanic crust type. Several geochemical results support the interpretation that the Afar hotspot contributes thermally as well as compositionally rather than the depleted mantle or lithospheric crust to magmatism at the Danakil Depression (Furman et al., 2004). The geochemical data and interpretations from previous studies (Barberi et al., 1980, Barrat et al., 1998) and this work confirm that the Danakil Depression is not at full-stage of oceanic crust nature. The contents of highly incompatible trace elements, REE, and their ratios are much higher than the contents of the Red Sea and Gulf of Aden basalts.

The Sr and Nd isotopic composition ranges observed among the Danakil Depression mafic lavas (^{87}Sr/^{86}Sr 0.7036–0.7041, ^{143}Nd/^{144}Nd 0.51286–0.51289; Fig. 7.14) is comparable to that of proposed common source values for mantle plume magmas, termed FOZO (Hart et al., 1992). Figure 14 a illustrates the Nd and Sr isotope composition of basalts from the Danakil Depression, the Gulf of Aden and Red Sea oceanic ridges, and Kenya rift. The Gulf of Aden and Red Sea, as previously described, are characterized by high ^{143}Nd/^{144}Nd and low
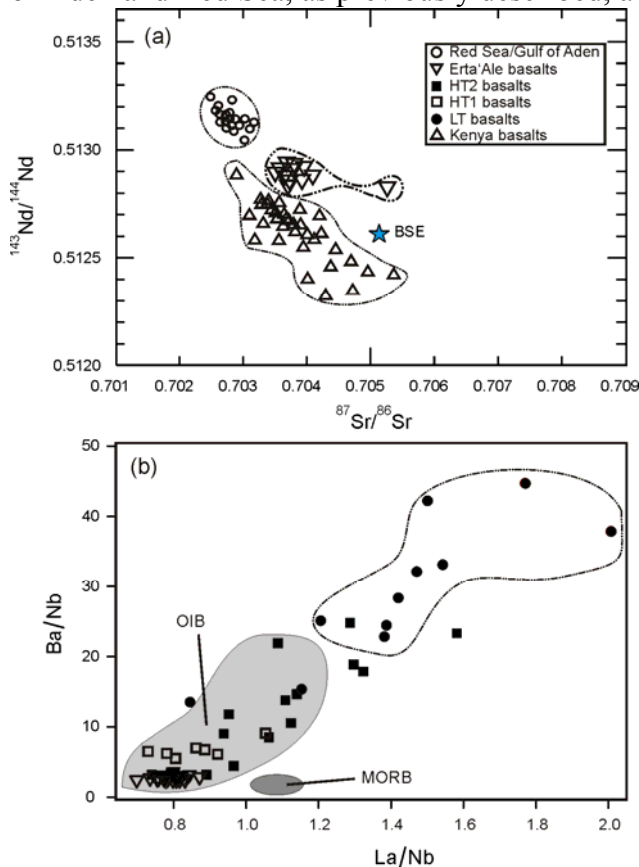
^{87}Sr/^{86}Sr, typical of MORB (Rogers, 2006). Lavas from the Danakil Depression, by contrast, have relatively lower ^{143}Nd/^{144}Nd and higher ^{87}Sr/^{86}Sr ratios than the Red Sea/Gulf of Aden rifts. Instead, the isotopic compositions of the Danakil Depression basalts have a tendency towards the Turkana basalts (Fig. 7.14a). The source composition that we recognize in the Danakil Depression has slightly higher ^{87}Sr/^{86}Sr than that suggested for Turkana basalts (^{87}Sr/^{86}Sr 0.7030–0.7035, ^{143}Nd/^{144}Nd 0.5129–0.5130; Furman et al., 2004).

Figure 7.14 (a) The Sr–Nd isotope range observed at Danakil Depression are very much clustered and plotted near the HIMU and PREMA. The Red Sea/Gulf of Aden and Kenya data (Eissen et al., 1989; Schilling et al., 1992; Rogers, 2006). (b) Selected trace element ratios diagram for the Danakil Depression basalts. The fields of OIB and MORB are from Sun and McDonough (1989). The HT2, HT1, and LT basalts (Pik et al., 1999) are plotted together here for comparison.

The Danakil Depression basaltic suite exhibits trace element ratios (La/Nb, Ba/Nb) that overlap with the lower field of OIBs (Fig. 7.14b; Sun and McDonough, 1989). These transitional–tholeiitic basalts exhibit high–low incompatible trace element contents that are characteristic of magmas formed by variable degrees of partial melting. The overall enrichment of the highly incompatible trace element contents in those Danakil Depression mafic lavas with LREE abundances ranging from a few tens times the chondritic abundance to hundreds and ^{87}Sr/^{86}Sr values ~0.7038 are hard to settle firmly with a depleted MORB mantle source, but are instead more consistent with contributions from a deep hot mantle plume.

7.5.3 Why are the Danakil Depression Basalts Compositionally Distinct?

The compositional variations within the entire EARS have been interpreted to reflect the varying degree of rift evolution representing an incipient breakup at its southern to highly evolved rift segment at its northern portions. From south to north, the compositional variation of the basalts is very wide covering almost the entire spectrum, basanites and nephelinites to tholeiites, respectively. These variations could be mainly because of the differences in: the degree of rifting (spatially controlled), the source region, and other petrogenetic processes such as crustal contaminations, degree and depth of melting.

There is no doubt that the basaltic rocks within the entire Afar floor, which covers an area of about 250,000 km^2, are not necessarily homogeneous suites. The rocks have been deposited throughout the rift evolution in a wide spatial and temporal variation, and hence chemical differences may result because of the variation in stage of rifting, magmatic sources, and possibly the degree and depth of melting. To avoid the spatial and temporal control over magmatic differentiations, in this study, rock sampling was mainly conducted from the northern terminus of the EARS called the 'Danakil Depression'. This depression is the northern and volcano-tectonically active zone of the Afar Depression. The nature of the crust is still under hot debate. Geophysical data reveal that the crust of the depression is an oceanic-type, where as geochemical data confirms that the nature of the Danakil Depression crust is not yet an oceanic crust type. For so many years basalts erupted at mid ocean ridges (MORs) and highly evolved continental rift segments were considered to represent homogeneous chemical composition. However, subsequent studies of specific mid oceanic ridge segments have revealed that basalts collected from the same ridge are not geochemically uniform and therefore there is no unique composition for MORB and more evolved continental rift basalts (Barberi et al., 1980, and references therein). This, in turn, raises a question that why basalts erupted at the same site are not compositionally identical.

At the Danakil Depression, all the shield volcanoes and fissure basalts erupted in a very short time period (late Quaternary/Holocene) and are emplaced very close to each other in a single and tectonically homogeneous segment, the Erta'Ale Range. Despite all these similarities, mineralogical and geochemical differences have been observed for basalts erupted within the short Erta'Ale spreading segment and/or axial range. The major contrast in composition is observed among the Erta'Ale and AleBagu shield basalts. The Erta'Ale shield basalts are characterized by low-Ti and relatively low contents of the incompatible trace elements. Whereas, the AleBagu shield basalts are instead high-Ti transitional rocks with high concentration of the highly incompatible trace elements and LREE.

Such compositional differences in basaltic rocks occur mainly because of the various petrogenetic processes. In the previous sections the basaltic rocks of the Danakil Depression have been treated if they have undergone contamination with the underlying thin continental and/or oceanic crust; however, the ratios of the most susceptible incompatible trace elements (Ce/Pb, B/U) to contamination/assimilation do not give any clue about this petrogenetic process to occur. The other most important process that could greatly influence the composition of the magmatic products is the involvement of more than one source region. In the entire Afar Depression, as the volcanic products vary in space and time, compositional differences might occur as a result of variation in the source region (Barbari et al., 1980; Barrat et al., 1998). However, in the Danakil Depression, where there is no variation in space, time, degree of rifting and, above all, no variation in the isotopic composition of 87Sr/86Sr, the assumption of different mantle source is difficult to consider.

The high-Ti contents and incompatible trace element abundances conferred to the AleBagu magmas a deeper emplacement of its magma chamber compared to the Erta'Ale shield basalts (Fig. 7.15). The observed range of $^{87}Sr/^{86}Sr$ and ratios of some of the highly incompatible elements allow us to support a model of genesis of the Danakil Depression basalts by different degrees and/or depths of partial melting from a homogeneous PREMA-type mantle source (Barberi et al., 1980, and references therein).
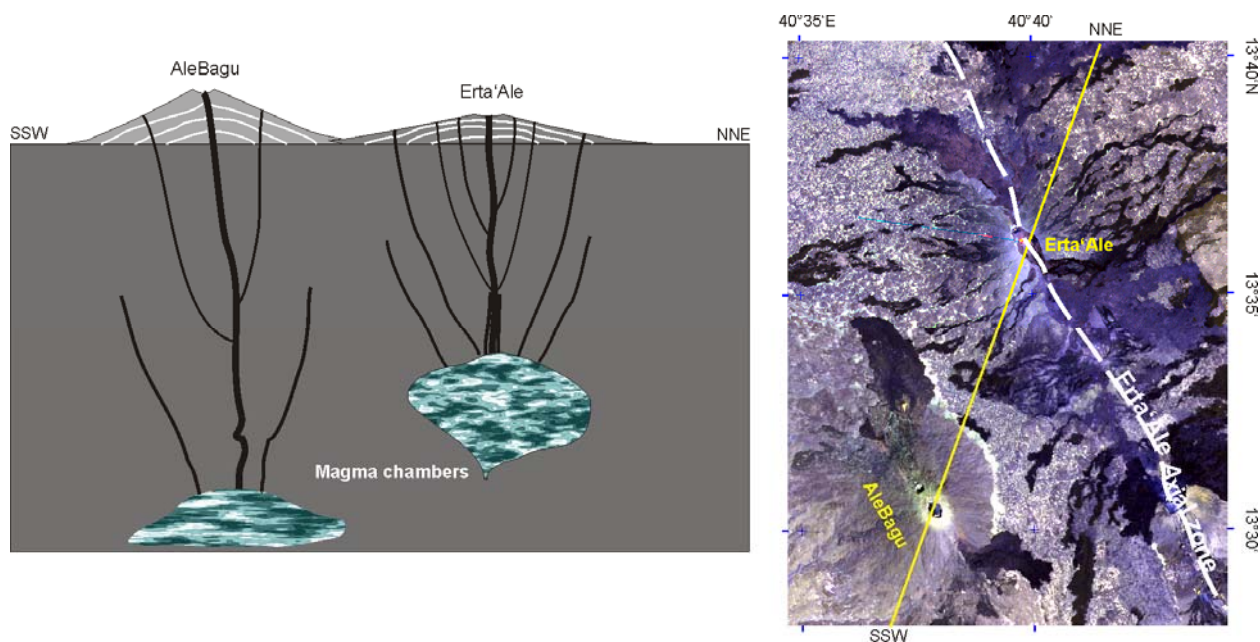
Figure 7.15 (a) schematic representation of the magmatic sources for the trace-element enriched AleBagu and depleted Erta'Ale shield basalts. (b) Mosaic and color composite landsat-5 image of AleBagu and Erta'Ale shields. Yellow line: a section where cross-section (a) is located; broken white line: axial zone of the Erta'Ale Range.

7.6 Conclusions

The young mafic lavas from the Danakil Depression, northern Afar Depression, provide the opportunity to understand the geochemical and tectonic transformation of a mature continental rift towards incipient sea-floor spreading. The Danakil Depression's eruptive products are compositionally diverse in the incompatible trace elements and some major elements, but similar in the Sr-Nd isotopic ratios. Three geochemically distinct magma groups are identified in the northern Afar/Danakil Depression. These are: the high-Ti and incompatible element enriched AleBagu shield basalts, the low-Ti and incompatible element depleted Erta'Ale-Alu shield basalts, and the Erta'Ale fissure-fed basalts, which have intermediate geochemical characteristics between the two end-members.

The measured highly incompatible trace elements (e.g., La, Th, Ta, and Nb) and Sr and Nd isotopes confirm that the Danakil Depression basalts are derived from the plume-tail, the last phase of the Afar mantle plume. The large contrast in geochemical characteristics between the high-Ti and low-Ti basaltic suites may be due to differences in the depth and degree of melting of the magma chambers. According to this hypothesis, the AleBagu basalts are derived from a deeper magma chamber, whereas the Erta'Ale shield basalts along the rift axis are derived from a shallower magma chamber (Fig. 7.15). The Danakil Depression is, therefore, a place where one can easily differentiate various magmatic products in a highly evolved rift zone, which was previously thought to be homogeneous.

References:

Abbate E., Passerini P., and Zan L. 1995. Strike-slip faults in a rift area: A transect in the Afar Triangle, east Africa. Tectonophysics 241, 67–97.

Audin L., Quidelleur X., Coulie E., Courtillot V., Gilder S., Manighetti I., Gillot P. Y., Tapponnier P., and Kidane T. 2004. Palaeomagnetism and K-Ar and ^{40}Ar/^{39}Ar ages in the Ali Sabieh area (Republic of Djibouti and Ethiopia): constraints on the mechanism of Aden ridge propagation into southeastern Afar during the last 10 Myr. Geophysical Journal International 158, 327–345.

Ayalew D., Barbey P., Marty B., Reisberg L., Yirgu G., and Pik R. 2002. Source, genesis, and timing of giant ignimbrite deposits associated with Ethiopian continental flood basalts. Geochimica et Cosmochimica Acta 66, 1429–1448.

Barberi F. and Varet J. 1970. The Erta'Ale Volcanic Range (Danakil Depression, Northern Afar, Ethiopia). Bulletin Volcanologique 34, 848–917.

Barberi F. and Varet J. 1975. Recent volcanic units of Afar and their structural significance. In: Pilger A. and Rösler A. (Eds.), Afar Depression of Ethiopia. Schweizerbart, (Inter-Union Commission on Geodynamics Scientific Report 14), Stuttgart, Germany, 174–178.

Barberi F. and Varet J. 1977. Volcanism of Afar: small-scale plate tectonics implication. Geological Society of America Bulletin 88, 1251–1266.

Barberi F., Ferrara G., Santacroce R., and Varet J. 1975. Structural evolution of the Afar triple junction. In: Pilger A. and Rösler A. (Eds.), Afar Depression of Ethiopia. Schweizerbart, (Inter-Union Commission on Geodynamics Scientific Report 14), Stuttgart, Germany, 38–54.

Barberi F., Civetta L., and Varet J. 1980. Sr Isotopic composition of Afar volcanics and its implication for mantle evolution. Earth and Planetary Science Letters 50, 247–259.

Barrat J.A., Fourcade S., Jahn B.M., Cheminee J.L., and Capdevila R. 1998. Isotope (Sr, Nd, Pb, O) and trace-element geochemistry of volcanics from the Erta'Ale range (Ethiopia). Journal of Volcanololgy and Geothermal Research 80, 85–100.

Beyene A. and Abdelsalam M.G. 2005. Tectonics of the Afar Depression: A review and synthesis. Journal of African Earth Sciences 41, 41–59.

Black R., Morton W.H., and Rex D.C. 1975. Block tilting and volcanism within the Afar in the light of recent K/Ar age data, In: Pilger A. and Rösler A. (Eds.), Afar Depression of Ethiopia. Schweizerbart, (Inter-Union Commission on Geodynamics Scientific Report 14), Stuttgart, Germany, 296–300.

Boccaletti M., Getaneh A., Mazzuoli R., Tortorici L., and Trua T. 1995. Chemical variations in a bimodal magma system: The plio Quaternary volcanism in the Dera Nazret area (Main Ethiopian Rift, Ethiopia). African Geoscience Review 2, 37–60.

Boccaletti M., Bonini M., Mazzuoli R., Abebe B., Piccardi L., and Tortorici L. 1998. Quaternary oblique extensional tectonics in the Ethiopian Rift (Horn of Africa). Tectonophysics 287, 97–116.

Collet B., Taud H., Parrot J.F., Bonavia F., and Chorowicz J. 2000. A new kinematic approach for the Danakil Block using a digital elevation model representation. Tectonophysics 316, 343–357.

Corti G. 2009. Continental rift evolution: From rift initiation to incipient breakup in the Main Ethiopian Rift, East Africa. Earth Science Reviews 96, 1–53.

Deniel C., Vidal P., Coulon C., Vellutini P.J., and Piguet P. 1994. Temporal evolution of mantle sources during continental rifting: The volcanism of Djibouti (Afar). Journal of Geophysical Research 99, 2853–2870.

Ebinger C..J., Yemane T., Woldegabriel G. Aronson J.L., and Walter R.C. 1993. Late Eocene-Recent volcanism and rifting in the southern main Ethiopian rift. Journal of the Geological Society, London, 150, 99–108.

Eissen J. P., Juteau T., Joron J. L., Dupre B., Humler E., and Al'Mkhamedov A. 1989. Petrology and geochemistry of basalts from the Red Sea axial rift at 18 ° N. Journal of Petrology 30, 791–739.

Furman T. 2007. Geochemistry of East African Rift basalts: An overview. Journal of African Earth Sciences 48, 147–160.

Furman T., Bryce J.G., Karson J., and Iotti A. 2004. East African Rift System (EARS) plume structure: insights from Quaternary mafic lavas of Turkana, Kenya. Journal of Petrology 45, 1069–1088.

George R., Rogers N., and Kelly S. 1998. Earliest magmatism in Ethiopia: evidence for two mantle plumes in one flood basalt province. Geology 26, 923–926.

Govindaraju K. 1989. 1989. Compilation of working values and sample description for 272 geostandards. Geostandards Newsletter 13, 1–113.

Harris J.L., Carniel R., and Jones J. 2005. Identification of variable convective regimes at Erta' Ale Lava Lake. Journal of Volcanology and Geothermal Research 142, 207–223.

Hart W.K., WoldeGabriel G., Walter R.C., and Mertzmann S.A. 1989. Basaltic volcanism in Ethiopia: constraints on continental rifting and mantle interactions. Journal of Geophysical Research 94, 731–748.

Hart S. R., Hauri E. H., Oschmann L. A., and Whitehead J. A. 1992. Mantle plumes and entrainment: isotopic evidence. Science 256, 517–520.

Hayward N. and Ebinger C.J. 1996. Variations in the along-axis segmentation of the Afar Rift System. Tectonics 15, 244–257.

Hofmann A.W., Jochum K.P., Seufert M., and White W.M. 1986. Nb and Pb in oceanic basalts: new constraints on mantle evolution. Earth and Planetary Science Letters 79, 33–45.

Hofmann C., Courtillot V., Feraud G., Rochette P., Yirgu G., Ketefo E., and Pik R., 1997. Timing of the Ethiopian flood basalt event and implications for plume birth and global change. Nature 389, 838–841.

Jarosewich E., Clarke R.S.J., and Barrows J.N. 1987. The Allende meteorite reference sample. Smithsonian Contribution to Earth Sciences 27, 1–49.

Kieffer B., Arndt N., Lapierre H., Bastien F., Bosch D., Pecher A., Yirgu G., Ayalew D., Weis D., Jerram A.D., Keller F., and Meugniot C. 2004. Flood and Shield basalts from Ethiopia: magmas from the African superswell. Journal of Petrology 45, 793– 834.

Koeberl C. 1993. Instrumental neutron activation analysis of geochemical and cosmochemical samples: A fast and reliable method for small sample analysis. Journal of Radioanalytical and Nuclear Chemistry 168, 47–60.

Lahitte P., Gillet P.Y., and Courtillot V. 2003a. Silicic central volcanoes as precursor to rift propagation: the Afar case. Earth and Planetary Science Letters 207, 103–116.

Lahitte P., Gillot P., Kidane T., Courtillot V., and Bekele A. 2003b. New age constraints on the timing of volcanism in central Afar, in the presence of propagating rifts. Journal of Geophysical Research B, 108, ECV 10.1–10.17.

Le Bas M.L., Le Maitre R.W., Streckeisen A., and Zanettin B. 1986. A chemical classification of volcanic rocks based on the total alkali – silica diagram. Journal of Petrology 27, 745–750.

Le Guern F., Carbonelle J., and Tazieff H. 1979. Erta'Ale lava lake: heat and gas transfer to the atmosphere. Journal of Volcanology and Geothermal Research 6, 27–48.

Macdonald R., Rogers N. W., Fitton J. G., Black S., and Smith M. 2001. Plume-lithosphere interactions in thegeneration of the basalts of the Kenya Rift, East Africa. Journal of Petrology 42, 877–900.

Mader D. and Koeberl C. 2009. Using instrumental neutron activation analysis for geochemical analyses of terrestrial impact structures: Current analytical procedures at the University of Vienna Geochemistry activation analysis laboratory. Applied Radiation and Isotopes 67, 2100–2103.

Maguire P.K.H., Keller G.R., Klemperer S.L., MacKenzie G.D., Keranen K., Harder S., O'Reilly B., Thybo H., Asfaw L., Khan M.A., and Amha M. 2006. Crustal structure of the Northern Main Ethiopian Rift from the EAGLE controlled-source survey; a snapshot of incipient lithospheric breakup. In: Yirgu G., Ebinger C.J., and Maguire, P.K.H. (Eds.), The Afar Volcanic Province within the East African Rift System. Geological Society, London, Special Publication, 259, 269–292.

Makris J. and Ginzburg A. 1987. The Afar Depression; transition between continental rifting and sea-floor spreading. Tectonophysics 141, 199–214.

Pik R., Deniel C., Coulon C., Yirgu G., and Marty B. 1999. Isotopic and trace element signatures of Ethiopian flood basalts: Evidence for plume-lithosphere interactions. Geochimica Cosmochimica Acta 63, 2263–2279.

Rogers N.W. 2006. Basaltic magmatism and the geodynamics of the East African Rift System. In: Yirgu G., Ebinger C.J., and Maguire P.K.H. (Eds.), The Afar Volcanic Province within the East African Rift System. Geological Society, London, Special Publication 259, 77–93.

Rogers N., Macdonald R., Fitton J.G., George R., Smith M., and Barreiro B. 2000. Two mantle plumes beneath the East African rift system: Sr, Nd and Pb isotope evidence from Kenya Rift basalts. Earth and Planetary Science Letters 176, 387–400.

Rollinson H.R. 1993. Using Geochemical Data: Evaluation, Presentation, Interpretation. Longman, Essex, 352 pp.

Schilling J.G., Kingsley R.H., Hanan B.B., and McCully B.L. 1992. Nd–Sr–Pb isotopic variations along the Gulf of Aden; evidence for Afar mantle plume-continental lithosphere interaction. Journal of Geophysical Research 97, 10,927–10,966.

Son T.H. and Koeberl C. 2005. Chemical variations within fragments of Australasian tektites. Meteoritics and Planetary Sciences 40, 805–815.

Sun S. S. and McDonough W. F. 1989. Chemical and isotopic systematics of oceanic basalts: Implications for mantle composition and processes.. In: Saunders A. D. and Norry M. J. (Eds.), Magmatism in the Ocean Basins. Geological Society of London 42, 313–345.

Tefera M., Chernet T., and Haro W. 1996. Geological map of Ethiopia; scale 1:2,000,000. Ministry of Mines and Energy. Ethiopian Institute of Geological Surveys, Addis Ababa, Ethiopia.

Thurmond A.K., Abdelsalam M.G., and Thurmond J.B. 2006. Optical radar-DEM remote sensing data integration for geological mapping in the Afar Depression, Ethiopia. Journal of African Earth Sciences 44, 119–134.

Varet J. 1975. Geological map of Afar, Centre National de la Recherche Scientifique (CNRS), Paris.

Varet, J. and Gasse F. 1978. Geology of Central and Southern Afar (Ethiopia and Djibouti Republic). Editions de Centre National de la Recherche Scientifique Report, Paris, 124 pp.

Verma S.P., Torres-Alvarado I.S., and Sotelo-Rodriguez Z.T. 2002. SINCLAS: standard igneous norm and volcanic rock classification system. Computers and Geosciences 28, 711–715.

Vidal P., Deniel C., Vellutini P.J., Piguet P., Coulon C., Vincent J., and Audin J. 1991. Changes of mantle sources in the course of rift evolution: the Afar case. Geophysical Research Letters 18, 1913–1916.

Waltham T. 2005. Extension tectonics in the Afar Triangle. Geology Today 21, 101–107.

Wiart P. and Oppenheimer C. 2005. Large magnitude silicic volcanism in north Afar: the Nabro Volcanic Range and Ma-alalta volcano. Bulletin of Volcanology 67, 99–115.

Wolfenden E., Ebinger C., Yirgu G., Deino A., and Ayalew D. 2004. Evolution of the northern Main Ethiopian rift: birth of a triple junction. Earth and Planetary Science Letters 224, 213–228.

Yirgu G., Ebinger C.J., and Maguire P.K.H. (Eds.), 2006. The Afar Volcanic Province within the East African Rift System. Geological Society, London, Special Publication, 259, 1–6.

CHAPTER 8

CHAPTER 8: THE NORTHWESTERN AND AFAR DEPRESSION FLOOD BASALTS: FROM PLUME-HEAD– TO TAIL VOLCANISM

Abstract– The Afar mantle plume in the northeastern Africa is the sole plume structure beneath continental lithosphere that has been continually outpouring magmatic products to the surface for the last ~30 Ma. The first plume-driven basalts exhibit a wide range of geochemical and isotopic compositions that reflect heterogeneity in both source region and petrogenetic process. The dominant suites in the north-western Ethiopian plateau are the high-Ti and low-Ti basalts. Even after 30 Ma the Afar mantle plume is still active giving rise to the Afar Depression basalts in general and the Erta'Ale Range basalts in particular. The main aim in this chapter was to investigate and identify the geochemical characteristics of the plume head (high-Ti and low-Ti) and the plume tail (Erta'Ale range) basalts. The plume head basalts exhibit contrasting geochemical signatures with alkaline and incompatible element enriched high-Ti basalts at one end, and tholeiitic and incompatible element depleted low-Ti basalts at the other end. The plume tail (Erta'Ale Range) basalts, on the other hand, show transitional-tholeiitic in composition and contain significant concentrations of the highly incompatible trace elements. From both the geochemical and isotopic characteristics, the Quaternary Erta'Ale Range basalts are much alike with the Oligocene High-Ti (HT2) basalts. These two end members of the Afar mantle plume have high to very high contents of the highly incompatible trace elements (La, Nb, Ta, Th) and their isotopic composition ($^{87}Sr/^{86}Sr$; 0.7039–0.7040; $^{143}Nd/^{144}Nd$; 0.51288–0.51295). The HT2 and Erta'Ale basalts were derived from an ocean island basalt-like mantle component that corresponds to the initial and final material of the Afar mantle plume.

8.1 Introduction

Understanding the temporal and spatial distribution of magmatism and associated continental rifting provides vital constraints on the tectonic evolution of continental breakup (Audin et al., 2004). Continental flood volcanism (CFV) is often associated with rupturing of the earth's lithosphere. As continental breakup advances towards that of oceanic rifts, the geochemical characteristics of magmas generally evolve toward that of oceanic magmas, reflecting the increasing involvement of the depleted mantle (Pik et al., 1999). Although most continental flood basalt (CFB) provinces are entirely linked with deep-rooted hotspots or mantle plumes (Richards et al., 1989), the roles of depleted and lithospheric mantle and crustal components play significant role in the genesis of the plume-driven magmas (Pik et al., 1999).

These days, there is an agreement that deep mantle origin hot plumes are involved in producing CFB and other large igneous provinces, however, the eruption rates for the different magmatic provinces are apparently variable by orders of magnitude (Baker et al., 1996). The presence of variable eruption rates among the CFB provinces reveals either the involvement of more than one mantle plume sources or the influence of lithospheric structure and associated stress fields (i.e., the far-field or local stresses). According to Baker et al. (1996), the relatively slow drift of the Arabian plates (~16 mm/yr) relative to the stable African plate is a consequence of the slow rate of eruption of the Afro-Arabian volcanism. Moreover, the slow rates of eruption in this province may be responsible for the bimodal character of continental flood volcanism and the rather Oligocene–Present (long-lived) record of eruption in the Afar volcanic province (e.g., Baker et al., 1996; Yirgu et al., 2006).

Different models assume that the uprising of huge volume of hot mantle material to the asthenosphere–lithosphere boundary caused the lift of the Ethiopian dome, and subsequent magmatism and rifting (Beyene and Abdelsalam, 2005), which is a manifestation of active rifting processes in the region. Gass (1975) supposed that the northward movement of the African Plate stopped sometime in the Eocene (i.e., ~40 Ma) and the high heat flux concentrated on the same lithospheric target enabled the Afro-Arabian landmass bulge upwards. The concentrated heat flow beneath the present East Africa had provoked the production of voluminous chambers of magma in the upper mantle (Gass, 1975) and then followed by major phase of magmatism in the Eocene–Oligocene periods (Ebinger et al., 1993; Hofmann et al., 1997; George et al., 1998).

Initial phase of volcanism in the East African plateaus began in southwestern Ethiopia ~45 Ma (George et al., 1998), followed by widespread flood basalts and associated felsic lavas in central– to northern Ethiopia and Yemen at ~30–26 Ma (Baker et al., 1996; Hofmann et al., 1997; Pik et al., 1999). However, this spatial and temporal gap between the early phase of volcanism in southern Ethiopia and the flood basalt activity in northwestern Ethiopia raises an essential geodynamic debate concerning the volcano-tectonic evolution of the EARS (Furman et al., 2004).

To account for the volcano-tectonic evolution of the East African intra-continental rifting, the presence of a single channeled or two hot plumes has been applied in different models (Pik et al., 2006). Ebinger and Sleep (1998) explained that magmatism along the entire EARS is the result of a single hot mantle plume impact that triggered initial volcanism in southern Ethiopia during the late Eocene. After the first episode of magmatism, the mobile

mantle plume propagates north–south beneath the pre-existing lithospheric weaknesses, generated during Mesozoic and Tertiary (Rogers, 2006).

Other groups, (e.g., George et al., 1998; Rogers et al., 2000; George and Rogers, 2002) have recommended that two compositionally distinct mantle plumes are required to adequately explain the East African volcanism: one beneath the present Ethio-Afar dome and the other beneath the Kenya Plateau. In the two-mantle plume model, the Eocene basalts of southern Ethiopia are manifestations of the Kenya plume head volcanism and, as the African plate drifted northwards, succeeding magmatic episode are represented by increasingly younger activities more to south through Kenya, Uganda and into Tanzania (Corti, 2009, and references therein). Most of the Ethiopian CFB erupted during the late Oligocene (~30 Ma, during a short 1–2 My period) to form a thick (~2000 m) pile of volcanic plateau (Hofmann et al., 1997) followed by the rift-triggered Miocene–Recent magmatism in the Afar Depression.

Pliocene–Recent magmatism in the Ethiopian highland is very limited in space (e.g., Tana and Axum volcanics). Quaternary magmatism is largely confined to tectonic and magmatic segments within the embryonic seafloor spreading centers in Afar Depression, and axial zones of MER (Vidal et al. 1991; Boccaletti et al. 1998). Thus, the Ethio-Kenya volcanic province has experienced a complex and long episode of basaltic and felsic volcanism since the late Eocene, with the voluminous eruptions tied to the onset of the Afro-Arabian continental breakup and Red Sea oceanic spreading at ~30 and ~4 Ma, respectively, (e.g., Wolfenden et al., 2004; Yirgu et al., 2006). The region, therefore, records the complete sequence of volcano-tectonic activities from the plume head– to tail and from incipient intra-continental rifting to seafloor spreading.

The Ethiopian volcanic province is an exceptional area to study the evolution of volcanism during continental rifting, from plume head lavas (pre-rift CFBs) up to plume tail lavas or mid oceanic ridge basalts (Pik et al., 1998). From the previous works, we can realize that the Ethiopian flood basalts are evolved from two distinct sources: the ocean island basalt-type (OIB) and the depleted mantle sources (Pik et al., 1999); however, the nature and type of the Erta'Ale Range (Danakil Depression) basalts remained undiscovered. Here, we focus our attention on the geochemical characteristics of Oligocene magmatism of the northwestern Ethiopian Plateau and the Quaternary volcanism of the Erta'Ale Range. In this chapter, we will try to understand the progressive evolution of the Afar mantle plume, from its head– to tail.

8.2 Geological Background

The Ethio-Yemen CFV extends over a large area, spanning from northwestern Ethiopia through Eritrea and Djibouti to western Yemen (Fig. 8.1; Ukstine et al., 2002). The Ethiopian CFBs (high-Ti and low-Ti basalts; Pik et al., 1998, 1999) were associated with the evolution of the Red Sea and Gulf of Aden rifts in late Oligocene–early Miocene times (Féraud et al., 1991) and the Afar Depression volcanism with the initiation of sea floor spreading in both the Gulf of Aden (~16.5 Ma; D'Acremont et al., 2005) and the Red Sea (~5 Ma; Wolfenden et al., 2005). The magmatism of the Afar Depression and the associated Main Ethiopia rift, and volcanism of the northwestern Ethiopian flood basalts including the Yemenite series represent one of the well preserved continental igneous provinces currently active on Earth (Rogers et al., 2000).

The Ethiopian and Yemenite flood basalts are supposed to be the oldest volcanic markers of the Afro-Arabian continental breakup and are found on the western, northern, and northeastern topographic margins of the Afar Depression (Fig. 8.1). Before rifting along the Red Sea, these two CFB areas were a continuous magmatic province producing a volume of ~1–1.5 million km3 before erosion (Courtillot et al., 1999). More than 80 vol% of the CFB province crops out in Ethiopia, whereas the rest is located on the eastern side of the Red Sea, in Yemen and as small patches in Eritrea (Baker et al., 1996) (Fig. 8.1). This voluminous magmatic product (~350,000 km^3 after erosion) in the Ethiopian plateau, which forms a thick pile of ~2,000 m and covers ~600,000 km^2 (Mohr and Zanettin, 1988), was erupted 30 Ma ago, immediately after the initial crustal extension in the Gulf of Aden (D'Acremont et al., 2005) and prior to or contemporaneous with the Red Sea extension (Courtillot et al., 1987; Pik et al., 1998). Based on previously published $^{40}Ar/^{39}Ar$ data, the massive outpouring of lava was during the late Oligocene–early Miocene (~32–21 Ma) with most of the flood basalt activity occurring between 30 and 29.5 Ma (Hofmann et al., 1997), followed by the central Ethiopian shield volcanic episode from 23 to 10 Ma (Kieffer et al., 2004) and a period of rift triggered volcanic activities associated with the seafloor spreading in the southern Red Sea from 3.5 Ma to present (Choukroune et al., 1988; Courtillot et al., 1984).

In the highly evolved magmatic segments, Afar Depression and the Main Ethiopian rift, Pliocene–Quaternary volcanism is concentrated along the active rift axes either as fissural eruption (the Afar Stratoid series) or, more frequently, as central vent-type eruptions (the Erta'Ale shield volcanoes). The Afar Stratoid series, which is predominantly of trap-like basaltic lava, constitutes about two-thirds of the Afar Depression and has been dated at 3.5 to

0.6 Ma (Lahitte et al., 2003). In Afar, volcanism of the last 4 Ma has been bimodal, but with basic rocks predominating over acidic lavas and pyroclastic products (Lahitte et al., 2003). About 80% of the volcanic products of Afar Depression are transitional–tholeiitic basalts; whereas the remaining 20% constitutes felsic lavas and pyroclastic materials of the same composition (Barberi and Santacroce, 1999). Towards the center of the depression, the Afar Stratoid series is overlain by the Quaternary age axial range basalts called the 'Aden Series' (Lahitte et al., 2003). This volcanism is mainly confined to the active tectonic segments of the Afar Depression (Vidal et al., 1991; Schilling et al., 1992; Boccaletti et al., 1998). They are mainly composed of transitional–tholeiitic basalt flows and shields built along the Erta'Ale Range (Tefera et al., 1996).
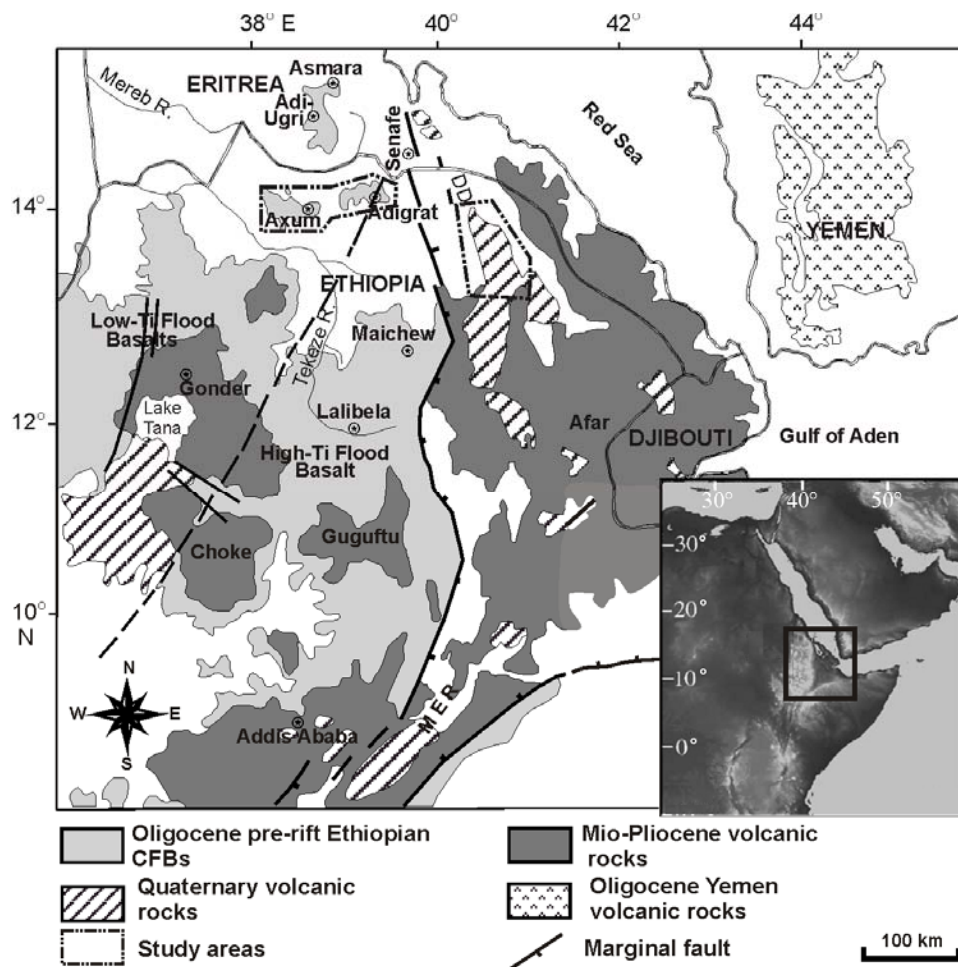
Figure 8.1 Simplified volcanic map of the central, northwestern and northern parts of the Ethiopian plateau and the Afar Depression with boxes showing the location maps of the study areas (Axum and Danakil Depression). The dividing line between high-Ti and low-Ti basalt province is marked by a dashed line (modified from Merla et al., 1979 and Pik et al., 1998). Inset map is from Beyene and Abdelsalam, 2005.

8.3   Major Volcanic Phases in the Northwestern Ethiopia and Afar Depression

The Ethiopian CFV is presumed to be associated with the Afar hot mantle plume and comprises voluminous sub-aerial alkaline–tholeiitic basalts and significant amount of felsic lavas and pyroclastic products at the upper eruptive levels (Ayalew et al., 2002). The late Oligocene to present magmatism of Ethio-Afar volcanic province covers an area in excess of 1,000,000 km^2 (Peccerillo et al., 2007). The oldest flood basalts are found in the northwestern Ethiopian highland and erupted 30 Ma ago, during a short 1 Ma period, to form a thick and vast volcanic plateau (Hofmann et al., 1997). Although the basalts were erupted in a short period and confined space, compositionally they were heterogeneous. Mohr (1983) constructed for the first time a general volcanic stratigraphy for the north and northwestern Ethiopian volcanic rocks based on type localities, and then extrapolated these formations to other volcanic rocks of the region. According to these and other authors, the Ethiopian CFV is classified from bottom to top as: Ashange, Aiba, Alage, and Tarmaber formations. However, this strato-type classification was with some limitations. First, it did not concentrate on the spatial control on the compositional framework of the province; and secondly, it could not represent the whole portion of the Ethiopian volcanic province. Pik et al. (1998, 1999), however, divided the northwestern Ethiopian flood basalts into three types on the basis of Ti and incompatible element concentrations. These authors recognized groups of 'high-Ti' basalts (HT1 and HT2) and 'low-Ti' basalts (LT).

Shortly after the peak of the northwestern Ethiopian flood basalt activity, a number of central volcanoes were emplaced on the surface of the flood basalts between 22 and 10 Ma (Kieffer et al., 2004). These central/shield volcanoes erupted sporadically and cover large period of time from the late Oligocene to the late Miocene and in some places to the Pliocene. The geochemical characteristics of these shield basalts are entirely related with the underlying flood basalts. The composition of the northwestern shield basalts and underlying LT basalts is characterized by subalkaline or slightly alkaline lavas (Kieffer et al., 2004). In the central part, the Choke and Guguftu shield volcanoes overlying the HT basalts are alkaline in composition. Younger shield volcanoes aged between 20 and 3 Ma are reported at both the northern and southern margins of the province (Zanettin, 1992; Ukstins et al., 2002).

The Afar Depression magmatic activities began shortly after eruption of the Ethiopian flood basalts contemporaneous with most of the older shield basalts of the plateau. The earliest magmatic series in Afar, the Adolei basalts, erupted during the late Oligocene–early Miocene, from 27–19 Ma, (Barberi et al., 1975; Deniel et al., 1994; Audin et al., 2004) and

outcrops in restricted areas, east of the Afar Depression (Lahitte et al., 2003). In the Afar Depression, there was a time of non-deposition from 19–16 Ma or if any covered by the massive Stratoid series. After 3–4 My of non-deposition, the Mabla series, which outcrop only on the margins of the Ali Sabieh and Danakil Microplates, erupted from 16 to 9 Ma (Varet, 1975). The sporadic and low rate of volcanism ended with the eruption of the Dahla series between ~8 and ~6 Ma (Lahitte et al., 2003). All the above mentioned formations constitute only small portion in the depression and outcrop only in a restricted area on the northeastern and southeastern margins of the Afar Depression (Lahitte et al., 2003) and are not the major volcanic out crops in the region.

The widely exposed volcanic formation in Afar Depression, both in aerial coverage and volume, is the 1– to 2-km-thick fissure-fed lavas called the 'basaltic Stratoid series'. This series covers more than 2/3 of the Afar floor and partly overlies the Adolie and Mabla volcanic series on the western side of the Ali Sabieh block (Audin et al., 2004). The Afar Stratoid series, erupted during the oceanization of the southern Red Sea, consist of a series of fissure basaltic flows but are overlain by Quaternary fissural basalts and shield volcanoes of the axial range (Lahitte et al., 2003). The Afar Stratoid series has been dated for the first time using the conventional K-Ar technique and ages between 4.4 and 0.4 Ma (Barberi et al., 1975). In subsequent investigations, Courtillot et al. (1984) proposed a younger age and narrower range, 2.3–1.4 Ma, for the main phase of eruption of the series, whereas according to Choukroune et al. (1988) these series were emplaced from 3.5 to 1.3 Ma and was contemporaneous with the Tadjoura series that corresponds with the onset of onland propagation of the Gulf of Aden through Gulf of Tadjoura (Zumbo et al., 1995).

The Afar Depression is still a site of different young and active volcanoes. Most of the recent lavas, Aden series, are confined in the active axial fault belts of the depression (e.g., Erta'Ale Range, Tendaho-Manda Hararo graben, Manda Inakir, Asal rift, and the Wonji Fault Belt (WFB). Particularly at the northern part, the Danakil Depression, volcanic activities are quite young (e.g., September 2005 and November 2008 volcanic eruptions) and is the sole place in EARS where extremely fresh basalts and long-lived lava lake exist. Paleomagnetic and conventional K-Ar data indicate that nearly all Aden series lavas are younger than 0.7 Ma (Courtillot et al., 1984). The complete sequence of the major phases of eruption in the Ethiopian plateau and Afar Depression are compiled in the form of a Table and composite sections (Table 8.1, Fig. 8.2).

Table 8:1. Summary of the volcanic rocks of north-western Ethiopian flood basalts and Afar Depression.

Age range	Group name	Basalt type	Description	Chemical characteristics
Quaternary 700 Ka - Present	Aden series (Axial range)	Axial zone	Such volcanic series are found along the axial ranges of actively expanding rift system, Afar Depression and MER.	Transitional – tholeiitic basalt
Pliocene-Pleistocene 3.5 – 1.25 Ma	Stratoid series	Axial zone	Fissure –fed, mainly basaltic, volcanic sequence that covers the entire floor of Afar Depression.	Transitional - tholeiitic
Miocene-Pliocene 7 – 4 Ma	Axum post-trap basalt	Continental	Pliocene age post-trap basalt; mainly found around Axum town.	Alkali – mildly alkali basalt
Miocene 16 – 6 Ma	Dahla seires Mabla series	Rift Rift	Confined to the northeast and southeast portion of the Afar Depression, in the Republic of Djibouti.	
Oligocene-Miocene 10.8 Ma 18.7 Ma 22.4 Ma 23.3 Ma 27 – 20 Ma	Guna shield Semien shield Choke shield Guguftu shield Adolei series	Continental Continental Continental Continental Rift	Alkali volcanics erupted from dispersed sites such as the late veneer on the Simien shield and the entire Guna shield The oldest rift basalts and mainly associated with the breakup of the Depression.	Alkali – mildly alkali basalt
Oligocene 31 – 29 Ma	Low-Ti High-Ti	Continental Continental	The first appearance of volcanism in the northwestern Ethiopian plateau. Both the LT and HT flood basalts are temporally undifferentiated but spatially controlled	High-Al_2O_3 tholeiitic basalt Alkaline to mildly alkaline low in Al_2O_3

Age ranges are from Varet (1975); Courtillot et al. (1984); Choukroune et al. (1988); Hofmann et al. (1997); Lahitte et al. (2003); Audin et al. (2004); Kieffer et al. (2004).
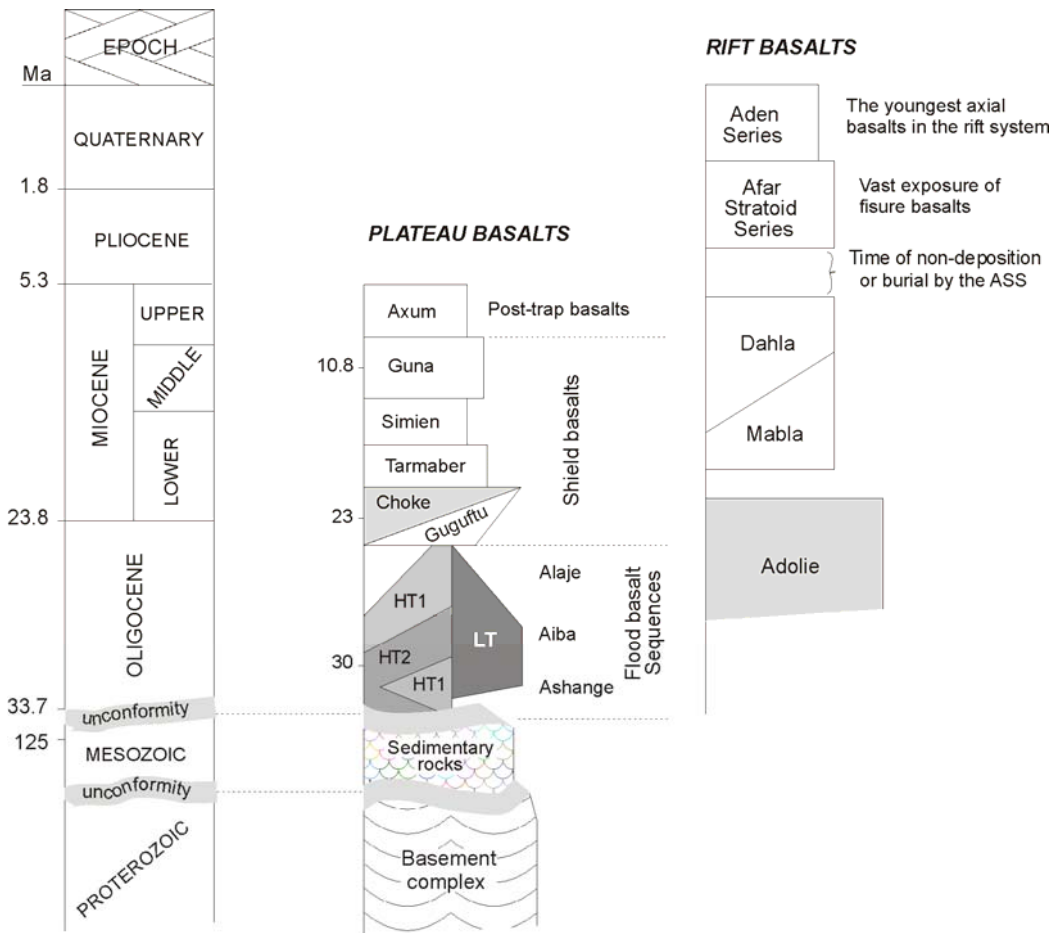
Figure 8.2 Column sections of the northwestern Ethiopian plateau and Afar Depression basalts. Age data for all the basalts are from (Hofmann et al., 1997; Lahitte et al., 2003; Kieffer et al., 2004).

8.4 Geochemical Characteristics of the Plateau and Rift Basalts

It is now universally accepted that there is a strong relationship between CFB volcanism and continental breakup (Coulie et al., 2003). Behind all CFB volcanism and the associated continental rifting, there is a driving force called mantle plume, which normally originate at the core-mantle boundary and rises upwards. The Ethio-Afar mantle plume, in this case, is the most active geologic phenomenon beneath the east African plate that continuously jars huge volume of lava to the surface. All available geological and geophysical data from the Ethio-Afar volcanic province provide concrete evidence for the east African rift initiation above a single or two mantle plumes. However, a controversy exists concerning the depth, extent, location and continuity of the hot asthenospheric material with the deep mantle anomaly beneath east Africa (Yirgu et al., 2006). A number of models were applied to synthesize a coherent outlook for the Ethio-Afar volcanic province. One of the widely accepted models is the 'Two mantle plume' model beneath the East African Rift System

211

proposed first by George et al. (1998) and later refined by Rogers et al. (2000). Recent geochemical and geophysical data from the east African volcano-tectonic province provide evidence for the occurrence of two active mantle plumes beneath the EARS: the Afar hot mantle plume beneath the Ethiopia dome and the Kenyan plume at present positioned beneath Lake Victoria (George et al., 1998). However, the idea of the two mantle plume model in the East African Rift was critically questioned by Ebinger and Sleep (1998). According to these authors, magmatism throughout the east– to central Africa could be related to a channeled single plume that initiated the oldest basaltic volcanism in southern Ethiopia at ~45 Ma. The main intent of this chapter is not to verify whether the two mantle plume model works or not, instead is aiming to characterize the geochemical modification of the well known plume, the Afar mantle plume, as volcanism progressed from the plume-head, northwestern Ethiopian flood basalts, to the plume-tail, the Quaternary Afar Depression basalts.

The northwestern Ethiopian volcanic province including the Afar Depression is a site of active volcanism and tectonism spanning in time from the late Oligocene (about 30 Ma) to present. Magmatic activities have continuously poured lavas to the surface for the last 30 My with a major shift from plateau to rift floor basalts (Table 8.1). Concurrent with the Ethiopian flood basalts, the Arabian plate splits up from Africa forming the Red Sea–Gulf of Aden rift system, centered in the Afar region. The Afar triple junction is, therefore, a classic example to study the complete process of the mantle plume dynamics from its incipient to almost a complete oceanization stage (the Red Sea and Gulf of Aden). Throughout the history of the Afar plume, magmatism has been highly diversified specially at the onset of the Ethiopian flood basalts, alkaline–tholeiitic, and gradually shifted to a less diversified transitional–tholeiitic rift basalts.

8.4.1 Major Elements

The northwestern flood basalts, named as low-Ti (LT) and high-Ti (HT2 and HT1) basalts (Pik et al., 1998, 1999), are markers of the first appearance of the Ethio-Afar mantle plume head to the surface, and erupted approximately at ~30 Ma, over a period of 1 My or less (Hofmann et al., 1997). In previous works, the type composite sections of the Ethiopian CFB province were described differently as: Ashangi, Aiba, Alaji and Termaber formations (Mohr 1983, Berhe et al., 1987). However, such classifications were much localized and could not represent the whole portion of the northwestern Ethiopian flood basalts.

The northwestern Ethiopian plateau basalts have erupted lavas over a wide compositional spectrum ranging from pure basalts to basanites. From the total alkalis-silica

(TAS) classification diagram (Fig. 8.3) it is apparent that the Ethiopian plateau basalts comprise a variety of basaltic rock types (i.e., basanite, basalt, trachy-basalt, basaltic andesite, and basaltic trachy-andesite) spanning the alkaline-subalkaline fields. All the LT and some HT2 basalts plot in the tholeiitic field, whereas most HT1 and some HT2 basalts display a stronger alkaline affinity. However, the major distinction occurs in the contents of TiO_2, Al_2O_3, and Fe_2O_3. The LT lavas display the lowest TiO_2 contents (1–2.6 wt%) and correspond to the low-Ti magma group, commonly described in CFB provinces. In contrast, the other two lava groups display much higher TiO_2 (2.5–4.2 wt% TiO_2, HT1; 2.6–5 TiO_2 wt%, HT2) and Fe_2O_3 contents. Although both the HT2 and HT1 basalts have more or less the same characteristics in the major element contents, they show paradoxes in the contents of Al_2O_3 and CaO (Fig. 8.4b and d). The HT2 and HT1 basalts have the lowest contents of Al_2O_3 and CaO, respectively.

For the last 30 My or more, since the Oligocene to Present, the Afar mantle plume has been directly or indirectly, the driving force for all the volcanic activities in the region. The Afar Depression volcanics, particularly the Erta'Ale Range lavas, evolved from the last phase of the Afar mantle plume, is one of the best examples in the region that presents an excellent opportunity to investigate the geochemistry of the mantle plume tail. Somewhat different models have been formulated about the magmatism of the Afar Depression. However, most of the authors agreed that Afar Depression is underlain by a thinned continental crust receiving its lavas from an OIB-like source beneath the depression.

All rocks from the Danakil Depression have compositions that plot, with one or two exceptions, in the transitional–subalkaline field. In the TAS classification of Le Bas et al. (1986), the rocks belong to basalts, basaltic andesites, and andesites. The Danakil Depression volcanic rocks show a range of SiO_2 contents from 46.5 to 63.5 wt%, although they are dominantly basaltic (46.5–51.0 SiO_2 wt%) and well clustered in the transitional–tholeiitic fields (Fig. 8.3). Variations in the content of major element oxides among the depression basalts and within their counter flood basalts are seen in the bivariate plots of TiO_2, Al_2O_3, Fe_2O_3, CaO, K_2O, and P_2O_5 vs. SiO_2 (Fig. 8.4). All the basalts, those from the Dalaffilla and Erta'Ale shield volcanoes, have lower TiO_2 (<2.6 wt%) and Fe_2O_3 (<12.0 wt%) contents. In contrast, the off-axis shield volcanoes, AleBagu and Afdera for example, have moderately high and high TiO_2 contents (3.27 and 3.91 wt%, respectively) and relatively high Co and Zn (not plotted) compared with the along-axis shield volcanoes, Dalaffilla and Erta'Ale shield basalts. Moreover, the AleBagu and Afdera volcanoes have distinct major and trace element characteristics.
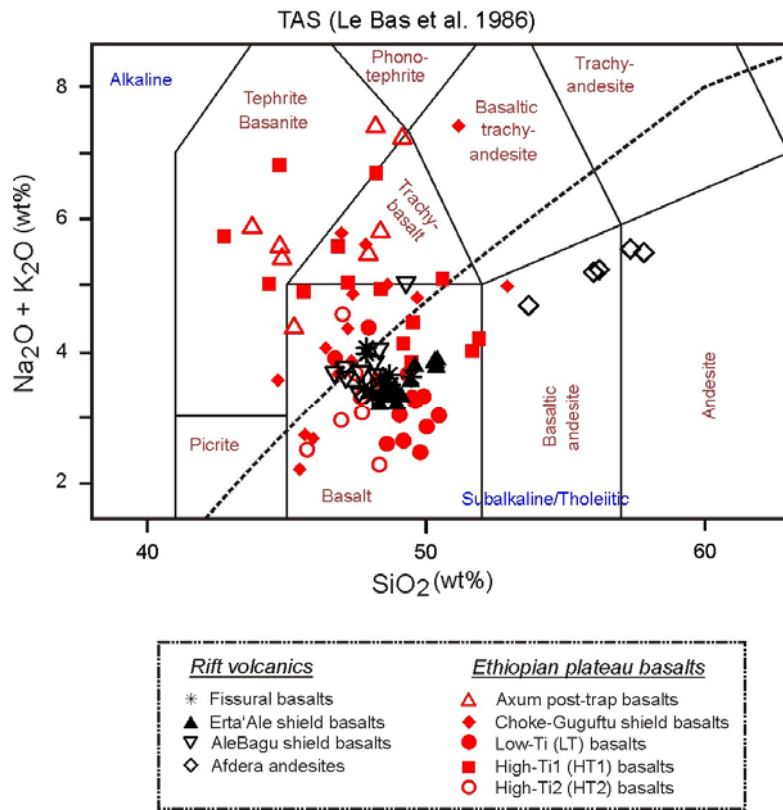
Figure 8.3   Total alkali-silica diagram (Le Bas et al., 1986) showing a wide distribution of basaltic rocks from Oligocene – Holocene. All samples of the rift volcanics and Axum basalts are from this study and remaining samples are presented by Pik et al. (1998), and Kieffer et al. (2004).
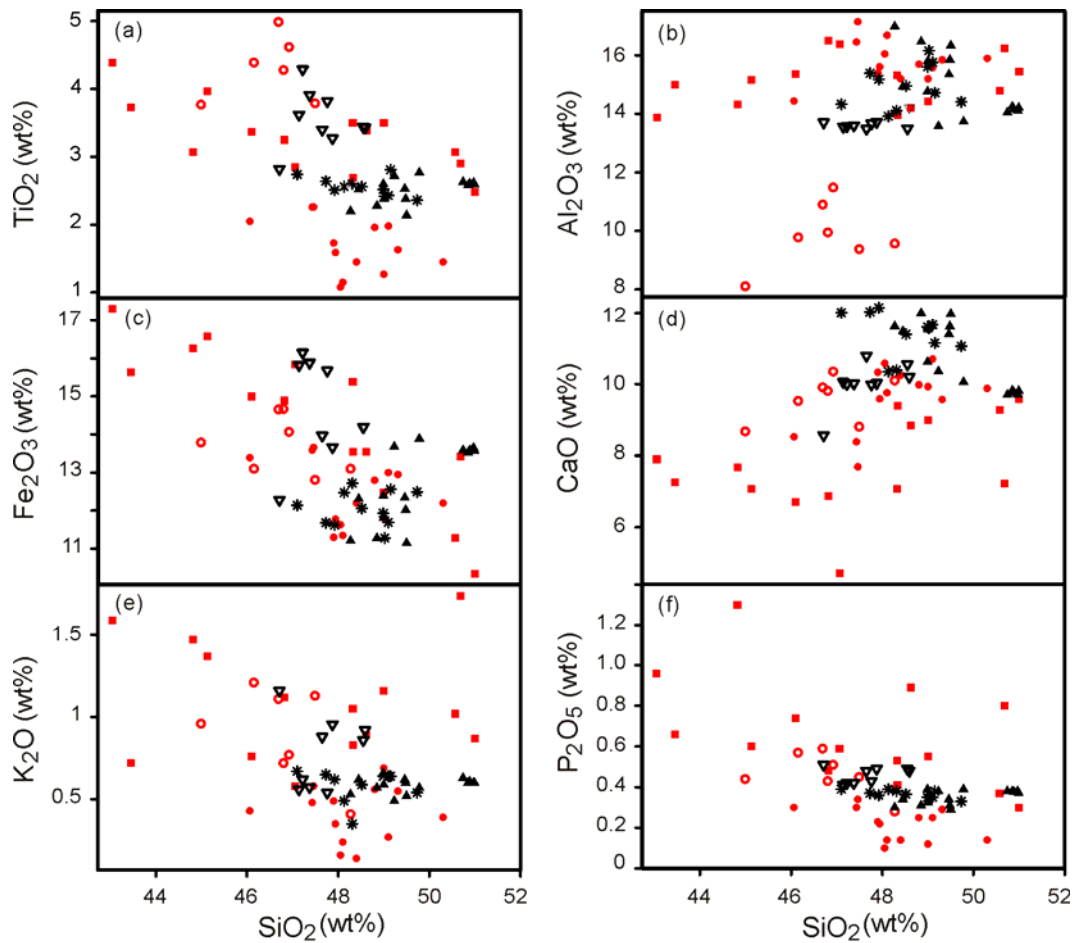
Figure 8.4 Harker variation diagrams for the northwestern Ethiopian flood and Danakil Depression basalts. Geochemical data are compiled from this study, Pik et al., 1998 and Kieffer et al., 2004. All the major oxides are characterized by their unique trend as SiO_2 progress from 43–51 wt%. Symbols as in Figure 8.3.

8.4.2 Trace Elements

The proximity of the Ethiopian volcanic province to the Afar mantle plume and the evolution of the Gulf of Aden–Red Sea–Main Ethiopian Rift in a radiating manner above the Ethiopian dome provide all rounded opportunity to study the evolution of a plume-driven igneous province from the early continental breakup to the embryonic seafloor spreading occurred in Afar Depression (George et al., 1998). Through the entire evolution of the Afar Depression, magmatic products show a stronger heterogeneity in their trace element contents than the variation in their major element contents. Though, the LT and HT magma types of the region were contemporaneously erupted at about 30 Ma, they show a wide range in trace element contents. The LT suite displays the lowest incompatible trace element contents. The strong contrast between the depleted LT basalts and the highly enriched HT2 lavas is well illustrated in the binary plots (Fig. 8.5). The LT basalts, having a tholeiitic tendency, exhibit the lowest contents of the highly incompatible elements (e.g., Nb, La, Nb, Hf, Ta, Th). In contrast, the

HT2 and HT1 lavas display higher contents of the incompatible trace elements. This contrasting geochemical characteristic between the LT and HT basalts from the Afar plume head represents the involvement of two or more magmatic sources (Pik et al., 1999).
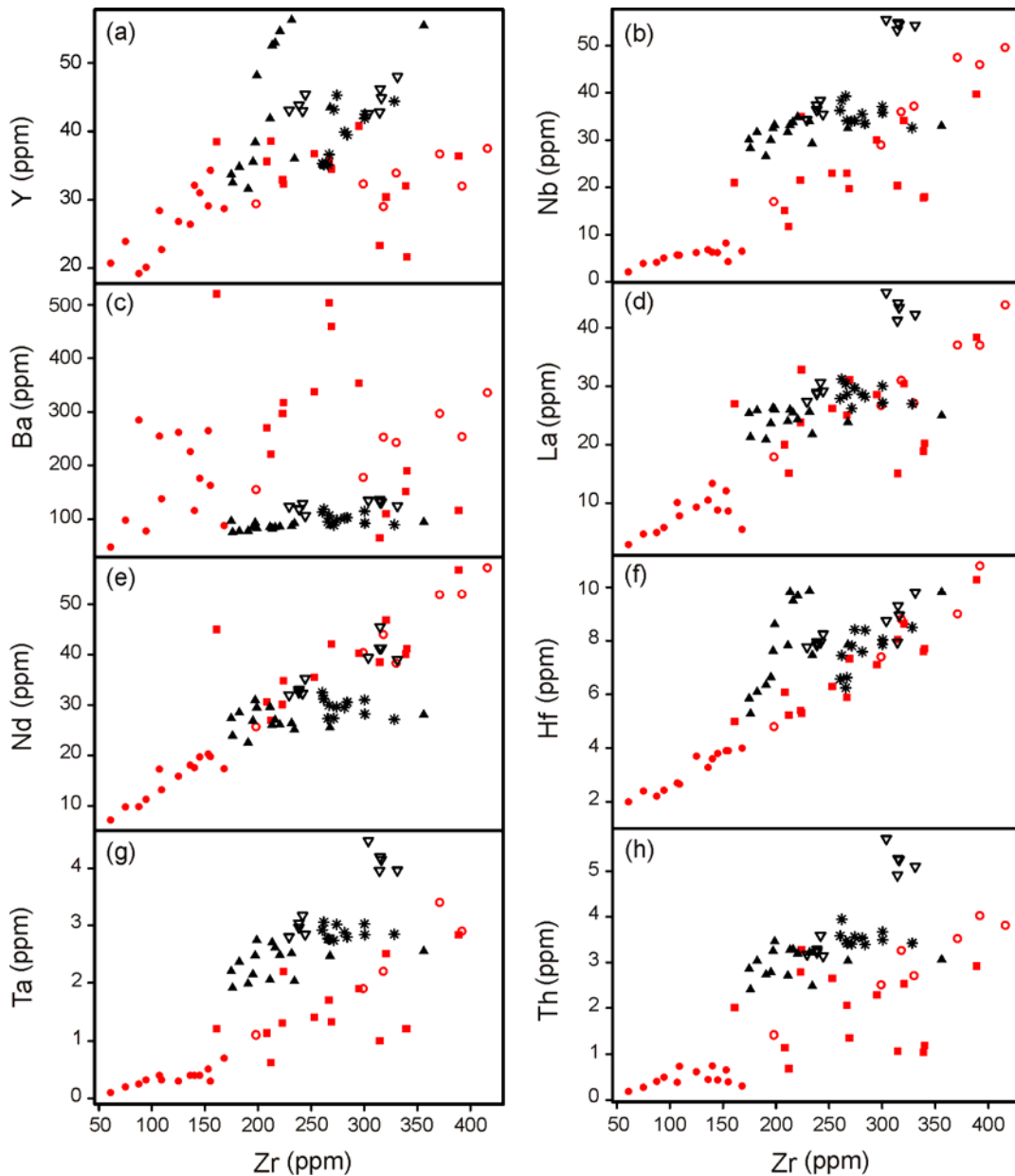
Figure 8.5 Plots of selected trace elements (ppm) against Zr (ppm) for the northwestern Ethiopian flood and Danakil Depression basalts. The binary plots of the contents of Y, Nb, Ba, La, Nd, Hf, Ta, and Th versus Zr illustrate the compositional variation among the several volcanic suites of the region. Trace element data for the HT2, HT1, and LT basalts are compiled from Pik et al. (1999), and Kieffer et al. (2004). Symbols as in Figure 8.3.

Like the plateau basalts, the northern Afar Depression (Danakil Depression) basaltic lavas show a wide variation in incompatible trace element abundances. Abundances of the highly incompatible elements (Th, Ta, and Nb) and light REE (La, Ce, and Nd) greatly vary from one shield basalt to another when plotted against Zr (Fig. 8.5). The AleBagu shield

basalts have the highest degree of incompatible trace element enrichment, whereas the Erta'Ale shield basalts show the least. The AleBagu basalts have the highly incompatible element contents at a level about twice of those of the Erta'Ale shield basalts. However, the primitive mantle-normalized trace element patterns for all the Danakil Depression basalts are somewhat similar to each other. Primitive mantle-normalized incompatible trace element diagrams show generally consistent behavior throughout the Danakil Depression, but few elements show substantial negative anomalies.

8.5   Comparison between the Plume-head and Plume-tail Basalts

The earth's surface has experienced finitely many plume-driven volcanic activities; however, quite few of them are currently recognized as continental flood basalts and most others are either recycled under the subduction zones or altered and transformed to other solid state. The only continental flood basalt on the globe/worldwide that records the complete episode of volcanism starting from the plume head to the plume tail is the Ethiopian flood basalt province. This province, therefore, offers the unique opportunity for studying the plume-dynamics from the early stages of continental breakup to continental drift and seafloor spreading.

Large portion of the northwestern Ethiopian plateau was covered by the ~30 Ma (Hofmann et al., 1997) mantle plume driven flood basalts. At the incipient of volcanism, the basaltic lavas of the region had three major compositional makeups (Pik et al., 1998, 1999): the high-Ti, alkaline to mildly alkaline basalts (HT2); the low-Ti, tholeiitic basalts (LT), and the third group (HT1) is somehow intermediate between the two. After the end of Oligocene, volcanic activities did not proceed at the same rate and style as the major phase of volcanism (i.e., 31–29 Ma), instead magmatism was so sporadic with the main change in space from plateau to rift floor. The genesis of all magmatic rocks erupted during this transition period (~26–4 Ma) is highly complicated. It is, therefore, after ~26 My that the continental flood basalt type magmatism (Afar Stratoid and Aden Series) poured into the floor of the Afar Depression. The mantle plume signature is much enhanced with the eruption of the Stratoid and Aden series. In the comparison of the plume head and plume tail magmatism, the geochemical data were collected only from the Ethiopian flood basalts (LT and HT) and Aden basalt series (Danakil Depression). All other basalts are excluded from this discussion because of the very reason that they are not markers of the two end members of the mantle

plume. For simplicity of the discussion, all the Danakil Depression basalts are named as 'Erta'Ale basalts' throughout the discussion.

All available geochemical data (trace element data and the Sr–Nd isotope ratios) suggest that two or more petrogenetic processes have been involved for the generation of the above mentioned basalt groups. In the first place, the northwestern Ethiopian flood basalts are categorized into two (LT and HT). On the other hand, the Erta'Ale basalts belong to one group. They all are well illustrated by plotting the ratios of most sensitive incompatible trace elements against Zr, La, and La/Nb (Fig. 8.6).

The progressively decreasing CaO/Al_2O_3 values from the HT2 through Erta'Ale to LT basalts show clinopyroxene was continually fractionating from the LT lavas; while plagioclase becomes steadily more important (Fig. 8.6a). The Ethio-Afar basalt groups (LT, HT1, HT2, and Erta'Ale) are identified clearly in the Ba/La vs. La diagram and define a general decreasing trend from LT to Erta'Ale basalt compositions (Fig. 8.6b). The Ba/La value of the LT basalts points towards the values of continental crust and subduction zone lavas; whereas the Ba/La values of the HT2 and Erta'Ale lavas overlap the field of OIB-basalts. The Zr/Nb ratios in volcanic rocks are good indicators of crustal assimilation or variation in degree of partial melting (Wilson et al., 1995; Kamber and Collerson, 2000). The distinct increase in the Zr/Nb ratio for the LT basalts (Fig. 8.6c) reflects crustal and/or depleted mantle involvements. The content of Zr in the LT basalts is low (~1/2 of that of HT2) but Nb is radically dropped by a factor of 1/3 from the Nb content of the HT2 and Erta'Ale basalts, and for this reason, the value of the Zr/Nb ratio escalated to maximum. Nb is more perceptive to variations in degrees of partial melting than Zr, and hence can be used to constrain the influence of variable degrees of melting (Kamber and Collerson, 2000).

Constancy of the highly incompatible trace element ratios among various basaltic suites (Zr/Nb, Nb/La, Nb/Y La/Nb, Ba/Nb; Fig. 8.6c, d, e, and f) is often cited as strong evidence for the source region and other petrogenetic processes. The La/Nb and Ba/Nb values measured from both the HT2 and Erta'Ale basalts are very low (Fig. 8.6f). Low La/Nb and Ba/Nb values are also observed among the younger post-rift basalts from southern Ethiopia and Pik et al. (1999) inferred such low values as mantle plume-derived melts (Furman et al., 2004). The LT basalts instead have higher values of Ba/Nb and La/Nb ratios, and this is not because of the radical enrichment in the contents of Ba and La, instead, it is most probably because of the drastic drop in the content of Nb (Fig. 8.5b, c and d, and Fig. 8.6f). Most of the LT basalts have been thought to be a subcontinental lithospheric mantle derived melts, and

their Nb content is often modified by fluids and sediments in subduction zones (Pik et al., 1999, and references therein).

The trace element and isotopic signatures of the HT (HT2 and HT1), LT, and Erta'Ale basalts indicate that more than one source components have been involved in their petrogenesis (Fig. 8.7). The HT2 lavas exhibit Sr–Nd isotopic compositions (^{87}Sr/^{86}Sr = 0.7040; ^{143}Nd/^{144}Nd = 0.51295) close to the average value of OIBs (Pik et al., 1999). Therefore, the HT2 basalts of the northwestern plateau are the sole volcanic suite in the Ethiopian volcanic province that represents the geochemical signature of the Afar mantle plume head composition. The LT basalts, on the other hand, exhibit Sr–Nd isotopic compositions (^{87}Sr/^{86}Sr = 0.70343; ^{143}Nd/^{144}Nd = 0.51288) close to the ranges of depleted source components. Even though, the involvement of both OIB- and DM-type lavas in a temporally and spatially restricted region needs further analyses, the involvement of depleted mantle and lithospheric crust components is important to consider for the less radiogenic Sr values of most of the LT and some HT1 basalts of the province (Fig. 8.7b; Pik et al., 1999).

The isotopic composition ranges observed among the Erta'Ale /Danakil Depression basalts (^{87}Sr/^{86}Sr 0.7036–0.7041 and ^{143}Nd/^{144}Nd 0.51286–0.51289) is equivalent to the common source values for most hot mantle plume-derived lavas (Furman et al., 2004). Figure 7a illustrates the Nd and Sr isotope composition of basalts from the Erta'Ale and Ethiopian flood basalts (HT2, HT1, and LT); the range of Red Sea/Gulf of Aden spreading centers and Kenyan rift basalts are taken for comparison. Basalts from the Erta'Ale have slightly lower ^{143}Nd/^{144}Nd and ^{87}Sr/^{86}Sr ratios than the HT2 basalts, but still in the same range. However, the Sr isotopic composition of the Erta'Ale basalts is higher than the values of LT basalts and is much closer to the plume range.
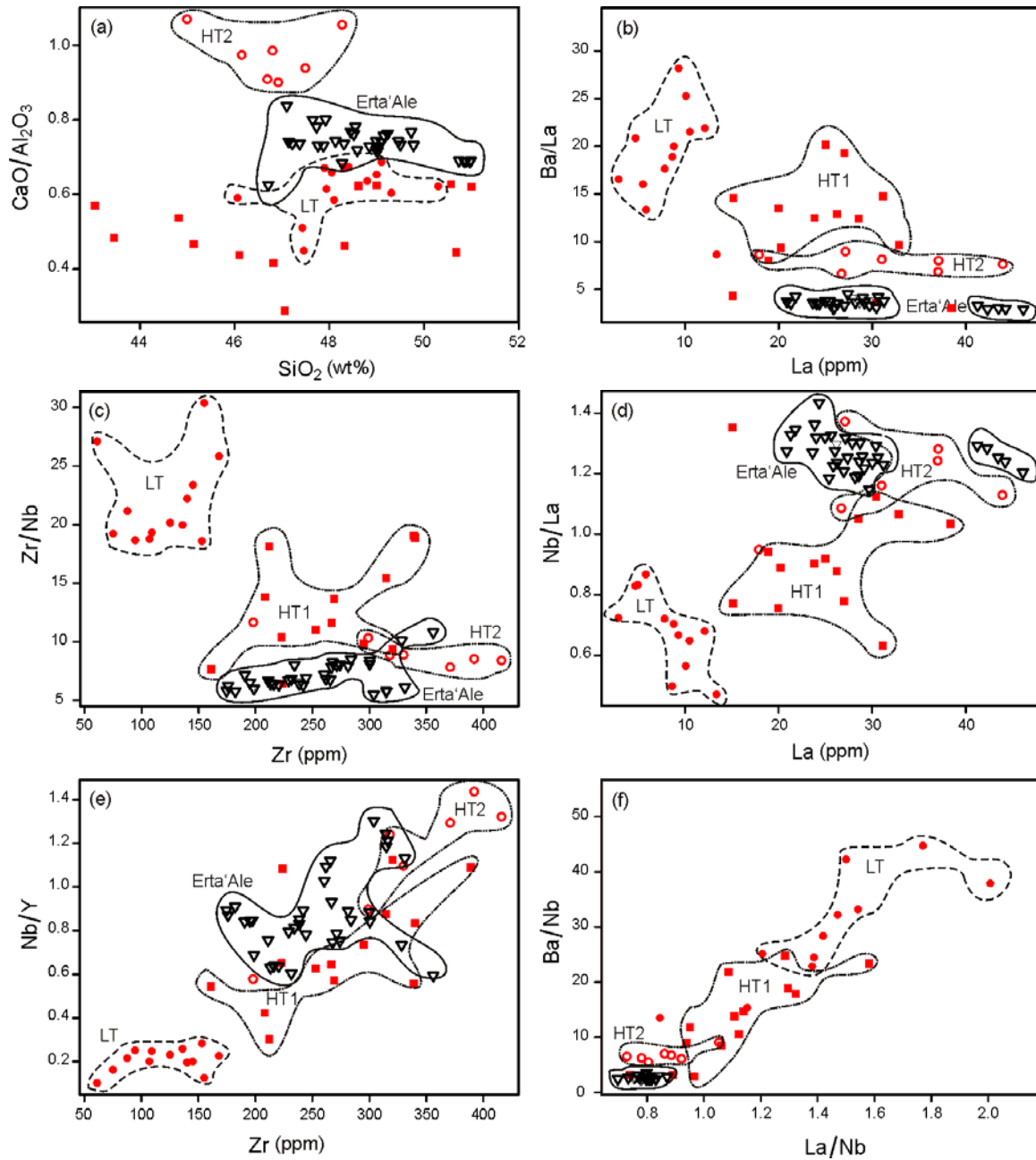
Figure 8.6 Binary plots of major element and trace element ratios comparing the Danakil Depression basalts with the northwestern Ethiopian flood basalts (HT and LT); (a) ration of major oxides vs. SiO_2 (wt %); (b - f) ratios of the highly incompatible trace elements (La, Nb, Ba) vs. La, Zr, and La/Nb ratio.
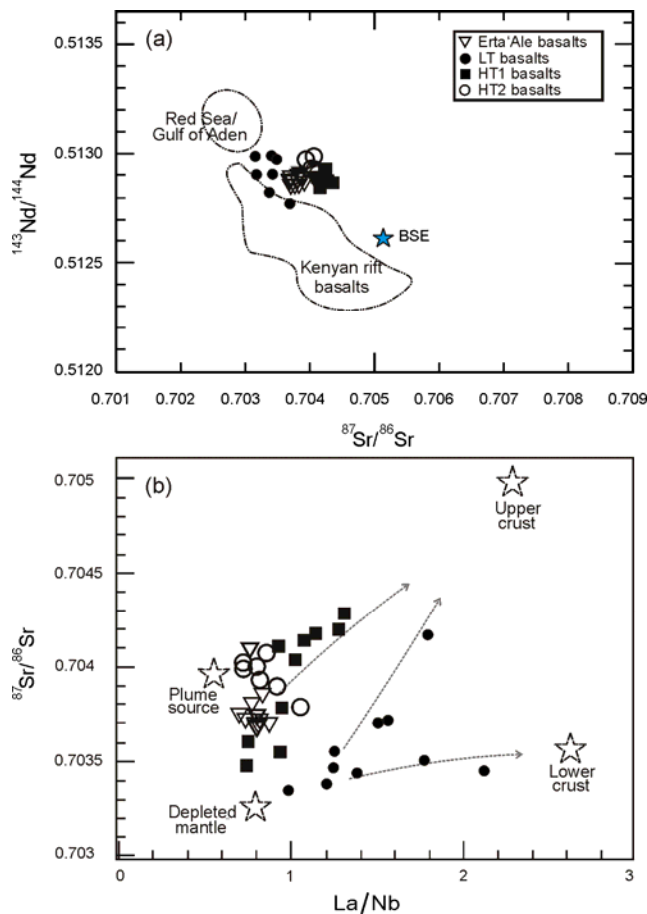
Striking differences in the compositional setup of the Ethio-Afar basalts is well observed in the $^{87}Sr/^{86}Sr$ vs. La/Nb diagram (Fig. 8.7b). All the HT2 and Erta'Ale basalts plot in the same region close to the mantle plume sources; whereas all the LT basalts have a depleted mantle source affinity but show two arrays that indicate strong involvement of the lower and upper crust components (Pik et al., 1999). The HT1 basalts, on the other hand, have still a mantle plume-derived melt tendency but with moderate involvement with the depleted mantle and upper crust components (Fig. 8.7).

Figure 8.7 (a) Isotopic compositions of the north-western Ethiopian plateau and Danakil Depression basalts. The Isotopic range of the Red Sea/Gulf of Aden and Kenyan rift data are from Eissen et al. (1989), Schilling et al. (1992), and Roger (2006). (b) $^{87}Sr/^{86}Sr$ vs. La/Nb diagram for the northwestern Ethiopian plateau and Danakil Depression basalts. Broken arrows show the assimilation of Plume and depleted mantle derived magmas with the upper and lower crust. HT2, HT1, and LT data are from Pik et al. (1999) and Kieffer et al. (2004).

8.6   Conclusions

The pre– to post-rift mafic lavas from the Ethio-Afar region provide a complete evolutionary history of the Afar mantle plume dynamics. The Afar volcanic products display a wide range in major element concentrations as well as incompatible trace element abundances, which were thought to be the result of variations in source composition, depth and melting conditions. At the first manifestation of the plume-driven volcanism in the Ethio-Afar volcanic province, magmatic products have two contrasting geochemical signature: the HT2 basalts, which are signs of uncontaminated, deep but low degree of melting; and the LT basalts, which are symbols of magma mixing, shallow and high degree of melting. Right after 30 My from the first magmatic appearance, volcanism is mainly confined in the axial zones of the Afar Depression. One of the most active axial zone basalts in the depression is the

Erta'Ale Range. Although there is slight geochemical variation among the Erta'Ale basalts themselves, overall they are transitional to tholeiitic in composition and enriched with the highly incompatible trace elements (Nb, La, Hf, Ta, Th). In terms of the enrichment of the incompatible trace elements and their ratios such as: La/Nb, Ba/Nb, Zr/Nb, Ba/La, and Ce/Pb, the Erta'Ale Range basalts are strongly related with the HT2 lavas of the Ethiopian province.

Unlike the incompatible trace elements, the Sr–Nd isotopic composition of the Ethio-Afar volcanic province (i.e., HT2, HT1, LT, and Erta'Ale Range) display a narrow range ($^{87}Sr/^{86}Sr$ = 0.703151–0.704305, and $^{143}Nd/^{144}Nd$ = 0.512778–0.512987); however, it is still sufficient enough to discriminate into three magma groups: the HT2 basalts display a tendency towards the OIB-like compositions; the LT basalts, on the other hand, show a depleted mantle composition tendency, and the Erta'Ale Range basalts are intermediate between but with strong affinity towards the HT2 basalts. It can be generalized that even after 30 My of magmatic evolution; the Afar mantle plume has the leading role in producing the transitional–tholeiitic basalts of the Erta'Ale range.

References:

Audin L., Quidelleur X., Coulié E., Courtillot V., Gilder S., Manighetti, I., Gillot, P.Y., Tapponnier P., and Kidane T. 2004. Palaeomagnetism and K-Ar and ^{40}Ar/^{39}Ar ages in the Ali Sabieh area (Republic of Djibouti and Ethiopia): constraints on the mechanism of Aden ridge propagation into southeastern Afar during the last 10 Ma. Geophysical Journal International 158, 327–345.

Ayalew D., Barbey P., Marty B., Reisberg L., Yirgu G., and Pik R. 2002. Source, genesis and timing of giant ignimbrite deposits associated with Ethiopian continental flood basalts. Geochimica et Cosmochimica Acta 66, 1429–1448.

Baker J., Snee L., and Menzies M. 1996. A brief Oligocene period of flood volcanism in Yemen: implications for the duration and rate of continental flood volcanism at the Afro-Arabian triple junction. Earth and Planetary Science Letters 138, 39–55.

Barberi F. and Santacroce, R. 1999. The Afar Stratoid Series and the magmatic evolution of East African rift system, in Colloque Rift d'Asal: Reunion Extraordinaire de la Societe Geologique de France, edited by Anonymous, Societe Geologique de France, Paris, France 891–897.

Barberi F., Ferrara G., Santacroce R., and Varet J. 1975. Structural evolution of the Afar triple junction. In: Pilger A. and Rösler A. (Eds.), Afar Depression of Ethiopia. Schweizerbart, (Inter-Union Commission on Geodynamics Scientific Report 14), Stuttgart, Germany, 38–54.

Berhe S.M., Desta B., Nicoletti M., and Teferra M. 1987. Geology, geochronology and geodynamic implications of the Cenozoic magmatic province in W and SE Ethiopia. Journal of the Geological Society, London 144, 213–226.

Beyene A. and Abdelsalam M.G. 2005. Tectonics of the Afar Depression: A review and synthesis. Journal of African Earth Sciences 41, 41–59.

Boccaletti M., Bonini M., Mazzuoli R., Abebe B., Piccardi L., and Tortorici L. 1998. Quaternary oblique extensional tectonics in the Ethiopian Rift (Horn of Africa). Tectonophysics 287, 97–116.

Choukroune P., Francheteau B., Auvray B., Auzende J. M., Brun J. P., Sichler B., Arthaud F., and Le´pine J. C. 1988. Tectonics of an incipient oceanic rift. Journal of Geophysical Research 9, 147–163.

Corti G. 2009. Continental rift evolution: From rift initiation to incipient breakup in the Main Ethiopian Rift, East Africa. Earth Science Reviews 96, 1–53.

Coulié E., Quidelleur X., Gillot P.Y., Courtillot V., Lef´evre J.C., and Chiesa S. 2003. Comparative K-Ar and Ar/Ar dating of Ethiopian and Yemenite Oligocene volcanism: Implications for timing and duration of the Ethiopian Traps. Earth and planetary Science Letters 206, 477–492.

Courtillot V., Achache J., Landre F., Bonhommet N., Montigny R., and Feraud G. 1984. Episodic spreading and rift propagation; new paleomagnetic and geochronologic data from the Afar nascent passive margin. Journal of Geophysical Research 89, 3315–3333.

Courtillot V., Armijo R., and Tapponnier P. 1987. Kinematics of the Sinai triple junction and a two phase model of Arabia-Africa rifting. In: Coward M.P., Dewey J.F., and Hancock P.L.

(Eds.), Continental extensional tectonics. Geological Society of America Special Paper 28, 559–573.

Courtillot V., Jaupart C., Manighetti I., Tapponnier P., and Besse J. 1999. On causal links between flood basalts and continental breakup. Earth and Planetary Science Letters 166, 177–199.

Deniel C., Vidal P., Coulon C., Vellutini P.J., Piguet P. 1994. Temporal evolution of mantle sources during continental rifting: The volcanism of Djibouti (Afar). Journal of Geophysical Research 99, 2853–2870.

D'Acremont E., Leroy S., Beslier M.O., Bellahsen N., Fournier M., Robin C., Maia M., and Gente P. 2005. Structure and evolution of the eastern Gulf of Aden conjugate margins from seismic reflection data. Geophysical Journal International 160, 869–890.

Ebinger C. and Sleep N.H. 1998. Cenozoic magmatism in central and east Africa resulting from impact of one large plume. Nature 395, 788–791.

Ebinger C.J., Yemane T., WoldeGabriel G., Aronson J.L., and Walter R.C. 1993. Late Eocene-Recent volcanism and rifting in the southern main Ethiopian rift. Journal of the Geological Society, London 150, 99–108.

Eissen J. P., Juteau T., Joron J. L., Dupre B., Humler E., and Al'Mkhamedov A. 1989. Petrology and geochemistry of basalts from the Red Sea axial rift at 18° N. Journal of Petrology 30, 791–739.

Féraud G., Zumbo V., and Sebai A. 1991. ^{40}Ar/^{39}Ar age and duration of tholeiitic magmatism related to the early opening of the Red Sea Rift. Geophysical Research Letters 18, 195–198.

Furman T., Bryce J.G., Karson J., and Iotti A. 2004. East African Rift System (EARS) plume structure: insights from Quaternary mafic lavas of Turkana, Kenya. Journal of Petrology 45, 1069–1088.

Gass I.G. 1975. Magmatic and tectonic processes in the development of the Afro-Arabian Dome. In: Pilger A. and Rösler A. (Eds.), Afar Depression of Ethiopia. Schweizerbart, (Inter-Union Commission on Geodynamics Scientific Report 14), Stuttgart, Germany, 10–18.

George R.M. and Rogers N.W. 2002. Plume dynamics beneath the African plate inferred from the geochemistry of the Tertiary basalts of southern Ethiopia. Contributions to Mineralogy and Petrology 144, 286–304.

George R., Rogers N., and Kelly S. 1998. Earliest magmatism in Ethiopia: evidence for two mantle plumes in one flood basalt province. Geology 26, 923–926.

Hofmann C., Courtillot V., Feraud G., Rochette P.,Yirgus G.,Ketefo E., and Pik R. 1997. Timing of the Ethiopian flood basalt event and implications for plume birth and global change. Nature 389, 838–841.

Kamber B.S. and Collerson K.D . 2000. Zr/Nb Systematics of Ocean Island Basalts Reassessed—the Case for Binary Mixing. Journal of Petrology 41, 1007–1021.

Kieffer B., Arndt N., Lapierre H., Bastien F., Bosch D., Pecher A., Yirgu G., Ayalew D., Weis D., Jerram A.D., Keller, F., and Meugniot C. 2004. Flood and Shield basalts from Ethiopia: magmas from the African superswell. Journal of Petrology 45, 793–834.

Lahitte P., Gillot P., Kidane T., Courtillot V., and Bekele A. 2003. New age constraints on the timing of volcanism in central Afar, in the presence of propagating rifts. Journal of Geophysical Research B, 108, ECV 10.1–10.17.

Le Bas M.L., Le Maitre R.W., Streckeisen A., and Zanettin B. 1986. A chemical classification of volcanic rocks based on the total alkali – silica diagram. Journal of Petrology 27, 745–750.

Merla G., Abbate E., Azzaroli A., Bruni P., Canuti P., Fazzuoli M., Sagri M., and Tacconi P. 1979. Comments to the geological map of Ethiopia and Somalia. Consiglio Nazionale delle Ricerche 89–95.

Mohr P. 1983. Ethiopian flood basalt province. Nature 303, 577–584.

Mohr P. and Zanettin B. 1988. The Ethiopian food basalt province. In: Macdougall, J.D. (Eds.), Continental flood basalts. Kluwer Academic Publishers 63–110.

Peccerillo A., Donati C., Santo A.P., Orlando A., Yirgu G., and Ayalew D. 2007. Petrogenesis of silicic peralkaline rocks in the Ethiopian rift: Geochemical evidence and volcanological implications. Journal of African Earth Sciences 48, 161–173.

Pik R., Deniel C., Coulon C., Yirgu G, Hofmann C., and Ayalew D. 1998. The northwestern Ethiopian Plateau flood basalts: Classification and spatial distribution of magma types, Journal of Volcanology and Geothermal Research 81, 91–111.

Pik R., Deniel C., Coulon C., Yirgu G., and Marty B. 1999. Isotopic and trace element signatures of Ethiopian flood basalts: Evidence for plume-lithosphere interactions, Geochimica et Cosmochimica Acta 63, 2263–2279.

Pik R., Marty B., Hilton D.R. 2006. How many mantle plumes in Africa? The geochemical point of view. Chemical Geology 226, 100–114.

Richards M. A., Duncan R. A., and Courtillot V.E. 1989. Flood basalts and hotspot tracks: Plume heads and tails. Science 246, 103–107.

Rogers N.W. 2006. Basaltic magmatism and the geodynamics of the East African Rift System. In: Yirgu G., Ebinger, C.J., and Maguire, P.K.H. (Eds.), The Afar Volcanic Province within the East African Rift System. Geological Society, London, Special Publication 259, 77–93.

Rogers N., Macdonald R., Fitton J. G., George R., Smith M., and Barreiro B. 2000. Two mantle plumes beneath the East African rift system: Sr, Nd and Pb isotope evidence from Kenya Rift basalts. Earth and Planetary Science Letters 176, 387–400.

Schilling J.G., Kingsley R.H., Hanan B.B., and McCully B.L. 1992. Nd–Sr–Pb isotopic variations along the Gulf of Aden; evidence for Afar mantle plume-continental lithosphere interaction. Journal of Geophysical Research 97, 10,927–10,966.

Tefera M., Chernet T., and Haro W. 1996. Geological map of Ethiopia; scale 1:2,000,000. Ministry of Mines and Energy. Ethiopian Institute of Geological Surveys, Addis Ababa, Ethiopia.

Ukstins I., Renne P., Wolfenden E., Baker J., Ayalew D., and Menzies M.A. 2002. Matching conjugate volcanic rifted margins: [40]Ar/[39]Ar chronostratigraphy of pre- and syn-rift bimodal flood volcanism in Ethiopia and Yemen. Earth and Planetary Science Letters 198, 289–306.

Varet J. 1975. Geological map of Afar. Centre National de la Recherche Scientifique (CNRS), Paris.

Vidal P., Deniel C., Vellutini P.J., Piguet P., Coulon C., Vincent J., and Audin J. 1991. Changes of mantle sources in the course of rift evolution: the Afar case. Geophysical Research Letters 18, 1913–1916.

Wilson M., Downes H., and Cebriá J. 1995. Contrasting fractionation trends in coexisting continental alkaline magma series. Cantal, Massif Central, France. Journal of Petrology 36, 1729–1753.

Wolfenden E., Ebinger C., Yirgu G., Deino A., and Ayalew D. 2004. Evolution of the northern Main Ethiopian rift: birth of a triple junction. Earth and Planetary Science Letters 224, 213–228.

Wolfenden E., Ebinger C., Yirgu G., Renne P., and Kelley S.P. 2005. Evolution of the southern Red Sea rift: birth of a magmatic margin. Geological Society of America Bulletin 117, 846–864.

Yirgu G., Ebinger C.J., and Maguire P.K.H. (Eds.) 2006. The Afar Volcanic Province within the East African Rift System. Geological Society, London, Special Publication 259, 1–6.

Zanettin B. 1992. Evolution of the Ethiopian Volcanic Province. Memorie Lincee Scienze Fisiche e Naturali 1, 155–181.

Zumbo V., Féraud, G., Vellutini, P., Piguet, P., and Vincent, J. 1995. First ^{40}Ar/^{39}Ar dating on Early Pliocene to Plio-Pleistocene magamatic events of the Afar-Republic of Djibouti. Journal of Volcanology and Geothermal Research 65, 281–295.

APPENDIX 1: DETAILED PETROGRAPHIC DESCRIPTIONS OF THE NORTHERN AFAR DEPRESSION

Sample code	Sample type	Location (in UTM)	Description
ER03	Vesicular basalt	648392E 1541847N	Euhedral – subhedral phenocrysts of plagioclase and few subhedral – anhedral clinopyroxene and olivine; all inbedded in fine grained plagioclase-rich matrix. The phenocrysts account for about 15 vol%. Plagioclase phenocrysts are randomly aligned but show simple twinning.
ER04	Aphanitic basalt	655321E 1537944N	Medium-grained rock containing euhedral – subhedral, mega-phenocrysts of clinopyroxene and few olivine. No plagioclase as phenocryst, but they are dominant in the matrix. Opaque minerals are present but in small amount.
ER07	Aphanitic basalt	653483E 15343553N	Fine-grained plagioclase-rich matrix with good flow texture and simple twinning. Phenocrysts are absent, if present only small amount of euhedral-subhedral pyroxene. No olivine and opaque minerals.
ER09	Vesicular basalt	661012E 1527977N	Medium-grained plagioclase dominated matrix with small amount of clinopyroxene and olivine. Phenocrysts are rare but with equal proportion of plagioclase and clinopyroxene. Opaque minerals (Magnetite and Ilmenite) are common.
ER11	Vesicular basalt	651890E 1528356N	Needle-like, fine – medium-grained plagioclase-laths and clinopyroxene with 3:1 ratio. Phenocrysts of all kind are absent. The plagioclase are elongated in shape and show good flow texture.
ER14	Vesicular basalt	664065E 1512024N	Coarse-grained plagioclase and clinopyroxene-rich matrix with some opaques. It is highly porphyritic with ~30 vol% phenocrysts. Phenocrysts are dominated by plagioclase (~6 mm) with some pyroxene. The plagioclase phenocrysts are polysynthetic and euhedral – subhedral in texture.
ER16	Vesicular basalt	658409E 1511334N	Fine – medium-grained, elongated plagioclase and equant clinopyroxene in the matrix. Phenocrysts are absent……
ER17	porphyritic basalt	674112E 1497965N	Coarse-grained, plagioclase and clinopyroxene dominated matrix consisting few olivine. It is highly porphyritic. Phenocrysts are mainly polysynthetic and zoned, euhedral–anhedral plagioclase (~5 mm). Inclusions of euhedral pyroxene and olivine are present. Opaques exist but limited in amount. Phenocrysts may account up to 25 vol%.
ER20	Porphyritic basalt	674094E 1498561N	Medium-grained, plagioclase and clinopyroxene-rich matrix with few olivine in it. Extremely porphyritic. Phenocrysts are purely plagioclase (plagioclase-phyric) with excellent polysynthetic and zoned texture. Phenocrysts range from micro – mega size (~10 mm) and account ~35 vol%.
ER23	Aphanitic basalt	673076E 1500339N	Very fine-grained matrix constituting plagioclase and pyroxene with few olivine. Plagioclase, clinopyroxene and olivine as micro-phenocrysts, and plagioclase and clinopyroxene as mega-phenocrysts. All phenocrysts constitute <10 vol%.
ER24	Aphanitic basalt	679697E 1504420N	Very fine-grained and randomly aligned, plagioclase dominated matrix. The matrix contains mega phenocrysts (5 – 12 mm) of euhedral – subhedral plagioclase and few meso-phenocrysts of clinopyroxenes. Plagioclase phenocrysts are zoned and polysynthetic in texture. No olivines but some opaque minerals. Total phenocrysts account 5 – 10 vol%.
ER26	Porphyritic basalt	679526E 1504356N	Fine – medium grained plagioclase and pyroxene-rich groundmass with few olivine crystals. Phenocrysts are extremely large mainly euhedral – anhedral, zoned and polysynthetic

			plagioclase with medium-size clinopyroxene phenocrysts. All phenocrysts constitute ~15 vol%.
ER28	Vesicular basalt	678002E 1502935N	Medium-grained matrix with equal proportions of plagioclase and clinopyroxenes. Few olivine crystals are also present. Phenocrysts are dominated by euhedral and zoned plagioclase with scattered medium-size clynopyroxene and olivine crystals.
ER31	Vesicular basalt	674189E 1501500N	Medium-grained equigranular basalt rich in plagioclase and pyroxene. Phenocrysts are not common but very scattered euhedral plagioclase and subhedral–anhedral clinopyroxenes are present.
ER34	Vesicular basalt	670494E 1499190N	Medium – coarse-grained plagioclase and pyroxene as groundmass. The plagioclase are elongated but randomly aligned. Phenocryst are rare, but if present euhedral – anhedral clinopyroxene dominated.
ER36	Vesicular basalt	676688E 1475072N	Midium – coarse-grained inequigranular plagioclase and pyroxene-rich groundmass. Phenocrysts are rare but subhedral – anhedral plagioclase and very few anhedral clinopyroxene.
ER38	Aphanitic basalt	701273E 1460530N	Very fine-grained plagioclase and pyroxene-rich groundmass. Very few mega-phenocrysts (5 – 9 mm) of plagioclase-phyric. Total phenocrysts do not exceed 3 vol%.
ER42	Basalt	700911E 1460316N	Fine – coarse-grained basalt. Grains are randomly aligned and dominated by highly elongated (0.5 – 1 mm) plagioclase showing simple twining. Pyroxenes with minor amount of olivines are also common but mostly exist as fine-grain. Some opaques (mostly ilmenites and magnetites) are present. No phenocrysts are present.
ER44a	Basaltic andesite	706747E 1455071N	Medium – coarse-grained plagioclase and clinopyroxene rich rocks. The plagioclase are equigranular where as the pyroxenes are inequigranular. No phenocrysts are observed.
ER46	Vesicular basalt	706999E 1455316N	Medium-grained plagioclase and pyroxene-rich basalt. The plagioclase crystals are elongated and show good flow texture. They are commonly equigranular showing simple twinning. The pyroxenes are inequigranular and anhedral in shape. Phenocrysts and other minerals are absent from the thin-section.
ER48	Aphanitic basalt	708770E 1453290N	Very fine-grained rock. Matrix is dominated by elongated but equigranular plagioclase some pyroxene and few opaques. Highly scattered subhedral to anhedral plagioclase and clinopyroxen constituting less than 2 vol%
ER49	Vesicular basalt	712929E 1443627N	Medium – coarse-grained euhedral – subhedral plagioclase and fine – medium-grained clinopyroxene (3:1) with very few olivine crystals. It is moderately porphyritic (5 – 8 vol%). Phenocrysts are still plag –rich but with considerable amount of cpx. Inclusions of plagioclase are also present.
AS50	Porphyritic basalt	603732E 1354163N	Highly porphyritic basalt. The matrix is dominantly composed of plagioclase and some pyroxene and few opaques. Phenocrysts are still euhedral plag-rich but with few anhedral clinopyroxene. Plagioclase crystals are twinned and in some zoned.
AS55	Basalt	597365E 1364527N	
AX004	Porphyritic basalt	472099E 1562095N	Needle-like, medium-grained plagioclase-laths and hornblende (>60 vol%) with few anhedral shape micro–mega phenocrysts of olivines, clinopyroxenes and very few opaque minerals. The plagioclases are carlsbad twinned but irregularly aligned. No flow texture.
AX08	Aphanitic basalt	479601E 1564013N	Fine-grained plagioclase (ground-mass) incorporating very few phenocrysts of pyroxenes and some secondary quartz crystals (agate). No olivine crystals were observed.
AX20	Aphanitic basalt	472639E 1551783N	Fine-grained matrix (dominated by plagioclase) and all size (micro – mega) phenocrysts of olivines, clinopyroxenes and

			some plagioclases. Phenocrysts constitute about 30 vol%. Few opaques are present.
AX21	Columnar basalt	472805E 1551143N	Plagioclase-laths dominated matrix. Euhedral–subhedral shaped, medium-grained phenocrysts of olivine. No opaque minerals.
AX24	Porphyritic basalt	474185E 1550132N	Medium-grained, elongated plagioclase and tabular hornblende (ground-mass) with medium size phenocrysts of olivines and few but very large and perfectly zoned phenocrysts of clinopyroxenes. Opaque minerals are not common.
AX29	Dolerite/ diabase	464013E 1557294N	Coarse-grained plagioclase-laths interfingering with the anhedral shaped, olivine mega-phenocrysts. The plagioclase shows Carlsbad-type twinning but poor flow texture.
AX31	Vesicular basalt	464206E 1557432N	Needle-like, medium-grained plagioclase (ground-mass) with very few pyroxene micro-phenocrysts. The matrix constitute >90 vol% and the plagioclase in the ground mass shows good flow texture.
AX32	Aphanitic basalt	463129E 1560422N	Carlsbad twinned medium-grained plagioclase (ground-mass). No phenocryst minerals found but medium-grained (the same size as the plagioclase) olivines and few opaque minerals are common.
AX34	Aphanitic basalt	473529E 1552248N	Carlsbad twinned, fine-grained plagioclase-laths matrix with varying size (micro–mega) phenocrysts of olivines and pyroxenes. The plagioclases show good flow texture and the phenocrysts are euhedral –anhedral in shape.
AX38	Aphanitic basalt	474033E 1556172N	Fine–medium-grained, elongated–equant plagioclase-laths (50–60 vol%). Micro–mega, Euhedral–subhedral shaped phenocrysts of olivines and zoned and un-zoned phenocrysts of pyroxenes.
AX43d	Columnar basalt	466516E 1564320N	Tabular, medium-grained plagioclase with few olivine phenocrysts. The phenocrysts are subhedral–anhedral in shape. Some opaque minerals are present.
AX44	Basalt	465459E 1563351N	Euhedral–subhedral shaped olivine phenocrysts (about 5 – 8 vol%) embedded in fine-grained matrix of equant–elongated plagioclase-laths and few olivines.
AX46	Aphanitic basalt	469365E 1562236N	Needle- like plagioclase and hornblende constituting about 90 vol% with very few olivine micro-phenocrysts. No opaques.
AX47b	Aphanitic basalt	474973E 1555646N	Needle-like equant shape, fine–medium-grained plagioclase-laths with medium-size olivine phenocrysts.
AX63	Aphanitic basalt	460147E 1552044N	Extremely large, euhedral–anhedral shaped pyroxene and olivine phenocrysts. The pyroxenes are multiply zoned and some altered/secondary minerals are developed at the rims of the phenocrysts. The ground-mass is still dominated by very fine-grained plagioclase with very few of the above- mentioned minerals.
AX79	Basalt	479293E 1560281N	Needle-like, Medium–course-grained plagioclase with few olivine micro-phenocrysts. No visible pyroxene and opaque minerals.

APPENDIX 2: REPRESENTATIVE MICROPROBE ANALYSIS OF THE ERTA'ALE RANGE BASALTS

Sample	Mineral	Na_2O	SiO_2	MgO	Al_2O_3	K_2O	CaO	TiO_2	FeO	MnO	Cr_2O_3	NiO	BaO	Total
Er05	Plag-Core	4.73	53.6	0.13	28.2	0.17	11.8	0.16	0.78	0.02			<0.01	99.46
Er05	Plag-Rim	6.57	57.7	0.06	25.4	0.39	8.43	0.26	0.97	0.01			<0.01	99.73
Er05	Plag	4.45	52.6	0.13	29.0	0.17	12.4	0.15	0.71	0.01			0.05	99.70
Er05	Plag-Core	5.78	55.9	0.10	26.7	0.27	9.85	0.22	0.89	0.02			0.00	99.70
Er05	Plag-Rim	8.46	61.5	0.04	23.0	0.66	5.14	0.16	0.92	0.01			0.05	99.89
Er05	Plag	5.77	55.7	0.08	26.7	0.26	9.92	0.18	0.90	<0.01			0.04	99.59
Er05	Plag	4.86	53.9	0.15	28.0	0.18	11.6	0.18	0.84	<0.01			<0.01	99.73
Er05	Plag	4.61	53.0	0.12	28.3	0.17	12.0	0.16	0.84	<0.01			0.01	99.27
Er05	Plag-Rim	8.20	61.9	0.03	22.8	1.01	4.64	0.19	0.97	<0.01			0.08	99.82
ER21	Plag	3.68	67.6	0.20	13.6	5.20	1.08	0.47	3.87	0.12			0.11	95.96
ER21	Plag	7.00	58.7	0.01	25.2	0.50	7.74	0.05	0.37	0.01			0.06	99.73
ER21	Plag	7.57	60.3	0.03	24.0	0.60	6.29	0.03	0.37	0.04			0.05	99.29
ER21	Plag	6.78	58.6	0.02	25.4	0.47	7.85	0.06	0.40	<0.01			0.04	99.63
ER21	Plag	6.99	59.2	0.02	24.8	0.57	7.32	0.04	0.39	<0.01			<0.01	99.40
ER21	Plag	7.27	59.2	0.03	24.7	0.48	7.16	0.05	0.43	<0.01			0.07	99.40
ER21	Plag	6.93	59.1	0.02	25.2	0.49	7.40	0.05	0.42	0.02			0.03	99.70
ER21	Plag	7.58	60.6	0.03	24.2	0.68	6.14	0.05	0.28	0.00			0.09	99.65
ER21	Plag	7.53	60.3	0.02	24.0	0.58	6.31	0.02	0.34	0.03			0.06	99.15
ER21	plag-Core	6.17	57.0	0.02	26.3	0.36	9.01	0.06	0.42	0.01			<0.01	99.34
ER21	plag-Core	5.95	56.4	0.03	27.0	0.36	9.59	0.06	0.46	0.01			0.09	99.95
ER21	Plag-Rim	7.52	60.5	0.03	24.1	0.60	6.46	0.04	0.40	0.01			0.09	99.76
ER21	Plag-Rim	7.64	60.5	0.01	24.0	0.63	6.26	0.07	0.39	<0.01			0.08	99.57
ER21	plag-Core	6.58	58.1	0.02	25.9	0.47	7.97	0.05	0.33	0.01			<0.01	99.35
ER21	Plag-Rim	7.41	60.5	0.02	24.3	0.67	6.31	0.04	0.49	<0.01			0.12	99.78
ER21	Plag-Rim	7.02	59.8	0.04	24.4	0.63	6.70	0.06	0.38	<0.01			0.12	99.14
ER21	CPx	0.27	49.8	8.47	0.84		18.1	0.41	20.2	0.99	0.01	<0.01		99.11
ER27	Plag	2.54	48.9	0.15	32.0	0.08	16.0	0.08	0.53	<0.01			<0.01	100.21
ER27	Plag	1.72	46.9	0.12	33.2	0.09	17.6	0.02	0.54	<0.01			<0.01	100.14
ER27	Plag	4.39	52.9	0.23	28.4	0.21	12.4	0.11	0.72	0.01			<0.01	99.41
ER27	Plag	2.06	47.6	0.15	32.4	0.08	16.6	0.05	0.62	<0.01			0.07	99.63
ER27	Plag	1.94	47.3	0.14	32.6	0.05	17.0	0.05	0.56	<0.01			<0.01	99.67
ER27	Plag	2.18	47.9	0.17	31.7	0.08	16.6	0.04	0.60	<0.01			<0.01	99.31
ER27	Plag-Core	2.83	49.4	0.17	30.8	0.10	15.4	0.04	0.57	0.01			<0.01	99.33
ER27	Plag-Rim	3.11	49.8	0.20	30.5	0.12	14.7	0.05	0.59	0.01			<0.01	99.01
ER27	Plag	2.45	48.6	0.16	31.5	0.11	15.7	0.07	0.60	0.01			0.03	99.31
ER27	Plag	1.93	47.2	0.15	32.5	0.08	16.8	0.04	0.63	<0.01			0.00	99.26
ER27	Plag	2.08	47.4	0.13	32.3	0.09	16.7	0.03	0.65	0.02			0.09	99.51
ER30	Plag	1.91	46.6	0.13	32.2	0.05	17.0	0.04	0.51	0.00			<0.01	98.44
ER30	Plag	1.74	46.6	0.15	32.7	0.05	17.2	0.06	0.49	0.03			0.02	99.03
ER30	Plag	2.79	49.4	0.20	31.2	0.10	15.4	0.07	0.63	0.01			<0.01	99.79
ER30	Plag	2.95	49.5	0.20	30.6	0.08	15.3	0.06	0.52	0.02			0.04	99.28
ER30	Plag	2.20	48.1	0.18	32.1	0.08	16.3	0.05	0.53	<0.01			<0.01	99.54
ER30	Plag	2.14	47.4	0.16	32.3	0.06	16.5	0.04	0.55	0.03			<0.01	99.15
ER30	Plag	2.12	47.6	0.17	32.6	0.07	16.7	0.07	0.52	0.01			0.02	99.88
ER30	Plag&CPx	2.35	48.3	7.88	9.57	1.27	10.3	3.12	14.7	0.33			0.07	97.89
ER30	Plag&CPx	2.05	49.1	8.25	8.49	1.46	10.1	3.24	15.2	0.27			0.06	98.21
ER33	Plag	3.65	51.8	0.16	29.5	0.18	13.6	0.09	0.67	0.04			<0.01	99.62
ER33	Plag	4.10	52.5	0.20	29.0	0.24	12.7	0.15	0.78	0.02			0.06	99.70
ER33	Plag	4.18	52.6	0.17	28.4	0.26	12.8	0.15	0.81	<0.01			0.04	99.36
ER33	Plag	2.78	49.5	0.15	31.1	0.12	15.3	0.09	0.55	0.01			<0.01	99.64
ER33	Plag	4.35	53.0	0.17	28.6	0.23	12.5	0.12	0.93	<0.01			0.03	99.96
ER33	Plag	4.07	52.3	0.17	29.1	0.24	13.1	0.14	0.83	0.02			<0.01	99.96

APPENDIX 2: CONTINUED

Sample	Mineral	Na$_2$O	SiO$_2$	MgO	Al$_2$O$_3$	K$_2$O	CaO	TiO$_2$	FeO	MnO	Cr$_2$O$_3$	NiO	BaO	Total
ER33	Plag	3.18	50.7	0.16	30.2	0.15	14.3	0.07	0.66	0.02			0.02	99.54
ER33	Plag-Core	2.69	49.0	0.13	31.2	0.11	15.4	0.06	0.68	0.01			<0.01	99.26
ER33	Plag-Rim	3.61	51.2	0.16	29.6	0.17	13.8	0.12	0.61	<0.01			0.04	99.36
ER33	Plag-Rim	4.05	52.3	0.19	28.7	0.23	13.0	0.12	0.79	0.01			<0.01	99.44
ER33	Plag	2.66	49.5	0.14	31.2	0.11	15.1	0.11	0.63	<0.01			<0.01	99.43
ER40	Plag	2.08	47.5	0.14	32.6	0.03	16.6	0.04	0.71	0.01			<0.01	99.59
ER40	Plag	5.14	55.3	0.12	27.4	0.38	10.8	0.14	0.68	0.01			0.01	99.97
ER40	Plag	2.05	47.7	0.13	32.4	0.05	16.7	0.07	0.71	<0.01			0.02	99.76
ER40	Plag	1.84	47.1	0.10	32.7	0.03	17.2	0.04	0.64	<0.01			<0.01	99.65
ER40	Plag	1.88	47.0	0.12	33.1	0.03	17.3	0.05	0.59	<0.01			0.03	100.08
ER40	Plag	4.99	54.7	0.16	27.5	0.37	10.8	0.13	0.88	<0.01			<0.01	99.49
ER40	Plag	1.76	47.0	0.14	32.9	0.05	17.1	0.05	0.67	<0.01			<0.01	99.56
ER40	Plag	2.08	47.8	0.17	32.2	0.08	16.6	0.04	0.63	0.02			<0.01	99.71
ER40	Plag	2.15	47.5	0.15	32.0	0.08	16.2	0.07	0.70				<0.01	98.84
Er05	CPx	0.45	48.5	14.1	4.63		21.6	2.30	7.17	0.12	0.48	0.01		99.34
Er05	CPx-Core	0.34	51.5	16.0	2.33		21.0	1.17	6.92	0.17	0.35	0.03		99.74
Er05	CPx-Rim	0.45	49.2	12.6	2.46		20.1	1.94	12.0	0.32	<0.01	0.04		99.07
Er05	CPx-Core	0.48	49.4	14.6	4.37		21.4	1.68	6.92	0.14	0.62	0.04		99.61
Er05	CPx	0.34	51.5	15.9	2.47		21.0	1.23	6.83	0.12	0.30	0.02		99.69
Er05	CPx-Rim	0.47	48.6	14.2	4.58		21.6	1.92	6.91	0.12	0.55	0.01		99.00
Er05	CPx-Core	0.37	51.1	15.6	2.30		20.4	1.40	8.40	0.21	0.08	0.07		99.98
Er05	CPx-Rim	0.48	49.1	12.5	2.77		20.5	2.30	11.5	0.25	<0.01	0.05		99.46
Er05	CPx	0.53	48.6	12.8	3.03		20.4	2.63	11.3	0.25	<0.01	<0.01		99.47
ER21	CPx-Rim	0.29	49.4	8.52	0.91		18.3	0.38	19.7	0.95	0.04	<0.01		98.49
ER21	CPx	0.29	49.9	9.05	0.87		18.5	0.41	19.4	0.95	<0.01	0.01		99.35
ER21	CPx	0.28	49.9	8.42	0.83		18.5	0.43	20.3	0.91	<0.01	<0.01		99.54
ER21	CPx	0.27	49.9	8.68	0.86		18.4	0.41	19.7	0.94	0.01	0.02		99.20
ER21	CPx	0.31	50.1	8.96	0.86		18.5	0.42	19.3	0.94	0.01	0.03		99.45
ER27	CPx-Inc	0.69	45.3	11.5	3.30		12.4	4.68	19.5	0.38	0.03	0.02		97.85
ER27	CPx	0.24	49.9	15.7	3.58		19.8	1.66	8.09	0.22	0.33	0.05		99.47
ER27	CPx	0.85	45.9	11.3	3.98	0.68	11.7	3.99	19.6	0.37	0.02			98.27
ER27	CPx	0.75	45.1	10.3	4.18		11.7	5.05	19.5	0.34	0.02	0.01		97.00
ER27	CPx	0.25	51.5	16.2	2.82		21.5	0.75	5.9	0.15	0.34	<0.01		99.52
ER27	CPx	0.32	48.1	14.6	4.93		18.3	2.29	10.4	0.21	<0.01	<0.01		99.05
ER27	CPx	0.80	45.8	11.6	4.08		11.8	4.14	19.0	0.33	0.03	0.01		97.50
ER27	CPx	0.27	52.0	16.3	2.80		21.4	0.71	5.95	0.14	0.32	0.01		99.84
ER27	CPx	0.95	44.9	11.6	2.75		12.3	4.32	19.9	0.40	0.02	0.04		97.21
ER27	CPx-Inc	0.85	46.1	11.4	4.27		12.2	4.33	17.7	0.37	0.03	0.01		97.22
ER27	CPx-Inc	0.93	44.4	10.5	3.00		11.2	4.70	22.2	0.39	0.05	0.01		97.45
ER30	CPx	1.19	49.8	7.30	11.4	1.27	10.7	2.58	14.0	0.26			0.04	98.55
ER30	CPx	0.23	51.2	16.1	2.55		21.1	0.82	6.49	0.17	0.26	<0.01		98.98
ER30	CPx	0.20	51.7	16.4	2.23		21.1	0.81	6.26	0.11	0.24	0.05		99.08
ER30	CPx	0.25	52.2	16.2	2.34		21.0	0.73	6.41	0.18	0.30	0.02		99.60
ER30	CPx	0.23	51.7	16.1	2.60		21.2	0.83	6.29	0.17	0.23	<0.01		99.39
ER33	CPx	0.33	48.9	14.1	3.71		19.0	2.11	10.3	0.24	0.01	0.04		98.70
ER33	CPx	0.21	51.4	16.0	1.61		17.1	1.12	11.2	0.29	0.04	0.03		99.08
ER33	CPx	0.20	51.8	16.8	2.02		17.2	1.14	10.4	0.29	0.03	0.01		99.83
ER33	CPx	0.25	51.4	16.1	2.20		18.9	1.07	9.41	0.27	0.05	0.03		99.64
ER33	CPx	0.25	50.6	15.6	2.62		19.0	1.48	9.54	0.26	0.02	<0.01		99.39
ER33	CPx	0.32	47.7	13.6	4.42		19.5	2.85	10.7	0.22	0.06	<0.01		99.44
ER40	CPx	0.27	50.8	15.1	2.47		16.8	1.26	11.7	0.33	0.05	0.04		98.84
ER40	CPx-Cor	0.31	50.8	14.4	2.39		20.5	1.04	9.48	0.31	0.01	0.04		99.31
ER40	CPx-Rim	0.30	49.7	15.2	4.00		20.2	1.42	8.26	0.21	0.09	0.03		99.46
ER40	CPx-Rim	0.33	50.5	14.7	2.32		18.4	1.41	11.5	0.29	0.03	0.01		99.40

APPENDIX 2: CONTINUED

Sample	Mineral	Na$_2$O	SiO$_2$	MgO	Al$_2$O$_3$	K$_2$O	CaO	TiO$_2$	FeO	MnO	Cr$_2$O$_3$	NiO	BaO	Total
ER40	CPx	0.22	52.0	16.7	1.34		16.5	0.86	11.5	0.33	0.01	0.03		99.47
ER40	CPx	0.30	49.6	14.5	3.94		20.0	1.57	9.30	0.22	0.02	0.02		99.46
ER40	CPx	0.32	49.6	15.1	3.71		18.4	1.53	10.1	0.27	0.09	0.02		99.23
ER40	CPx	0.34	47.6	13.4	5.66		20.4	2.30	9.85	0.21	0.04	0.01		99.81
Er05	Olivine	0.06	30.4	6.04	0.03		0.77	0.32	59.1	1.31	0.01	<0.01		98.12
Er05	Oliv-Core		39.4	42.4	0.05		0.27	<0.01	17.3	0.27	0.04	0.19		99.92
Er05	Oliv-Rim		38.5	39.7	0.05		0.36	0.03	20.9	0.34	0.01	0.16		100.06
Er05	Oliv-Core		39.4	42.9	0.01		0.24	0.02	16.9	0.25	<0.01	0.21		100.01
Er05	Oliv-Rim		38.7	39.9	0.03		0.35	0.02	20.2	0.31	0.01	0.17		99.71
Er05	Oliv-Core		38.4	39.6	0.02		0.37	0.02	20.9	0.29	0.04	0.12		99.69
Er05	Oliv-Rim	0.01	38.5	39.4	0.04		0.41	0.05	20.7	0.32	0.03	0.11		99.52
Er05	Olivine	0.05	30.4	4.82			0.65	0.34	60.6	1.28	<0.01	<0.01		98.05
Er05	Olivine	0.01	39.6	42.4	0.02		0.23	0.03	17.6	0.26	0.05	0.23		100.45
Er05	Olivine		38.9	40.4	0.03		0.26	0.03	20.1	0.32	0.03	0.12		100.23
Er05	Olivine	0.04	30.2	5.26	0.02		0.76	0.38	60.5	1.30	<0.01	<0.01		98.52
ER21	Olivin		31.7	10.5			0.32	0.05	54.7	2.01	<0.01	<0.01		99.31
ER21	Olivin		31.6	10.6	0.01		0.31	0.06	54.7	1.96	<0.01	<0.01		99.24
ER21	Olivin		31.6	9.90	0.01		0.39	0.05	54.8	2.00	0.03	0.01		98.81
ER27	Olivin	0.02	38.9	39.8	0.04		0.35	0.04	20.2	0.32	0.06	0.06		99.73
ER27	Olivin		38.8	40.0	0.04		0.32	<0.01	20.2	0.31	<0.01	0.14		99.90
ER27	Olivin		38.9	40.1	0.03		0.34	0.02	20.1	0.28	0.02	0.15		99.90
ER27	Olivin		38.8	40.2	0.06		0.35	<0.01	20.3	0.32	0.01	0.09		100.16
ER30	Olivin	0.20	36.8	25.6	1.09		0.77	0.20	34.2	0.51	<0.01	0.06		99.40
ER30	Olivin		39.0	40.5	0.03		0.32	<0.01	20.0	0.30	0.03	0.11		100.23
ER30	Olivin		39.0	41.1	0.02		0.32	0.04	18.9	0.32	0.04	0.16		99.94
ER30	Olivin		39.1	40.6	0.04		0.33	0.02	19.4	0.27	0.05	0.15		99.92
ER30	Olivin	0.01	38.8	40.2	0.03		0.34	0.02	20.0	0.31	0.04	0.09		99.76
ER30	Olivin	0.01	39.3	41.1	0.03		0.35	<0.01	18.8	0.30	0.02	0.11		99.99
ER30	Olivin		39.2	41.4	0.03		0.35	0.03	18.7	0.30	<0.01	0.15		100.23
ER30	Olivin	0.01	39.0	40.9	0.03		0.36	0.01	19.4	0.31	0.01	0.10		100.11
ER33	Olivin		36.7	31.2	0.05		0.41	0.05	30.1	0.47	0.01	0.03		98.92
ER33	Olivin		37.0	31.3	0.02		0.37	0.09	30.3	0.49	0.01	0.07		99.70
ER33	Olivin	0.01	37.7	35.5	0.02		0.36	0.05	25.3	0.44	<0.01	0.09		99.46
ER33	Olivin		37.0	32.4	0.04		0.34	0.04	29.2	0.42	0.02	0.05		99.43
ER33	Olivin	0.02	38.0	36.5	0.05		0.35	0.03	24.5	0.33	<0.01	0.12		99.87
ER33	Olivin		36.9	31.5	0.05		0.36	0.05	29.8	0.46	<0.01	0.09		99.20
ER33	Olivin	0.02	37.3	33.9	0.03		0.33	0.05	27.4	0.43	0.01	0.08		99.58
ER33	Olivin	0.01	37.5	34.7	0.03		0.33	0.04	26.7	0.41	0.03	0.12		99.95
ER33	Olivin		37.9	36.9	0.04		0.32	0.06	24.0	0.37	0.02	0.14		99.80
ER33	Olivin		36.7	31.5	0.05		0.40	0.08	30.2	0.52	0.01	0.06		99.49
ER33	Olivin		37.2	33.2	0.04		0.34	0.07	28.1	0.41	0.01	0.05		99.41
ER33	Olivin		37.7	35.3	0.04		0.40	0.05	26.0	0.41	<0.01	0.03		99.94
ER33	Olivin		38.4	38.4	0.04		0.33	0.08	22.4	0.33	<0.01	0.11		100.08
ER40	Olivin		36.4	30.0	0.04		0.37	0.07	32.2	0.45	0.01	0.04		99.57
ER40	Olivin		36.5	29.8	0.03		0.30	0.10	32.4	0.50	<0.01	0.07		99.74
ER40	Olivin	0.04	36.6	30.8	0.04		0.29	0.11	31.3	0.47	0.01	0.04		99.63
ER40	Olivin	0.01	36.3	30.1	0.05		0.31	0.08	32.2	0.44	<0.01	0.09		99.61
ER40	Olivin	0.01	32.5	12.6	0.64		0.59	0.16	49.9	0.77	0.01	<0.01		97.21
ER40	Olivin		33.8	18.5	0.05		0.36	0.14	45.4	0.74	0.04	0.03		99.06

APPENDIX 2: CONTINUED

Sample	Mineral	Na$_2$O	SiO$_2$	MgO	Al$_2$O$_3$	K$_2$O	CaO	TiO$_2$	FeO	MnO	Cr$_2$O$_3$	NiO	BaO	Total
ER40	Olivin		35.7	26.4	0.04		0.40	0.06	36.0	0.57	<0.01	0.04		99.32
ER40	Olivin		35.5	25.9	0.03		0.33	0.07	37.2	0.56	0.02	0.01		99.62
ER40	Olivin		34.3	21.4	0.01		0.33	0.22	42.1	0.63	0.03	0.02		99.08
ER40	Olivin		36.5	30.5	0.01		0.33	0.07	31.4	0.45	<0.01	0.07		99.33
Er05	Ti-Magt		0.14	0.86	1.19		0.20	21.4	70.0	0.50	0.03	0.07		94.35
ER21	Ti-Magt		0.14	0.93	0.91		0.18	21.7	69.6	0.91	0.02	0.02		94.40
ER21	Ti-Magt		0.11	0.81	1.32		0.03	22.1	70.3	0.98	0.01	<0.01		95.62
ER21	Ti-Magt	0.01	0.12	0.94	1.35		0.06	22.2	69.7	0.89	0.04	<0.01		95.31
ER21	Ti-Magt		0.15	0.94	1.39		0.02	22.2	70.8	0.90	0.01	<0.01		96.33
ER21	Ti-Magt	0.02	0.10	0.78	1.27	<0.01	<0.01	22.2	70.6	1.05			0.10	96.11
ER21	Ti-Magt		0.11	0.89	1.49		0.04	22.1	70.4	0.91	0.01	<0.01		95.96
ER21	Ti-Magt		0.15	1.03	1.20		0.07	21.6	70.1	0.96	0.02	0.01		95.17
ER21	Ti-Magt		0.14	0.90	1.54		0.34	21.2	69.6	0.91	<0.01	0.01		94.66
ER27	Ti-Magt	0.28	7.65	0.84	3.19		0.88	21.6	58.5	0.51	0.04	0.05		93.54
ER27	Ti-Magt	0.05	1.16	0.55	2.02		0.25	23.3	65.6	0.48	0.01	0.02		93.44
ER33	Ti-Magt	0.04	0.60	1.36	2.55		0.29	25.7	63.8	0.61	0.07	0.04		95.13
ER33	Ti-Magt		0.21	1.52	2.66		0.16	25.0	64.4	0.55	0.12	0.01		94.66
ER33	Ti-Magt		0.11	3.58	3.12		0.10	21.9	65.8	0.45	0.08	0.02		95.15
ER33	Ti-Magt		0.14	3.58	3.05		0.11	21.9	65.8	0.44	0.13	0.04		95.15
ER33	Ti-Magt	0.02	0.16	1.86	2.88		0.26	22.9	66.0	0.48	0.15	0.04		94.76
ER33	Ti-Magt	0.03	0.18	1.77	2.90		0.34	22.9	65.8	0.50	0.16	<0.01		94.54
Er05	Ilmenite	0.02	0.27	0.85	0.14		0.64	46.8	46.7	0.52	0.01	<0.01		95.93
Er05	Ilmenite	0.02	0.13	0.53	0.21		0.21	46.0	48.3	0.57	0.01	<0.01		96.00
ER40	Ilmenite	0.03	0.08	0.55	0.10		0.20	47.6	47.2	0.50	0.06	<0.01		96.29
ER40	Ti-Magt		0.20	1.04	1.55		0.19	23.0	67.6	0.47	0.08	0.02		94.25
ER40	Ti-Magt		0.22	1.07	1.52		0.16	22.5	66.7	0.49	0.06	<0.01		92.72
ER40	Ti-Magt		0.16	0.84	1.53		0.14	21.7	69.4	0.45	0.08	<0.01		94.29
ER40	Ti-Magt	0.02	0.17	0.70	1.66		0.23	23.1	63.0	0.41	0.08	0.02		89.34
Er05	Spin-core		0.08	8.37	15.4		0.05	4.49	39.2	0.29	28.6	0.10		96.55
Er05	Spin-Rim		0.04	5.17	9.43		0.04	8.10	49.1	0.29	23.7	0.09		95.88
Er05	Spin-inclu		0.10	9.50	16.8		0.02	3.70	36.4	0.24	28.9	0.15		95.89
Er05	Spin-inclu		0.14	6.93	9.36		0.09	9.34	47.6	0.33	21.2	0.13		95.01
Er05	Spin-inclu	0.03	0.09	9.55	17.3		0.02	3.73	35.7	0.23	29.4	0.17		96.24
Er05	Spin-inclu	0.02	0.07	6.74	8.72		0.04	9.13	48.6	0.30	21.4	0.14		95.22
Er05	Orthoclase	3.21	48.8	1.52	15.1	7.79	11.1	3.86	5.30	0.08			0.04	98.37

APPENDIX 3: DETAILED PETROGRAPHIC DESCRIPTIONS OF THE ETHIOPIAN PLATEAU AND AFAR DEPRESSION BASALTS.

SAMPLE	AXUM FLOOD BASALT							ERT'ALE BASALT											
	AX04	AX09	AX29	AX32	AX42	AX44	AX63	ER01	ER03	ER08	ER09	ER10	ER13	ER24	ER25	ER26	ER27	ER28	ER29
	Basalt	Basalt	Basalt	Basalt	Basalt	Basalt	Basalt	Basalt	Basalt	Basalt	Basalt	Basalt	Basalt	Basalt	Basalt	Basalt	Basalt	Basalt	Basalt
(wt.%)																			
SiO_2	43.05	45.13	48.32	46.82	50.68	47.06	44.82	49.23	49.78	50.74	50.97	50.99	50.85	48.99	48.27	48.45	48.85	49.46	49.48
TiO_2	4.39	3.97	3.50	3.25	2.90	2.85	3.07	2.72	2.77	2.63	2.62	2.59	2.58	2.60	2.20	2.52	2.28	2.53	2.38
Al_2O_3	13.88	15.16	15.32	16.51	16.24	16.38	14.32	13.58	13.74	14.05	14.11	14.21	14.25	14.77	16.99	14.94	16.47	15.35	15.85
Fe_2O_3	17.32	16.58	15.39	14.89	13.42	15.84	16.26	13.68	13.89	13.59	13.65	13.57	13.53	12.39	11.21	12.31	11.28	12.34	12.02
MnO	0.21	0.18	0.20	0.17	0.19	0.14	0.24	0.22	0.22	0.22	0.22	0.22	0.22	0.19	0.17	0.19	0.18	0.19	0.18
MgO	7.22	5.44	4.60	5.22	3.63	3.52	5.66	5.88	5.74	5.47	5.80	5.68	5.56	6.50	5.95	6.08	6.01	6.05	6.50
CaO	7.90	7.07	7.08	6.87	7.22	4.71	7.68	10.36	10.06	9.70	9.71	9.81	9.82	10.62	11.62	11.48	12.00	11.40	11.62
Na_2O	4.17	3.46	3.87	3.86	3.35	5.94	5.34	3.02	3.20	3.24	3.26	3.19	3.27	2.62	2.63	2.75	2.79	2.79	2.73
K_2O	1.59	1.37	1.05	1.12	1.74	0.58	1.47	0.49	0.57	0.63	0.60	0.60	0.60	0.66	0.53	0.62	0.57	0.62	0.60
P_2O_5	0.96	0.60	0.53	0.48	0.80	0.59	1.30	0.38	0.39	0.38	0.38	0.37	0.38	0.39	0.30	0.34	0.31	0.34	0.31
LOI	0.72	2.88	1.89	1.53	1.18	3.08	1.05	0.73	0.12	-0.11	-0.59	-0.40	-0.30	0.95	1.47	0.67	0.10	-0.10	-0.20
sum	101.4	101.8	101.8	100.7	101.4	100.7	101.2	100.3	100.5	100.5	100.7	100.8	100.8	100.7	101.3	100.4	100.8	100.9	101.5
(ppm)																			
V	199	211	207	266	225	76.3	139	442	443	434	443	428	418	343	304	358	318	365	339
Cr	14.9	39.0	11.0	39.3	23.6	28.8	8.00	57.6	54.3	24.0	23.6	23.8	25.5	160	168	146	128	127	187
Co	44.2	42.0	35.5	52.0	34.6	38.5	32.0	41.1	40.6	37.9	39.1	41.3	41.7	41.9	36.4	39.3	34.7	36.5	41.3
Ni	33.5	12.7	21.8	51.7	27.1	46.3	11.6	39.1	36.9	25.7	26.6	28.0	24.6	62.0	47.4	41.1	45.7	41.2	51.6
As	1.04	1.06	<1.5	<1.5	0.32	<1.5	1.17	<1.5	<3.4	<1.9	0.55	<3.3	2.01	<2.1	0.6	<1.0	<2.1	<1.3
Se	<1.7	2.45	<2.9	3.05	<2.8	<2.3	<2.8	<2,09	<2,17	<2,13	0.20	<2,12	<2,12	2.69	<2.5	0.68	<2.0	<2.2	<2.3
Br	<0.7	<2.5	<3.86	<3.9	<3.5	<4.0	<5.1	1.14	0.92	1.21	1.32	1.22	1.04	0.70	0.56	0.62	0.60	0.49	0.69
Rb	41.1	17.7	12.3	19.6	51.8	16.2	21.3	12.2	18.6	13.7	17.5	9.12	18.6	17.4	14.5	17.7	11.5	13.1	14.0
Sr	989	614	619	680	760	1020	1207	269	261	255	249	251	257	333	330	321	337	324	320
Y	30.4	35.7	38.6	35.6	34.5	23.3	36.4	43.5	55.5	54.7	56.3	52.6	48.2	38.4	31.6	34.8	32.5	41.9	33.7
Zr	321	267	212	208	269	315	389	268	356	221	232	213	199	197	191	182	176	211	175
Nb	34.2	23.0	11.7	15.1	19.7	20.4	39.7	32.5	33.0	34.9	34.0	33.2	33.2	32.5	26.6	31.7	28.3	31.7	30.1
Cs	0.42	0.46	<0.2	0.36	0.61	3.18	0.48	0.15	0.18	0.14	0.14	0.13	0.18	0.26	0.22	0.23	0.16	0.24	0.17
Ba	110	504	221	270	460	65	116	88	95	86	87	82	83	93	78	77	76	85	96
La	30.4	25.0	15.2	20.0	31.1	15.1	38.4	23.9	25.0	24.3	25.6	26.0	26.0	26.3	20.9	25.9	21.3	24.0	25.4
Ce	72.6	47.3	38.2	47.4	72.0	44.8	90.3	55.6	55.2	53.3	59.4	65.5	64.6	75.4	65.5	59.8	53.8	56.5	54.0
Nd	46.9	37.2	27.0	30.6	42.1	38.5	56.9	25.5	28.1	26.1	26.4	29.5	31.0	22.6	28.5	23.9	29.6	27.4
Sm	11.3	9.40	7.27	8.38	10.4	10.6	14.3	7.73	6.72	5.94	6.34	6.44	6.90	6.79	5.26	6.53	5.37	5.86	6.41
Eu	4.25	3.53	2.62	2.85	3.27	3.49	4.59	2.22	2.25	2.21	2.23	2.32	2.33	2.27	1.81	2.21	1.79	1.95	1.89
Gd	9.00	10.5	9.20	10.2	11.2	12.4	15.2	7.50	7.84	6.26	9.85	6.87	6.40	7.52	6.02	5.81	4.71	5.00	5.38
Tb	1.46	1.73	1.16	1.39	1.56	1.33	1.17	1.01	1.00	1.14	1.05	1.07	1.11	1.04	0.85	1.07	0.85	0.92	0.95
Tm	0.37	0.49	0.67	0.75	0.82	0.36	0.54	0.71	0.73	0.72	0.71	0.75	0.80	0.52	0.44	0.49	0.43	0.46	0.44
Yb	1.80	2.78	2.81	2.85	3.63	1.37	2.03	3.11	3.33	3.19	3.11	3.34	3.40	2.66	2.3	2.84	2.31	2.54	2.62
Lu	0.22	0.27	0.43	0.45	0.54	0.17	0.24	0.50	0.51	0.51	0.51	0.52	0.54	0.35	0.30	0.35	0.3	0.33	0.35
Hf	8.63	5.89	5.23	6.08	7.33	8.04	10.3	7.86	9.82	9.68	9.86	9.82	8.61	7.62	6.35	6.09	5.28	7.82	5.85
Ta	2.51	1.70	0.62	1.13	1.32	1.00	2.84	2.47	2.55	2.49	2.51	2.70	2.74	2.48	1.98	2.36	1.91	2.06	2.20
Th	2.53	2.06	0.69	1.15	1.36	1.07	2.92	3.03	3.06	3.19	3.21	3.27	3.46	3.25	2.73	3.03	2.41	2.71	2.86

APPENDIX 3: CONTINUED

	ERTA'ALE BASALT																			
SAMPLE	ER30	ER22	ER33	ER35	ER37	ER32	ER38	ER41	ER43	ER47	ER04	ER06	ER07	ER14	ER15	ER16	ER17	ER20	ER34	ER36
	Basalt	Basalt	Basalt	Basalt	Basalt	Basalt	Basalt	Basalt	Basalt	Basal	Basalt	Basalt	Basalt	Basalt	Basalt	Basalt	Basalt	Basalt	Basalt	Basalt
(wt.%)																				
SiO_2	49.50	48.55	47.65	48.59	46.71	47.88	47.76	47.22	47.37	47.14	48.13	48.31	49.73	48.99	49.10	49.15	47.92	49.02	47.10	47.73
TiO_2	2.14	3.44	3.40	3.43	2.82	3.27	3.82	4.29	3.91	3.62	2.56	2.60	2.36	2.52	2.43	2.81	2.51	2.42	2.74	2.64
Al_2O_3	16.34	13.50	13.49	14.20	13.71	13.73	13.67	13.58	13.60	13.56	13.92	14.11	14.41	15.61	15.76	14.72	15.18	16.16	14.33	15.39
Fe_2O_3	11.15	14.19	13.97	14.22	12.28	13.67	15.68	16.15	15.88	15.82	12.47	12.72	12.49	11.93	11.69	12.56	11.62	11.28	12.14	11.68
MnO	0.17	0.22	0.22	0.22	0.20	0.22	0.23	0.23	0.23	0.23	0.18	0.18	0.20	0.19	0.18	0.19	0.20	0.18	0.19	0.18
MgO	6.34	6.05	6.30	5.71	5.21	5.82	5.37	5.48	5.46	5.53	8.59	8.18	6.31	5.96	6.11	6.31	6.43	6.39	6.34	5.97
CaO	11.98	10.55	10.79	10.20	8.57	10.03	9.99	10.00	10.02	10.06	10.35	10.39	11.06	11.60	11.66	11.15	12.15	11.56	12.01	12.03
Na_2O	2.69	2.79	2.79	2.94	3.60	3.03	2.84	3.08	3.03	3.18	3.48	3.72	3.07	2.77	2.86	3.02	2.66	2.76	2.70	2.72
K_2O	0.52	0.86	0.88	0.92	1.16	0.96	0.54	0.62	0.57	0.56	0.49	0.35	0.54	0.64	0.64	0.64	0.62	0.65	0.67	0.65
P_2O_5	0.29	0.49	0.48	0.48	0.51	0.49	0.43	0.42	0.42	0.41	0.39	0.38	0.33	0.35	0.35	0.38	0.36	0.35	0.39	0.37
LOI	-0.28	0.07	0.14	-0.33	5.48	1.34	0.43	-0.48	-0.14	-0.36	0.16	0.12	0.25	0.11	0.08	-0.07	0.82	-0.10	0.55	0.51
sum	**100.8**	**100.7**	**100.1**	**100.6**	**100.3**	**100.4**	**100.8**	**100.6**	**100.4**	**99.8**	**100.7**	**101.1**	**100.8**	**100.7**	**100.9**	**100.9**	**100.5**	**100.7**	**99.2**	**99.87**
(ppm)																				
V	315	411	403	407	404	406	513	518	512	505	354	361	372	347	334	392	331	321	344	342
Cr	146	45.1	47.3	24.9	35.1	38.1	20.3	17.1	18.6	18.5	332	269	25.7	114	126	59.7	90.1	91.4	59.3	97.2
Co	35.7	45.7	48.3	42.3	35.4	42.9	49.6	49.6	49.1	48.2	50.0	42.0	44.1	38.9	38.9	36.9	40.8	41.6	37.5	41.1
Ni	51.9	41.1	46.6	34.9	20.7	35.83	14.5	17.4	17.9	21.7	144.2	120.5	23.9	43.1	47.8	40.6	53.8	54.2	47.7	44.7
As	<3	0.68	<3.9	<5	0.82	0.37	0.73	0.79	0.65	0.77	<3.3	<2.1	<3.3	<3.0	<2.7	<2.7	<2.8	<2.1	<3.3	<3.1
Se	<1.8	<2.5	<2.2	<1.9	<1,67	0.00	1.12	<2,53	0.37	<2,52	<2,167	<2,10	<2,21	<2,14	0.76	<2,44	<2,02	<2,06	<1.8	<2
Br	0.57	0.68	0.69	0.58	0.71	0.66	0.63	0.64	0.66	0.73	0.73	0.65	0.74	0.60	0.56	0.58	0.60	0.59	0.61	0.65
Rb	12.5	20.0	28.0	21.1	29.3	24.6	11.7	12.9	11.6	10.7	8.72	9.64	13.9	12.5	14.9	12.7	14.2	13.3	10.3	11.1
Sr	328	405	415	426	447	423	396	418	402	395	345	374	346	340	341	346	394	408	406	419
Y	36.0	46.2	42.6	48.0	42.8	44.9	45.4	43.0	43.8	43.1	41.9	42.5	44.4	36.6	39.5	43.2	35.3	45.3	35.1	35.1
Zr	234	315	304	331	314	316	244	242	239	229	300	301	328	267	284	271	260	274	266	262
Nb	29.3	54.8	55.5	54.3	53.3	54.5	35.5	38.4	37.4	34.3	37.1	35.8	32.6	34.1	33.5	34.0	36.3	34.1	39.3	38.4
Cs	0.08	0.35	0.27	0.22	0.43	0.32	0.23	0.43	0.29	0.18	<0.2	<0.19	0.15	0.19	0.22	0.09	0.11	0.16	0.12	0.15
Ba	92	132	135	125	136	132	106	129	117	124	115	92	89	107	103	89	113	98	95	118
La	21.8	44.2	46.1	42.3	41.2	43.5	29.1	30.6	28.7	27.4	30.0	27.1	27.0	28.6	28.2	26.2	27.9	29.7	30.4	31.2
Ce	49.9	110	106	115	102	108	77.2	84.4	45.3	75.2	60.0	75.7	64.3	60.0	65.2	65.3	71.2	78.9	75.2	73.0
Nd	25.2	45.5	39.4	39.0	41.3	41.3	35.3	32.3	32.5	32.0	31.0	28.2	27.1	29.9	30.6	27.4	32.5	29.6	27.3	31.2
Sm	5.20	9.85	9.87	8.90	8.64	9.32	8.12	8.02	7.96	7.83	7.06	5.92	6.74	6.62	6.61	5.95	6.43	6.54	6.45	7.09
Eu	1.75	2.83	3.14	2.73	2.83	2.88	2.86	2.92	2.78	2.57	2.38	2.18	2.24	2.29	2.19	2.21	2.26	2.34	2.2	2.45
Gd	4.34	8.6	8.33	8.48	7.70	8.28	8.29	7.72	7.90	6.98	7.93	6.98	7.28	7.16	6.95	6.24	6.67	5.03	5.43	6.6
Tb	0.89	1.31	1.28	1.18	1.37	1.28	1.42	1.39	1.38	1.37	1.05	0.93	1.02	0.99	0.94	0.91	0.92	0.95	0.95	0.98
Tm	0.33	0.62	0.59	0.51	0.59	0.58	0.54	0.57	0.55	0.54	0.74	0.67	0.74	0.69	0.69	0.61	0.69	0.70	0.58	0.65
Yb	2.21	3.33	3.27	3.19	3.23	3.26	3.05	2.93	2.93	2.81	2.69	2.45	2.66	2.60	2.63	2.46	2.34	2.40	2.30	2.52
Lu	0.33	0.40	0.46	0.42	0.47	0.44	0.45	0.44	0.44	0.42	0.43	0.38	0.43	0.40	0.40	0.39	0.38	0.37	0.38	0.40
Hf	7.47	9.3	8.74	9.8	7.94	8.94	8.24	7.94	7.83	7.76	7.86	8.03	8.49	6.62	8.39	7.80	6.57	8.41	6.24	7.45
Ta	2.03	4.2	4.48	3.97	3.96	4.15	2.84	3.17	3.04	2.80	3.02	2.84	2.85	2.76	2.79	2.74	2.92	3.02	2.77	3.06
Th	2.48	5.27	5.71	5.10	4.91	5.25	3.14	3.58	3.22	3.17	3.67	3.49	3.42	3.41	3.39	3.40	3.58	3.56	3.46	3.94

APPENDIX 3: CONTINUED

SAMPLE	HT1 BASALT							HT2 BASALT						LT BASALT	
	E215	E217	E70	E235	E223	E228	E230	E33	E35	E37	E38	E225	E232	E218	E216
	Basalt	Basalt	Basalt	Basalt	Basalt	Basalt	Basalt	Basalt	Basalt	Basalt	Basalt	Basalt	Basalt	Basalt	Basalt
(wt.%)															
SiO_2	46.10	43.45	48.62	48.33	51.00	49.00	50.57	46.80	46.92	46.69	47.49	48.27	46.15	47.43	46.06
TiO_2	3.37	3.73	3.39	2.69	2.48	3.50	3.07	4.28	4.62	4.99	3.79	2.62	4.39	2.26	2.05
Al_2O_3	15.36	15.00	14.20	13.96	15.44	14.43	14.79	9.95	11.49	10.90	9.38	9.57	9.78	16.46	14.44
Fe_2O_3	15.00	15.64	13.54	13.54	10.34	12.47	11.28	14.67	14.07	14.66	12.81	13.10	13.10	13.59	13.39
MnO	0.16	0.20	0.22	0.19	0.16	0.18	0.16	0.20	0.19	0.18	0.17	0.18	0.19	0.19	0.18
MgO	5.48	7.08	5.10	5.44	4.86	5.42	4.48	10.60	7.05	6.84	13.61	13.51	10.00	6.17	9.78
CaO	6.71	7.26	8.84	9.40	9.58	9.00	9.28	9.81	10.35	9.91	8.81	10.10	9.53	8.39	8.53
Na_2O	4.72	4.18	3.16	2.90	3.23	3.21	2.88	2.20	2.46	2.48	1.90	1.84	3.25	3.00	3.39
K_2O	0.76	0.72	0.89	0.83	0.87	1.16	1.02	0.72	0.77	1.11	1.13	0.41	1.21	0.48	0.43
P_2O_5	0.74	0.66	0.89	0.41	0.30	0.55	0.37	0.43	0.51	0.59	0.45	0.28	0.57	0.30	0.30
LOI	1.31	1.37	1.18	1.45	2.43	1.18	1.41	1.52	1.94	2.71	1.66	0.75	1.67	1.17	1.95
sum	**99.71**	**99.29**	**100.03**	**99.14**	**100.69**	**100.10**	**99.31**	**101.18**	**100.37**	**101.06**	**101.20**	**100.63**	**99.84**	**99.44**	**100.50**
(ppm)															
Rb	9.00	8.90	17.0	9.50	27.7	18.7	13.5	19.0	12.0	25.3	26.0	7.90	22.9	3.90	8.40
Sr	928	908	597	463	482	533	522	483	567	687	467	320	442	469	431
Y	21.6	32.0	38.5	32.3	32.9	40.8	36.7	29.0	32.0	37.5	33.9	29.4	36.7	34.3	28.7
Zr	340	339	161	224	223	295	253	318	392	416	330	198	371	155	168
Nb	18.0	17.8	21.0	35.0	21.5	30.0	23.0	36.0	46.0	49.6	37.2	17.0	47.5	5.1	6.5
Cs	0.12	0.18	0.34	0.37	0.70	0.14	0.20	0.26	0.12	--	--	0.15	0.66	0.04	1.03
Ba	190	152	521	317	297	354	338	253	254	336	243	155	297	163	88
La	20.2	18.9	27.0	32.8	23.8	28.5	26.2	31.0	37.0	43.9	27.1	17.9	37.1	8.63	5.49
Ce	57.3	54.1	65.5	69.4	54.9	68.5	61.5	70.0	87.0	103.6	65.0	40.7	87.8	24.5	18.7
Nd	41.2	40.1	45.0	34.8	30.1	40.3	35.5	44.0	52.0	57.3	38.3	25.7	51.9	19.8	17.4
Sm	9.26	9.46	10.1	7.09	6.67	8.89	8.00	9.60	11.1	12.3	8.54	6.15	11.4	5.30	4.96
Eu	3.15	3.22	4.00	2.22	2.15	2.98	2.50	3.00	3.50	3.60	2.56	1.99	3.50	1.96	1.81
Gd	8.46	8.93	10.3	6.99	6.69	8.94	8.02	9.30	10.7	10.8	7.94	6.55	10.7	6.08	5.53
Tb	1.09	1.17	1.40	0.99	0.97	1.27	1.12	1.40	1.50	1.46	1.10	0.94	1.40	0.92	0.82
Tm	0.19	0.33	0.47	0.39	0.39	0.45	0.40	0.40	0.45	0.41	0.33	0.32	0.38	0.43	0.35
Yb	1.02	1.88	2.90	2.35	2.28	2.72	2.43	2.40	2.70	2.40	1.98	1.97	2.08	2.75	2.25
Lu	0.13	0.26	0.44	0.36	0.36	0.40	0.37	0.35	0.39	0.34	0.27	0.29	0.30	0.41	0.33
Hf	7.70	7.60	5.00	5.30	5.40	7.10	6.30	8.80	10.8	--	--	4.80	9.00	3.90	4.00
Ta	1.20	1.20	1.20	2.20	1.30	1.90	1.40	2.20	2.90	--	--	1.10	3.40	0.30	0.70
Th	1.20	1.05	2.01	3.27	2.79	2.29	2.65	3.26	4.02	3.81	2.71	1.42	3.52	0.40	0.31

APPENDIX 3: CONTINUED

	LT BASALT										
SAMPLE	E210 Basalt	E90 Basalt	E88 Basalt	E84 Basalt	E202 Basalt	E178 Basalt	ETH104 Basalt	ETH105 Basalt	ETH106 Basalt	ETH107 Basalt	ETH108 Basalt
(wt.%)											
SiO_2	47.46	47.94	48.05	48.10	49.31	49.10	48.80	47.90	48.40	49.00	50.30
TiO_2	2.26	1.59	1.08	1.15	1.63	1.98	1.96	1.73	1.45	1.27	1.45
Al_2O_3	17.15	15.61	16.05	16.69	15.85	15.58	15.70	15.40	15.20	15.20	15.90
Fe_2O_3	13.66	11.78	11.63	11.35	12.95	13.00	12.80	11.30	12.20	11.80	12.20
MnO	0.17	0.17	0.17	0.18	0.19	0.18	0.17	0.16	0.19	0.17	0.17
MgO	5.96	6.60	8.67	7.74	6.51	6.41	5.67	5.75	6.99	7.68	6.65
CaO	7.69	9.59	10.58	9.76	9.57	10.70	9.98	10.33	10.25	9.93	9.88
Na_2O	3.72	2.76	2.38	2.71	3.08	2.34	2.67	2.67	2.23	2.08	2.60
K_2O	0.58	0.35	0.16	0.24	0.55	0.27	0.56	0.49	0.14	0.69	0.39
P_2O_5	0.34	0.22	0.10	0.14	0.29	0.25	0.25	0.23	0.14	0.12	0.14
LOI	1.27	2.88	1.04	1.18	1.02	0.62	1.11	3.96	1.67	1.56	0.34
sum	100.26	99.49	99.91	99.24	100.95	100.43	99.67	99.92	98.86	99.50	100.02
(ppm)											
Rb	10.8	2.00	1.00	3.00	2.60	8.20	3.87	5.74	0.68	8.35	5.46
Sr	754	423	224	288	439	322	418	464	280	330	333
Y	31.0	26.8	20.7	23.9	28.4	32.1	29.1	26.4	20.1	19.2	22.7
Zr	145	125	61	75	107	140	153	136	94	88	109
Nb	6.2	6.2	2.3	3.9	5.7	6.3	8.2	6.8	5.1	4.1	5.6
Cs	0.29	0.01	0.01	0.03	0.01	0.10	--	--	--	--	--
Ba	176	262	48	98	255	116	265	226	78	285	138
La	8.80	9.30	2.90	4.70	10.1	13.4	12.1	10.5	5.83	4.97	7.82
Ce	24.9	23.0	8.2	12.5	24.8	24.4	30.0	26.0	15.1	13.0	19.3
Nd	19.7	15.9	7.20	9.80	17.3	17.6	20.3	18.1	11.3	9.86	13.2
Sm	5.22	4.10	2.40	2.90	4.46	4.69	5.32	4.69	3.26	2.94	3.70
Eu	1.92	1.50	1.00	1.10	1.58	1.64	1.74	1.56	1.17	1.06	1.32
Gd	5.92	5.00	3.30	3.70	5.17	5.34	5.82	5.12	3.69	3.57	4.09
Tb	0.89	0.80	0.56	0.64	0.79	0.84	0.92	0.81	0.62	0.57	0.68
Tm	0.40	0.36	0.29	0.33	0.37	0.38	--	--	--	--	--
Yb	2.41	2.30	1.90	2.10	2.37	2.30	2.55	2.17	1.75	1.60	1.92
Lu	0.39	0.35	0.29	0.33	0.35	0.36	--	--	--	--	--
Hf	3.80	3.70	2.00	2.40	2.70	3.60	3.90	3.28	2.43	2.21	2.66
Ta	0.40	0.30	0.10	0.20	0.40	0.40	0.51	0.40	0.32	0.25	0.32
Th	0.44	0.62	0.19	0.28	0.39	0.75	0.66	0.45	0.50	0.41	0.74

CURRICULUM VITAE:

MIRUTS HAGOS GHIDEY
Date of Birth: Jan.15, 1974
Nationality: Ethiopian

Current Address:
Brigittenauer Lände 224-228/6836
1200 Vienna, Austria

EDUCATIONAL BACKGROUND:
2007–now**:**   PhD at the University of Vienna, Department of Lithospheric Research
....   Impact research, Petrography, Geochemistry
Research title: ″Geochemical and Petrographic Studies of the Volcano-Tectonic Evolution of Northern Afar: Implications for the Structural Setup of the Actively Expanding Erta'Ale Depression″
Supervisor: Prof. Dr. Christian Koeberl

Second Degree (M.Sc):
Name of institution   Addis Ababa University
Department   Geology and Geophysics
Specialization (Major)   Structural Geology and Tectonics
Year of Graduation   February, 2004
Title of MSc. Thesis: **Rift Margin development: the case of Southern Afar**
....   **Depression, DireDawa area**

First degree (B.Sc)
Name of institution   Addis Ababa University
Faculty   Natural Science
Department   Geology and Geophysics
Major   Geology
Year of graduation   July, 1999 G.C

High School: 1986-1994
          Queen-Sheba Senior secondary school

WORK EXPERIENCE

►Immediately after BSc degree in 1999-2000: as junior geologist at the Commission for Sustainable Agricultural and Environmental Rehabilitation in Tigray (CoSAERT), Ethiopia.
►From 2000–2007, academic staff at the Department of Earth Sciences, Mekelle University, Ethiopia.
Positions:
Director of the Institute of Paleo-Anthropology Human Evolution and Culture (IPAHECA), Mekelle University.

CONFERENCE PARTICIPATION:
- o Geological Parameters for Environmental Protection, organized by Addis Ababa University, Department of Geology and Geophysics, held in Addis Ababa from Jan. 20-24, 2000.

- Organizer of the International Conference on Science, Natural Heritage, Cultural Heritage and Eco-tourism held in July 2005 at Mekelle, Tigray, Ethiopia.
- Highland2006 conference: Environmental change, geomorphologic processes, land degradation and rehabilitation in tropical and subtropical highlands; held in Mekelle from Sept. 19-25, 2006.
- International conference on Enriching the Development of Tourism in Ethiopia. February 28 – March 1, 2010, Addis Ababa, Ethiopia.
- Geoscience Education in Ethiopia: Opportunities and Challenges. 27 – 28 August 2010, Addis Ababa, Ethiopia

LIST OF PUBLICATIONS:

Papers published in refereed journals:
- Schmid T., Koch M., DiBlasi M., and **Hagos M. 2008.** Spatial and spectral analysis of soil surface properties for an archaeological area in Aksum, Ethiopia, applying high and medium resolution data. Catena 75, 93–101.
- **Hagos M.**, Koeberl C., Kabeto K., and Koller F. 2010. Geology, petrology and geochemistry of the basaltic rocks of the Axum area, Northern Ethiopia. In: Ray J., Sen G., and Ghosh B. (Eds.), Topics in Igneous Petrology. A Tribute to Prof. Mihir K. Bose, Springer, Heidelberg , in press.
- **Hagos M**., Koeberl C., Kabeto K., and Koller F. 2010. Geochemical characteristics of the alkaline basalts and the phonolite-trachyte plugs of the Axum area, northern Ethiopian. Austrian Journal of Earth Sciences, in press.